Navier-Stokes Simulation of Steep Breaking Water Waves with a Coupled Air-Water Interface

by

Kelli L. Hendrickson

Submitted to the Department of Ocean Engineering
in partial fulfillment of the requirements for the degree of

Doctor of Science

at the

MASSACHUSETTS INSTITUTE OF TECHNOLOGY

February 2005

Author .....
Department of Ocean Engineering
December 17, 2004

Certified by .....
Dick K.P. Yue
Professor of Hydrodynamics and Ocean Engineering
Thesis Supervisor

Accepted by .....
Michael Triantafyllou
Professor of Ocean Engineering Chairman, Departmental committee
on Graduate Studies Department of Ocean Engineering

Navier-Stokes Simulation of Steep Breaking Water Waves with a Coupled Air-Water Interface

by

Kelli L. Hendrickson

Submitted to the Department of Ocean Engineering
on December 17, 2004, in partial fulfillment of the
requirements for the degree of
Doctor of Science

Abstract

Wave breaking on the ocean surface significantly facilitates the transfer of mass, momentum, heat and energy across the air-sea interface. In the context of the near field flow about a surface ship, the breaking bow wave is a key element to the bubbly signature and an appreciable portion of the wave drag of the ship. Yet, despite its direct effect on many aspects of ocean engineering, this phenomenon is not well understood even at a basic level. Most of the knowledge has been contributed by experiments in the laboratory and the field although results are often limited due to the difficulty in taking measurements of local quantities during the breaking event. Numerical solution of the breaking wave problem has generally been limited to the pre-breaking phase as it avoids complex mechanisms such as surface re-entry, spray formation, air entrainment and strong turbulence. Additionally, relatively few experimental or numerical studies exist which dynamically couple the air-water interface.

The objective of this thesis is to contribute to the knowledge of steep breaking waves in the context of the coupled air-water interface. Of central importance are basic kinematics and dynamics, the rate of energy dissipation and energy flux at the interface during the breaking event. To this end, a systematic study of a range of breaking waves is performed by direct numerical simulation (DNS) of the Navier-Stokes equations using an Eulerian interface capturing method. The advantage of the DNS approach is that all physical scales are resolved and no turbulence closure models are necessary. However, because of this, DNS is limited to the study to moderate Reynolds numbers with a relatively high computational cost for each simulation. For this reason, this study is limited to two-dimensional flows at Reynolds number $O(10^3)$. The interface capturing method used is a modified form of the level set method which is better suited for simulating coupled air-water flows. The level set method provides a natural numerical treatment of the coupled air-water interface through complex surface topology changes. Thus, no *ad-hoc* treatment of the air-water interface during the breaking event is necessary.

The key findings of this thesis represent new contributions to the study of breaking waves in three distinct areas. The first is the kinematics and dynamics of deep water

breaking waves for both spilling and plunging types. For the waves in this study, there was no indication of flow reversal or separation in the water while the air flow showed separation on the front face of the wave and over the crest. Localized shear regions are found in spilling breaking waves and curvature effects are identified as the dominant mechanism of vorticity generation in both types of breaking waves.

The second area is the energy dissipated by breaking waves. The volumetric dissipation rates as well as its spatial variation for both air and water are presented for the range of waves in this study. While the water volume experienced an increase in dissipation rate during the breaking event, the increase is more pronounced in the air volume to the point that it becomes the same order of magnitude as that in the water for some waves. The amount of energy in the wave lost due to breaking is quantified as a function of the energy in the wave prior to breaking. A threshold below which waves do not break is identified and qualitative comparisons to experiment are made when applicable.

The third area is the transfer of energy at the air-water interface during breaking which is an aspect of the breaking process that has not received much attention in the literature. In this thesis, the formulation of a term in the energy equation which accounts for the energy flux rate at the air-water interface is presented. The waves in this numerical study give evidence that this quantity is appreciable. Although the calculation of this term is sensitive to errors associated with the conservation of energy, values as high as 25% of the energy lost to breaking are found. At the Reynolds numbers in this study, the dominant mechanism for each type of wave is identified as inviscid for spilling breaking waves and viscous for plunging breaking waves.

This numerical effort has contributed to the basic knowledge of wave breaking at moderate Reynolds numbers. Through the inclusion of the coupled air-water interface, unique insight to the kinematics, dynamics, dissipation and energy fluxes of breaking waves was obtained. The information gained in this study provides an initial step towards physics-based turbulence models for the study of wave breaking at larger scales.

Thesis Supervisor: Dick K.P. Yue
Title: Professor of Hydrodynamics and Ocean Engineering

For my parents

who taught me I could do anything.

For Heath, Annaleise, and Geneva

who inspired me to finish what I started.

Acknowledgments

This day has been a long time coming and there are many, many people who deserve credit for helping me get to this point. If I miss someone, I can only hope that I thanked you along the way for the help you provided.

I can not thank my thesis advisor and friend Dick K. P. Yue enough for his tireless support academically and financially. Our spirited "discussions" have taught me not just about hydrodynamics but also how to communicate my work, teach others and manage projects. He took a naive Aerospace engineer with a mild interest in boats and turned her into a hydrodynamicist with a passion for the ocean. He has always respected my desires to balance my personal and professional life within the meat grinder which is MIT. For that alone, I am eternally grateful.

I also wish to thank the other members of my committee Professors Michael Triantafyllou and Nicholas Makris and Dr. Doug Dommermuth who have helped not just with their physical insights and experience regarding the problem, but in their patience and understanding over the years. While our paths never directly crossed at a professional level, Dr. Yuming Liu has lent me his support, guidance and unwavering confidence for which I will always be grateful. I would also like to gratefully acknowledge the Office of Naval Research for funding the various research projects that have lead to this dissertation. The contracts first monitored by Dr. Edwin P. Rood and now by Dr. Patrick L. Purtell have provided not just the financial and computational support for this thesis but an arena for scientific discussion.

I would not be where I am today without the tutelage and friendship of Dr. Lian Shen who mentored me almost as a second advisor shortly after I arrived at MIT. In my early days at MIT, his continuous open door policy and tireless answering of my questions taught me much about hydrodynamics and computational fluid dynamics. In the later years, his example of "how to do research" inspired me to always "dig deep" on a topic and not be satisfied with "good enough". His friendship over the years has always helped keep my spirits up and his frank conversations always provided me with the reality check I sometimes so desperately needed.

At a personal level, I owe a sincere debt to Mr. John Levesque of Cray, Inc. who has had many professional affiliations over the span of my knowing him. He has always been my computer guru. To say that he taught me everything I know about high performance computing would be an understatement. He taught me what was necessary to make the countless versions of this code "slicker than snot". His knowledge about all of the various platforms I have come across over the years has greatly contributed to this thesis whether he will admit it or not.

For his endless discussions about the Red Sox and the Patriots, politics, pressure solvers, hydrodynamics and just about anything else in life, I am indebted to Ben Connell for his friendship. While it started off as me mentoring him about computational fluid dynamics in the way that Lian mentored me, it has grown to be a sincere friendship that happens to discuss computational fluid dynamics along with politics and sports.

My sincere gratitude goes to my friend of many years, Guangyu Wu for all of the discussions about CC Mei's homework in the early days, raising babies in the later days and the seemingly endless help with the lab throughout it all. Somehow we became friends and it seems to have stuck for which I am grateful.

To Alexandra Techet, I thank her not just for her friendship and help with 13.021 but for laughing at people's inability to tell us apart. To Arcti Kiara, I thank her for her friendship and refreshing outlook on life. I would also like to thank all of my friends in the VFRL over the years who have provided me with interesting discussions and amusing experiences as lab manager. In particular, I would like to thank all of you for leaving me alone this last year.

I turn now to those that have influenced me the longest and the deepest throughout my life. My parents always encouraged me to be whomever and whatever I wanted to be. They didn't grieve too long when I put flute and piano aside after high school to study rockets and become the first woman on the moon. They didn't blink when I married a boy from Indiana (a.k.a the Yankee) and moved to Boston (somewhere north of Texas) to study the ocean instead of rockets. They politely stopped asking when I would finish after about the fourth year. Through it all, as long as I was

happy with the path that I had set myself, they supported me without question. I will always be grateful for that life lesson and I can only hope to do as good a job at supporting my children in their life decisions as they have done with both my brother and myself.

Though my brother will not admit to having had anything to do with the completion of this thesis, he has in his own way. In the time that I have been dawdling about the comfort of MIT, he has climbed 80-foot poles for the power company to master his fear of heights, become a father and joined the Army to provide for his family. His induction into the Army Rangers as a special forces medic in July 2001 was one of the proudest moments of my life. His ability to jump out of perfectly good airplanes in the dark amidst the "fog of war" amazes me to this day, especially as he never quite conquered that fear of heights. His numerous tours of service in Afghanistan and Iraq since September 11th has simultaneously scared me to death and made me infinitely proud of him. In it all, he has been a constant reminder of what a person can accomplish if they set their mind to it. For that, I will always be thankful.

Lastly, and most important of all, I thank my husband, Heath, for his never-ending love, friendship and support over these almost nine years of marriage. For selling cars and working at DRC when we first moved here. For the infinite patience when things weren't going well. For being an unbelievably good father to our daughters. For picking up the slack these past few months. For never, ever asking when I would finish when he, of all people, had the right to ask. For the multitude of other little and big things too numerous and private to be listed here, I thank you.

Most people leave some jewel of wisdom or witty comment at the end of their acknowledgements, so I will leave anyone who reads this with the motto which has helped me make many decisions in life: "You don't *have* to do anything you don't want to do. You just have to be willing to accept the consequences of your (in)actions." Take it for what you will, but it has always kept my life in perspective.

And now, in the famous words of Annaleise Jean (not but 2): "Mama bye-bye."

Contents

List of Figures

List of Tables

Chapter 1

Introduction

The dynamics of the ocean surface have been an important topic of study as long as man has answered the call of the sea. The dangers present in the ocean must have been of particular interest as ocean travel involved fishing, exploration and trade. All of these activities still comprise a significant portion of the global economy as well as aspects of the ever present search for crude oil and the dependance of a nation's national security on its Naval defense force for transportation of its armed services and protection of its ports. The role of the ocean in the global climate change is also distinctly vital as we are learning how local oceanic occurrences such as *El Niño* effects the weather patterns on a global scale. Wave breaking plays an important role in the dynamics of the ocean surface and thus touches just about every aspect of human life. Yet, the complexity of the physical problem and our ability to quantify it has severely hampered our understanding of it.

At a basic level, wave breaking effects the rates of transfer of energy, momentum, heat and mass between the air and the sea and can drive many atmospheric and oceanic circulation processes. This gives them a direct effect on the global climate. Additionally, the absorbtion of atmospheric gases by the ocean plays an important role in climate modeling and prediction [96, 44]. Ocean wave breaking effects the air-water gas exchange through turbulence under the surface and wave breaking [7]. Thus, it has a large effect on climate modeling efforts. From a layman's point of view, poor understanding of the coupling between the atmosphere and the ocean effects all

aspects of weather prediction from basic day to day effects to better prediction of hurricane tracks.

In deep water, wave breaking not only effects climatology efforts, but causes significant dynamic loading on ocean engineering structures such as off-shore research platforms and oil exploration efforts. At present, predicting the magnitude, duration and occurrence probabilities of the wave impact pressure is difficult as current prediction efforts are considered unreliable [79]. The severe loading on such structures can cause significant fatigue and ultimately result in damage or loss of structures. In the surf or coastal zones, breaking waves contribute to extensive erosion of the coastline and damage to harbor and coastal structures such as sea walls. Thus, it has direct effect on coastal management policies about the world.

Within the context of ships, the breaking of the bow wave is partly responsible for the bubbly wake of surface ships. This signature plays a key role in remote detection and counter-measure development which is of vital interest to Naval defense forces. The energy lost in the breaking bow wave of a surface ship can account for up to 15% of the drag of a surface ship [2]. Shaving even a modest percentage of drag from a surface ship can lead to a substantial increase in the fuel efficiency of not just Naval vessels but of the entire maritime trade industry. Additionally, as the Navy presses the design envelope further to unconventional hull forms and unconventional operational zones, current computational design packages are used outside of their limitations. These design capabilities have little or poor wave breaking, spray formation and air entrainment modeling capabilities.

As wave breaking is such a vital area of concern, it is an active area of research. There are many recent review articles on the subject. In fact, much of the information in this chapter is based on information from these reviews. For a recent review of wave breaking effects on air-sea interactions, see Melville [75]. It discusses aspects of the topic from an experimentalist point of view such as measurement techniques, recent wind-wave modeling efforts, wave breaking dissipation, the ocean boundary layer, gas transfer and acoustic signatures.

Deep water wave breaking is reviewed in Banner and Peregrine [4] again from an

experimentalist point of view. Measurement techniques for the field and laboratory are discussed. Theories associated with wave breaking and wind-wave modeling are also discussed. Finally, the effects of air entrainment and bubble clouds are also cited. Although there is some duplication, a similar review by Banner [3] is also recommended.

A thorough discussion of the aspects of spilling breaking waves is done by Duncan [31]. This review discusses the definition of spilling breaking waves and the effects of surface tension. Unsteady and steady breaking waves are discussed in detail for long and short waves as well as two- and three-dimensional wave breaking. The review is again mainly from an experimentalist point of view; however, there is also a brief discussion on available numerical results.

1.1 Types of Wave Breaking

The criteria for classifying breaking waves is relatively vague and dates back to the effort to classify beach conditions during World War II [34, 47, 71]. In the open ocean, there are generally two types of broad classifications used in the literature which are plunging and spilling breaking waves. In coastal zones, a third type called surging is also commonly referenced. In plunging breaking waves, the wave crest forms a jet which overturns. The sheet of water which makes the jet, plunges down on the front face of the wave, creating an air pocket and a secondary splashing event. In general, once the sheet of water impacts the wave, bubbles, spray and turbulence form almost instantaneously. Plunging breaking waves are in general an unsteady event; however, in the context of ship breaking waves, this is not necessarily the case. Plunging breaking waves are less common in deep water. They tend to be more dominant in coastal regions where bottom topology and shoaling forces the energy of the wave to produce a plunging breaker. This can be seen on every beach and in the more fantastic "pipes" loved by surfers.

Spilling breaking waves are associated with a rough patch on the crest of the wave which falls down its front face or potentially spills off of the back. There is a

characteristic formation of a bulge on the front face of the wave. The bottom of the bulge is generally called the toe and usually has an associated capillary wave train extending from it and continuing down the face of the wave [66]. The presence of the capillary wave train at the base of the bulge is believed to trigger an instability which causes the bulge or rough patch to travel down the face of the wave. In some disciplines such as physical oceanography, spilling breaking is defined when a patch of "white water" is seen to move along the face of the wave [4]. This white water or air entrainment is not necessarily a criteria for spilling breaking waves in other fields where the formation of the bulge is considered a criteria [31]. This is mainly a function of the scale investigated as smaller scale spilling breakers do not usually have white water associated with them. There has been an effort in the physical oceanography community to recognize breaking not associated with white water which they call microbreakers due to their relative size in the open ocean ($\lambda < 30$cm)[4]. For the purposes of this study, we will call any breaking wave which does not form a jet a spilling breaking wave. In general, most breaking in the ocean is of spilling type and is unsteady in nature. However, again in the context of ship waves or waves behind submerged bodies, this is not necessarily the case.

Breaking waves are also classified by their temporal evolution as either unsteady or steady (or quasi-steady) events. An unsteady breaking wave is a brief event, generally within a wave period, and relatively random in the open ocean. Once the mechanism which initiated the breaking event has expired, unsteady breaking waves no longer continue to break. For example, if the wave is breaking because of a local excess of energy due to focusing, once the increased dissipation in the wave has dissipated this energy, the breaking event stops shortly thereafter. Unsteady breaking waves may even have periodic events of breaking caused by a periodic focusing of energy as a wave passes through a region. However, each event is relatively short and unique.

Steady breaking waves are a sustained event and generally occur near submerged moving objects or still objects subject to a current. Within the reference frame of a ship, the breaking bow wave is considered to be a quasi-steady breaking wave. It has a plunging component near the ship which becomes a spilling breaker in the near

field. Because steady breakers have a sustained source of energy (namely the presence of the body), the wave will continue to break as it must continuously dissipate the energy which the body is inputting. A quasi-steady (two-dimensional) breaking wave is always a spilling breaking wave. It has an associated bulge and toe, but unlike the unsteady spilling breaking wave, they do not propagate down the front face of the wave. In general, the bulge is described as a region which has separated from the wave flow underneath and continuously injects a turbulent wake into the fluid surface. The quasi-steady aspect of the description has developed over the years as researchers have identified a low frequency oscillation of the breaking region on the wave face. For experimental efforts in steady wave breaking, the reader is referred to the works by Duncan [30, 29] as well as Lin and Rockwell [59]. Theoretical work in the area was done by Cointe and Tulin [15] in which a model for two-dimensional steady breaking was developed. Numerical efforts in this area were performed by various authors in an effort to use Duncan's experiments as a benchmark for viscous numerical simulations [45]. One might argue that quasi-steady breaking might entail a cyclic breaking event such as a train of waves impacting a seawall over a long period of time [60]. The forces on the seawall will be dominated by the repetitive action of the wave on the wall such that on a long time scale, the event could be considered quasi-steady and information regarding the mean loadings, etc. could be computed.

Finally, a short comment about two- and three-dimensional breaking. In my humble opinion, the concept of two-dimensional breaking is really an invention of numerical methods and to some extent experimental investigations. Waves which begin as two-dimensional wave trains traveling down a wave tank will develop three-dimensional flows as soon as the wave breaks and turbulence is formed. Even two-dimensional steady breakers have three-dimensional flow components to them as the flow in the bulge is turbulent. For plunging breaking waves, Perlin *et al.* showed the existence of a longitudinal variation along the front before it plunges and Longuet-Higgins [67] described the breakup of the jet of a plunging wave as a distinctly three-dimensional process.

These arguments make it appear as if two-dimensional studies of breaking waves

are not relevant. However, the saying "we must walk before we run" comes to mind. The investigation of wave breaking using two-dimensional techniques has helped answer many basic questions regarding breaking mechanisms as up until the breaking point the three-dimensional effects are minimal. A two-dimensional investigation is also not out of the question for small wavelength waves where the Reynolds number is moderate and the formation of turbulence generally reserved for the most violent of breaking events. This is also the case for infinite Reynolds numbers where the flow is modeled using potential flow. Inviscid numerical methods can compute up to the breaking event and have contributed to a significant amount of knowledge on pre-breaking effects in plunging breaking waves. However, due care must be taken in addressing issues regarding scale and the physics of air entrainment and bubbles. As turbulence becomes more prominent after the breaking event for larger wavelengths (and thus Reynolds numbers), many conclusions must be made with caution. That being said, however, the predominance of current numerical and experimental investigations are based within the context of two-dimensional flows. Investigations of truly three-dimensional waves are relatively few in number [80, 107, 128, 62].

1.2 Breaking Mechanisms

There are various mechanisms which have been identified as causing wave breaking. Initially addressed by Stokes [106], there is a theoretical limit to the wave steepness ($ak = 0.4432$). Once a wave has reached this steepness, the particle speed in the crest of the wave is equal to the phase speed. Anything greater will produce a breaking wave. However, many researchers have found that instabilities contribute to breaking at much smaller slopes. Experiments have shown that for slopes less than 0.3, two-dimensional Benjamin-Feir stabilities can cause waves to break [73]. Numerical simulations show that this instability, which consists of a wave with a central frequency and small-amplitude sidebands, can see waves break with slopes as small as 0.1 [19, 69]. The Benjamin-Feir instability slowly develops and can take on the order of 100 wavelengths before it causes a wave to break [31]. Thus, its importance in the

open ocean is questionable as other factors may take precedence before this instability has time to develop. For instance, in three dimensional waves, instabilities cause the wave to break much more rapidly [107].

For the open ocean where waves propagate in an infinite number of directions and the environment is not controlled, the dominant mechanisms for breaking in the open ocean are cited as wave-wave, wave-current and wind-wave interactions. At some level, all of these mechanisms are associated with the energy in the wave. Wave-wave interactions form through dispersion or wave focusing. In the case of dispersion where waves traveling with different speeds and different directions can focus in one location. If the focusing is adequate, it yields an unsteady breaking event. This type of dispersive focusing technique is used primarily in laboratory experiments as the location of the breaking event and many quantities about the breaking wave can be controlled. Another wave-wave interaction which may lead to breaking is the modulation of a group of waves by their envelope. It has been reported that waves are prone to periodic breaking as they passed through a group [25]. Banner and Tian [5] show that the modulation of a wave group can lead to recurrence of the wave group (no breaking) or a breaking event. However, the existence of groups in the open ocean is an abstract concept and difficult to confirm [103]. Even so, a modulation can lead to wave breaking.

Wave-current interactions happen anywhere a current exists in the ocean. However, they are much more prominent where tidal effects set up currents in and out of harbors and along coastal regions with naturally occurring inlets. Depending on the relative velocity between the current and the wave group, the wave energy can be reflected from the current. This causes a focusing of energy near the reflection area and if sufficient, will cause waves to break.

Wind-wave interactions occurs as the wind blows over the ocean surface. Through surface friction, the wind, imparts energy into the waves. Depending on the wind speed, the wave age (how long the wind has been blowing), and the fetch (the area over which the wind blows), the waves will develop until they break. Each of these parameters have a profound effect on the breaking event as well. As the wind is an

ever present quantity in the open ocean, this topic has received considerable attention in field experiments. In fact, it is difficult to find field measurements of breaking waves where the wind is not a part of the picture.

Perusal of the literature associated with wave breaking reveals that the breaking event is a complex phenomenon. The multitude of breaking mechanisms and the large range of scales associated with wave breaking can skew the results in a particular direction. For example, the energy lost in wave breaking in the laboratory experiments which use dispersive focusing is sensitive to the three-dimensionality of the wave [80] and the gain on the wavemaker [54]. Breaking waves at smaller scales dissipate energy but do not entrain air or form white water on their faces. As the air entrainment is also a factor in dissipation, waves which entrain air should have more dissipation than those that don't [55]. Waves generated in a steady breaking experiment have an order of magnitude greater than unsteady breaking waves [74]. Thus, the results of any breaking wave study may critically depend on the breaking mechanism involved.

1.3 Missing Links in the Knowledge of Breaking Waves

As breaking waves are an active area of research, much is known about the kinematics of wave breaking, especially at length scales around 1m which is the common wavelength for laboratory experiments. However, there are three broad areas where the lack of knowledge is painfully obvious and relatively restrictive in the advancement of the field. They are the dissipation associated with breaking waves in a global and local sense as well as its effect on the spectral evolution of waves, the effect breaking waves have on the fluxes at the air-water interface, and a universal breaking criteria.

One important area of research is wind-wave forecasting. While a rigorous theoretical foundation for the prediction of wave evolution does not yet exist [75], the use of the radiative transfer equation [87, 51] has become the predominant method of wind-wave forecasting. The radiative transfer equation is based on evolution of the

wave action spectral density $N(\vec{\mathbf{k}}) = gF(\vec{\mathbf{k}})/\sigma$:

$$\frac{dN}{dt} = \frac{\partial N}{\partial t} + \left(\vec{\mathbf{c_g}} + \vec{\mathbf{U}}\right) \cdot \nabla N = S_w - S_{NL} - S_{diss} \tag{1.1}$$

This simply states that by evolving the wave action spectral density, it is possible to predict what waves make up a region of the ocean surface a little later in time. This is all dependent upon the quality of the models on the right-hand side of the radiative transfer equation which makes it an active area of research. S_{NL} is the term responsible for nonlinear wave-wave interactions and was formulated by Hasselmann [43]. The only challenge associated with this term is effectively and efficiently calculating it. Parameterizing the effect of wind input (S_w) and the dissipation (S_{diss}) on the spectrum comprises the bulk of the wave forecasting prediction problem. There are some commonly accepted models for each term, for which I refer the reader to Komen *et al.* [52] for the most up-to-date treatment of these terms. However, it should be pointed out that the dissipation term is the least well understood term. A few models exist which use equilibrium range assumptions to deduce the spectral slopes. Yet, how the dissipation affects the spectrum of the waves in the ocean for a large range of wave numbers is still elusive.

A clearer picture of the dissipation of a single wave or group of waves has begun to form with the help of laboratory experiments. As the wave generation is much more controllable in the laboratory verses the field, parametric studies can be made. For two-dimensional wave groups, Rapp and Melville [92] performed extensive measurements of the energy dissipation and momentum flux for a range of breaking waves caused by dispersive focusing. Their study characterized the global momentum flux and energy lost during breaking as a function of an integral slope parameter. They also included an investigation of the spectral evolution of the wave group through breaking where they were able to identify a build up of energy in high frequencies and quantify change in the spectrum after breaking. Finally, they found that most of the energy lost to the breaking event had been dissipated by turbulence in about four wave periods which shows that the turbulence dissipation is significantly higher

after breaking.

The only three-dimensional breaking waves performed in the laboratory where dissipation was measured were done by Nepf *et al.* [80] where a similar technique of dispersive wave focusing was used to generate breaking waves in a wave basin. They found that in the three-dimensional case, the amount of energy dissipated during the breaking event was somewhere between that of a spilling and plunging breaking wave as the three-dimensional breaking event itself was a plunging breaking wave in the center which tapered to spilling events at the edge.

These experimental efforts have provided a great step forward in quantifying the energy dissipation during breaking for dispersively focused waves. Yet, until just recently, the investigations have only been focused on dissipation as a global quantity. While a global measure of the energy lost to breaking can provide important information, it is incapable of providing information regarding local relationships. Determining the local dissipation rate for breaking is essential for developing physics-based numerical models. Having adequate numerical models for wave breaking dissipation is a remaining challenge in the computations of the near field flow around a surface ship and extending the knowledge of wave breaking at relevant physical scales. Not only will computations help with the design of advanced hull forms and help fill in the gaps of information unattainable by experiments, they have the potential of helping focus experiments in particular areas of interest. Thus, while the current body of experiments have added to our understanding of breaking wave dissipation, there is considerable work which needs to be done.

The second area where our knowledge of breaking waves is lacking is on its effect of the fluxes at the air-water interface. Through the increased velocity and turbulent fields in the breaking region as well as air entrainment, the mass, momentum and energy fluxes are significantly altered by wave breaking. Much attention has been placed on the wind energy input into the wave field, but nothing has been placed on the reverse process. Experimental studies in the field have again provided most of the knowledge on the global and average properties. Current numerical studies generally do not couple the air and water boundary layers, leaving their influence on each other

as parameters. There has been very little computational effort expended to perform direct numerical simulations of the coupled air-water boundary layer much less in the context of the effects of wave breaking. As in the case of dissipation, understanding local effects of the energy fluxes is critically important to developing physics-based models which will enable numerical studies at larger scales which will enable further model development and parameterizations.

The final missing link is the development of a universal breaking criteria. For obvious modeling reasons, it is desirable to be able to look at some quantity of a wave, whether it be a local or global quantity and determine if it is going to break. In addition, to be able to tie that quantity to other aspects such as mechanical energy lost, gas transfer rates, thermal effects, air entrainment, etc. appears to be the "holy grail" of wave breaking investigations. Whether or not this will be successful is actively debated in the community. The difficulty of trying to reduce the entirety of the complex physics of a breaking wave to a single number is a daunting task which a few brave souls are attempting.

There are a multitude of proposed breaking criteria in the literature. They fall into four categories. The first is a geometric criteria based on local and global wave steepness similar to the idea behind Stokes limiting wave. The local criteria which is cited considers asymmetry and crest front steepness. The global wave steepness is an integral slope parameter based on the sum of the spectral components. Yet, the presence of instabilities can affect these criteria and it has been pointed out that this type of criteria must be scale dependent [75]. The second type is a kinematic criteria which relates relative speeds in the wave. One version uses the particle speed compared to the crest phase speed. The other version considers the orbital speed in the crest to the group speed [122, 115]. The third type of criteria is a dynamic criteria which considers the evolution of the higher harmonic frequency range of the spectrum based on the type of observations made by Rapp and Melville. For a recent review of the criteria, the reader is referred to Wu and Nepf [127].

The fourth type of criteria which has been proposed recently which is based on a local growth rate. This type of criteria was introduced by Dold and Peregrine

[19] and championed further by Banner *et al.* [5, 103, 104]. The idea behind this criteria is that the there is a mean convergence of energy density as the wave group is modulated by the envelope. This returns to the wave-wave interaction idea where a local convergence of energy causes the wave to break.

As the relative usefulness of these criteria is still a hotly debated topic, few have tried to associate this to the strength of the breaking event or other breaking effects. Additionally, this type of study requires a large database of breaking waves and effects to make strong conclusions. Wu and Nepf [127] have centered on the kinematic criteria as it is easier to measure in the field. Rapp and Melville have keyed on the integral slope parameter as a global measure of the energy in the wave. However, there is some scatter in results once the threshold of breaking has been crossed. Song and Banner and Banner and Song [103, 104] have had some limited success in the criteria based on the growth rate. Yet, the sparsity of the data has limited the success of these criteria much less tying them to other breaking effects.

The applicability of these criteria in the open ocean is difficult. Many of the criteria are based on the existence of wave groups and characteristic information regarding the groups. The existence of groups in the open oceans has still not been confirmed. Other criteria are based on point measurements. A single point measurement when waves travel in all different directions represents the wave at an undetermined stage of evolution. This type of information makes it difficult to infer a breaking criteria and does not describe the intermittent occurrence of wave breaking in the open ocean. A better measure than surface kinematics and dynamics may be the process of interest [75]. A universal breaking criteria may not be within our reach at this time, but a criteria which governs the dissipation or heat transfer, etc. may be much more effective and easier to obtain.

While wave breaking is an active area of research, there are key areas where detailed knowledge is lacking. They are the dissipation and dissipation rates of breaking waves, the fluxes at the air-water interface during the breaking event and a universal breaking criteria. Experimental investigations have begun to scratch the surface in gaining this knowledge; however, measurements even in the laboratory during

the breaking event are extremely difficult especially if air entrainment is involved. Numerical investigations of the topic can lead to improved knowledge in the area, enhanced statistical quantities by expanding the available database, and help focus future experimental efforts.

1.4 Numerical Investigations

Up until the past few years, numerical studies of breaking waves have been dominated using two-dimensional potential flow methods. These methods make irrotational and incompressible flow assumptions and have no viscous effects [68, 24]. Some three-dimensional potential flow studies have also been accomplished recently [128, 62]. All of the methods available in this area are unable to go past the breaking event without some *ad-hoc* treatment of the interface at jet re-entry as well as dissipation effects necessary to model the energy lost during breaking. Thus, most of the work on wave breaking dynamics has been relegated to field and laboratory experiments.

Some very early works which include viscous effects are around [39]. However, the method involved in tracking the interface was low order and the quality of results in terms of determining kinematics, dynamics and dissipation effects is poor. More recent studies have used surface following grids in which the free-surface boundary layer could be resolved [31]. However, these methods can not do plunging events. Recent years has seen the application of a new class of interface capturing schemes such as volume-of-fluid, level set methods and smoothed particle hydrodynamics to wave breaking problems [13, 46, 120, 53, 98]. These methods allow for natural treatment of the surface re-entry and breakup; however, with the exception of the volume-of-fluid method, the interface capturing methods are in their infancy in development and rigorous proofs of convergence. Few works in the literature have been able to quantitatively answer the questions posed about dissipation, interface fluxes and breaking criteria. All of the recent viscous works are two-dimensional. The computational effort for a three-dimensional breaking wave which includes viscous effects is significant and it has not been attained in archival journals yet.

The main restriction in the viscous works is the limitation of the Reynolds number for direct numerical simulations (DNS). In waves, the Reynolds number scales as $\lambda^{3/2}/\nu$ and at the laboratory scale is $O(10^6)$. In general, the best Reynolds number attainable by viscous flow codes without turbulence closure is $O(10^4)$ providing that the free-surface boundary layer is resolved adequately. While the interface tracking methods which use a surface following grid are better suited for clustering points near the interface, they still are limited to cases where the surface remains single-valued and air is not entrained. Methods which use interface capturing do allow for multi-valued surfaces and air entrainment. However, unless a large number of grids is used, they require advanced gridding techniques to have adequate resolution near the air-water interface.

To increase the Reynolds number to scales seen in the laboratory let alone those seen in the field, a certain amount of turbulence closure modeling is needed. Such methods as Large-Eddy Simulation (LES) and Large-Wave Simulation (LWS) as well as RANS calculations have been computed [18, 14, 60]. However, as the turbulence closure modeling for steep breaking waves is also in its infancy, the results are promising at best. Significant progress has been made with the work of Brocchini and Peregrine /citeBrochPer as they have begun the step forward in developing a framework in which to begin these modeling efforts for RANS calculations. However, real progress will only be made if physics-based models are developed for use in these methods. These models can only be developed if a detailed picture of the physics involved can be achieved. This can only be accomplished using detailed experimental measurements or high quality DNS.

The application of numerical methods to the investigation of wave breaking has been around for a quarter of a century. They have enriched our understanding of waves prior to the breaking event. However, not until recently have numerical capabilities developed which allow us to simulate past the breaking event without some type of modeling effort. Direct numerical simulation is a necessary step towards developing physics-based turbulence closure models which can be implemented into larger scale computations such as LES and LWS as well as RANS.

1.5 Scope of Thesis

This thesis will attempt to begin to answer the some of questions posed in the previous section: namely to gain understanding of the kinematics and dynamics of breaking waves, their dissipation and the transfer of energy at the air-water interface. We choose direct numerical simulation of the Navier-Stokes equations to preclude the use of any turbulence closure models which may mask the physics involved. The air-water interface is modeled through the level set technique which allows for a natural treatment of plunging events and air entrainment. Simulating the effects of the entire coupled air-water boundary layer allows us to capture all of the physics governed by the Navier-Stokes equations. As this is a first attempt to fully simulate the coupled air-water boundary layer for wave breaking, effects such as salinity, surfactants, temperature, gas-exchange, etc. have been left for future work. This numerical investigation is a two-dimensional study; however, extension to three-dimensions is not hampered by the numerical method or governing equations but is also relegated to future work.

The outline of this thesis is as follows. In *Chapter 2*, the formulation of the multi-fluid governing equations (conservation of mass and momentum) presented within the context of the level set method. A description of the level set method is included as is the governing equation which evolves the air-water interface. The multi-fluid energy equation is derived using the level set method and the technique for determining the energy equation for a single fluid in a multi-fluid environment is described. Finally, an analysis of the level set method for the simulation of air-water flows is presented and improvements to the level set method in this type of flows are given.

Chapter 3 presents the current numerical implementation of the method as used in this study. For most of the work, established numerical techniques have been employed but are documented here as reference. However, in some cases established techniques were inadequate for the present study and either new techniques were developed for this method or various disparate techniques were combined. In the event that a new technique or combined technique was used, it is documented as such

in this chapter. These improvements allowed for a development of a robust numerical implementation of the level set method for the simulation of air-water interface flows.

Chapter 4 presents the methods used to generate breaking waves in this numerical study in the context of other methods available in the literature and the physical processes they are representing. In general, numerically generating breaking waves is an art form verses pure science and this chapter represents an effort to document the process for multi-fluid flows. There is also a brief presentation of methods which were developed but not used in this study. This chapter also contains a catalog of all of the waves generated in this study, the methods used to classify the type of breaking wave generated, and an assessment of the quality of the waves generated.

Chapter 5 contains a collection of the validation efforts for the numerical model. It shows validation tests for water droplet re-entry as an attempt to judge the capabilities of the numerical method for simulating the jet re-entry of a plunging breaking wave. It highlights the volume and mass conservation capabilities of the numerical implementation. As we are attempting to determine the dissipation rates of wave breaking and the transfer of energy across the air-water interface, the energy conservation is also described in detail in this chapter. Finally, a brief discussion of convergence is also included.

Chapter 6 is the first chapter devoted to the physics of wave breaking. This chapter addresses the kinematics and dynamics of breaking waves for both spilling and plunging breaking waves. Drawing on a few representative waves in this study, the evolution of the free-surface, the characteristic velocity field and vorticity and vorticity fluxes of spilling breaking waves is detailed. We identify two types of spilling breaking waves in this study – gentle and strong. While they are generally similar in nature, the strong spilling breaking waves last longer and have stronger vorticity and stresses than the gentle spilling waves. Comparison to findings in experiments and theoretical models are given as well. For plunging breaking waves we focus on the formation of the jet as compared to experiments and theory as well as the effects of the jet re-entry and breakup. Velocity, vorticity and stresses are shown for two types of plunging events – those that have a jet ejection and those which have air

entrainment. The entrainment of air is also discussed within the context of this two-dimensional study. Finally, the evolution of the spectrum for a variety of breaking wave types is discussed and compared to available experimental results. While the waves in this study have a fairly narrow banded spectrum, we find a similar growth in energy in high wave frequencies prior to breaking and a similar loss of this energy after breaking.

Chapter 7 is entirely devoted to the dissipation of breaking waves. It begins with a discussion of the dissipation rate and its spatial variation from non-breaking waves through spilling to plunging breaking waves. The variation of the dissipation rate through the breaking event as well as its correlation to regions of high vorticity are discussed. The unsteady nature of the breaking event is also shown. In respect to the experimental techniques available in the literature, the a global perspective of the energy lost during breaking is also discussed. Factoring out estimated losses due to laminar effects, the amount of energy lost purely to the breaking event is also presented. We found that it scales with the amount of energy in the wave prior to breaking better than to an integral slope parameter. There is a threshold energy value below which waves do not break. Above this threshold, there is some scatter in the amount of energy lost to breaking. While the amount of data is sparse at the upper range of the investigation, there appears to be an upper bound to this energy lost as well. Direct comparison to experiments is made in terms of the amount of potential energy lost during the breaking event. An assessment of a dimensionless dissipation rate compared to available unsteady and steady wave breaking is presented. Finally, within the context of this study an assessment of the breaking criteria based on wave growth is also discussed. Though the criteria in the literature is based on wave groups and the amount of available data in this study is sparse for definitive conclusions, the comparison is qualitatively (and quantitatively) good.

Chapter 8 addresses the topic of energy transfer during the breaking process. Through the use of the multi-fluid energy equation developed in chapter 2, a term which represents the energy flux rate at the air-water interface is derived and analyzed. Using a few representative cases from this study, an argument for the existence of this

term is also given. The amount of energy transferred through the interface during the breaking event is quantified and its importance is assessed within the context of the other physical processes involved. To within the error of the energy conservation for the waves, it was found that this energy transfer at the interface can be up to 25% of the energy lost due to the breaking process. By investigating the spatial variation of this energy flux rate in the breaking waves, for spilling and plunging events, the localization of the energy flux is identified. The dominant components of the flux rate are shown to be different in spilling and plunging events as well.

Finally, *Chapter 9* pulls together the conclusions in this thesis in a concise form. It cites the contributions of the thesis for both the numerical method and the physics investigated. There is also a brief discussion of areas of future work to which this investigation is a first and vital step towards.

Chapter 2

Level Set Formulation of the Navier-Stokes Equations

For this work, the Navier-Stokes equations are used to simulate the fluid motions of multiple fluids with varying properties using the level set method. This chapter outlines the formulation of the governing equations cast in the context of the level set method. It covers mass and momentum conservation as well as the advection of the level set function which captures the location of the two-fluid interface. The governing equations are cast in a primitive variable form which requires the solution of a Poisson equation for the pressure. Thus, this chapter discusses the derivation for this equation for multiple fluids and conditions for obtaining a unique solution. The boundary conditions for the governing equations are also discussed.

Finally, this chapter addresses the use of the level set method of air-water interface flows. The differences between the level set form of the governing equations with a smoothed interface and the common multi-fluid form (with sharp interface) are enumerated in detail and the consequences of using the smoothed interface form are discussed. A detailed analysis of the performance of the smoothed interface form for air-water flows is presented as is the comparison of the smoothing function to a filter. As a consequence of the performance of the traditional function, a new smoothing function is developed and tested for use in modeling flows for which the viscous boundary layer thicknesses are not comparable. This new smoothing function

substantially outperforms the traditional function used in the literature today.

2.1 Introduction

Many types of interface tracking/capturing methods exist in the literature today for viscous, incompressible flows, such as: level set, volume-of-fluid, marker-and-cell, and boundary-fitted methods. As discussed in chapter 1, the level set method was chosen over other numerical methods because of its ability to gracefully handle complex topology changes without any *ad-hoc* treatments at the interface. A relatively recent review of interface tracking methods was done by Kothe [53]. A review of the current state-of-the-art level set method was done by Sethian and Smereka [98].

The level set method is an Eulerian method based on the advection of a function ϕ to simulate the motion of the interface rather than marker points or color functions. The "level set function" is a higher-dimensional function of which its zero level set is the location of the interface. The level set function can be taken as a variety of representations. In fact, if taken to be a color function of zero or one, the formulation is essentially the popular volume-of-fluid (VOF) method. However, to avoid surface reconstruction which is necessary in VOF methods, the level set function is taken to be a signed normal distance from the interface. At any point on the Cartesian grid, the level set function represents the (normal) distance from the interface. The sign of the function indicates in which fluid the point resides. Therefore, at any time, the location of the interface is then the zero level set of ϕ.

The following nomenclature will be used throughout this formulation. Consider an arbitrary material volume Ω which has two incompressible fluids present. For simplicity and application, there are only two fluids in this system a light (ℓ) and dark (d) fluid. The interface between the two fluids is Γ. An example of this volume is shown in figure 2-1. For this derivation, the entire volume Ω is defined as $\Omega_\ell \cap \Omega_d$ and the interface between the two fluids Γ is defined as $\Omega_\ell \cup \Omega_d$. The material surface enclosing the material volume Ω is $\partial\Omega$. Likewise, the material surfaces enclosing Ω_ℓ and Ω_d are defined as $\partial\Omega_\ell$ and $\partial\Omega_d$.

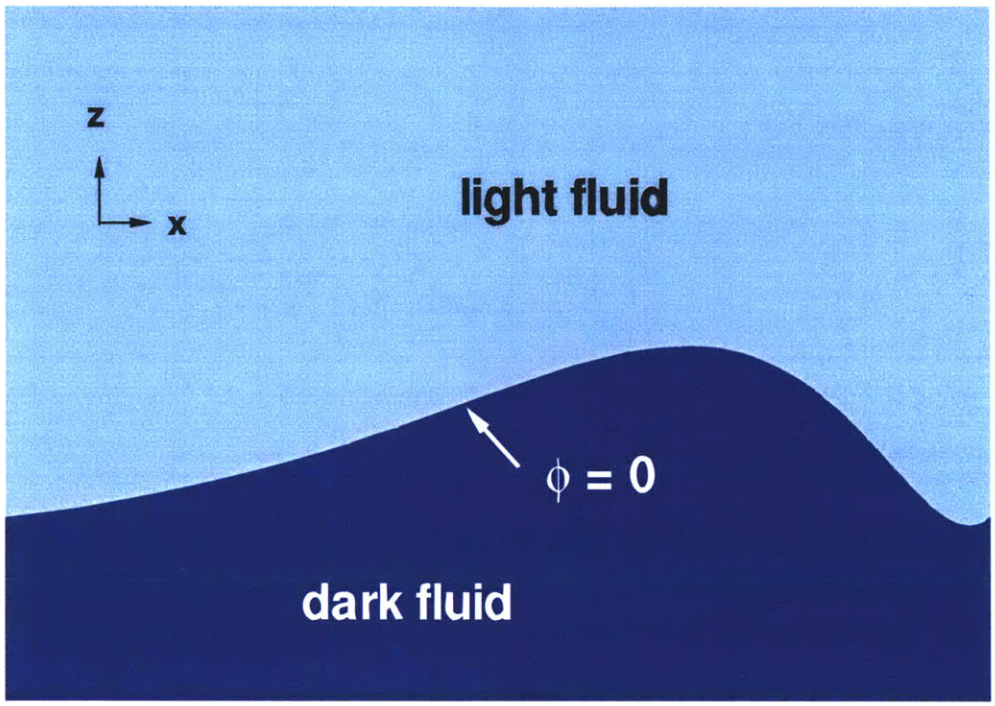

Figure 2-1: Schematic of general material volume Ω containing light and dark fluids. The interface between the two fluids is designated by the zero level set of a higher-dimensional function ϕ.

2.2 Field Equations

Many applications of the level set method have appeared in the literature in recent years [113, 12, 112, 46]. Each presents the field equations in a similar manner. The formulation used here is essentially presented in [12]. It is chosen because of its clarity and mathematical formalism.

2.2.1 Mass Conservation with a Level Set Treatment

The conservation of mass written from the perspective of an arbitrary material volume for each fluid is:

$$\int_{\Omega_\ell} \left[\frac{\partial \rho}{\partial t} + \nabla \cdot (\rho \vec{\mathbf{u}}) \right] \mathrm{d}\Omega_\ell = 0 \tag{2.1}$$

$$\int_{\Omega_d} \left[\frac{\partial \rho}{\partial t} + \nabla \cdot (\rho \vec{\mathbf{u}}) \right] \mathrm{d}\Omega_d = 0 \tag{2.2}$$

using the definition for the entire material volume in section 2.1, this can be rewritten in a single equation as:

$$\int_{\Omega} \left[\frac{\partial \rho}{\partial t} + \nabla \cdot (\rho \vec{\mathbf{u}}) \right] \mathrm{d}\Omega = 0 \tag{2.3}$$

Because the material volume is arbitrary and the integral is zero, the integrand is also zero which yields the conservation of mass in differential form is:

$$\frac{\partial \rho}{\partial t} + \nabla \cdot (\rho \vec{\mathbf{u}}) = 0 \tag{2.4}$$

If we assume that both fluids are incompressible $\left(\frac{D\rho}{Dt} = 0\right)$, then the continuity equation is obtained:

$$\nabla \cdot \vec{\mathbf{u}} = 0 \tag{2.5}$$

Note that the continuity equation applies for any point in the domain, whether it lies in the light or dark fluid.

2.2.2 Navier-Stokes Equations with a Level Set Treatment

If the fluid in the general volume moves with velocity $\vec{\mathbf{u}}(\vec{\mathbf{x}}, t)$, the momentum in the volume is given as:

$$\int_{\Omega} \rho \vec{\mathbf{u}} \mathrm{d}\Omega \tag{2.6}$$

For the purposes of this general derivation, only two forces acting on the fluid in the material volume will be considered. They are gravity and a general stress force. The volumetric force due to gravity is:

$$\int_{\Omega} \rho \vec{\mathbf{g}} \mathrm{d}\Omega \tag{2.7}$$

If σ_{ij} is the stress tensor and n_j the surface normal pointing into the light fluid, then the surface force (on the material surface $\partial\Omega$) is given by:

$$\int_{\partial\Omega} \sigma_{ij} n_j \mathrm{d}(\partial\Omega) \tag{2.8}$$

Using these forces and continuing with the incompressible fluid assumption, the rate of change of momentum for Ω is:

$$\int_{\Omega} \rho \frac{D\vec{\mathbf{u}}}{Dt} = \int_{\Omega} \rho \vec{\mathbf{g}} \mathrm{d}\Omega + \int_{\partial\Omega} \sigma_{ij} n_j \mathrm{d}(\partial\Omega) \tag{2.9}$$

With the definitions of the multiple fluids in section 2.1, this can be rewritten:

$$\int_{\Omega} \rho \frac{D\vec{\mathbf{u}}}{Dt} = \int_{\Omega} \rho \vec{\mathbf{g}} \mathrm{d}\Omega + \underbrace{\int_{\partial\Omega_\ell} \sigma_{ij} n_j \mathrm{d}(\partial\Omega_\ell)}_{I} + \underbrace{\int_{\partial\Omega_d} \sigma_{ij} n_j \mathrm{d}(\partial\Omega_d)}_{II} + \int_{\Gamma} [\sigma_{ij} n_j] \mathrm{d}\Gamma \tag{2.10}$$

where $[\sigma_{ij} n_j]$ is the jump of the stress tensor across the fluid interface Γ. In this form, the divergence theorem can be applied to integrals I and II in equation (2.10) to transform them from surface integrals to volume integrals over their respective volumes.

The free-surface boundary condition which accounts for the discontinuity of the

normal stress across the interface gives:

$$[\sigma_{ij} n_j] = \gamma \kappa \vec{\mathbf{n}} \tag{2.11}$$

where γ is the surface tension coefficient, κ is the curvature of Γ and $\vec{\mathbf{n}}$ is the *outward* pointing normal along Γ (inward being into the dark fluid).

A method to treat a surface force within a volume without directly locating the interface on which the force is applied was developed by Brackbill *et al.* [9]. Within the context of a volume of fluids type application, the authors consider two fluids that are separated by a transition region of finite width. A force density is defined that is proportional to the desired surface force and normalized such that, as the transition region thickness goes to zero, the actual surface force on the interface is recovered. This method is valid for two or three dimensions and surface reconstruction is not necessary.

The surface force in this application is given by the right hand side of equation 2.11. The normal vector of the surface can be calculated from the level set function in the region near the interface, providing that the distance function is maintained (i.e. $||\nabla \phi|| = 1$):

$$\vec{\mathbf{n}} = \frac{\nabla \phi}{||\nabla \phi||} \tag{2.12}$$

Additionally, the curvature of the surface can be defined from the normal vector:

$$\kappa \equiv -(\nabla \cdot \vec{\mathbf{n}}) \tag{2.13}$$

To ensure that the force density is only applied in the region near the interface ($\phi = 0$), the force is multiplied by the Dirac delta function. This allows the surface integral in equation 2.10 to be converted to a volume integral.

$$\int_{\Gamma} \gamma \kappa \vec{\mathbf{n}} \mathrm{d}\Gamma = \int_{\Omega} \gamma \kappa \delta(\phi) \nabla \phi \mathrm{d}\Omega \tag{2.14}$$

The momentum balance of equation 2.10 can be rewritten as a single integral over

the arbitrary material volume.

$$\int_{\Omega} \rho \frac{D\vec{\mathbf{u}}}{Dt} - \frac{\partial \sigma_{ij}}{\partial x_j} - \rho\vec{\mathbf{g}} - \gamma\kappa\delta(\phi)\nabla\phi \ \ \mathrm{d}\Omega = 0 \tag{2.15}$$

As in the mass conservation derivation, the integrand is zero because Ω is arbitrary and the integral is zero. This provides a multi-fluid form of the momentum equations.

$$\rho\left(\frac{\partial \vec{\mathbf{u}}}{\partial t} + \vec{\mathbf{u}} \cdot \nabla\vec{\mathbf{u}}\right) = \frac{\partial \sigma_{ij}}{\partial x_j} + \rho\vec{\mathbf{g}} + \gamma\kappa\delta(\phi)\nabla\phi \tag{2.16}$$

For applications involving a Newtonian fluid, the stress tensor will be defined to be $\sigma_{ij} \equiv -\Pi\bar{\mathbf{I}} + 2\mu\overline{\mathbf{D}}$ where Π is the static pressure, $\overline{\mathbf{D}}$ is the deformation tensor and $\bar{\mathbf{I}}$ is the identity matrix. The Navier-Stokes equations, using a volumetric force for surface tension effects, can be written in the following, primitive-variable and non-conservative form:

$$\rho\frac{\partial \vec{\mathbf{u}}}{\partial t} + \vec{\mathbf{u}} \cdot \nabla\vec{\mathbf{u}} = -\nabla\Pi + \nabla \cdot (2\mu\overline{\mathbf{D}}) + \rho\vec{\mathbf{g}} + \gamma\kappa\delta(\phi)\nabla\phi \tag{2.17}$$

In conservative form, providing that $\nabla \cdot \vec{\mathbf{u}} = 0$ and dividing equation (2.17) by ρ, the Navier-Stokes equations become:

$$\frac{\partial \vec{\mathbf{u}}}{\partial t} + \nabla \cdot (\vec{\mathbf{u}}\vec{\mathbf{u}}) = -\frac{1}{\rho(\phi)}\nabla\Pi + \frac{1}{\rho(\phi)}\nabla \cdot (2\mu(\phi)\overline{\mathbf{D}}) + \vec{\mathbf{g}} + \frac{1}{\rho(\phi)}\gamma\kappa\delta(\phi)\nabla\phi \tag{2.18}$$

The density and viscosity have been made functions of the level set function. This vector equation is the primitive variable form of the level set treatment of the Navier-Stokes equations.

2.2.3 Constitutive Properties

The constitutive properties of the fluid, namely density ρ and viscosity μ, are discontinuous in multi-fluid formulations. In the level set method, this discontinuity is mapped to a continuous function ϕ. In this application, ϕ is taken to be the signed normal distance from the interface. The mapping of the constitutive properties of the

fluid is done using a Heaviside function $H(\phi)$. The reverse mapping of the density and viscosity from the level set function is done as follows:

$$\rho(\phi) = \rho_\ell + (\rho_d - \rho_\ell)H(\phi) \tag{2.19}$$

$$\mu(\phi) = \mu_\ell + (\mu_d - \mu_\ell)H(\phi) \tag{2.20}$$

Ideally, the Heaviside function would represent a sharp transition between the two fluids. In general however, the Heaviside function is smoothed over a small distance by a "smoothing function", $f(\phi;\epsilon)$. Recent works by Fedkiw [83], show promise in using sharp interfaces. For this work, the Heaviside function is smoothed.

$$H(\phi;\epsilon) = \begin{cases} 1 & \phi > \epsilon \quad \text{if } \vec{\mathbf{x}} \in \text{water} \\ f(\phi;\epsilon) & |\phi| < \epsilon \quad \text{if } \vec{\mathbf{x}} \in \Gamma_\epsilon \\ 0 & \phi < -\epsilon \quad \text{if } \vec{\mathbf{x}} \in \text{air} \end{cases} \tag{2.21}$$

The Dirac delta function is related to the Heaviside function by:

$$\delta(\phi) = \frac{\mathrm{d}H(\phi)}{\mathrm{d}\phi} \tag{2.22}$$

The overall effects of smoothing the interface are discussed in detail in section 2.7. Through the development of this work, it was determined that a smoothing function other than the traditional level set smoothing function was appropriate for smoothing air-water interface flows. The reasons for this and the new form of the smoothing function is discussed in this same section. However, because the traditional smoothing function is used in almost all of the current literature, its form and origins will be discussed for completeness.

Origins of Traditional Smoothing Function

The traditional smoothing function $f(\phi;\epsilon)$ results from early work in the numerical simulation of blood flow in the heart by Peskin [86]. Peskin's mollified delta function

(or distribution function) is based on the Fourier series of a delta function.

$$\delta(x) = \frac{1}{2L} + \frac{1}{L}\sum_{n=1}^{\infty}\cos(\frac{n\pi x}{L}) \tag{2.23}$$

The delta function has many desirable properties which make it a good place to start. Specifically, its integral over all x is unity and it is zero away from its region of interest (in this notation, $x = 0$). However, because it is a sharp function, it needs to be mollified. If only the first mode in equation 2.23 is considered and the length of the series L is set to the half-distance (ϵ) over which the function is smoothed, an equation can be obtained:

$$\delta(x) \sim \frac{1}{2\epsilon} + \frac{c}{\epsilon}\cos(\frac{\pi x}{\epsilon}) \tag{2.24}$$

Here, we have included a constant c. This constant is necessary to ensure that the function has compact support in the range of $-\epsilon \leq x \leq \epsilon$. For this to occur, c must equal 1/2.

$$\delta(x;\epsilon) = \frac{1}{2\epsilon}\left(1 + \cos(\frac{\pi x}{\epsilon})\right) \qquad \text{for } -\epsilon \leq x \leq \epsilon \tag{2.25}$$

This form of the mollified delta function is used throughout the literature for many applications, not just the level set method. To get the mollified form of the Heaviside function, equation 2.25 is integrated with respect to x. The constant of integration is determined such that at $x = 0$, the mollified Heaviside function is equal to 1/2. This gives us the smoothing function $f(\phi;\epsilon)$ which is used in all present level set formulations.

$$f(\phi;\epsilon) = \frac{1}{2}(1 + \frac{\phi}{\epsilon} + \frac{1}{\pi}\sin(\frac{\phi\pi}{\epsilon})) \tag{2.26}$$

As stated previously, a modified smoothing function was developed for this work. A detailed discussion of its development and its comparison with the traditional function are discussed in section 2.7. Equation 2.26 is symmetric about $\phi = 0$. It was determined that in cases where the viscous boundary layer thicknesses between the two fluids were not essentially the same size, that practical computational resolution was not sufficient to resolve the velocity gradients in the region where the boundary layer was smaller (in this case the air). The modified form is asymmetric about the

interface, reaching further into the region with the smaller viscous boundary layer. This essentially brings the ratio of level set boundary layer and viscous boundary layer for both fluids to be about the same.

2.2.4 Nondimensionalization

The nondimensionalization of the governing equations (2.18) chosen for this problem is based on properties of water.

$$\vec{\mathbf{x}} = L\vec{\mathbf{x}}' \quad \vec{\mathbf{u}} = U\vec{\mathbf{u}}' \quad t = (\frac{L}{U})t' \quad \Pi = \rho_d U^2 \Pi' \quad \rho = \rho_d \rho' \quad \mu = \mu_d \mu' \tag{2.27}$$

Dropping the primes for simplicity, the nondimensional form of the field equation becomes:

$$\frac{\partial \vec{\mathbf{u}}}{\partial t} + \nabla \cdot (\vec{\mathbf{u}}\vec{\mathbf{u}}) = -\frac{1}{\rho(\phi)}\nabla\Pi + \frac{1}{\rho(\phi)\mathcal{R}e_d}\nabla \cdot (2\mu(\phi)\overline{\mathbf{D}}) + \frac{\vec{\mathbf{k}}}{\mathcal{F}r^2} + \frac{1}{\rho(\phi)\mathcal{W}e}\kappa\delta(\phi)\nabla\phi \tag{2.28}$$

with the nondimensional parameters defined as follows.

$$\mathcal{R}e_d = \frac{\rho_d U L}{\mu_d} \qquad \mathcal{F}r^2 = \frac{U^2}{gL} \qquad \mathcal{W}e = \frac{\rho_d U^2 L}{\gamma} \tag{2.29}$$

As a result of the nondimensionalization, two normalized constitutive property parameters are also now defined: $\lambda \equiv \frac{\rho_\ell}{\rho_d}$ for density and $\eta \equiv \frac{\mu_\ell}{\mu_d}$ for viscosity. The nondimensional forms of equations (2.19) and (2.20) become:

$$\rho(\phi) = \lambda + (1-\lambda)H(\phi;\epsilon) \tag{2.30}$$

$$\mu(\phi) = \eta + (1-\eta)H(\phi;\epsilon) \tag{2.31}$$

2.3 Level Set Equations

2.3.1 Governing Equation of the Level Set Function

To move the interface with the velocity of the fluid at that point, an advection equation governs the level set function. The level set advection is done through a Lagrangian invariance equation, $D\phi/Dt = 0$:

$$\frac{\partial \phi}{\partial t} + \vec{\mathbf{u}} \cdot \nabla \phi = 0 \tag{2.32}$$

It has been rigorously proven by Osher and Sethian [84] that this advection equation accurately moves the interface based on the velocity field. Another method of proving this has been shown by Sussman *et al.* [111]. A less rigorous proof, which is easier to interpret physically, is the following.

Consider a two-dimensional plane progressive wave with free-surface elevation $\eta = a\cos(kx - \omega t)$ vertically centered at $z = 0$. If the zeroth level set of the function ϕ represents this same line and ϕ represents a signed distance function then it would be defined as follows:

$$\phi \approx \eta - z \tag{2.33}$$

If the velocity components of the wave field are (u, w) and both the velocity and the level set function are substituted into equation 2.32, the nonlinear kinematic free-surface boundary condition is the result when evaluated at $z = \eta$.

$$\eta_t + \eta_x u_{z=\eta} - w_{z=\eta} = 0 \tag{2.34}$$

This proves that the advection of the zero level set of ϕ represents the kinematic motion of the free surface. Yet, experience has shown that use of this advection equation where $\vec{\mathbf{u}} = \vec{\mathbf{u}}_{fluid}$ everywhere presents a minor difficulty in that the level set function can lose its distance function property.

The application of the form of the advection equation in equation 2.32 to the fluid mechanics application of the level set method has been questioned by Sethian [97].

The legacy of Marker and Cell methods which use Lagrangian particles has polluted the implementation of the level set method. In an Eulerian interface tracking method such as the level set method, only the interface should move with the velocity field of the fluid through the kinematic boundary condition. Because the level set utilizes a higher-dimensional function, using the fluid velocity of the entire fluid to advect the level set function implies that all other nonzero level sets move with the fluid velocity. This is not the case and doing so causes the level sets to either bunch up or spread out with a subsequent loss of the distance function characteristic. This inaccuracy makes it difficult to calculate the curvature of the surface and has forced the development of the reinitialization techniques in which much care must be taken to avoid volume conservation problems [97].

To understand the point raised by Sethian, we can continue with the two-dimensional plane progressive wave example which has amplitude a, frequency ω and wave number k. For a finite water depth of h, the velocity field of the plane progressive wave is given by:

$$\begin{aligned} u &= \mathcal{A}\cosh\left(k(z+h)\right)\cos\left(kx-\omega t\right) \\ w &= \mathcal{A}\sinh\left(k(z+h)\right)\cos\left(kx-\omega t\right) \end{aligned} \tag{2.35}$$

where $\mathcal{A} = gak/\omega$. If this velocity field is substituted into equation 2.32 along with equation 2.33 and evaluated at the bottom, $z = -h$, a different equation results:

$$\begin{aligned} a\omega\sin\left(kx-\omega t\right) + \mathcal{A}\cos\left(kx-\omega t\right)(-ak\sin\left(kx-\omega t\right)) + 0 &= 0 \\ \mathcal{A}k\cos\left(kx-\omega t\right) &= \omega \end{aligned} \tag{2.36}$$

Therefore if the advection velocity at the bottom is equal to the fluid velocity ($\vec{\mathbf{u}} = \vec{\mathbf{u}}_{fluid}$), equation 2.32 is violated and the level set function then loses its distance function property over the course of a simulation. This can be problematic in cases where the calculation of surface curvature is necessary. Reinitialization of the level set function is generally used to maintain the level set function as a distance function.

2.3.2 Reinitialization

To combat the loss of the distance function property, a various number of reinitialization techniques have been developed [12, 110, 82, 45, 83]. The methods are based on the definition of the level set function if it represents a distance function:

$$|\nabla\phi| = 1 \tag{2.37}$$

A partial differential equation is derived such that if iterated to steady state, equation 2.37 holds:

$$\frac{\partial\phi}{\partial t} + \text{sign}(\phi_0)\left(|\nabla\phi| - 1\right) = 0 \tag{2.38}$$

The initial condition for this equation is the initial position of the level set function, $\phi(\vec{\mathbf{x}}, t = 0) = \phi_0$. Equation 2.38 conserves volume within the domain bounded by the level set function because it does not change the position of the zero level set. However, numerically, this is not the case and if the interface is reinitialized using this technique, it has a tendency to stray [111]. Sussman and Fatemi [110] modified equation 2.38 to allow for an additional volume conserving requirement. The requirement is that within a general and fixed volume Ω:

$$\partial_t \int_\Omega H(\phi) = 0 \tag{2.39}$$

If equation 2.38 is defined as the operator $L(\phi_0, \phi)$, then the modified equation is

$$\frac{\partial\phi}{\partial t} = L(\phi_0, \phi) + \lambda f(\phi) \tag{2.40}$$

The Lagrange multiplier (λ) is defined to require volume conservation. Expanding 2.39 and using 2.40 yields an equation for λ.

$$\partial_t \int_\Omega H(\phi) = \int_\Omega H'(\phi)\phi_t = \int_\Omega H'(\phi)\left(L(\phi_0, \phi) + \lambda f(\phi)\right) = 0 \tag{2.41}$$

This can be solved for λ if it is assumed constant in Ω:

$$\lambda = \frac{-\int_\Omega H'(\phi) L(\phi_0, \phi)}{\int_\Omega H'(\phi) f(\phi)} \tag{2.42}$$

The function $f(\phi)$ is chosen to ensure that only the interface is corrected to remove any drift.

$$f(\phi) \equiv H'(\phi)|\nabla\phi| \tag{2.43}$$

To reduce the number of iterations, equation 2.40 can be iterated to a finite time. The accuracy of the level set function is only necessary in a narrow band near the free surface to adequately calculate the curvature. This can be seen if equation 2.38 is rewritten in a more familiar form:

$$\frac{\partial\phi}{\partial t} + \text{sign}(\phi_0)\frac{\nabla\phi}{|\nabla\phi|} \cdot \nabla\phi = \text{sign}(\phi_0) \tag{2.44}$$

This is a nonlinear hyperbolic equation with characteristic velocities $\vec{\mathbf{w}}$.

$$\vec{\mathbf{w}} = \text{sign}(\phi_0)\frac{\nabla\phi}{|\nabla\phi|} \tag{2.45}$$

Because $\frac{\nabla\phi}{|\nabla\phi|}$ is the normal of the interface, the characteristic velocities point outwards. Sussman and Fatemi take advantage of this by pointing out that the region nearest to the interface will be initialized first and then it will work away from the interface. Thus, a cutoff point of the reinitialization can be determined and the partial differential equation can be solved to some point in time equal to ϵ where ϵ is defined to be the distance around the interface to which an accurate distance function is needed.

A similar method was proposed by Chang *et al.* [12]. This method is based on an area/volume preserving form of equation 2.38. It is essentially a perturbed Hamilton-Jacobi equation which is solved to steady state.

$$\frac{\partial\phi}{\partial t} + (A_0 - A(t))(\kappa - 1)|\nabla\phi| = 0 \tag{2.46}$$

A_0 denotes the total volume for the initial condition (the perturbed level set function), $A(t)$ denotes the total volume corresponding to the level set function at time t and κ denotes the curvature of the interface. Both methods require that the partial differential equation be solved to some point, either a particular time or steady state. This also requires a CFL condition within the reinitialization steps for the time integration. Additionally, when three-dimensional simulations were done by Oka and Ishii [82], they found that both reinitialization steps were necessary in a three stage fashion to get adequate volume conservation.

Adalsteinsson and Sethian [1] propose computing what they call extension velocities that will propagate the nonzero level sets in such a manner that the distance function is maintained. The method does have some interesting advantages. By using a velocity field which becomes the interface velocity at the interface, reinitialization is not necessary. The method, while considered a "fast marching method", can be tedious if not implemented efficiently. It is unclear if this method is any better than the reinitialization technique discussed. In practice, most level set methods published in the literature use the method outlined by Sussman and Fatemi which is also the method used in this work. The implementation of their reinitialization technique is discussed in detail in section 3.8.

2.4 Multi-Fluid Energy Equation

The multi-fluid energy equation is derived using a control volume technique. The control volume is defined similarly to figure 2-1 where the volume ($\forall$) contains both fluids and the interface between them can be multi-valued or broken. The change in total kinetic energy ($\widehat{\kappa}$) of the control volume is determined by the net work done on the control volume $\frac{dW}{dt}$ [37].

$$\frac{D\widehat{\kappa}}{Dt} = \frac{dW}{dt} \tag{2.47}$$

The kinetic energy per unit volume is defined as $\kappa = (1/2)\rho\vec{\mathbf{u}}\cdot\vec{\mathbf{u}}$, thus the total kinetic energy in the volume is just the integral over the entire control volume:

$$\widehat{\kappa} = \int_{\forall} \kappa \mathrm{d}\forall = \int_{\forall} \frac{1}{2}\rho(\vec{\mathbf{u}}\cdot\vec{\mathbf{u}})\mathrm{d}\forall \tag{2.48}$$

The left-hand side of equation 2.47 simply becomes:

$$\frac{D\widehat{\kappa}}{Dt} = \frac{\partial}{\partial t}\int_{\forall} \kappa \mathrm{d}\forall + \oint_{S} \kappa\vec{\mathbf{u}}\cdot\mathrm{d}\vec{\mathbf{A}} \tag{2.49}$$

The right-hand side of equation 2.47 is made up of work from the pressure, viscous, surface tension and gravitational forces. Each term is defined below. First, the net flow work by the pressure field (Π) is given by:

$$= -\oint_{S} \Pi\vec{\mathbf{u}}\cdot\mathrm{d}\vec{\mathbf{A}} \tag{2.50}$$

Second, the rate of viscous (τ) work is given by:

$$= \oint_{S} \vec{\mathbf{u}}\cdot\tau\cdot\mathrm{d}\vec{\mathbf{A}} \tag{2.51}$$

Third, the rate of viscous dissipation which is also a function of τ is given by:

$$= -\int_{\forall} (\tau\cdot\nabla)\vec{\mathbf{u}}\mathrm{d}\forall \tag{2.52}$$

Fourth, the net work by the gravitational force is given by:

$$= -\int_{\forall} \rho g w \mathrm{d}\forall \tag{2.53}$$

Finally, any surface forcing such as surface tension or artificial surface forcing does work:

$$\vartheta = \vec{\mathbf{F}}\cdot\vec{\mathbf{u}} \tag{2.54}$$

where $\vec{\mathbf{F}}$ is the force which is applied at the surface.

Combining equations 2.50-2.54 with equations 2.47 and 2.49 yields the energy equation for a control volume.

$$\frac{\partial}{\partial t}\int_{\forall}\kappa \mathrm{d}\forall+\oint_{S}\kappa\vec{\mathbf{u}}\cdot\mathrm{d}\vec{\mathbf{A}}=-\oint_{S}\Pi\vec{\mathbf{u}}\cdot\mathrm{d}\vec{\mathbf{A}}+\oint_{S}\vec{\mathbf{u}}\cdot\tau\cdot\mathrm{d}\vec{\mathbf{A}}-\int_{\forall}(\tau\cdot\nabla)\vec{\mathbf{u}}\mathrm{d}\forall-\int_{\forall}\rho g w\mathrm{d}\forall+\vartheta \quad (2.55)$$

For the sake of notation, the dissipation rate per unit volume is defined as ε:

$$\varepsilon=(\tau\cdot\nabla)\cdot\vec{\mathbf{u}} \quad (2.56)$$

Thus, the energy equation for a multi-fluid control volume is given as the following:

$$\frac{\partial}{\partial t}\int_{\forall}\kappa \mathrm{d}\forall+\oint_{S}\kappa\vec{\mathbf{u}}\cdot\mathrm{d}\vec{\mathbf{A}}=-\oint_{S}\Pi\vec{\mathbf{u}}\cdot\mathrm{d}\vec{\mathbf{A}}+\oint_{S}\vec{\mathbf{u}}\cdot\tau\cdot\mathrm{d}\vec{\mathbf{A}}-\int_{\forall}\varepsilon\mathrm{d}\forall-\int_{\forall}\rho g w\mathrm{d}\forall+\vartheta \quad (2.57)$$

As the control volume is arbitrary, equation 2.57 can be evaluated on a single cell of size $(\mathrm{d}x,\mathrm{d}z)$ using a finite volume methodology. The following differential equation can be derived for the kinetic energy per unit volume:

$$\frac{\partial[\kappa]_o}{\partial t}+\nabla\cdot(\kappa\vec{\mathbf{u}}+\Pi\vec{\mathbf{u}})+[\rho g w]_o=\nabla\cdot(\tau\cdot\vec{\mathbf{u}})-\varepsilon+\vartheta \quad (2.58)$$

where $[f]_o$ is evaluated at the cell center.

2.4.1 Nondimensional Form of the Multi-fluid Energy Equation

To be consistent with the governing equations in section 2.2, we will choose the same nondimensionalization which is detailed in equation 2.27. Additionally, the level set form of the equation requires that $\rho=\rho(\phi)$ and $\mu=\mu(\phi)$. The nondimensional level set form of the multi-fluid energy equation then becomes:

$$\frac{\partial[\kappa]_o}{\partial t}+\nabla\cdot(\kappa\vec{\mathbf{u}}+\Pi\vec{\mathbf{u}})+\frac{1}{\mathcal{F}r^2}[\rho(\phi)w]_o=\frac{1}{\mathcal{R}e_d}\left(\nabla\cdot(\tau\cdot\vec{\mathbf{u}})-\varepsilon\right)+\vartheta \quad (2.59)$$

where the Reynolds and Froude number are defined in equation 2.29. Additionally, it is some times convenient to consider the gravitational effect as a rate of energy change verses the work done. In other words, the net gravitational work can be rewritten to a similar form as the kinetic energy. The potential energy per volume is given by ψ and is related to the work done as follows:

$$\frac{1}{\mathcal{F}r^2}[\rho(\phi)w]_o = \frac{\partial[\psi]_o}{\partial t} \tag{2.60}$$

A common notation which is used in the literature by many authors defines E as the total energy and F as the energy flux vector. To be compatible with this notation, we make the following definitions:

$$\begin{aligned} E &= [\kappa]_o + [\psi]_o \\ \vec{F} &= (\kappa + \Pi)\,\vec{\mathbf{u}} \\ \vec{\Sigma} &= \tau \cdot \vec{\mathbf{u}} \end{aligned}$$

Equation 2.59 now becomes:

$$\frac{\partial E}{\partial t} + \nabla \cdot \vec{F} = \frac{1}{\mathcal{R}e_d}\left(\nabla \cdot \vec{\Sigma} - \varepsilon\right) + \vartheta \tag{2.61}$$

2.4.2 Extracting the Energy Equation for a Single Fluid

To extract the information for each fluid from the energy equation, we will use the information which is supplied by the level set formulation, namely a signed function which smoothly varies across the interface. The smoothed Heaviside function will be used to help separate the air from the water in the control volume. We begin with equation 2.61 which represents the rate of change of total energy in the per unit volume and multiply it by the smoothed Heaviside function. For the sake of a cleaner notation, $H(\phi;\epsilon) = H_\phi$ is adopted.

$$H_\phi \frac{\partial E}{\partial t} + H_\phi \nabla \cdot \vec{F} = \frac{H_\phi}{\mathcal{R}e_d}\left(\nabla \cdot \vec{\Sigma} - \varepsilon\right) + H_\phi \vartheta \tag{2.62}$$

Because we have used the smooth form of the Heaviside function, H_ϕ can be brought into the derivatives using the chain rule. Consider the first term:

$$H_\phi \frac{\partial E}{\partial t} = \frac{\partial E H_\phi}{\partial t} - E \frac{\partial H_\phi}{\partial \phi} \frac{\partial \phi}{\partial t} \tag{2.63}$$

All of the terms associated with the divergence can be arranged as well. For a general vector $\vec{A}$, this is:

$$H_\phi \nabla \cdot \vec{A} = \nabla \cdot \left(\vec{A} H_\phi \right) - \vec{A} \frac{\partial H_\phi}{\partial \phi} \cdot \nabla \phi \tag{2.64}$$

This can be simplified further if we note that by definition

$$\frac{\partial H_\phi}{\partial \phi} = \delta_\phi \tag{2.65}$$

and by the governing equation of the level set function

$$\frac{\partial \phi}{\partial t} = -\vec{\mathbf{u}} \cdot \nabla \phi \tag{2.66}$$

This yields a differential equation for the total energy of the water in the control volume. A similar equation can be derived for the air in the control volume by multiplying equation 2.61 by $1 - H_\phi$ rather than H_ϕ.

$$\frac{\partial E_w}{\partial t} + \nabla \cdot \left(\vec{F}_w - \frac{\vec{\Sigma}_w}{\mathcal{R}e_w} \right) = -\frac{\varepsilon_w}{\mathcal{R}e_w} + \vartheta_w + \delta_\phi \nabla \phi \cdot \left(\vec{F} - \frac{\vec{\Sigma}}{\mathcal{R}e_w} - E\vec{\mathbf{u}} \right) \tag{2.67}$$

Equation 2.67 is essentially the same as the differential equation for the entire control volume except for an additional term which represents the transfer of energy at the interface between the air and water portions of the control volume. This term is discussed in detail in chapter 8.

2.5 Pressure Equation

2.5.1 Gravitational Body Force & Pressure Term

In most incompressible flows, the effect of gravity can be accounted for by separating the total pressure into a dynamic and hydrostatic component. Generally this hydrostatic component can be added to the solution at any time being that it is a constant. General viscous treatments of free-surface flows perform a similar method and only account for the change in free-surface elevation from the static water line as a contribution of the gravitational body force.

However, while in this problem both fluids are considered incompressible, the gravitational body force can not be neglected until the final solution is obtained. Because the density within the material volume changes in an Eulerian sense, the gravitational effects must be considered. Generally, in a physical sense it is easier to consider things in terms of dynamic pressure instead of total pressure within the discussion of incompressible flows. Dommermuth *et al.* [20] present a method of capturing the dynamic pressure contribution separate from the "hydrostatic" component and still maintain the gravitational body force effect on the volume. In this paper, the total pressure field is decomposed into a dynamic and a pseudo-hydrostatic component.

$$\Pi = P_d + P_h \tag{2.68}$$

The pseudo-hydrostatic component can be defined as any desired quantity and it will be used to absorb the gravitational body force term in equation (2.28).

$$P_h = -\int^z \frac{\rho(\phi(\vec{\mathbf{x}}))}{\mathcal{F}r^2} dz' \tag{2.69}$$

Recalling that the density is a function of space in this method, P_h will be a function of the horizontal directions. When the decomposed pressure field is substituted into the governing equation, the modified Navier-Stokes equation becomes:

$$\frac{\partial \vec{\mathbf{u}}}{\partial t}+\nabla\cdot(\vec{\mathbf{u}}\vec{\mathbf{u}}) = -\frac{1}{\rho(\phi)}\nabla P_d- \underbrace{\frac{1}{\rho(\phi)}\nabla_{(x,y)}P_h\cdot(\vec{\mathbf{i}},\vec{\mathbf{j}})}_{\text{gravitational effect}=\vec{\mathbf{P}}_\mathbf{h}} +\frac{1}{\rho(\phi)\mathcal{R}e_d}\nabla\cdot(2\mu(\phi)\overline{\mathbf{D}})+\frac{1}{\mathcal{W}e}\kappa\delta(\phi)\nabla\phi \tag{2.70}$$

The gravitational effect is imbedded in equation (2.70). The operator $\nabla_{(x,y)}$ is (∂_x, ∂_y).

2.5.2 Variable Density Projection Operator

A detailed discussion of the need for a link between the continuity and momentum equations for incompressible flows can be found in many computational fluid dynamics texts. Even though there are four equations (continuity plus the three momentum equations) and four unknowns (the three components of the velocity field and the pressure), because the flow is incompressible, no direct solution for the pressure exists. The method chosen to couple the continuity and momentum equations as well as determine a direct equation to solve for the pressure is the projection method.

The projection method uses the continuity equation (2.5) directly on the Navier-Stokes equation (2.70). This yields a Poisson equation with variable coefficients for the dynamic pressure field which ensures continuity. To illustrate this concept, the acceleration term of equation 2.70 is discretized using a simple forward Euler time discretization.

$$\frac{\vec{\mathbf{u}}^{n+1}-\vec{\mathbf{u}}^{n}}{\Delta t}+\frac{1}{\rho(\phi)}\nabla P_d = \underbrace{-\nabla\cdot(\vec{\mathbf{u}}\vec{\mathbf{u}})-\vec{\mathbf{P}}_\mathbf{h}+\frac{1}{\rho(\phi)\mathcal{R}e_d}\nabla\cdot(2\mu(\phi)\overline{\mathbf{D}})+\frac{1}{\mathcal{W}e}\kappa\delta(\phi)\nabla\phi}_{\vec{\mathbf{F}}} \tag{2.71}$$

To couple the continuity and momentum equations, the divergence of equation 2.71 is taken. This yields a Poisson equation with the divergence of the velocity field at two time steps as part of the source term.

$$\nabla\cdot\frac{1}{\rho(\phi)}\nabla P_d = \frac{\nabla\cdot\vec{\mathbf{u}}^{n}-\nabla\cdot\vec{\mathbf{u}}^{n+1}}{\Delta t}+\nabla\cdot\vec{\mathbf{F}} \tag{2.72}$$

The next natural step would be to use the continuity equation and set $\nabla \cdot \vec{\mathbf{u}} = 0$ for both time steps n and $n+1$. However, setting the n-th stage to zero has been shown to allow error to accumulate. Mathematically, this term is zero; however, numerical errors may cause this term to be a small, non-zero number. Including the error associated with this term not only prevents an error accumulation but also nonlinear instability. In this context, the Poisson equation for the dynamic pressure becomes:

$$\nabla \cdot \frac{1}{\rho(\phi)} \nabla P_d = \frac{\nabla \cdot \vec{\mathbf{u}}^n}{\Delta t} + \nabla \cdot \vec{\mathbf{F}} \tag{2.73}$$

Section 3.6 contains the discretization and solution of this equation for the dynamic pressure. Section 3.9 discusses the details of the interaction of the numerical integration scheme and the projection operator.

2.5.3 Solvability

The boundary conditions for the Poisson equation for the dynamic pressure are given in section 2.6 equation 2.84. They are periodic in the horizontal direction and homogeneous Neumann conditions in the vertical direction. Thus, they are such that the pressure can only be solved up to a given constant. A solvability condition is necessary [102]. This should entail nailing down the solution at a given point. Additionally, because of the nature of the problem (strong discontinuous coefficients) a compatibility condition is also necessary. For this type of problem, the natural compatibility condition is based on the divergence theorem.

A general divergence theorem for discontinuous variables can be derived. Consider a volume V which is contained entirely within the surface S. An arbitrary surface Γ divides V into two sub-volumes V_1 and V_2 which are contained within S_1 and Γ and S_2 and Γ for V_1 and V_2 respectively.

For a vector $\vec{F}$, the divergence theorem says:

$$\int_V \nabla \cdot \vec{F} dV = \oint_S \vec{F} \cdot \vec{n} dS \tag{2.74}$$

where $\vec{n}$ is the outward facing normal of S. This applies when $\vec{F}$ is C^2, i.e. it and its partial derivatives are continuous. However, when $\vec{F}$ is only C^1 a more general form of equation 2.74 must be derived. To begin this derivation, we will examine the right-hand side of equation 2.74:

$$\oint_S \vec{F} \cdot \vec{n} dS = \oint_{S_1} \vec{F} \cdot \vec{n_1} dS_1 + \oint_{S_2} \vec{F} \cdot \vec{n_2} dS_2 + \oint_{S_+} \vec{F} \cdot \vec{n_+} dS_+ + \oint_{S_-} \vec{F} \cdot \vec{n_-} dS_- \quad (2.75)$$

Referring to the notation in section 2.1, S_+ and S_- are Γ for the 1 and 2 surfaces respectively. Since $\vec{F}$ is C^1 and $\vec{n_-} = -\vec{n_+}$, the following can be said,

$$\oint_{S_+} \vec{F} \cdot \vec{n_+} dS_+ = - \oint_{S_-} \vec{F} \cdot \vec{n_-} dS_- \quad (2.76)$$

These two terms cancel and the right-hand side of equation 2.74 becomes:

$$\oint_S \vec{F} \cdot \vec{n} dS = \oint_{S_1} \vec{F} \cdot \vec{n_1} dS_1 + \oint_{S_2} \vec{F} \cdot \vec{n_2} dS_2 \quad (2.77)$$

Now, it is left to examine the left-hand side of equation 2.74:

$$\int_V \nabla \cdot \vec{F} dV = \int_{V_1} \nabla \cdot \vec{F} dV_1 + \int_{V_2} \nabla \cdot \vec{F} dV_2 + \int_\Gamma [\nabla \cdot \vec{F}] d\Gamma \quad (2.78)$$

where $[\cdot]$ represents the jump in the quantity across Γ. Putting both sides together, this more general form of the divergence theorem is:

$$\int_V \nabla \cdot \vec{F} dV = \oint_S \vec{F} \cdot \vec{n} dS - \int_\Gamma [\nabla \cdot \vec{F}] d\Gamma \quad (2.79)$$

This equation can now be used to determine a compatibility condition for a Poisson equation where $\vec{F} = \frac{1}{\rho(\phi)} \nabla P_d$. A discrete form of the equation is discussed in section 3.6.

2.6 Boundary Conditions

There are two types of boundary conditions for the domains utilized in this thesis depending on the canonical problem considered. They will both be discussed in this section and then only referenced in later chapters. While these conditions are the only ones considered in this work, the numerical method is not limited to those discussed here.

2.6.1 Periodic Wave Tank

To reduce the domain size necessary for a wave tank, periodic horizontal boundary conditions are used for the velocity, pressure and level set function within the length of domain L.

$$\vec{\mathbf{u}}(L) = \vec{\mathbf{u}}(0) \tag{2.80}$$

$$P_d(L) = P_d(0) \tag{2.81}$$

$$\phi(L) = \phi(0) \tag{2.82}$$

The domain is considered to be contained within a set of free-slip walls above and below. The walls allow no flux through them and a zero-gradient extrapolation is used for the terms that slip.

$$\begin{aligned} \frac{\partial \vec{\mathbf{u}} \cdot \vec{\mathbf{t}}}{\partial n} &= 0 \\ \vec{\mathbf{u}} \cdot \vec{\mathbf{n}} &= 0 \end{aligned} \tag{2.83}$$

Additionally, there is zero (dynamic) pressure gradient at the walls.

$$\frac{\partial P_d}{\partial n} = 0 \tag{2.84}$$

Finally, because the level set function is a distance function, a zero-gradient extrapolation is an insufficient boundary condition. To this end, a linear extrapolation

method based on the sign of the level set function is employed.

$$\frac{\partial \phi}{\partial n} = \text{sign}(\phi) \tag{2.85}$$

2.6.2 Open Channel

For cases where periodicity of the horizontal flow would pollute the region of interest, an open channel with free-slip walls has been used. The boundary conditions vertically are the same as that in the periodic wave tank, namely equations 2.83 and 2.84 for the velocity and pressure, respectively. The inlet conditions are that of a steady, uniform inflow.

$$\begin{aligned} \vec{\mathbf{u}} &= (U_o, 0, 0) \\ \vec{\mathbf{u}} \cdot \vec{\mathbf{n}} &= 0 \end{aligned} \tag{2.86}$$

The outlet conditions use zero gradient extrapolation.

$$\frac{\partial \vec{\mathbf{u}}}{\partial \vec{\mathbf{n}}} = 0 \tag{2.87}$$

The dynamic pressure also uses zero gradient extrapolation on all boundaries.

$$\frac{\partial P_d}{\partial n} = 0 \tag{2.88}$$

Finally, the level set function uses the same extrapolation idea as in equation 2.85 for all boundaries.

2.7 LSM for Air-Water Interface Flows

A key component to successful implementation of the level set method is the smoothing of the fluid interface over a few points. Many authors simply justify this by minimizing the number of grid points over which this occurs. In their paper on front-tracking flows, Unverdi and Tryggvason [121] make two strong arguments in regards

to smoothing a sharp interface. The first applies to methods where an indicator function is used to determine the location of the interface. They point out that with a sharp indicator function, an uncertainty principle exists in that "it is not possible to specify a precise location and zero thickness simultaneously". If, from one grid point to the next, the indicator function goes from 0 to 1, the only thing which can be said is that the interface lies somewhere between those two points. Because of the nature of the level set function, this argument does not directly apply because the location of the interface will be known at a given point. However, Unverdi and Tryggvason's uncertainty principle is still applicable in the sense that, in the governing equations, if the function which maps the level set function to a density or viscosity is sharp, the property will change sharply between grid points essentially bringing the order of the method back to a marker-and-cell type method.

Their second argument, which is more applicable to the level set method, is to consider smoothing the interface just as an approximation of a sharp function. Such that when a parameter which defines the smoothness goes to zero, the function becomes sharp. Thus, as any finite-difference approximation of a derivative or trapezoidal approximation of an integral becomes a derivative or integral as the step size goes to zero, the same can be said for the smoothing function as its width goes to zero.

2.7.1 Overall Effect of Smoothing the Interface

To look at the global effect of smoothing the interface, we will consider the Navier-Stokes (NS) equations for a sharp and smooth interface. If the location of the interface Γ is known, the NS equations can be written for both fluids (air and water for this discussion). Regardless of the discretization difficulties associated with a surface of complex topology, for a given velocity $\vec{u}$ the conservative form of the NS equations for both fluids can be written as two separate equations (refer to equation 2.18). For

simplicity in notation, the effect of surface tension has been ignored.

$$\frac{\partial \vec{\mathbf{u}}_w}{\partial t} + \nabla \cdot (\vec{\mathbf{u}}_w \vec{\mathbf{u}}_w) = -\nabla \Pi + \frac{1}{\mathcal{R}e_d} \nabla \cdot (2\overline{\mathbf{D}}_\mathbf{w}) + \frac{\vec{\mathbf{k}}}{\mathcal{F}r^2} \tag{2.89}$$

$$\frac{\partial \vec{\mathbf{u}}_a}{\partial t} + \nabla \cdot (\vec{\mathbf{u}}_a \vec{\mathbf{u}}_a) = -\frac{1}{\lambda} \nabla \Pi + \frac{\eta}{\lambda \mathcal{R}e_d} \nabla \cdot (2\overline{\mathbf{D}}_\mathbf{a}) + \frac{\vec{\mathbf{k}}}{\mathcal{F}r^2} \tag{2.90}$$

In equations 2.89 and 2.90, $\overline{\mathbf{D}}$ is the deformation tensor and the density and viscosity ratios are represented by $\lambda = \rho_a/\rho_w$ and $\eta = \mu_a/\mu_w$. The nondimensional parameters are based on the properties of the water and defined as:

$$\mathcal{R}e_d = \frac{\rho_w U L}{\mu_w} \qquad \mathcal{F}r^2 = \frac{U^2}{gL} \tag{2.91}$$

In general, the density and viscosity are governed by their own advection equations. However, with a sharp interface, they are discontinuous making their advection numerically troublesome. The level set formulation maps the discontinuous density and viscosity functions as a smooth function of the distance to the interface (ϕ) making its advection straight forward. The discontinuities only exist in the NS equations. Using this mapping gives us equation 2.17 which is repeated here for simplicity:

$$\frac{\partial \vec{\mathbf{u}}}{\partial t} + \nabla \cdot (\vec{\mathbf{u}} \vec{\mathbf{u}}) = -\frac{1}{\rho(\phi)} \nabla \Pi + \frac{1}{\rho(\phi) \mathcal{R}e_d} \nabla \cdot (2\mu(\phi)\overline{\mathbf{D}}) + \frac{\vec{\mathbf{k}}}{\mathcal{F}r^2} \tag{2.92}$$

with the density and viscosity functions represented using a Heaviside function which is 0 in the air and 1 in the water.

$$\rho(\phi) = \lambda + (1-\lambda) H(\phi;\epsilon) \tag{2.93}$$

$$\mu(\phi) = \eta + (1-\eta) H(\phi;\epsilon) \tag{2.94}$$

If the Heaviside function is sharp, equation 2.92 will recover equations 2.89 and 2.90 if written out for each fluid. This brings us to our first conclusion in regards to the level set form of the NS equations. If S is defined as the solution to equations 2.89 and 2.90 and $\tilde{S}$ is the solution to equation 2.92, then

1. $\tilde{S} = S$ provided the Heaviside function is sharp.

For complex surface topologies, the solution $\tilde{S}$ (and S for that matter) for sharp Heaviside functions is numerically difficult. Using the justification of Unverdi and Tryggvason [121], the Heaviside function is customarily smoothed over a small distance, say 2ϵ. The smoothed Heaviside function then becomes a function of the distance to the interface (the level set function, ϕ).

$$H(\phi;\epsilon) = \begin{cases} 1 & \phi > \epsilon \quad \text{if } \vec{\mathbf{x}} \in \text{water} \\ f(\phi;\epsilon) & |\phi| < \epsilon \quad \text{if } \vec{\mathbf{x}} \in \Gamma_\epsilon \\ 0 & \phi < -\epsilon \quad \text{if } \vec{\mathbf{x}} \in \text{air} \end{cases} \tag{2.95}$$

This is the same as equation 2.21. Here, $f(\phi;\epsilon)$ is called a smoothing function. It is a function of the signed distance to the interface and uses a parameter ϵ to define the thickness of the smoothing, or in other words, the thickness of the interface. To understand the overall effect of smoothing the interface, the exact form of the smoothing function is irrelevant. Thus, to keep the discussion clear, the details of the form will be discussed in detail in 2.7.2.

To classify the effect of the smoothing distance ϵ, a few more parameters need to be defined. First, a common notation in level set methods is α which represents the number of points in ϵ.

$$\alpha = \frac{\epsilon}{\Delta} \tag{2.96}$$

Here, Δ is the grid spacing. Generally, the majority of all level set implementations in the literature use $\alpha = 2.5$ such that they claim the interface is smoothed "over only a few grid points" or within the width of a typical second-order finite-difference stencil. In addition to α, an additional parameter will be useful which measures the ratio of viscous boundary layer thickness to interface thickness (level set boundary layer thickness).

$$\gamma_w = \frac{\delta_w}{\epsilon} \tag{2.97}$$

There is an equivalent γ definition based on the properties of the air. One important item of note is because of the relative values of density and viscosity for air and water, the relationship from water to air can be found easily.

$$\gamma_a \sim \sqrt{10}\gamma_w \tag{2.98}$$

To finally address the effect of the thickness of the interface, we need to quantify the error associated with smoothing the interface. We shall represent the error between the smoothed and sharp solution as $\tilde{e}$:

$$\tilde{e} = \tilde{S} - S \tag{2.99}$$

The second conclusion that we can draw regarding the overall effect of smoothing the interface is:

2. For a fixed $0 < \gamma_w < \infty$, there is a limiting smoothed solution where $\tilde{e}(\gamma_w) \neq 0$.

This can be seen if one considers the thickening of the interface as actually applying a level set boundary layer (of size 2ϵ) over the discontinuity which appears in the sharp solution. In general boundary layer theory, the process of finding the global solution involves finding an inner and outer solution and then matching the boundary conditions at the seam between the inner and outer solutions [6]. However, the partial differential equations under consideration (eqn. 2.92) are being solved only in the global sense, using boundary conditions only at outer the boundaries. Because the governing equations are different in the global sense, there will always be an "error" associated with their solution. With this in mind, convergence tests should always be done at the same γ.

The third conclusion that we can draw is that of the approximation argument of Unverdi and Tryggvason in that as the level set boundary layer thickness goes to zero, the sharp solution is recovered:

3. As γ_w approaches ∞, $\tilde{e}(\gamma_w) \to 0$.

A final conclusion (or consequence of conclusion 3) involves the numerical discretization of the level set NS equations.

4. As α approaches 0, $\tilde{e}(\gamma_w) \to 0$.

Because the numerical sharpness of the Heaviside function is reliant on α, one can actually recover S using a poorly resolved $\tilde{S}$. For this under resolved case, (particularly $\alpha < 1$), numerically it would seem as though there was no level set boundary layer. If a numerical implementation of this case were done using a model with high numerical dissipation, one might recover something which resembled the sharp solution. This is not a recommended approach.

The consequence of these four conclusions is that properly resolved direct numerical simulation (DNS) of the NS equations using the level set method is not equivalent to solving the multi-fluid DNS presented in equations 2.89 and 2.90. In other words, *level set DNS is not DNS of the multi-fluid NS equations.* It *is* DNS of the level set NS equations. With this in mind, what becomes the issue is the consequences of using the level set NS equations and striking a balance between the resolution of the smoothed layer, the viscous boundary layer for both fluids and realistic computational costs.

2.7.2 Performance of Traditional LSM

As a test of the performance of the traditional smoothing function in the context of the Navier-Stokes equations, a canonical problem of a vortex pair rising towards the air-water interface is considered. The initial conditions for the test is a flat interface with two sets of counter rotating vortices (arranged as image pairs) positioned far away from the interface. The induced velocities of the vortex pairs (in the water) causes them to rise towards the surface. The results of particular interest for this problem are the deformation of the interface and the formation of secondary vorticity at the interface which were highlighted in the works of Tsai and Yue [118] for cases with and without surfactants in two dimensions and in three dimensions by Dommermuth [22].

Tsai and Yue's clean case is the most relevant for this comparison. They noted an

increase in surface elevation at the centerline with a scar or indentation of the surface (over the location of the vortex). Additionally, at the wave trough there was a peak of negative vorticity due to convection of the primary vortex horizontally under the surface and the strength of this secondary vorticity is about 20% of the primary vorticity. The nondimensional parameters for Tsai and Yue are $\mathcal{R}e = 180$, $\mathcal{F}r^2 = 0.15$ and $\mathcal{W}e = 1$ and $\mathcal{W}e = 20$. Figure 2-2 is an instantaneous snapshot of the interface location using the level set method for three different resolutions for a constant interface thickness for $\mathcal{R}e = 200$, $\mathcal{F}r^2 = 0.5$ and $\mathcal{W}e = 12.5$. The agreement between this and Tsai and Yue's results are quite good qualitatively and quantitatively if the difference in $\mathcal{F}r$ is considered. The maximum free-surface elevation at the time shown for Tsai and Yue is around 0.22. The level set method shows a maximum elevation at this time to be around 0.6, which scales with the difference in Froude number. Additionally, considering the minimal difference in results at the three resolutions, one might consider this to be a converged result. However, as seen in figure 2-3, the secondary vorticity which forms at the interface, while having qualitatively similar results to what is expected, has an increasing amount of "spurious" vorticity as the resolution decreases. The presence of the spurious vorticity also becomes increasingly more significant if the interface thickness decreases as can be seen in figure 2-4.

Two questions arise from these tests. First, what is the source of this spurious vorticity and second, since the vorticity at and near the interface effects the free-surface elevation, why does the result in figure 2-2 appear converged?

To answer the first question, it is easier to consider a simplified problem which can be solved analytically. Namely, the solution of linear Poiseuille-Couette flow for two-fluids between moving (in opposite direction) parallel plates. The steady, linear (one-dimensional) form of the NS equations for the water and air are given in equations 2.100 and 2.101, respectively. Both are non-dimensionalized by the water characteristics.

$$\frac{1}{\mathcal{R}e_w}\nabla^2 u_w = \nabla P \tag{2.100}$$

$$\frac{\eta}{\mathcal{R}e_w}\nabla^2 u_a = \nabla P \tag{2.101}$$

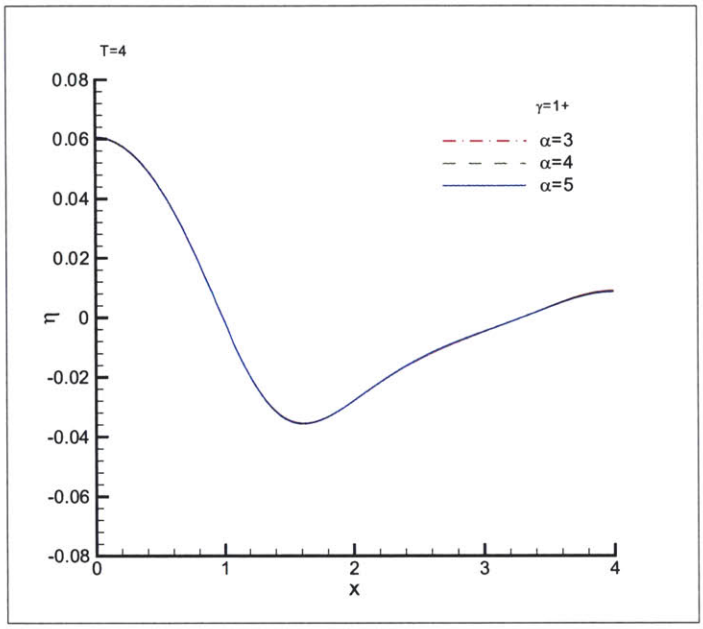

Figure 2-2: Instantaneous free-surface elevation (η) for half of the domain at $T = 4$ for three cases: (i) $\alpha = 3$ (red); (ii) $\alpha = 4$ (green); and (iii) $\alpha = 5$ (blue). The interface thickness is fixed for $\gamma_w = 1+$. $\mathcal{R}e = 200$, $\mathcal{F}r^2 = 0.5$ and $\mathcal{W}e = 12.5$

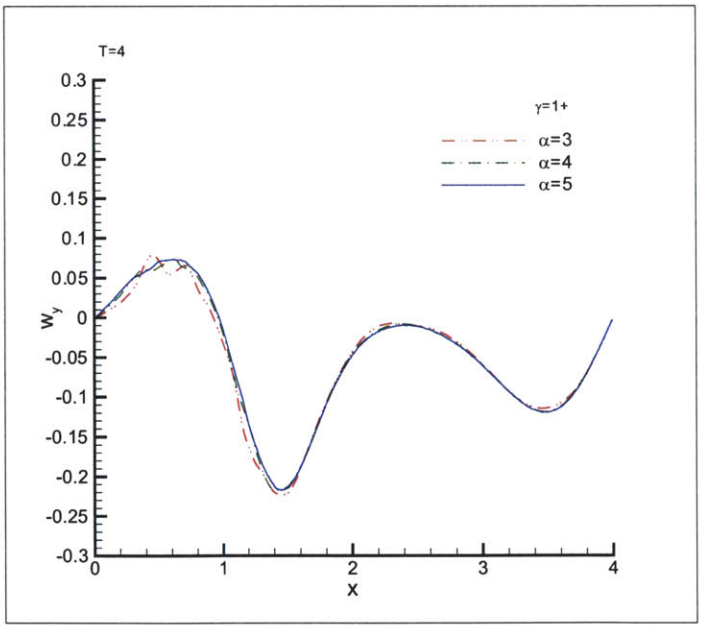

Figure 2-3: Instantaneous surface vorticity (ω_y) for half of the domain at $T = 4$ for three cases: (i) $\alpha = 3$ (red); (ii) $\alpha = 4$ (green); and (iii) $\alpha = 5$ (blue). The interface thickness is fixed for $\gamma_w = 1+$. $\mathcal{R}e = 200$, $\mathcal{F}r^2 = 0.5$ and $\mathcal{W}e = 12.5$

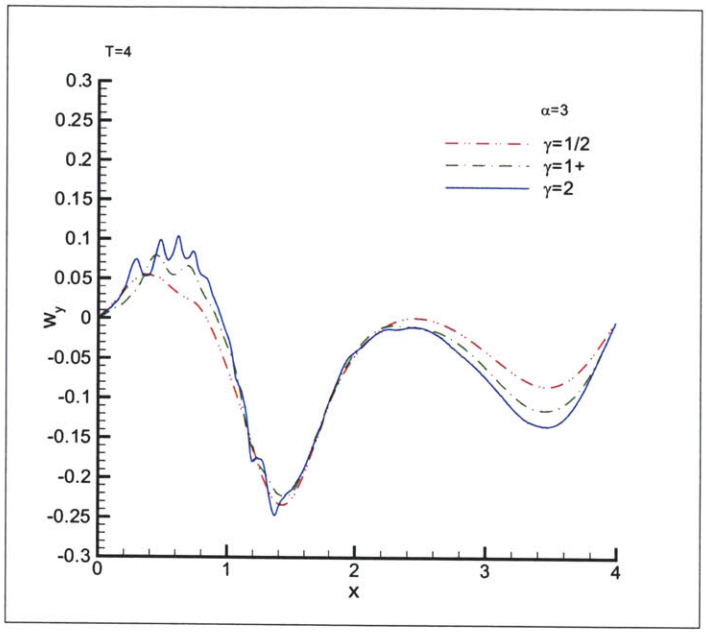

Figure 2-4: Instantaneous surface vorticity (ω_y) for half of the domain at $T = 4$ for three cases: (i) $\gamma_w = 1/2$ (red); (ii) $\gamma_w = 1+$ (green); and (iii) $\gamma_w = 2$ (blue). The resolution of the interface thickness is foxed at $\alpha = 3$. $\mathcal{R}e = 200$, $\mathcal{F}r^2 = 0.5$ and $\mathcal{W}e = 12.5$

Again, η in this context is the ratio of viscosities between air and water. The boundary conditions for equations 2.100 and 2.101 are no-slip at the top and bottom of the domain, no-slip at the air-water interface and a continuous shear at the interface. The solution of this problem can be obtained analytically.

The level set formulation of this problem, non-dimensionalized by the water, is

$$\frac{1}{\mathcal{R}e}\nabla \cdot (2\mu_\epsilon(\phi)\overline{D}) = \nabla P \tag{2.102}$$

with $\mu_\epsilon(\phi)$ continuous and equal to $\eta + (1-\eta)H_\epsilon(\phi)$. Because a smoothed Heaviside function is used, equation 2.102 can be rewritten in a form similar to the sharp equations:

$$\mu_\epsilon(\phi)\nabla^2 u + 2\overline{D} \cdot \nabla\phi(1-\eta)\delta_\epsilon(\phi) = \mathcal{R}e_w \nabla P \tag{2.103}$$

Equation 2.103 is another proof that the level set form of the Navier-Stokes equations is not the same as the sharp form of the two-fluid equations. In addition to the

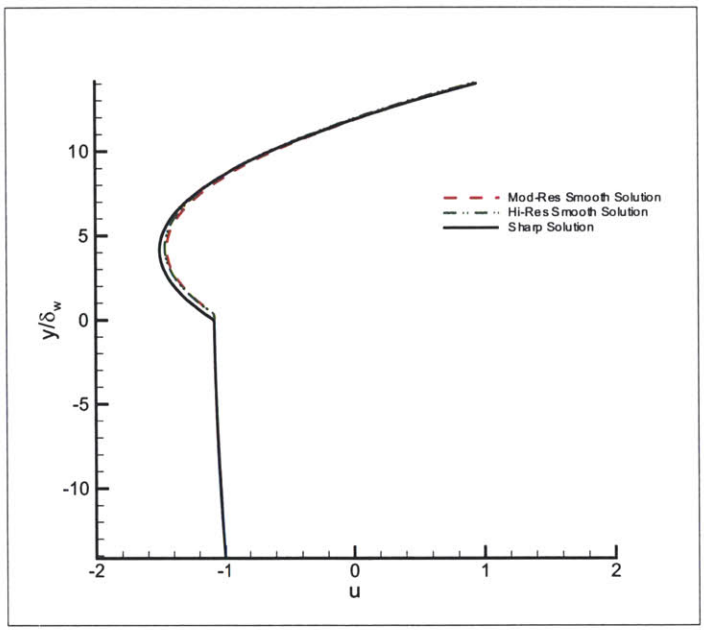

Figure 2-5: Comparison of solutions to the two-fluid Couette-flow problem for a single case $\gamma_w = 2$: (i) analytic (black); (ii) high-resolution (green); (iii) moderate resolution (red). $\mathcal{R}e_w = 200$ and $P = 5e^{-4}$

form of the equation, the equation is a global equation and only subject to boundary conditions at the top and bottom of the domain (no-slip walls). There are no specific boundary conditions at the interface. The no-slip condition at the interface is taken care of by the continuous flow assumption and the balanced shear condition is a consequence of the statement of the shear forces being continuous in a fluid. The second term of the equation can be interpreted as a forcing function which helps enforce the stress balance in the interface region verses the exact interface.

Figure 2-5 shows the solution of the analytic sharp solution compared to both a highly-resolved and moderately-resolved solution of equation 2.102 numerically, using a tridiagonal solver. The effect of solving the level set formulation globally is evident as is the effect of the shear balance over the interface region.

Considering the velocity solution shows us the effect of solving the two different sets of equations but not until the velocity gradients and shear stresses are considered does the source of the spurious vorticity become evident. Figure 2-6 shows the solution of this problem for a fixed γ_w at a high resolution (which we consider the exact solution

for the sake of the discussion) and at more reasonable computational resolutions. The slope of the velocity and the shear stress are shown here. Surprisingly, the fluctuations of the shear actually occur at the transition between the smoothed layer and viscous air boundary layer and not at the interface as one might expect.

To understand why this is the case, we need to reconsider the physics of the problem we are considering. Because of the differences in viscosity between the two fluids, whether the interface is sharp or smoothed, the velocity gradients in the air boundary layer are a hundred times larger than the water. It is common knowledge that, providing the velocity and length scale between the two fluids are the same, there is a factor three difference in the viscous boundary layer thickness for air and water. With air being the larger of the two boundary layers resolved on the same grid, the number of points in the viscous air boundary layer is by default three times that in the water boundary layer. However, even using three times more points in the air boundary layer, it is difficult to resolve gradients that change by a factor of 100. This is quite evident in the plot of the velocity slope in figure 2-6. Remembering that as γ becomes large, the sharp solution is obtained, what might be considered a suitable value for the water flow (say 2) yields a very high (say about 6) value for the air flow. This makes the solution in the air portion of the flow seem as if the interface were sharp with only a few points in it. This is verified up to sixth order finite difference schemes. The poor resolution of these very high gradients leads to the formation of non-physical vorticity.

This is not necessarily a new problem in the computation of multi-fluid flows but has not been discussed in the level set literature. One of the benefits of the level set method outside of its ability to model complex topological changes is that it provides a mapping of the interface such that *a-priori* knowledge of which points are in which fluid is not necessary. However, in trying to remove a numerical implementation issue we've potentially affected the modeling of the physics. There are two ways to attack this problem. First is to adequately resolve the transition between the smoothed interface and the viscous air boundary layer. Using the analytical solution showed that the computational requirements for this are extreme. They show that α's as

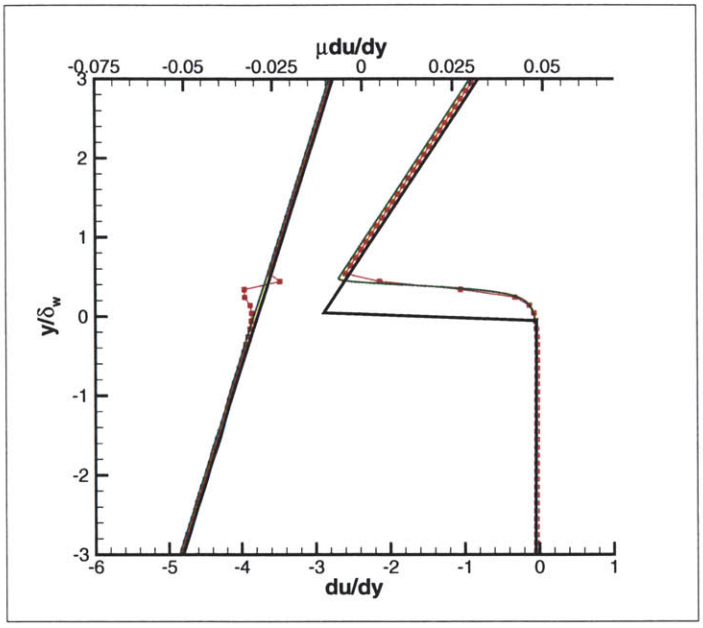

Figure 2-6: Velocity slope and shear stress using traditional smoothing function for a single case $\gamma_w = 2$: (i) analytic (black); (ii) high-resolution (green); (iii) moderate resolution (red).

high as 20 still have a small amount of error for γ_w of 2. The second is to allow the level set boundary layer to smooth the air boundary layer without paying a penalty in the water. This solution is addressed in the next section.

The second question as to why the spurious free-surface vorticity does not seem to affect the free-surface elevation can now be answered based on the knowledge just gained. The conservative form of the governing equation of the level set function is:

$$\frac{\partial \phi}{\partial t} + \nabla \cdot (\vec{\mathbf{u}}\phi) = 0 \tag{2.104}$$

For the advection of the level set function, the relevant velocity gradients are (u_x, w_z). The nature of vorticity for a two-dimensional problem at the interface is that it is actually a function of u_z and w_x. Because the vortex pair problem has very weak vertical gradients in the vertical velocity and weak horizontal gradients in general, the only effect of these poorly resolved vertical gradients in the air boundary layer is in the calculation of the vorticity.

2.7.3 Development of a Modified Smoothing Function

For the purposes of this study, it is desirous to have a modified smoothing function $g(\phi;\epsilon)$ which extends the smoothing properties of the level set boundary layer further into the air boundary layer than the traditional model.

Development of a smoothing function, also called a kernel, has been addressed by many authors. Some general properties are identified by Williams *et al.* [125] which are applicable here. The authors state that the smoothing function should: (i) have compact support, (ii) be monotonically decreasing with respect to the distance from the center, (iii) be symmetric, (iv) be sufficiently smooth, (v) have a normality property, and (vi) approach the sharp function as the smoothing parameter goes to zero. While they state that symmetry is desirable, they also note that it is not required. Because we are actually looking for a function which has a larger extent in the air boundary layer, the modified smoothing function developed here will not be symmetric. The list of requirements translate into the following conditions for a well-behaved, non-symmetric smoothing function:

1. $g(0;\epsilon) = 1/2$
2. $g(\epsilon;\epsilon) = 1$
3. $g(-h\epsilon;\epsilon) = 0$
4. $dg/d\phi(\epsilon;\epsilon) = 0$
5. $dg/d\phi(-h\epsilon;\epsilon) = 0$
6. $d^2g/d\phi^2(\epsilon;\epsilon) = 0$
7. $d^2g/d\phi^2(-h\epsilon;\epsilon) = 0$
8. $dg/dx > 0$

The factor (h) which represents the additional extent into the air boundary layer is left as a variable at this point. Conditions 1 through 3 satisfy the recovery of the sharp function as ϵ goes to zero. Conditions 4 and 5 satisfy the normality property. Conditions 6 and 7 supply sufficient smoothness and condition 8 provides the monotonically decreasing requirement. A polynomial can be generated to satisfy these conditions and keep the kernel form simple. Solving the first seven conditions gives all of the polynomial coefficients as a function of h and an eighth coefficient. The eighth coefficient is chosen albeit somewhat randomly to satisfy condition 8 for a given h. Experience has shown that $h < 2$ may not be sufficient to adequately smooth out the gradients in the air boundary layer. Therefore, we choose $h = 2$, i.e. the level

set boundary layer in the air is twice the width of the water value. The coefficients become:

$$\begin{aligned} c_0 &= \frac{1}{2} & c_4 &= -11c_7 - \frac{61}{1296} \\ c_1 &- -8c_7 + \frac{301}{324} & c_5 &= -3c_7 + \frac{173}{1296} \\ c_2 &= 12c_7 - \frac{19}{648} & c_6 &= 3c_7 + \frac{47}{1296} \\ c_3 &= 6c_7 - \frac{677}{1296} & c_7 &= 0.015 \end{aligned} \tag{2.105}$$

where the polynomial is given for completeness as:

$$g(x = \phi/\epsilon) = c_0 + c_1 x + c_2 x^2 + c_3 x^3 + c_4 x^4 + c_5 x^5 + c_6 x^6 + c_7 x^7 \tag{2.106}$$

Figure 2-7 shows the behavior of the new smoothing function compared to the traditional function for a fixed γ_w and α. It is important to note that, while there has been some additional smoothing of the level set solution in the air, the γ_a can still be chosen such that it is greater than 1. By increasing the extent of the level set smoothing in the air boundary layer from ϵ to 2ϵ, the effective γ_a has been cut by half. This yields us with the new form of equation 2.98:

$$\gamma_a \sim \frac{1}{2}\sqrt{10}\gamma_w \tag{2.107}$$

Providing that γ_w is chosen such that $\gamma_a \geq 1$, there will still be a portion of the air boundary layer which is not in the smoothed region.

Performance of Modified Smoothing Function

Returning to the performance of the modified smoothing function, we will first determine its performance in the one-dimensional test case of two-fluid Couette flow.

Figure 2-8 compares the velocity, its slope and the shear stress of the modified smoothing function with the traditional smoothing function results. The performance is markedly improved in the region of the air solution solely because of the increased

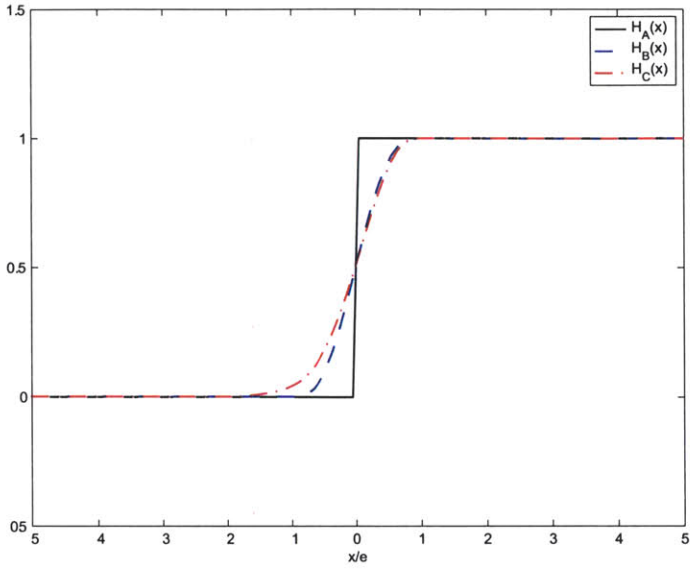

Figure 2-7: Comparison of the smoothing functions for $\gamma_w = 2$ and $\alpha = 5$.

extent of the level set boundary layer. This decreases the jump in slope which must be resolved.

Finally, it is left to consider the modified smoothing function in conjunction with the full Navier-Stokes equations and return to the simulation of the vortex pair rising towards the free-surface. Figures 2-9 and 2-10 compare the surface elevation and surface vorticity between the two smoothing functions, respectively. The "spurious" vorticity is now absent.

2.7.4 Smoothing Functions as Filters

A useful approach to further understanding the consequences of the smoothing function is to consider the spectrums of the functions. For example, consider two signals in one-dimensional space: $H_A(x)$ and $H_B(x;\epsilon)$.

$$H_A(x) = \begin{cases} 1 & x > 0 \\ 1/2 & x = 0 \\ 0 & x < 0 \end{cases} \qquad H_B(x;\epsilon) = \begin{cases} 1 & x > \epsilon \\ f(x;\epsilon) & |x| < \epsilon \\ 0 & x < -\epsilon \end{cases} \tag{2.108}$$

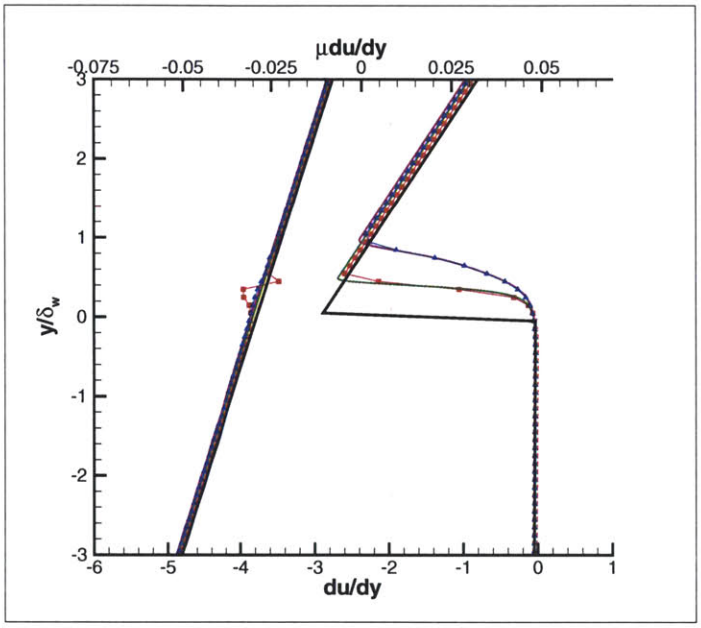

Figure 2-8: Velocity slope and shear stress comparison between the traditional and modified smoothing functions for a single case $\gamma_w = 2$: (i) analytic (black); (ii) high resolution $f(\phi)$ (green); (iii) moderate resolution $f(\phi)$ (red); (iv) high resolution $g(\phi)$ (purple); (v) moderate resolution $g(\phi)$ (blue)

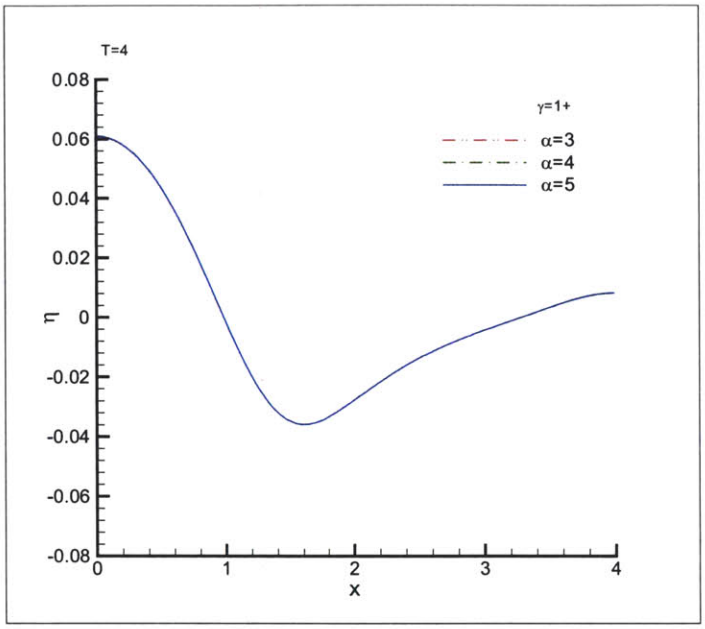

Figure 2-9: Instantaneous free-surface elevation (η) for half of the domain at $T = 4$ for three cases using modified smoothing function at $\gamma_w = 1+$: (i) $\alpha = 3$ (red); (ii) $\alpha = 4$ (green); and (iii) $\alpha = 5$ (blue).

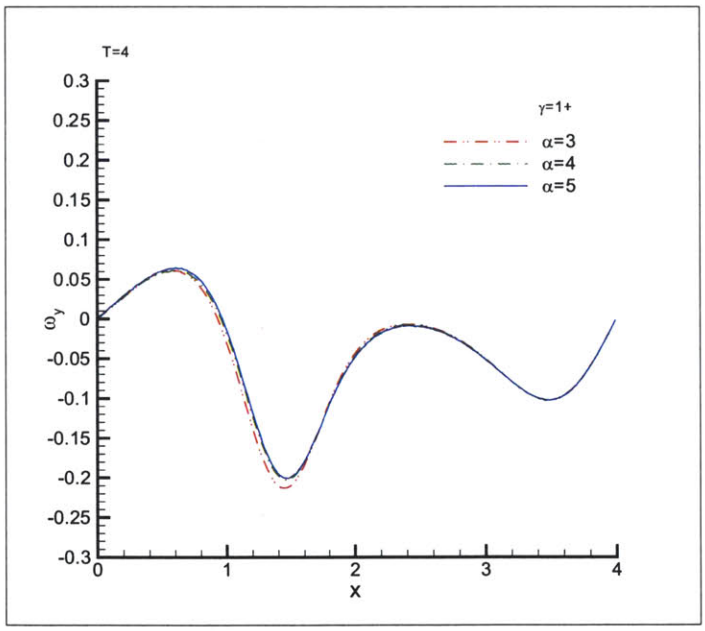

Figure 2-10: Instantaneous surface vorticity (ω_y) for half of the domain at $T = 4$ for three cases using modified smoothing function at $\gamma_w = 1+$: (i) $\alpha = 3$ (red); (ii) $\alpha = 4$ (green); and (iii) $\alpha = 5$ (blue).

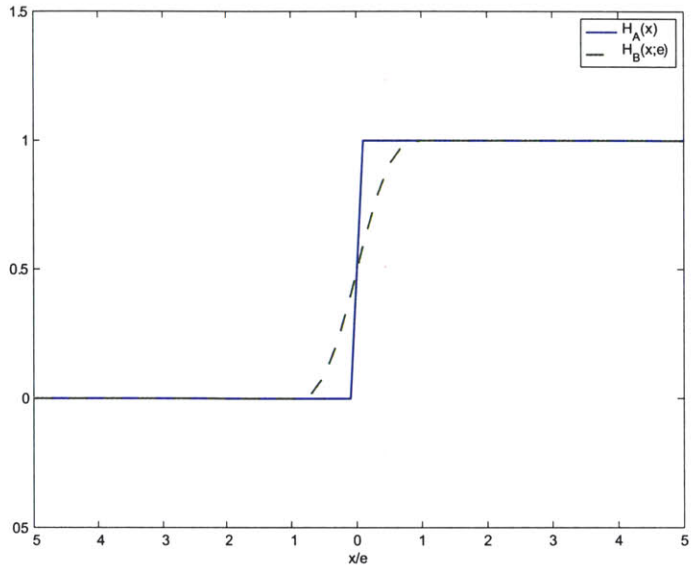

Figure 2-11: Signals A (sharp interface) and B (smooth interface). The distance is nondimensionalized by the smoothing distance ϵ.

where $f(x;\epsilon)$ is that defined in equation 2.26. A plot of these two signals is shown in figure 2-11. In this context, if we assume that signal B started out as signal A, it looks as if it has passed through a filter. The ratio of the spectrums of the two signals will show how the smoothing function modifies the spectrum of the sharp function. The filter can be calculated by considering the ratio of the spectrums $S(k)$ of each signal at each wave number. For example:

$$\mathcal{F}_{AB}(k) = \frac{S_B(k;\epsilon)}{S_A(k)} \tag{2.109}$$

To simplify the discussion and analysis, we will modify signals A and B (eqns. 2.108) so that they are periodic and symmetric about $x = 0$.

$$\widehat{H}_A(x) = \begin{cases} 0 & x > 1/2 \\ 1/2 & x = 1/2 \\ 1 & -1/2 < x < 1/2 \\ 1/2 & x = -1/2 \\ 0 & x < -1/2 \end{cases} \qquad \widehat{H}_B(x;\epsilon) = \begin{cases} 0 & x > 1/2 + \epsilon \\ 1 - f(x_2;\epsilon) & 1/2 - \epsilon \leq x \leq 1/2 + \epsilon \\ 1 & -1/2 + \epsilon \leq x \leq 1/2 - \epsilon \\ f(x_1;\epsilon) & -1/2 - \epsilon \leq x \leq -1/2 + \epsilon \\ 0 & x < -1/2 - \epsilon \end{cases} \tag{2.110}$$

The modified signal B contains the variables x_1 and x_2 which are equal to $x + 1/2$ and $x - 1/2$, respectively. The spectrum of these two modified signals can be calculated over a length L using Fourier series. The Fourier coefficients for the series for the modified sharp Heaviside function (signal A) are:

$$\begin{aligned} a_{A_0} &= \frac{1}{2L} \\ a_{A_n} &= \frac{2}{n\pi} \sin\left(\frac{n\pi}{2L}\right) \\ b_{A_n} &= 0 \end{aligned} \tag{2.111}$$

For the modified smoothed Heaviside function (signal B), these coefficients are:

$$\begin{aligned} a_{B_0} &= \frac{1}{2L} \\ a_{B_n} &= \frac{2L^3}{\pi^2 n^2 \epsilon (L^2 - n^2\epsilon^2)} \sin\left(\frac{n\pi}{2L}\right) \sin\left(\frac{n\pi\epsilon}{L}\right) \\ b_{B_n} &= 0 \end{aligned} \tag{2.112}$$

The spectrum for each signal is defined as follows, where $k = n\Delta x$:

$$S(k) = \frac{1}{2}\sqrt{a_k^2 + b_k^2} \tag{2.113}$$

The spectrums for the two modified signals A and B are shown in figure 2-12. Initially, some of the wavenumber energy is preserved until $k\epsilon_w = 0.0044$ or $n\epsilon_w = 1$. After

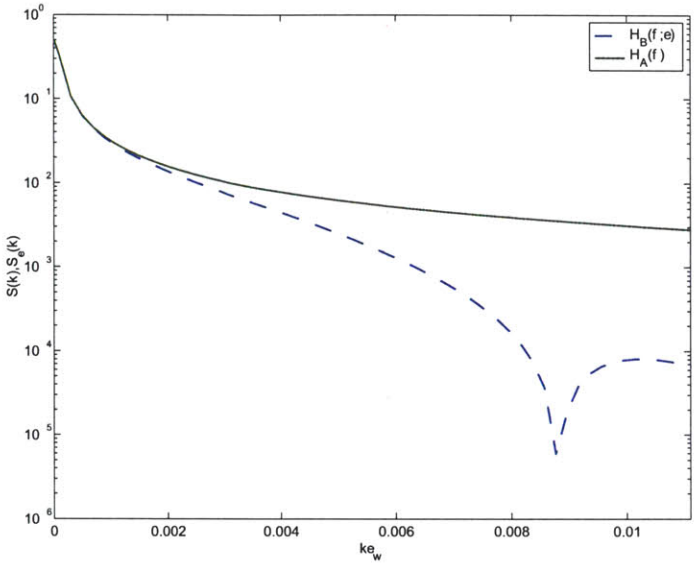

Figure 2-12: The spectrums for the two modified signals (sharp (A) in green and smooth (B) in blue) against $k\epsilon_w$.

this there is a significant drop in the amount of wavenumber energy present until a "notch" appears at $k\epsilon_w = 0.0088$ or $n\epsilon_w = 2$. The filtering effect of the smoothing function can be seen if we examine the ratio of the spectrums. This is shown in figure 2-13. The filter goes to essentially zero where the notch occurs in the spectrum of signal B with a small rebound afterwards.

Figure 2-14 shows the effect of changing ϵ_w (i.e. γ_w) for a fixed α. Within the context of the resolved wavenumbers, for a fixed number of points over which the smoothing function operates (α), the filter is variable with respect to γ_w when plotted against the nondimensional wavenumber $k\epsilon_w$. This is important for the idea for convergence tests. Keeping α fixed and refining the grid makes ϵ_w smaller (γ_w larger). Because the physics of the problem being modeled will depend on the filtering effect of the smoothing function, to ensure that the problem is consistent, ϵ_w should only be calculated from γ_w and not α and Δ. If the filters are plotted against the dimensional wavenumber, they lie on top of each other. The effect of the variation of γ_w is then to only stretch or shrink the filter range.

Figure 2-15 shows the effect of increasing resolution (α) of the level set boundary

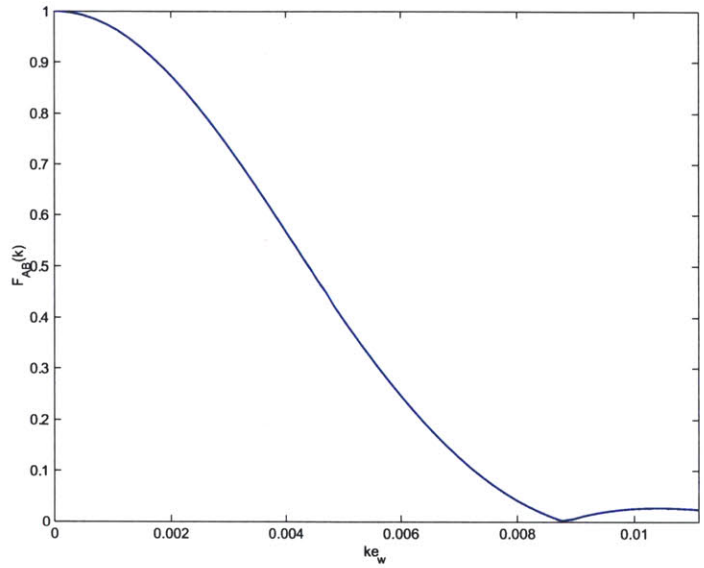

Figure 2-13: The filter from signals A to B for $\gamma_w = 2$ with $\alpha = 5$.

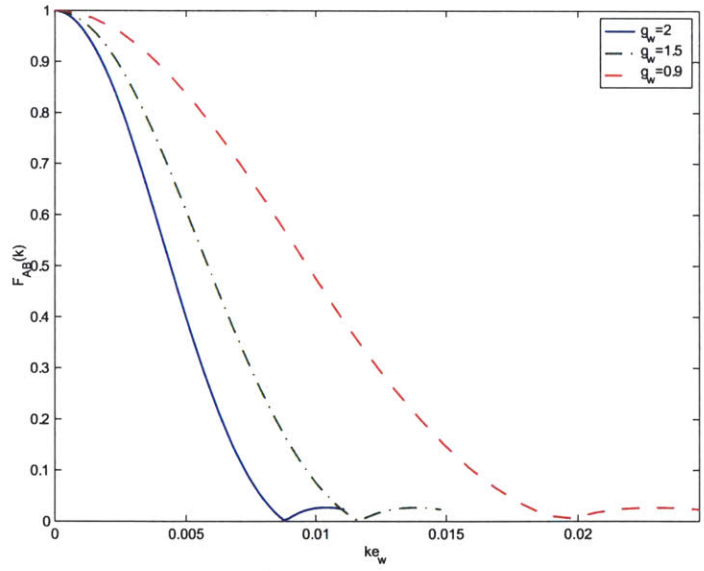

Figure 2-14: The filter from signals A to B for varying γ_w with α fixed and equal to 5.

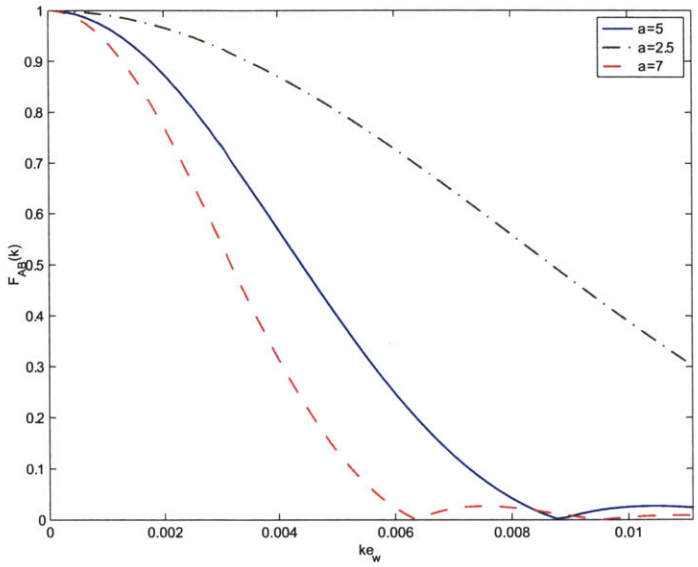

Figure 2-15: The filter from signals A to B for a range of α with γ_w fixed and equal to 2.

layer for a fixed $\gamma_w = 2$. As the resolution is decreased, the filter (and thus the physics being modeled) changes dramatically. This is consistent with previous conclusions that a "poorly" resolved smoothed interface will appear sharp. Figure 2-15 also points out that the physics being modeled is mainly a function of how well resolved the smoothed layer is.

Because this work will use a modified smoothing function, we should consider its filter behavior and compare it to the original smoothing function. The Fourier coefficients can be calculated through a similar, albeit more tedious, analysis. After plugging in the coefficients in equation 2.105, they become equation 2.114.

Figure 2-16 compares the spectrum of the traditional filter and modified filter for a fixed γ_w and α. Because the modified smoothing function smooths the function out over a greater distance than the traditional smoothing function, there should be a greater loss of signal energy, which can be seen in the filter in figure 2-16. There is a small peak at the zeroth wavenumber which is expected due to the value of a_{c_0}. Essentially, the area under the new smoothing function is not the same as the traditional function. After some inspection it seems impossible to determine a

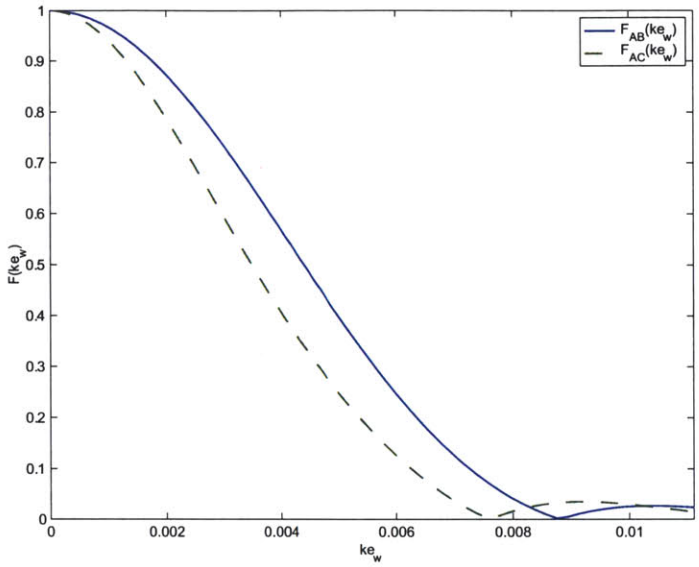

Figure 2-16: Comparison of the filters from signal A to B and from signal A to C for $\gamma_w = 2$ and $\alpha = 5$.

polynomial which simultaneously satisfies the same area and ensures that the delta function and its derivative are well behaved for $h = 2$. This is possible for smaller h values, however testing of these functions with the Poiseuille-Couette flow discussed in sections 2.7.2 and 2.7.3 shows that they do not perform well for air-water flows.

$$
\begin{aligned}
a_{C_0} &= \frac{1}{2L}\left(\frac{709\epsilon}{14000} + L\right) \\
a_{C_n} &= \frac{L^3}{\epsilon^3\pi^4\, n^4}\left(\frac{2173}{450}\cos\left(\frac{\epsilon\, n\pi}{L}\right)\cos\left(\frac{n\pi}{L}(\epsilon+\frac{1}{2})\right) - \frac{18949}{900}\cos\left(\frac{n\pi}{L}(\epsilon-\frac{1}{2})\right) - \frac{2173}{900}\cos\left(\frac{n\pi}{2L}\right)\right) \\
&\quad + \frac{L^4}{\epsilon^4\pi^5\, n^5}\left(\frac{21323}{225}\sin\left(\frac{n\pi}{L}(\epsilon-\frac{1}{2})\right) - \frac{9094}{225}\cos\left(\frac{\epsilon\, n\pi}{L}\right)\sin\left(\frac{n\pi}{L}(\epsilon+\frac{1}{2})\right) + \frac{4547}{225}\sin\left(\frac{n\pi}{2L}\right)\right) \\
&\quad + \frac{L^5}{\epsilon^5\pi^6\, n^6}\left(\frac{28871}{135}\cos\left(\frac{n\pi}{L}(\epsilon-\frac{1}{2})\right) - \frac{4838}{27}\cos\left(\frac{\epsilon\, n\pi}{L}\right)\cos\left(\frac{n\pi}{L}(\epsilon+\frac{1}{2})\right) + \frac{2419}{27}\cos\left(\frac{n\pi}{2L}\right)\right) \\
&\quad + \frac{L^6}{\epsilon^6\pi^7\, n^7}\left(\frac{16684}{45}\cos\left(\frac{\epsilon\, n\pi}{L}\right)\sin\left(\frac{n\pi}{L}(\epsilon+\frac{1}{2})\right) - \frac{2414}{9}\sin\left(\frac{n\pi}{L}(\epsilon-\frac{1}{2})\right) - \frac{8342}{45}\sin\left(\frac{n\pi}{2L}\right)\right) \\
&\quad + \frac{L^7}{\epsilon^7\pi^8\, n^8}\left(\frac{1512}{5}\cos\left(\frac{\epsilon\, n\pi}{L}\right)\cos\left(\frac{n\pi}{L}(\epsilon+\frac{1}{2})\right) - \frac{756}{5}\cos\left(\frac{n\pi}{L}(\epsilon-\frac{1}{2})\right) - \frac{756}{5}\cos\left(\frac{n\pi}{2L}\right)\right) \\
b_{C_n} &= 0
\end{aligned}
\tag{2.114}
$$

2.8 Conclusions

This chapter has presented the mathematical formulation of the governing equations utilized in this work in the context of the level set method. The field equations (mass and momentum conservation) were derived from a material volume perspective and, because the material volume was general, the differential forms could be determined. The origins and necessity for the Poisson equation for the pressure field were highlighted as was the fairly unique treatment of the hydrostatic pressure contribution. Because the Poisson equation for this problem has no unique solution, techniques required to obtain a unique solution are discussed, including the development of a divergence theorem for functions which are not C^2 continuous.

The mapping of the quickly varying constitutive properties, namely density and viscosity, using a smooth distance function was also discussed. The governing equations were nondimensionalized and two types of boundary conditions (the periodic wave tank and an open channel) were outlined.

The governing equations for the level set function were defined from Lagrangian invariance. The consequences of using the fluid velocity as the advection velocity were discussed in detail with focus on the reinitialization technique used to correct the errors this introduces.

The use of the level set method for air-water interface flows is analyzed in detail to understand issues regarding convergence testing and consequences of smoothing the interface. Finally, a modified smoothing function which is asymmetric about the interface, reaching further into the air boundary layer than the traditional method does, is developed, tested and analyzed to ensure that the resulting physics are what should be expected.

Chapter 3

Numerical Implementation

This chapter details the numerical implementation of the governing equations described in chapter 2. In general, the method is implemented to a second-order accuracy in space and time. The grid uses a staggered-MAC type grid which is prevalent in the literature.

As discussed in chapter 2, an algorithm based on the projection method is used to solve the level set form of the Navier-Stokes equations. This entails the solution of a variable coefficient Poisson equation for the dynamic pressure. The momentum equations are integrated in time using a second-order low storage Runge-Kutta scheme. This type of implementation is by no means new; however, the multi-fluid aspect of the problem leads to situations where great care must be taken in the discretization to ensure that numerical dissipation is minimized. The numerical technique of including surface tension in an Eulerian interface capturing method is detailed. The discretization and integration of the level set governing equations are discussed as well as the nuances of implementing a level set reinitialization scheme which accurately conserves volume. Finally, the numerical algorithm is outlined to show how the Navier-Stokes equations and level set governing equations are coupled with the reinitialization scheme.

Figure 3-1: Schematic of the MAC-type grid used in the discretization of the level set formulation.

3.1 Grid Discretization

Discretization of the flow solver is done on a MAC-type grid [39]. For each cell, the level set function, fluid density, viscosity and pressure are computed on the cell centers. The horizontal velocity is computed on a grid staggered in the x-direction and the vertical velocity is computed on a grid staggered in the z-direction. This is shown in figure 3-1.

In general, to move variables between various grids, such as the u velocity from the z-centered to the z-staggered grid, a simple averaging is done. This is adequate only if the grid or variables on the grid do not change drastically from point to point. It is also best suited for Cartesian rather than general boundary-fitted grids. There are instances when the constitutive properties will be needed on the staggered grid. Most volume of fluid and many current level set implementations treat the constitutive properties in much the same way as the velocity fields when moving them between grids. For example, consider the hypothetical situation in figure 3-2. To determine the value of $\rho(2.5, 2)$ given that $\rho(2, 2) = 0.07$ and $\rho(3, 2) = 1.0$, an average would assign that value to be 0.54. If a biquadratic interpolation is used, the density value at the point of interest actually evaluates at 0.65. The question becomes, which is right? One argument is to use even higher order interpolation. Eventually, a sufficiently large enough order interpolation scheme would converge to the appropriate value. While a valid argument, these interpolation schemes involve increasingly more points. As the surface topology becomes complex, accurately interpolating functions that rapidly

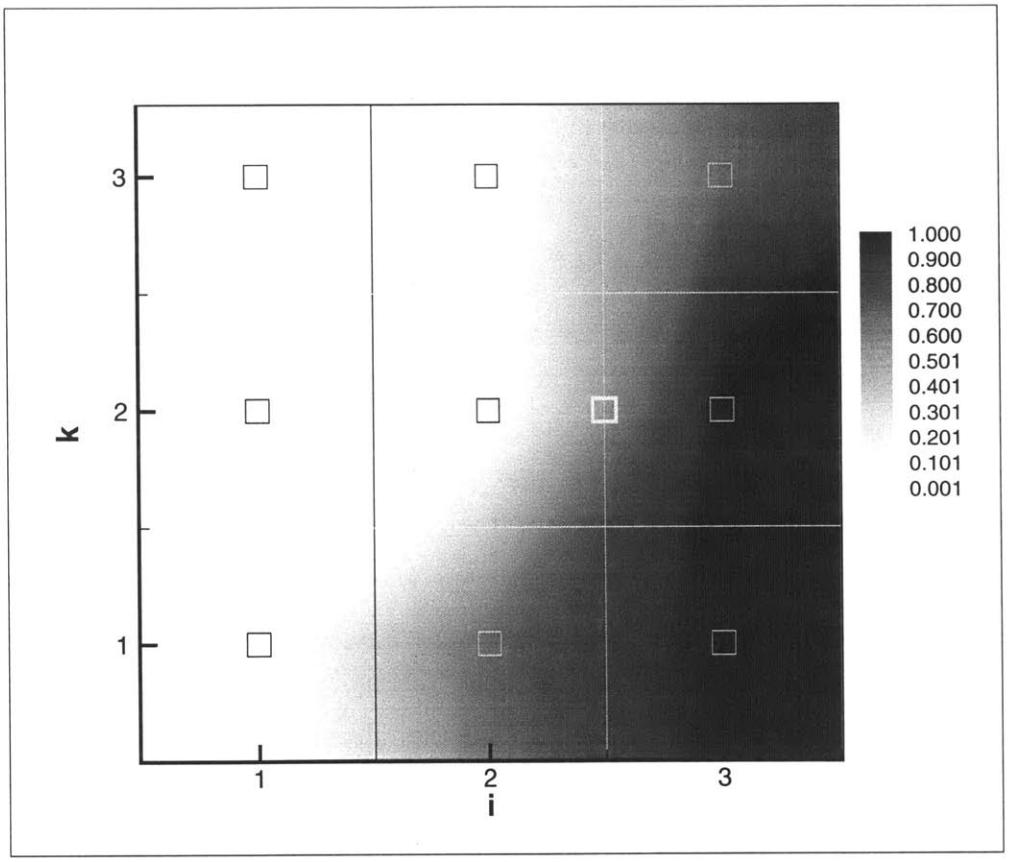

Figure 3-2: A hypothetical example of the interface crossing through a cell. The density (0.001 in air and 1.0 in water) is shown.

vary three orders of magnitude within a larger interpolation domain would be difficult to converge. The interpolated values of the density and viscosity play significant roles in the solution of the pressure field and calculation of shear forces at the interface. Even small errors here will be very problematic.

One of the main advantages that the level set method has is that it has mapped the rapidly changing and discontinuous functions (i.e. density and viscosity) to a continuous function (i.e. the distance to the interface). Even as the interface topology becomes complex, the level set function itself varies much more slowly than the constitutive properties. Therefore, providing that an accurate level set function exists in the smoothed region, an interpolation scheme can be used to move the level set function between grids and the constitutive properties can then be evaluated using

the interpolated value. Based on these arguments, the level set function is moved between grids using biquadratic interpolation and the density and viscosity are evaluated using these interpolated values and equation 2.31.

3.2 Convective Terms

The level set form of the governing equations (equation 2.70) uses a conservative treatment of the convection term. The convection term is defined as:

$$\nabla \cdot (\vec{u}\vec{u}) \tag{3.1}$$

Discretization of this term takes advantage of the MAC-type grid as done by Harlow and Welch [39]. The differentiation is done via a compact stencil of the width of one cell which is the same as the classic finite volume discretization using a Cartesian grid. Simple averaging is done to compute the values of the flux components on the cell faces. Because the interface is smoothed, averaging is not an issue providing the resolution of the velocity gradients in the smoothed region is adequate.

Using the notation from figure 3-3 where the grid notation is made such that $i' = i - 1/2$ and $k' = k - 1/2$, the treatment of the convective term for the $x-$direction equation is:

$$\begin{aligned}
\frac{\partial(uu)}{\partial x}|_{i',k} &= \frac{1}{4(x_i - x_{i-1})} \quad \{(u_{i'+1,k} + u_{i',k})^2 - (u_{i',k} + u_{i'-1,k})^2\} \\
\frac{\partial(uw)}{\partial z}|_{i',k} &= \frac{1}{4(z_{k'+1} - z_{k'})} \quad \Big\{ (u_{i',k+1} + u_{i',k})(w_{i,k'+1} + w_{i-1,k'+1}) \\
&\qquad -(u_{i',k} + u_{i',k-1})(w_{i,k'} + w_{i-1,k'}) \Big\}
\end{aligned} \tag{3.2}$$

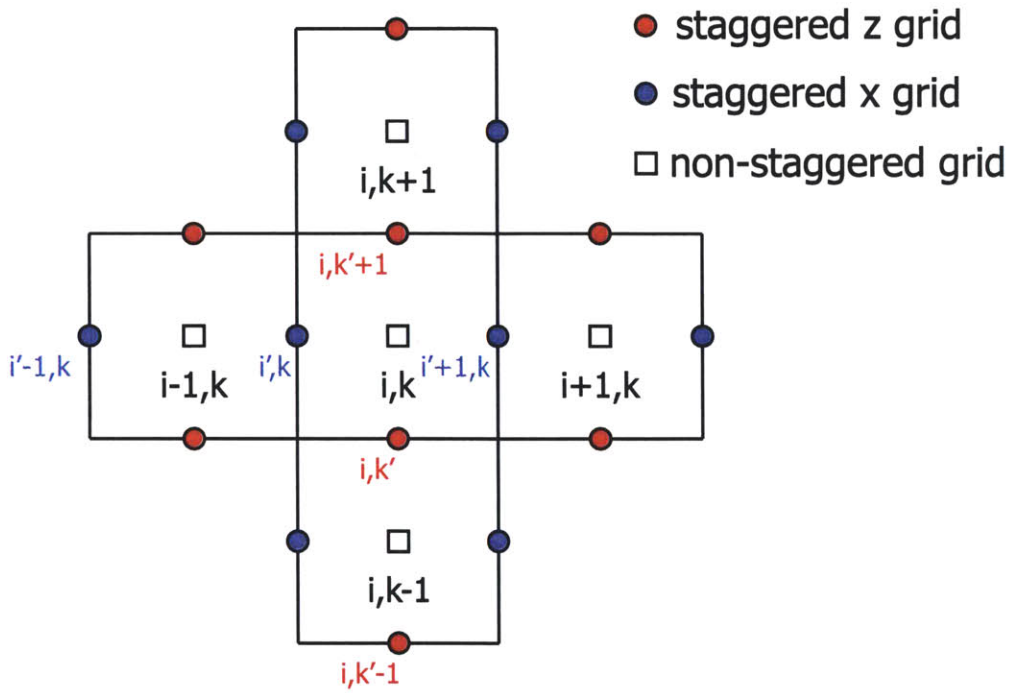

Figure 3-3: Expanded schematic of the MAC-type grid used in the discretization of the level set formulation.

For the $z-$direction, the discretized form of the conservative convective term is:

$$\begin{aligned}
\frac{\partial(uw)}{\partial x}|_{i,k'} &= \frac{1}{4(x_{i'+1}-x_{i'})} \quad \Big\{ (u_{i'+1,k}+u_{i'+1,k-1})(w_{i+1,k'}+w_{i,k'}) \\
&\qquad\qquad -(u_{i',k}+u_{i',k-1})(w_{i,k'}+w_{i-1,k'}) \Big\} \\
\frac{\partial(ww)}{\partial z}|_{i,k'} &= \frac{1}{4(z_k-z_{k-1})} \quad \{(w_{i,k'+1}+w_{i,k'})^2-(w_{i,k'}+w_{i,k'-1})^2\}
\end{aligned} \tag{3.3}$$

It should be noted here that while the grid spacing in the denominator has not been assumed to be constant, that using a simple average to compute the values between grid points is only viable if the grid spacing does not change drastically from point to point. If such a case is considered, a more advanced treatment is necessary.

The convective term in the level set governing equation also requires the movement of terms as the velocity field and level set function are not represented on the same grids. A compact stencil is used to calculate $\nabla\cdot(\vec{\mathbf{u}}\phi)$, thus the level set function must

be moved to the staggered grid. This is done with averaging:

$$\frac{\partial(u\phi)}{\partial x} = \frac{1}{2}\left(\frac{u_{i'+1,k}(\phi(i+1,k)+\phi(i,k)) - u_{i',k}(\phi(i,k)+\phi(i-1,k))}{x_{i'+1}-x_{i'}}\right) \tag{3.4}$$

$$\frac{\partial(w\phi)}{\partial z} = \frac{1}{2}\left(\frac{w_{i,k'+1}(\phi(i,k+1)+\phi(i,k)) - w_{i,k'}(\phi(i,k)+\phi(i,k-1))}{z_{k'+1}-z_{k'}}\right) \tag{3.5}$$

3.3 Shear Forces

Because of the variable viscosity, the shear forces in the level set formulation are based on the Euler form of the momentum conservation equations. Generally in most Navier-Stokes solvers for incompressible flows, a term that is of the form $\nu\nabla^2\vec{\mathbf{u}}$ appears on the right hand side of the momentum equation. Instead, as seen in equation 2.70, the term is of the form:

$$\frac{1}{\rho(\phi)\mathcal{R}e_d}\nabla\cdot\underbrace{(2\mu(\phi)\overline{\mathbf{D}})}_{\tau} \tag{3.6}$$

The shear stress is computed assuming a Newtonian fluid of non-constant viscosity. In two-dimensions this yields four components to the stress tensor of which two are symmetric.

$$\tau_{i,k} = \mu(\phi)\begin{bmatrix} 2\frac{\partial u}{\partial x} & \frac{\partial u}{\partial z}+\frac{\partial w}{\partial x} \\ \frac{\partial u}{\partial z}+\frac{\partial w}{\partial x} & 2\frac{\partial w}{\partial z}\end{bmatrix} \tag{3.7}$$

In most current level set implementations, the discretization of each of the components of the stress tensor in equation 3.7 is done with a compact stencil over one cell and uses averages where necessary to get the velocity (and viscosity) values at cell faces. In addition to the errors associated with averaging the viscosity (see section 3.1), this introduces additional numerical dissipation even in the region where the viscosity is a constant. In this implementation, the stencils for the stress terms and their derivatives are formed such that in regions where the viscosity is constant, the resulting discretization recovers a second-order central difference scheme for the term $\nu\nabla^2\vec{\mathbf{u}}$. This tactic is important in reducing numerical dissipation.

For example, the desired stencil for $\frac{\partial\tau_{11}}{\partial x}|_{i',k}$ when the viscosity is constant is $(u_{i'+1,k} - 2u_{i',k} + u_{i'-1,k})/(\Delta x^2)$. To obtain this, the differentiation of τ_{11} needs to

be calculated on the non-staggered grid, namely $(\tau_{11}|_{i,k} - \tau_{11}|_{i-1,k})/(\Delta x)$. Recalling the definition of τ_{11} from equation 3.7 yields a compact stencil for the calculation of the stress and its x-derivative which are in equation 3.8. It can be easily worked out that, when the viscosity and grid spacing are constant, the desired central-difference stencil is recovered.

$$\begin{aligned} \tau_{11}|_{i,k} &= 2\mu(\phi)_{i,k}\left(\frac{u_{i'+1,k} - u_{i',k}}{x_{i'+1} - x_{i'}}\right) \\ \frac{\partial \tau_{11}}{\partial x}|_{i',k} &= \left[\frac{\tau_{11}|_{i,k} - \tau_{11}|_{i-1,k}}{x_i - x_{i-1}}\right] \end{aligned} \tag{3.8}$$

A similar analysis of the other normal stress τ_{33} and its vertical derivative yields that it too should be calculated on the non-staggered grid using a compact stencil.

$$\begin{aligned} \tau_{33}|_{i,k} &= 2\mu(\phi)_{i,k}\left(\frac{w_{i,k'+1} - w_{i,k'}}{z_{k'+1} - z_{k'}}\right) \\ \frac{\partial \tau_{33}}{\partial z}|_{i,k'} &= \left[\frac{\tau_{33}|_{i,k} - \tau_{33}|_{i,k-1}}{z_k - z_{k-1}}\right] \end{aligned} \tag{3.9}$$

The shear stresses τ_{13} and τ_{31} are differentiated horizontally and vertically, and contribute to both x-staggered and z-staggered grids. For the desired stencils to be recovered, the shear stresses are calculated on a grid which is staggered in both x and z.

$$\begin{aligned} \tau_{13}|_{i',k'} &= 2\mu(\phi)_{i',k'}\left(\frac{u_{i',k} - u_{i',k-1}}{z_k - z_{k'-1}} + \frac{w_{i,k'} - w_{i-1,k'}}{x_i - x_{i-1}}\right) \\ \frac{\partial \tau_{13}}{\partial z}|_{i',k} &= \left[\frac{\tau_{13}|_{i',k'+1} - \tau_{13}|_{i',k'}}{z_{k'+1} - z_{k'}}\right] \\ \frac{\partial \tau_{31}}{\partial x}|_{i,k'} &= \left[\frac{\tau_{13}|_{i'+1,k'} - \tau_{13}|_{i',k'}}{x_{i'+1} - x_{i'}}\right] \end{aligned} \tag{3.10}$$

The only interpolation between grids which is now done is of the viscosity which is treated as in section 3.1. Therefore, because all velocities are calculated at points where they are directly represented, the numerical dissipation of this discretization is decreased compared to the typical level set implementations.

3.4 Surface Tension

As discussed in section 2.2.2, the surface tension is applied via the continuous surface force method within the volume. The volumetric body force which represents the surface tension force is repeated here for reference:

$$\frac{1}{\rho(\phi)\mathcal{W}e}\kappa\delta(\phi)\nabla\phi \tag{3.11}$$

All of the derivatives for this term are computed using the standard second order central difference scheme. The delta function is given in equation 2.22. The surface tension force is evaluated on the cell centers and translated to the staggered grids by averaging when necessary.

An example of the computed surface tension force is shown in figure 3-4. The surface tension force was calculated for a circle of radius 0.25 on a 1x1 grid. The ratio of the level set boundary layer to the water boundary layer (γ_w) is 2. For this example, the Reynolds number in the water is 2000 and the Weber number is 738. The force density is equally weighted throughout the transition region.

3.5 Treatment of Hydrostatic Body Force

Particular consideration must be given to the treatment of the "hydrostatic pressure" term in equation 2.69 such that its differentiation in equation 2.70 yields a conservative body force. The definition is repeated here for convenience.

$$P_h = -\int^z \frac{\rho(\phi(\vec{\mathbf{x}}))}{\mathcal{F}r^2}dz' \tag{3.12}$$

Theoretically, the gradient of P_h produces a term that cancels out the body force term ($\frac{\vec{\mathbf{k}}}{\mathcal{F}r^2}$) and leaves the horizontal gradients as a modified body force term in the Navier-Stokes equations.

$$\nabla_{(x,y)}P_h \cdot (\vec{\mathbf{i}},\vec{\mathbf{j}}) \tag{3.13}$$

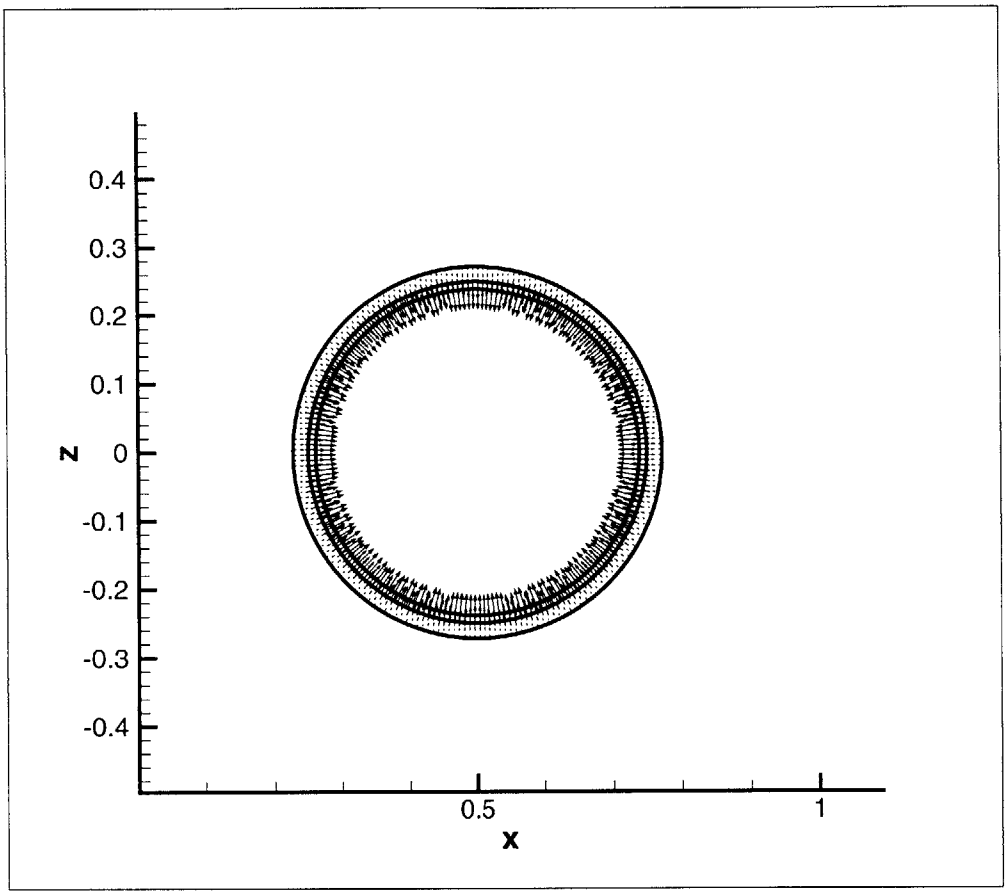

Figure 3-4: Surface tension force vector for a circle of radius 0.25 on a 1x1 grid. Black lines represent boundary of level set boundary layer.

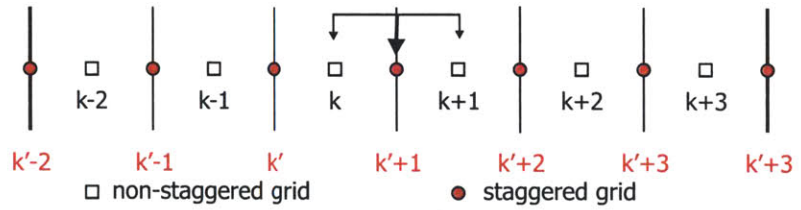

Figure 3-5: Schematic of the integration scheme derived to generate a conservative body force.

Due to numerical error, this may not be the case and it will produce a nonconservative body force. This generally occurs in the smoothed interface region where the density changes rapidly. Despite the fact that a vertical derivative is not actually taken in the implementation, P_h should be constructed such that it is a conservative body force or its effects will be seen with very large gradients at the interface, seemingly giving the fluid very large accelerations.

Derivation of the integration scheme is done in reverse, from the desired numerical differentiation. If a compact central difference stencil about the vertical staggered grid point where the vertical gradient term should contribute is used, a trapezoidal integration scheme can be worked out.

For example, consider the schematic of the grid shown in figure 3-5. Using compact central differences and assuming a nonconstant grid spacing, the gradient of the integral I at point $k'+1$ is:

$$\frac{\partial I_{k'+1}}{\partial z} = \frac{I_{k+1} - I_k}{z_{k+1} - z_k} \tag{3.14}$$

If I is the integral of a function f, then by definition $\frac{\partial I_{k'+1}}{\partial z} = f_{k'+1}$. Equation 3.14 can be rewritten to reflect the contribution to the total integral I at point $k'+1$:

$$\Delta I_{k'+1} = \int_{z_k}^{z_k+1} f(z)dz = f_{k'+1}\left(z_{k+1} - z_k\right) \tag{3.15}$$

Integration is done from the top of the domain to the bottom. Additionally, to allow for jumps in the integrand, since it is in this case a function of the density, the interpolation process discussed in section 3.1 is used to calculate the value of f on the cell faces.

3.6 Solution of the Projection Operator

Both [12] and [111] remove the complication of solving for a variable coefficient Poisson solver by solving the governing equations in the stream function formulation. By taking the curl of the Navier-Stokes equation, the pressure contribution disappears ($\nabla \times \nabla P_d \equiv 0$). This limits their work to either two-dimensional or axisymmetric flows. As discussed in Chapter 2, to allow for simple extension to a three-dimensional flow solver, the governing equations are solved in the primitive variable formulation. In the primitive variable formulation for incompressible flow, the pressure can be obtained via the projection method. This is repeated from section 2.5 equation 2.73 for convenience.

$$\nabla \cdot \frac{1}{\rho(\phi)} \nabla P_d = \frac{\nabla \cdot \vec{\mathbf{u}}^n}{\Delta t} + \nabla \cdot \vec{\mathbf{F}} \tag{3.16}$$

To ensure that the pressure which results from the solution of the Poisson equation yields a divergence free velocity field, all of the divergence operators in equation 3.16 must be done consistently. Thus, the divergence operator used in equation 3.16 uses a compact central difference stencil based at the cell center. On a grid with non-constant grid spacing, this operator is:

$$(\nabla \cdot \vec{q})_{i,k} = \left(\frac{\partial q_x}{\partial x}\right)_{i,k} + \left(\frac{\partial q_z}{\partial z}\right)_{i,k}$$

where

$$\begin{aligned} \left(\frac{\partial q_x}{\partial x}\right)_{i,k} &= \frac{q_{xi'+1,k} - q_{xi',k}}{x_{i'+1} - x_{i'}} \\ \left(\frac{\partial q_z}{\partial z}\right)_{i,k} &= \frac{q_{zi,k'+1} - q_{zi,k'}}{z_{k'+1} - z_{k'}} \end{aligned} \tag{3.17}$$

Once the dynamic pressure has been solved for using the implementation discussed below, its gradient must be added to the momentum equations before the time integration. The dynamic pressure resides on the cell centers and the momentum equations reside on the respective staggered grids. Thus, another compact central difference

stencil is necessary for this calculation which is similar to equation 3.17.

$$\left(\frac{1}{\rho(\phi)}\frac{\partial q}{\partial x}\right)_{i',k} = \left(\frac{1}{\rho(\phi)}\right)_{i',k}\left(\frac{q_{i,k}-q_{i-1,k}}{x_i - x_{i-1}}\right)$$
$$\left(\frac{1}{\rho(\phi)}\frac{\partial q}{\partial z}\right)_{i,k'} = \left(\frac{1}{\rho(\phi)}\right)_{i,k'}\left(\frac{q_{i,k}-q_{i,k-1}}{z_k - z_{k-1}}\right) \tag{3.18}$$

The movement of the density to the staggered grids which is required in equation 3.18 is done as discussed in section 3.1.

Returning to the solution of the projection operator, even with a smoothed interface, this Poisson equation has strongly variable coefficients. The discretization of this equation is addressed in section 3.6.1. Additionally, as was discussed in section 2.5.3, with the Neumann and periodic boundary conditions utilized in much of this work, the Poisson equation will be subject to a solvability condition. The discretized version of which is addressed in section 3.6.2.

3.6.1 Discretization of Dynamic Pressure Equation

Due to the large variation of the coefficients in this Poisson equation, straight forward central difference discretization of the Poisson equation can lead to spurious answers. Additionally, adaptive stencils within an iterative matrix can have an ill-effect on the damping of discontinuities by actually reinforcing them [36]. The discretization used here is a compact central difference stencil. The compact stencil is chosen to complement the staggered grid discretization and ensure that the divergence of the flow field is zero.

For simplicity of notation, P_d will be called ψ in this derivation and $\rho(\phi)$ will be replaced by ρ. Additionally, the grid notation is made such that $i' = i - 1/2$ and $k' = k - 1/2$. An expanded form of equation 3.16 at every point (i,k) is:

$$\underbrace{\frac{\partial}{\partial x}\frac{1}{\rho_{i,k}}\frac{\partial}{\partial x}\psi_{i,k}}_{X} + \underbrace{\frac{\partial}{\partial z}\frac{1}{\rho_{i,k}}\frac{\partial}{\partial z}\psi_{i,k}}_{Z} = \sigma_{i,k} \tag{3.19}$$

Discretization of the X term in equation 3.19 using the compact central difference

stencil outlined in equation 3.17 is:

$$\frac{1}{x_{i+1/2}-x_{i-1/2}}\left\{\frac{1}{\rho_{i+1/2,k}}\left(\frac{\psi_{i+1,k}-\psi_{i,k}}{x_{i+1}-x_i}\right)-\frac{1}{\rho_{i-1/2,k}}\left(\frac{\psi_{i,k}-\psi_{i-1,k}}{x_i-x_{i-1}}\right)\right\} \tag{3.20}$$

Discretization of the Z term in equation 3.19 yields a similar form.

$$\frac{1}{z_{k+1/2}-z_{k-1/2}}\left\{\frac{1}{\rho_{i,k+1/2}}\left(\frac{\psi_{i,k+1}-\psi_{i,k}}{z_{k+1}-z_k}\right)-\frac{1}{\rho_{i,k-1/2}}\left(\frac{\psi_{i,k}-\psi_{i,k-1}}{z_k-z_{k-1}}\right)\right\} \tag{3.21}$$

Collecting the common ψ terms, equations 3.20 and 3.21 yield, the discretized form of the Poisson equation.

$$\mathrm{C0}_{i,k}\psi_{i,k}+\mathrm{C1}_{i,k}\psi_{i+1,k}+\mathrm{C2}_{i,k}\psi_{i-1,k}+\mathrm{C3}_{i,k}\psi_{i,k+1}+\mathrm{C4}_{i,k}\psi_{i,k-1}=\sigma_{i,k} \tag{3.22}$$

where

$$\begin{aligned}
\mathrm{C1}_{i,k} &= \frac{1}{(x_{i+1/2}-x_{i-1/2})(x_{i+1}-x_i)}\frac{1}{\rho_{i+1/2,k}} \\
\mathrm{C2}_{i,k} &= \frac{1}{(x_{i+1/2}-x_{i-1/2})(x_i-x_{i-1})}\frac{1}{\rho_{i-1/2,k}} \\
\mathrm{C3}_{i,k} &= \frac{1}{(z_{k+1/2}-z_{k-1/2})(z_{k+1}-z_k)}\frac{1}{\rho_{i,k+1/2}} \\
\mathrm{C4}_{i,k} &= \frac{1}{(z_{k+1/2}-z_{k-1/2})(z_k-z_{k-1})}\frac{1}{\rho_{i,k-1/2}} \\
\mathrm{C0}_{i,k} &= -(\mathrm{C1}_{i,k}+\mathrm{C2}_{i,k}+\mathrm{C3}_{i,k}+\mathrm{C4}_{i,k})
\end{aligned} \tag{3.23}$$

The solution of this equation is done iteratively until the L_∞ norm is satisfied, namely:

$$\max_{x,z}|P_{i,k}^{n+1}-P_{i,k}^{n}|\leq \text{tolerance} \tag{3.24}$$

In general, the tolerance is set to be 10^{-8}. To modestly increase the convergence efficiency of the scheme, a line successive over-relaxation (LSOR) scheme is used in the z-direction where it is assumed that largest density gradients exist. This involves the solution of a tridiagonal matrix at each horizontal point. Parallel implementation of this Poisson solver is done through red-black implementation "zebra" stripes [129]

to reduce communication. Finally, Chebyshev acceleration [89] is used to further increase the convergence efficiency of the scheme.

3.6.2 Solvability of Dynamic Pressure Equation

There are two phases to the solvability of the dynamic pressure condition: compatibility and existence of a solution. The first part of solvability, namely the compatibility of the system of equations can be addressed using an additional equation such as the divergence theorem. When it is ensured that the system of equations is compatible, the existence of a solution must be guaranteed which is generally done by defining the solution at a point or subtracting its average.

In ensuring compatibility, because the interface has been smoothed, the divergence theorem (equation 2.74) in its typical form can be used because $\frac{1}{\rho(\phi)}\nabla P_d$ is at least C^2 continuous. If the interface were sharp, then equation 2.79 would have to be applied. Experience has shown that the implementation of equation 2.74 in its exact discretized form is superior to its natural form. To do this and include any non-homogenous boundary conditions for the pressure gradients, the divergence theorem will be rewritten moving the boundary integrals to the left hand side.

$$\int_V \nabla \cdot A\nabla\psi dV - \oint_S A\nabla\psi \cdot \vec{n} dS = 0 \tag{3.25}$$

Here, the substitutions of $\psi = P_d$ and $A = 1/\rho(\phi)$ have been made as a matter of notational convenience. In discrete form this becomes:

$$\sum_{i=\text{int}} \mathcal{L}_i \psi_i dV - \sum_{i=\text{bnd}} A_i \mathcal{D}_i \psi_i dS \approx 0 \tag{3.26}$$

which can be written in a general form

$$\sum_i \mathcal{G}_i \psi_i \mathcal{B}_i \approx 0 \tag{3.27}$$

where $\mathcal{G}_i$ is the linear operator $\mathcal{L}_i$ or the differential operator $\mathcal{D}_i$ and $\mathcal{B}_i$ is the dif-

ferential volume dV or area dS depending on whether the point is in the interior or on the boundary, respectively. Note here that if equation 3.27 is actually zero verses approximately zero that the system of equations has no solution. Thus, the compatibility condition takes a system which may have a solution which is essentially a function of the error and renders it unsolvable.

The next step is to apply the compatibility condition to the discretized Poisson equation. Consider the matrix equation:

$$\begin{bmatrix} \mathcal{G}_1 \\ \vdots \\ \mathcal{G}_N \end{bmatrix} \begin{bmatrix} \psi_1 \\ \vdots \\ \psi_N \end{bmatrix} = \begin{bmatrix} \sigma_1 \\ \vdots \\ \sigma_N \end{bmatrix} \tag{3.28}$$

Multiplying each side of the equation by $\mathcal{B}_i$ and summing for all points N, yields

$$\underbrace{\sum_i \mathcal{B}_i \mathcal{G}_i \psi_i}_{\iota} = \underbrace{\sum_i \mathcal{B}_i \sigma_i}_{\sigma_o} \tag{3.29}$$

Equation 3.29 provides the means to enforce the compatibility condition in a global sense. Subtracting this equation from the matrix of equations being solved will ensure that it is satisfied globally. Namely,

$$\begin{bmatrix} \mathcal{G}_1 \\ \vdots \\ \mathcal{G}_N \end{bmatrix} \begin{bmatrix} \psi_1 \\ \vdots \\ \psi_N \end{bmatrix} = \begin{bmatrix} \sigma_1 \\ \vdots \\ \sigma_N \end{bmatrix} - \Sigma_o \tag{3.30}$$

where

$$\Sigma_o = \frac{\iota - \sigma_o}{N} \tag{3.31}$$

While the problem is now compatible, i.e. the system of equations now has a solution, the matrix is still singular and the solution is non-unique [11, 102]. To remove the singularity, a common practice is to "nail the solution down" to a known value [78]. This is a common (and generally undocumented) practice. It is important to

point out that if the matrix is made solvable without ensuring that the equations are actually singular, all of the error Σ_o will collect where the solution has been defined. In the context of the solution of the pressure Poisson equation, this results in an accumulation of divergence at this point violating the mass conservation equation.

It is not necessary to change the matrix such that the solution is defined at a point when using an iterative solver. There are two ways of enforcing it iteratively. The first is to allow the point to float. Forsythe and Wasow prove that an iterative solver will converge to a solution and if so desired, a constant can be subtracted from it [33]. The second is similar to Forsythe and Wasow in that the constant is subtracted from the solution at every point, yet it is done at every iteration. The second tactic is what is applied in this work.

A One-Dimensional Example

To simplify this example, we will look at the problem in a single dimension. Because this is a linear problem, adding multiple dimensions is simple linear superposition. The one dimensional form of the Poisson equation with variable coefficients is:

$$\frac{\partial}{\partial x} A(x) \frac{\partial \psi}{\partial x} = \sigma \tag{3.32}$$

The discretized form of which is:

$$\frac{\partial}{\partial x} A \frac{\partial \psi}{\partial x} = \mathrm{C2}_i \psi_{i-1} + \mathrm{C0}_i \psi_i + \mathrm{C1}_i \psi_{i+1} = \sigma_i \tag{3.33}$$

The coefficients C0, C1, C2 are the one-dimensional forms of the coefficients in equation 3.23. They are actually irrelevant to this discussion because this method can be applied to any system with varying coefficients requiring a compatibility condition. A limited example using five points is shown below. The discretized matrix form of

the governing equation is the following (using periodic boundary conditions):

$$\begin{bmatrix} \mathrm{C0}_1 & \mathrm{C1}_1 & & & \mathrm{C2}_1 \\ \mathrm{C2}_2 & \mathrm{C0}_2 & \mathrm{C1}_2 & & \\ & \mathrm{C2}_3 & \mathrm{C0}_3 & \mathrm{C1}_3 & \\ & & \mathrm{C2}_4 & \mathrm{C0}_4 & \mathrm{C1}_4 \\ \mathrm{C1}_5 & & & \mathrm{C2}_5 & \mathrm{C0}_5 \end{bmatrix} \begin{bmatrix} \psi_1 \\ \psi_2 \\ \psi_3 \\ \psi_4 \\ \psi_5 \end{bmatrix} = \begin{bmatrix} \sigma_1 \\ \sigma_2 \\ \sigma_3 \\ \sigma_4 \\ \sigma_5 \end{bmatrix} \tag{3.34}$$

Summation of all five equations (multiplied by dV) leads to a single equation equivalent to equation 3.29.

$$\begin{aligned} \mathrm{LHS} &= \left(\begin{array}{c} \psi_1(\mathrm{C0}_1 + \mathrm{C2}_2 + \mathrm{C1}_5) + \psi_2(\mathrm{C1}_1 + \mathrm{C0}_2 + \mathrm{C2}_3) \\ +\psi_3(\mathrm{C1}_2 + \mathrm{C0}_3 + \mathrm{C2}_4) + \psi_4(\mathrm{C1}_3 + \mathrm{C0}_4 + \mathrm{C2}_5) \\ +\psi_5(\mathrm{C1}_4 + \mathrm{C0}_5 + \mathrm{C2}_1) \end{array} \right) dV \\ \mathrm{RHS} &= (\sigma_1 + \sigma_2 + \sigma_3 + \sigma_4 + \sigma_5)\, dV \end{aligned} \tag{3.35}$$

The $\mathcal{G}_i$ correction for the ι-sum is:

$$\mathcal{G}_i = (\mathrm{C0}_i + \mathrm{C2}_{i+1} + \mathrm{C1}_{i-1}) \tag{3.36}$$

and the overall correction for each point is calculated from:

$$\begin{aligned} \iota &= \sum_i \mathcal{G}_i \psi_i dV \\ \sigma_o &= \sum_i \sigma_i dV \end{aligned} \tag{3.37}$$

At each point, the equation which gets solved is now:

$$\mathrm{C2}_i \psi_{i-1} + \mathrm{C0}_i \psi_i + \mathrm{C1}_i \psi_{i+1} = \sigma_i - \Sigma_o \tag{3.38}$$

Testing of the solvability condition was performed at numerous resolutions for both periodic and Neumann boundary conditions. Discussed here is a sample (two resolutions using periodic boundary conditions) to illustrate its performance. The periodic

test function used in this example is:

$$\psi(x) = \begin{cases} \sin(2kx) & x < 0 \\ \sin(2k'x) & x > 0 \end{cases} \tag{3.39}$$

The test function 3.39 is applied on a domain that is of the size $\pi/k \leq (x, z) \leq \pi/k'$. The solvability is applied at the point $x = 0$. The variable coefficient is the inverse of the density $A = 1/\rho$ as it is in the pressure solver for the level set formulation. The only specific requirement for these test cases is $k' = k\lambda$ where λ is the ratio of the density in the two regions. These test functions actually use a case where the interface is sharp. However, the functions were designed such that there is no jump at the interface and thus the solvability condition as it was designed in this work is applicable.

Figure 3-6 shows the performance of the solvability for 32 grid points. It is clear that, without the compatibility condition, the solution deforms significantly to meet the Dirichlet condition at the center and keep its periodicity. However, its error compared to the case where solvability is used is large. Figure 3-7 shows the performance of the two solvability conditions for 512 grid points. Again, the effect of the solvability condition in the periodic direction is clear and the higher resolution reduces the error as expected.

3.7 ENO Derivatives

When the derivatives of the level set function are needed for an advection equation, such as during reinitialization, an essentially non oscillatory (ENO) scheme is used. The first ENO schemes were developed by Harten [40, 41] and relied on cell-averages and point values. A reconstruction procedure was necessary to extract the point values from the cell averages. In a multi-dimensional problem this generally becomes complicated [42]. More recent ENO schemes developed by Shu and Osher [100, 101] work with cell fluxes and not averages and remove any reconstruction phase, making

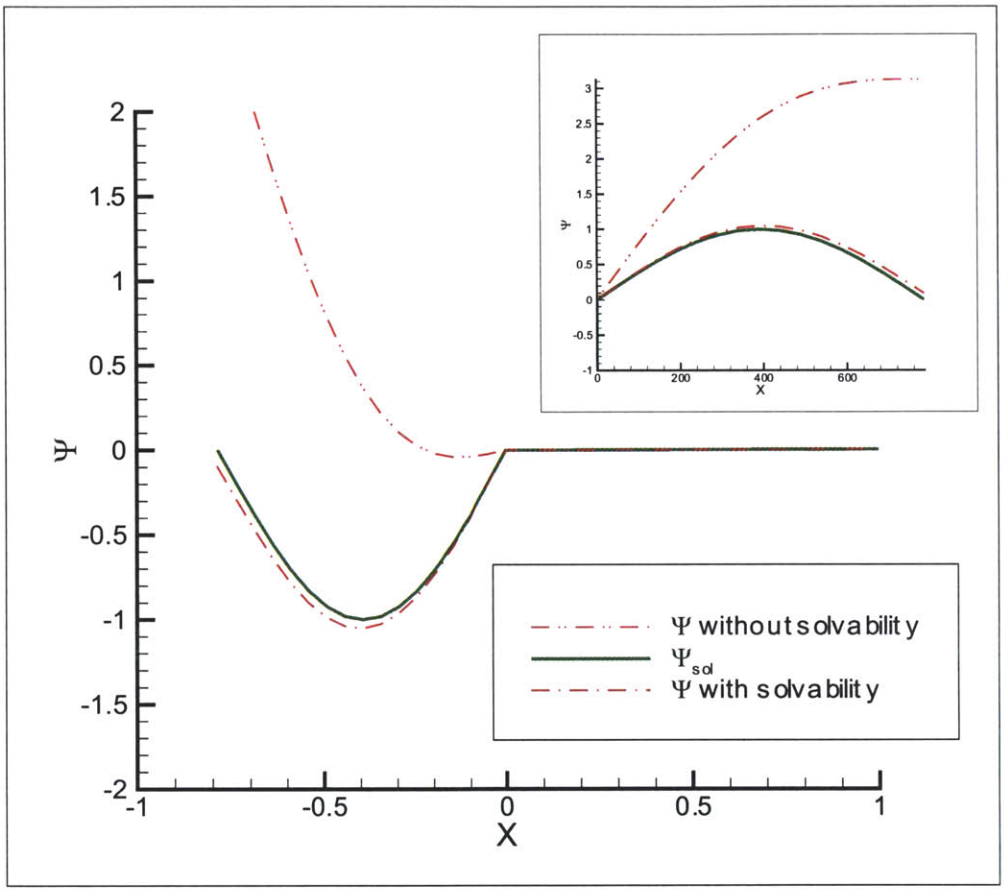

Figure 3-6: Test of x-direction solvability using periodic boundary conditions and 32 points. Inset is expanded view of entire domain.

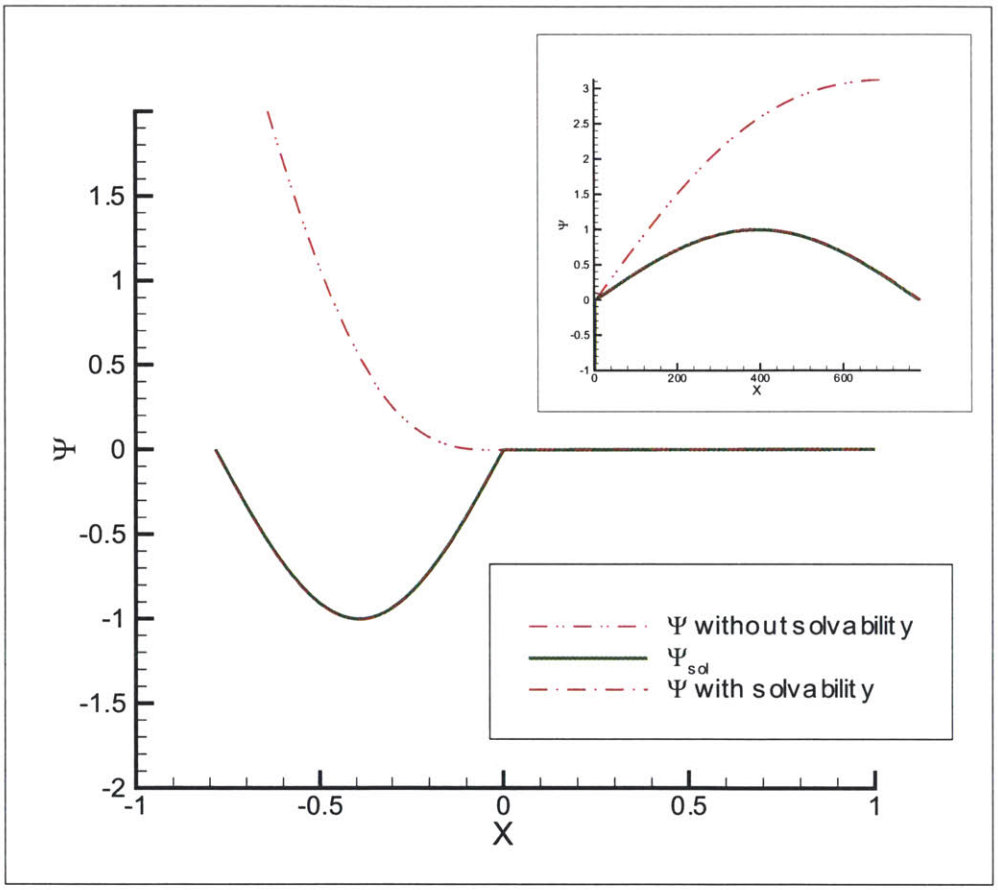

Figure 3-7: Test of x-direction solvability using periodic boundary conditions and 512 points. Inset is expanded view of entire domain.

them more efficient. These ENO schemes (up to second order) can be proven to be total variation (TV) stable.

The ENO scheme used in this work is based on Shu and Osher's Roe scheme [100, 101]. It is given this name because the first point of the stencil is chosen based on the local sign of the slope of the flux at the forward face of the cell. This is the Roe speed. This method gives uniformly high-order fluxes, even at discontinuities. However, it does admit an entropy violating expansion fan. Shu and Osher also introduce a straight forward "entropy fix" for this problem which is used only in the region of an expansion fan. The process of constructing this ENO scheme of any order for a general advection problem is explained in detail in Shu and Osher [101].

Sussman and Fatemi [110] describe the algorithm and the application of the entropy fix to the level set problem. The ENO scheme used in this work was derived from Sussman and Fatemi work within the context of nonuniform grid spacing. It is described in this section up to second order. For each direction, the derivative is taken as if it were a one-dimensional problem.

The first step is to compute a divided difference table. This is defined as follows:

$$\phi[x_i, x_i] = \phi_i \tag{3.40}$$

$$\phi[x_{i-k}, x_{i+\ell}] = (\phi[x_{i-k+1}, x_{i+\ell}] - \phi[x_{i-k}, x_{i+\ell-1}])/(x_{i+\ell} - x_{i-k}) \tag{3.41}$$

Shu and Osher determined that to provide high accuracy at discontinuities, that the building block for this method should not be the flux at a given point but rather a variable in which its derivative is the flux at that point. They call this variable Q. The zeroth order Q is defined to be the value of the level set function at the point i.

$$Q^0(x) = \phi[x_i, x_i] = \phi_i \tag{3.42}$$

To show the derivation of the second order derivative, it is necessary to show the steps for the first order derivative since the process is a building block system. For each point i and its neighboring point $i-1$, the following process is done. It is shown

in detail for the $i-1$ point. The first step is to compute the Roe speeds based on the divided difference table. The Roe speeds determine the direction of the stencil.

$$\begin{aligned} a^1 &= \phi[x_{i-2}, x_i] \\ b^1 &= \phi[x_{i-1}, x_{i+1}] \end{aligned} \tag{3.43}$$

The superscript a^1 denotes the order. Equation 3.43 becomes:

$$\begin{aligned} a^1 &= \frac{1}{x_i - x_{i-2}} \left(\frac{\phi_i - \phi_{i-1}}{x_i - x_{i-1}} - \frac{\phi_{i-1} - \phi_{i-2}}{x_{i-1} - x_{i-2}} \right) \\ b^1 &= \frac{1}{x_{i+1} - x_{i-1}} \left(\frac{\phi_{i+1} - \phi_i}{x_{i+1} - x_i} - \frac{\phi_i - \phi_{i-1}}{x_i - x_{i-1}} \right) \end{aligned} \tag{3.44}$$

The smallest Roe speed is chosen based on the following criteria:

$$c^1 = \begin{cases} a^1 & \text{if } ||a^1|| \leq ||b^1|| \\ b^1 & \text{otherwise} \end{cases} \tag{3.45}$$

The first order Q is computed.

$$\begin{aligned} Q^1(x) &= \phi[x_{i-1}, x_i](x - x_i) \\ Q^1(x) &= \frac{\phi_i - \phi_{i-1}}{x_i - x_{i-1}}(x - x_i) \end{aligned} \tag{3.46}$$

If only the first order ENO derivative was desired, this Q^1 and the Q^1 for point i would be used to compute the derivative. For the second order ENO scheme an additional step is taken. The second order Q is computed based on the following general equation:

$$Q^{\ell+1}(x) = Q^{\ell}(x) + c^{\ell} \prod_{k=i-1}^{k=i-1+\ell} (x - x_k) \tag{3.47}$$

where $\ell = r - 1$ and r is defined as the order of the method. Thus for the second

order scheme, Q^2 becomes the following:

$$Q^2(x) = Q^1(x) + c^1 \prod_{k=i-1}^{k=i} (x - x_k)$$

or

$$Q^2(x) = Q^1(x) + c^1(x^2 - x(x_i + x_{i-1}) + x_i x_{i-1})$$

and finally,

$$Q^2(x) = \frac{\phi_i - \phi_{i-1}}{x_i - x_{i-1}}(x - x_i) + c^1(x^2 - x(x_i + x_{i-1}) + x_i x_{i-1}) \tag{3.48}$$

To determine the flux at the point $i-1$, the derivative of Q^2 with respect to x is taken. We denote this flux $\frac{\partial \phi}{\partial x}^-$ because it is on the 'left' side of the cell.

$$\frac{\partial \phi}{\partial x}^- = \frac{\phi_i - \phi_{i-1}}{x_i - x_{i-1}} + c^1(x_i - x_{i-1}) \tag{3.49}$$

To compute the flux on the 'right' side of the cell, namely $\frac{\partial \phi}{\partial x}^+$, the process is repeated for the point i. This involves reevaluating equations 3.43 through 3.48, including computing a Roe speed for point i which will determine a new c^1. With the new Q^2 calculated for point i, the flux on the right side of the cell can be calculated by taking the derivative of Q^2 with respect to x.

$$\frac{\partial \phi}{\partial x}^+ = \frac{\phi_{i+1} - \phi_i}{x_{i+1} - x_i} - c^1(x_{i+1} - x_i) \tag{3.50}$$

At this point, the "entropy fix" needs to be incorporated which is done through a selection criteria based on the velocity of the characteristics $\vec{\mathbf{w}}$ calculated from each

side. This allows the entropy fix to only be in use in the region of expansion fans.

$$\frac{\partial \phi}{\partial x} \approx \begin{cases} \frac{\partial \phi}{\partial x}^{+} & \text{if } w_{xR} < 0 \text{ and } (w_{xR} + w_{xL}) < 0 \\ \frac{\partial \phi}{\partial x}^{-} & \text{if } w_{xL} > 0 \text{ and } (w_{xR} + w_{xL}) > 0 \\ 0 & \text{if } w_{xL} < 0 \text{ and } (w_{xR} + w_{xL}) > 0 \end{cases} \tag{3.51}$$

3.8 Reinitialization

The method used in this formulation is based on Sussman and Fatemi's Lagrange multipliers method [110]. Most works in the literature which discuss "mass conservation" and the level set method actually refer to conserving the volume of the fluid. This can cause some confusion as there is also the mass conservation governed by the continuity equation. The reinitialization process tries to conserve the volume of the fluid:

$$V(t) = \int_{\Omega} H(\phi; \epsilon, t) d\Omega \tag{3.52}$$

This specific numerical implementation of Sussman and Fatemi's method has been found to conserve the fluid volume in a domain within 0.7% for most applications investigated. Throughout this work, it was found that if special attention was paid to the ENO derivatives near the interface, this percentage could be dropped to 0.07%. This section will first discuss the numerical implementation in general and then address the "fix" which gave a tenfold increase in volume conservation.

Sussman and Fatemi's method integrates an initial value partial differential equation to a given time. This initial value problem is solved within a level set simulation such that the time in this problem is really a pseudo-time. This initial value problem is given in equation 2.38 and repeated here for convenience.

$$\begin{aligned} \frac{\partial \phi}{\partial t} &= L(\phi_0, \phi) \\ L(\phi_0, \phi) &= \text{sign}(\phi_0)\,(1 - |\nabla \phi|) \\ \phi_0 &= \phi(\vec{\mathbf{x}}, t = 0) \end{aligned} \tag{3.53}$$

It is essentially a two-stage scheme where at every time step, the level set function is updated based on equation 3.53 and then is corrected using Lagrange multipliers which help maintain the initial volumes of the fluid in each cell. The Lagrange multipliers are given in equation 2.40 and again repeated here for convenience.

$$\begin{aligned} \frac{\partial \phi}{\partial t} &= L(\phi_0, \phi) + \lambda H'(\phi_0)|\nabla \phi_0| \\ \lambda &= \frac{-\int_\Omega H'(\phi) L(\phi_0, \phi)}{\int_\Omega H'(\phi) f(\phi)} \end{aligned} \tag{3.54}$$

The first stage of the time step uses third-order Runge-Kutta as described in Sussman and Fatemi with second-order ENO derivatives described in section 3.7. The resulting level set function is labeled $\widetilde{\phi}_{n+1}$. The correction stage is then computed:

$$\phi_{n+1} = \widetilde{\phi}_{n+1} + \Delta t \lambda H'(\phi_0)|\nabla \phi_0| \tag{3.55}$$

The Lagrange multiplier is calculated as:

$$\lambda = \frac{-\int_\Omega H'(\phi) \left(\frac{\tilde{\phi}_{n+1} - \phi_0}{t - t_0} \right)}{\int_\Omega H'(\phi)^2 |\nabla \phi_0|} \tag{3.56}$$

The integrals in equation 3.56 are calculated using biquadratic interpolation. The initial value problem is generally solved to a time (or also distance) of 0.5. Also, it should be noted that it is not necessary to perform reinitialization at every time step of the level set simulation. The frequency that this is performed is really a balance between quality of results (in terms of volume conservation) and CPU time.

To test the accuracy and ability of this implementation of the reinitialization scheme, two tests have been devised [95]. The first involves performing reinitialization on a known distance function: concentric circles. An accurate reinitialization scheme with little dissipation or drift, should essentially return what it was given. The equation for the concentric circles distance function used in testing is:

$$\phi_0(\vec{\mathbf{x}}) = 4 - \sqrt{x^2 + z^2} \tag{3.57}$$

The test was performed on a square 5x5 grid using a variety of grid points. The drift in volume on each grid for the concentric circles case is shown in table 3.1. For each case, the level set smoothing distance is fixed to be $2.5\Delta x_{128}$ where Δx_{128} is the grid size defined on a grid of 128x128. This ensures that a convergence can be inferred. A Romberg integration scheme is used to calculate the volume for these test cases. As can be seen in table 3.1, even on what could be considered fairly course grids (N=64), the relative change in volume using this scheme is very small.

Table 3.1: Performance of reinitialization scheme for a test involving concentric circles.

N	$\Delta\forall$	Relative Change
64	9.9810^{-3}	0.0213%
128	3.2110^{-3}	0.0066%
256	8.8010^{-4}	0.0018%
512	2.3210^{-4}	0.0005%

The second test is to challenge the ability of the reinitialization scheme and involves using a test function which is signed but a poor representation of a distance function. The solution of this particular function is a set of concentric ellipses. The elliptic test function is given as [95]:

$$\begin{aligned} \phi_0(\vec{\mathbf{x}}) =& f(\vec{\mathbf{x}}) \left(\sqrt{\left(\frac{x^2}{A^2} + \frac{z^2}{B^2} \right)} - 1 \right) \\ f(\vec{\mathbf{x}}) =& \alpha + (x - x_0)^2 + (z - z_0)^2 \end{aligned} \tag{3.58}$$

On the same 5x5 grid as the circles test, the parameters are given by $A = 4$, $B = 2$, $\alpha = 0.1$, $x_0 = 3.5$ and $z_0 = 2$. Figure 3-8 shows the initial distribution of the distance function, the zero level set which represents the ellipse and the reinitialized distance function. The volume conservation for this ellipse using 128^2 points on the 5x5 grid is 0.33%.

As stated in the introduction to this section, the volume conservation for this

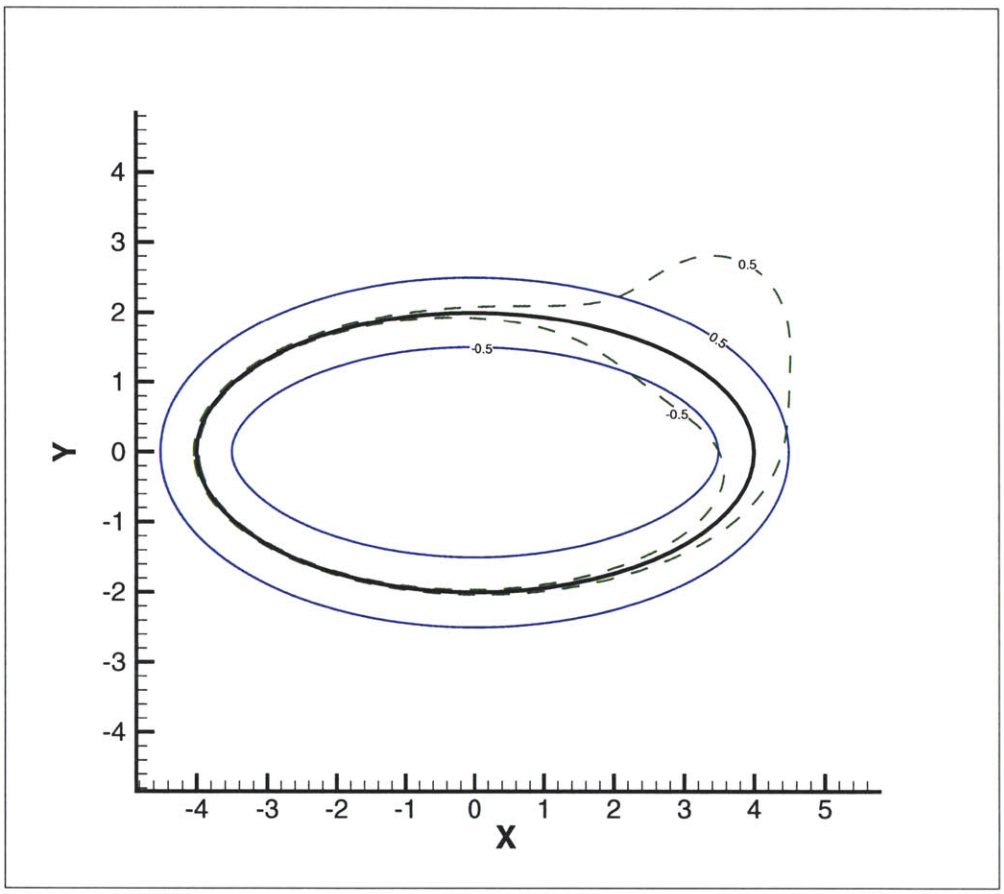

Figure 3-8: Reinitialization of a signed distance function. The interface is the heavy line. Contours of $\phi = \pm 0.5$ are shown for the initial distribution (dashed) and the final distribution (solid).

implementation is considerably good compared to other reinitialization or lower-order schemes. However, the drawback to having any volume loss is that the volume loss occurs at the interface. For air-water flows, a loss in volume is a "change" of water to air. This loss to the water can be detrimental to energy conservation in particular if the flow is very energetic. A brute force improvement would to be to increase the order of the scheme in general or look into using a more advanced implementation of the Lagrange multipliers. However, in this case, it is best to determine why volume conservation is still an issue with the use of Lagrange multipliers whose purpose is to prevent it.

A paper by Russo and Smereka [95] shows some insightful analysis which sheds light on the solution. The governing equation of the initial value problem (eqn. 3.53) can rewritten as a first order hyperbolic partial differential equation.

$$\frac{\partial \phi}{\partial t} + \underbrace{\text{sign}(\phi_0)\frac{\nabla \phi}{|\nabla \phi|}}_{\vec{\mathbf{w}}} \cdot \nabla \phi = \text{sign}(\phi_0) \tag{3.59}$$

Because the normal of the interface is $\nabla\phi/||\nabla\phi||$, the characteristics emanate from the interface in the normal direction. This fact is used in the reinitialization scheme to determine when to stop the solution of the initial value problem. A proper solution of the hyperbolic partial differential equation will propagate the initial signal along the characteristic line at the characteristic speed. When solving hyperbolic partial differential equations in a discretized sense, this requires that information from neighboring characteristics does not pollute the propagating signal (i.e. differentiation can not cross characteristic lines). Upwinded schemes, such as the ENO schemes used in this reinitialization process, use information about the characteristic velocity to ensure that only information from the characteristic line of interest influence the propagation of the solution.

The characteristic velocity along these $\vec{\mathbf{w}}$ characteristics actually changes signs as one crosses the interface. Thus, when w is calculated in a discrete sense, any differencing across the interface will be including information from the wrong char-

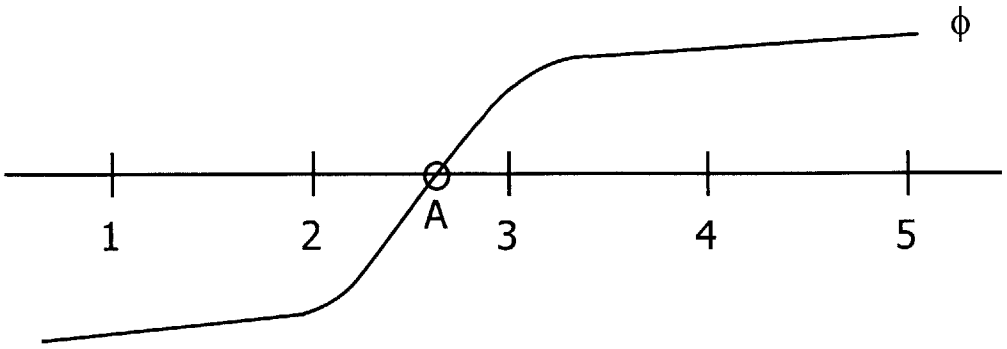

Figure 3-9: A schematic of the interface crossing a one-dimensional grid.

$i =$	1	2	3	4	5
ϕ	< 0	< 0	> 0	> 0	> 0
$\frac{\partial \phi}{\partial x}$	> 0	> 0	> 0	> 0	> 0
w	< 0	< 0	> 0	> 0	> 0

Table 3.2: General information about figure 3-9.

acteristic line and polluting the signal. The result is a tendency for the interface to drift towards the nearest grid point causing a loss in volume.

Russo and Smereka propose a "subcell fix" which is outlined extensively in their paper which includes a point in the stencil which represents the interface. This type of thinking can be applied to the ENO scheme discussed in section 3.7 with only a few modifications to the overall scheme. Consider the simple example shown in figure 3-9 with the corresponding table 3.2. The point of interest for this example is point 3. The second order ENO scheme would yield the following:

$$\begin{aligned} \frac{\partial \phi^+}{\partial x} &= \frac{\phi_4 - \phi_3}{\Delta x} - \frac{\phi_4 - 2\phi_3 + \phi_2}{\Delta x} \\ &= \frac{\phi_3 - \phi_2}{\Delta x} \\ \frac{\partial \phi^-}{\partial x} &= \frac{\phi_3 - \phi_2}{\Delta x} + \frac{\phi_3 - 2\phi_2 + \phi_1}{\Delta x} \\ &= \frac{2\phi_3 - 3\phi_2 + \phi_1}{\Delta x} \end{aligned} \tag{3.60}$$

with the characteristic velocities $w_{xL} > 0$ and $w_{xR} > 0$. It should be noted that both

derivatives cross the interface. Thus, unless equation 3.51 chooses neither (or chooses zero), the method will differentiate across the interface and the upwinded nature of the scheme will break down at this point. The characteristic velocities are a function of the gradient at that point (either from the + or − side) and the sign of the initial level set function ϕ_0. All of these quantities are positive. Based on this, equation 3.51 will pick $\frac{\partial \phi}{\partial x}^-$ for $\frac{\partial \phi}{\partial x}$.

To apply "sub-cell fix" proposed by Russo and Smereka to this ENO scheme means to add a point which represents the point on the interface to the stencil. If point A in figure 3-9 is included in the ENO scheme, equation 3.60 becomes:

$$\begin{aligned} \frac{\partial \phi}{\partial x}^+ &= \frac{\phi_4 - \phi_3}{\Delta x} - \frac{\phi_4 - 2\phi_3 + \phi_A}{\Delta x} \\ &= \frac{\phi_3 - \phi_A}{\Delta x} \\ \frac{\partial \phi}{\partial x}^- &= \frac{\phi_3 - \phi_A}{\Delta x} + \frac{\phi_4 - 2\phi_3 + \phi_A}{\Delta x} \\ &= \frac{\phi_4 - \phi_3 - 2\phi_A}{\Delta x} \end{aligned} \tag{3.61}$$

To determine the location of point A which is necessary to determine grid spacing, a third-order polynomial for $x(\phi)$ is fit and evaluated at $\phi = 0$. Again, because the sign of the characteristic velocities have not changed, equation 3.51 will still pick $\frac{\partial \phi}{\partial x}^-$ for $\frac{\partial \phi}{\partial x}$. With point A included in the stencil however, the differencing does not cross the interface as it did previously and the upwinded nature of the method is sustained.

The overall performance of the modified reinitialization scheme can be seen when comparing the overall volume conservation for actual simulations. Figure 3-10 shows the volume conservation over an entire simulation various breaking waves using the original implementation and the version which contains the sub-cell fix. The original implementation conserves volume with 0.7% as quoted earlier. There is a marked loss of volume during the breaking event which for this case occurs $4 \leq T \leq 10$ for this case. This case is actually a spilling breaking case, where the surface topology does not become very complex. The implementation which includes the sub-cell fix is shown for a spilling and plunging case. The volume conservation for the spilling

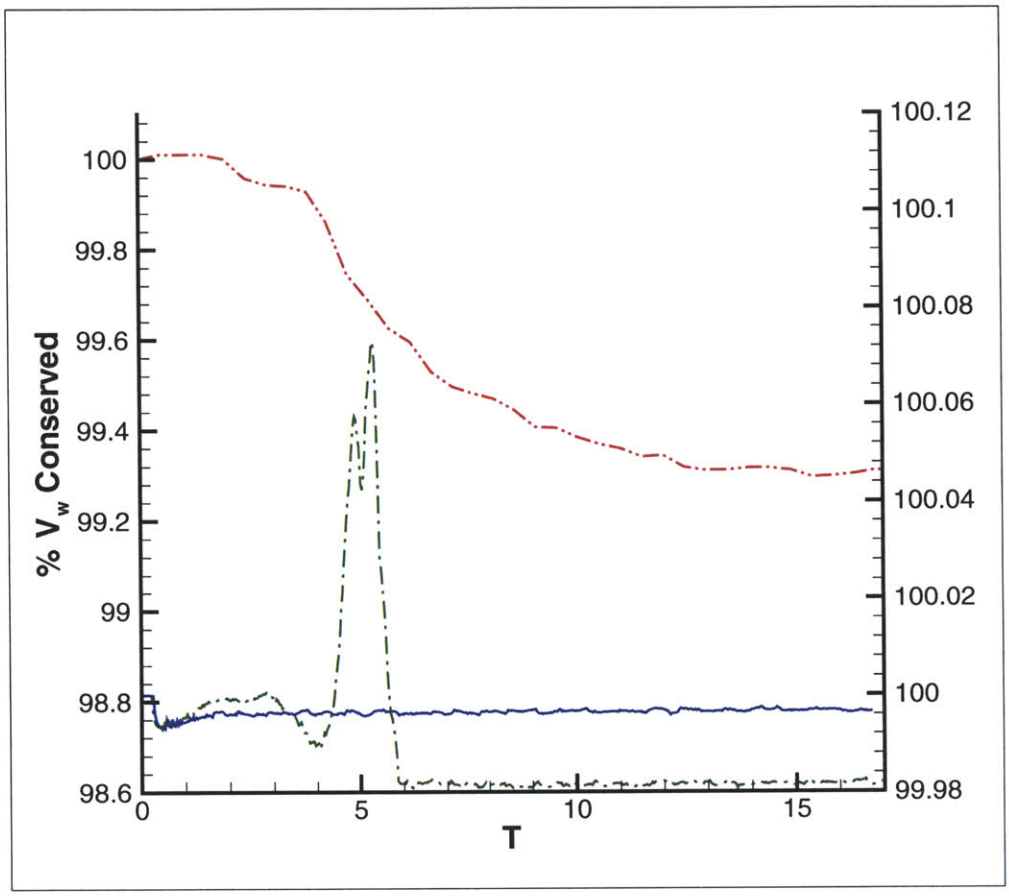

Figure 3-10: A comparison of the volume conservation for various breaking wave cases. The original implementation (-..-) is plotted against the left axis and is for a spilling breaking wave simulation. The version with the sub-cell fix is plotted against the right axis and is for a spilling (-) and plunging (-.-) case.

case is actually 0.003% but appears as a straight line on this scale. The plunging case conserves volume overall to 0.02% with a peak in actual volume increase of 0.07% during the breaking event. With this sub-cell fix included in the implementation of the reinitialization, the fluid volume is essentially conserved.

3.9 Time Integration Scheme

Time integration of the simulation is implemented via a low-storage Runge-Kutta scheme. This scheme is based on the arrangement developed by Williamson [126].

To illustrate this Runge-Kutta scheme, it will be described using the example differential equation:

$$\dot{x} = f(x) \tag{3.62}$$

For a second order scheme, the first stage is to compute the value at the second stage based on values at the current step (n):

$$\begin{aligned} q^1 &= hf(x^n) \\ x^1 &= x^n + b^1 q^1 \end{aligned} \tag{3.63}$$

where h is the discretization spacing and the superscript notation represents the stage (n,1, and 2:$n+1$). In the low-storage method, values for q^2 and x^{n+1} are a function of the current q^1 and x^1 values and overwrite those existing values in memory.

$$\begin{aligned} q^2 &= a^2 q^1 + hf(x^1) \\ x^{n+1} &= x^1 + b^2 q^2 \end{aligned} \tag{3.64}$$

The values of a^2, b^1 and b^2 are chosen to eliminate round-off error. They are $a^2 = -1$, $b^1 = 1$, and $b^2 = 1/2$.

3.9.1 Integration of Field Equations

The application of this time integration scheme to the level set formulation of the Navier-Stokes equations with the projection operator is outlined. For clarity, the stages in this presentation are represented as subscripts. The equation being discretized is the following:

$$\frac{\partial \vec{\mathbf{u}}}{\partial t} = -\frac{1}{\rho(\phi)} \nabla P_d + \vec{\mathbf{F}} \tag{3.65}$$

where

$$\vec{\mathbf{F}} = -\nabla \cdot (\vec{\mathbf{u}}\vec{\mathbf{u}}) - \frac{1}{\rho(\phi)} \nabla_{(x,y)} P_h \cdot (\vec{\mathbf{i}}, \vec{\mathbf{j}}) + \frac{1}{\rho(\phi)\mathcal{R}e_d} \nabla \cdot (2\mu(\phi)\overline{\mathbf{D}}) + \frac{1}{\mathcal{W}e} \kappa\delta(\phi)\nabla\phi \tag{3.66}$$

The first stage of the low-storage Runge-Kutta scheme is calculated as follows:

$$\vec{\mathbf{u}}_1 = \vec{\mathbf{u}}_n + b_1 \Delta t(-\frac{1}{\rho(\phi)} \nabla P_{dn} + \vec{\mathbf{F}}_n) \tag{3.67}$$

However, the pressure field at n is unknown. To find this value, we use the projection method discussed in the earlier section.

$$\nabla \cdot \vec{\mathbf{u}}_1 = \nabla \cdot \vec{\mathbf{u}}_n + b_1 \Delta t(-\nabla \cdot (\frac{1}{\rho(\phi)} \nabla P_{dn})) + \nabla \cdot \vec{\mathbf{F}}_n) \tag{3.68}$$

Forcing the dilation at stage 1 to be equal to zero, the pressure field at n can then be calculated.

$$\nabla \cdot (\frac{1}{\rho(\phi)} \nabla P_{dn}) = \frac{\nabla \cdot \vec{\mathbf{u}}_n}{b_1 \Delta t} + \nabla \cdot \vec{\mathbf{F}}_n \tag{3.69}$$

The new velocity field can now be evaluated using equation 3.67.

The low-storage method includes the contributions from the initial stage. To do so, new notation is introduced. The newly calculated velocity fields ($\vec{\mathbf{u}}_1$) are used to calculate $\vec{\mathbf{F}}'_1$.

$$\vec{\mathbf{F}}'_1 = a_2(\vec{\mathbf{F}}_n - \nabla \cdot (\frac{1}{\rho(\phi)} \nabla P_{dn})) + \vec{\mathbf{F}}_1 \tag{3.70}$$

With this notation, the second stage of the integration scheme is written.

$$\vec{\mathbf{u}}_{n+1} = \vec{\mathbf{u}}_1 + b_2 \Delta t(-\frac{1}{\rho(\phi)} \nabla P_{d1} + \vec{\mathbf{F}}'_1) \tag{3.71}$$

As in the first stage, the pressure field for the intermediate stage is unknown and is solved via the projection operator:

$$\nabla \cdot (\frac{1}{\rho(\phi)} \nabla P_{d1}) = \frac{\nabla \cdot \vec{\mathbf{u}}_1}{b_2 \Delta t} + \nabla \cdot \vec{\mathbf{F}}'_1 \tag{3.72}$$

With the pressure equation solved, equation 3.71 can now be evaluated for the velocities at the next time step.

3.9.2 Integration of the Level Set Equation

The governing equation for the level set is integrated in a similar manner. The equation being discretized is the following:

$$\frac{\partial \phi}{\partial t} = C \tag{3.73}$$

where

$$G = -\nabla \cdot (\vec{\mathbf{u}}\phi) \tag{3.74}$$

The first stage of the low-storage Runge-Kutta scheme is calculated as follows:

$$\phi_1 = \phi_n + b_1 G_n \Delta t \tag{3.75}$$

Unlike the field equations, all values are known (velocity and level set function at each stage) and no additional equations are necessary and equation 3.75 can be evaluated directly.

When the field equations have been integrated to give the velocity field for the intermediate stage (equation 3.67), the level set function at the next time step can be directly evaluated. The low-storage method includes the contributions from the previous stage. The notation used is the same as in section 3.9.1.

$$\overline{G_1} = a_2(G_n) + G_1 \tag{3.76}$$

With this notation, the second stage of the integration scheme is written.

$$\phi_{n+1} = \phi_1 + b_2 \overline{G_1} \Delta t \tag{3.77}$$

3.9.3 Dynamic Time Step Control

Because of the explicit time integration method used in the flow solver, a restriction on the time step is necessary to ensure stability. There are many factors involved in the time step restriction: capillary effects (when surface tension is considered), viscous

effects, gravitational effects, and the standard CFL number. When surface tension effects are considered, it is necessary to ensure that capillary waves are captured for stability [9]. For this to occur:

$$C_c < \frac{1}{2}\frac{\Delta x}{\Delta t_s} \tag{3.78}$$

where $\frac{\Delta x}{\Delta t_s}$ represents the wave speed of the grid based on the time step determined by surface tension effects, Δt_s and C_c is the capillary wave speed:

$$C_c = \frac{\sigma k}{\rho_q + \rho_w} \tag{3.79}$$

where k is the wavenumber. Combining equations 3.78 and 3.79 with the additional knowledge that the maximum wavenumber resolved by the grid is $k_{max} = \pi/\Delta x$ obtains:

$$\Delta t_s < \Delta x^{3/2}\left(\frac{\rho_a + \rho_w}{4\pi\sigma}\right)^{1/2} \tag{3.80}$$

In nondimensional form equation 3.80 becomes

$$\Delta t_s < \Delta x^{3/2}\left(\mathcal{W}e\frac{1+\lambda}{4\pi}\right)^{1/2} \tag{3.81}$$

The other time step restrictions are fairly well documented in any basic computational fluid dynamics text so they will only be listed here verses described in detail. Because of the explicit time integration scheme, there is a restriction due to the viscosity and the grid speed (the so-called CFL restriction). The nondimensional form of the viscous restriction for two fluids is:

$$\Delta t_\nu = \min\left(\frac{3}{14}\mathcal{R}e_w\frac{\rho(\phi)}{\mu(\phi)}\Delta x^2\right) \tag{3.82}$$

The CFL restriction is simply:

$$\Delta t_{\text{CFL}} = \min\left(\frac{\Delta x}{||\vec{\mathbf{u}}||}\right) \tag{3.83}$$

A final time-step restriction is necessary to resolve the gravity waves at the air-water interface. This restriction is generally never necessary as the other terms are much more restrictive.

$$\Delta t_g = \Delta x \mathcal{F}r^2 \tag{3.84}$$

The time step is dynamically chosen such that the minimum of all of the time-step restrictions and then given a factor of conservancy to ensure compliance.

$$\Delta t = 0.8 \min(\Delta t_g, \Delta t_{\text{CFL}}, \Delta t_\nu, \Delta t_s) \tag{3.85}$$

In general the time step restrictions which become limiting factors are the viscous and capillary (surface tension) restrictions. In most viscous applications, even those with free surfaces, the viscous restriction is the most limiting term. However, depending on the Weber number chosen for the restriction, the capillary restriction can be severe compared to the viscous restriction even though it is proportional to $\Delta x^{3/2}$ compared to Δx^2 for the viscous term.

3.10 Numerical Algorithm

A breakdown of the numerical algorithm is included for completeness in table 3.3. Each Runge-Kutta stage is essentially the same and will not be repeated. After both stages of the Runge-Kutta integration are completed, the time step is evaluated and modified as necessary according to section 3.9.3.

Table 3.3:

Outline of numerical algorithm for a single Runge-Kutta stage.

Step	Action	Reference
1.	Compute the source term for the Navier-Stokes	equation 3.66
2.	Evaluate the divergence of this source as the source term for the pressure equation.	equation 3.17
3.	Calculate the matrix coefficients for the projection operation	equation 3.23
4.	Iteratively solve for the dynamic pressure	section 3.6
5.	Update the source term for the Navier-Stokes equation with the gradient of the pressure field	equation 3.18
6.	Determine the intermediate values of the velocity field	equation 3.67
7.	Compute the source term for the level set function	equation 3.74
8.	Determine the intermediate value of the level set function	equation 3.75
9.	If reinitialization step, reinitialize the level set function	section 3.8

3.11 Conclusions

The numerical implementation of the governing equations were described in this chapter. Using a staggered-MAC type Cartesian grid, the treatment of all of the terms in the governing equations was described in detail. While many of the numerical implementations employed in this work are fairly standard to what is prevalent in the literature, some improvements have been made.

First and foremost, the movement of the constitutive properties between grids has been significantly improved over what is used in current level set implementations. These current implementations generally use direct averaging of the density and viscosity to calculate the values on points where the level set function is not represented. As the surface is represented by a smoothed region in which the density and viscosity vary by two to three orders of magnitude over a few points, significant errors and numerical dissipation can result through simple averaging techniques. As these errors and additional dissipation are located at the air-water interface and are integral in solving for the pressure and calculating the stresses at the location, an improved method was developed. As the level set function gives an accurate depiction of the distance of the point of interest from the interface, the level set function was interpolated to the grid points and the constitutive properties were evaluated based on these interpolated values. For very little additional computational effort, this method proved to be superior to the averaging method prevalent in the literature.

Second, the treatment of the stress forces was improved over current literature in that in the bulk of the fluid where the viscosity is constant, the discretization of the stress forces reduce to a second order central difference of the Laplacian. This detail significantly reduced the numerical dissipation in the treatment of the shear forces.

Third, the numerical implementation of the reinitialization of the level set function was significantly improved over what is used in literature. Through combining the basic method of Sussman and Fatemi [110] with the spirit of the idea behind Russo and Smereka's sub-cell fix [95], the volume conservation of the reinitialization scheme was increased by an order of magnitude.

And finally, this numerical implementation in general is second-order accurate in space and time. The numerical algorithm has been outlined in section 3.10. As a final note, the numerical model has been implemented on various distributed memory parallel and vector parallel platforms using MPI and Fortran90 without dependance on any architecturally dependent libraries. The model has been found to scale linearly and efficiently on a number of platforms.

Chapter 4

Initiating Numerical Breaking Waves

This chapter details the multiple methods employed in generating the waves in this study. While the topic of generating initial conditions for numerical simulations is not new, the process is generally not well documented in the literature. Additionally, the presence of a multi-fluid domain makes it difficult for direct application of "standard" methods commonly used in literature.

The predominance of the literature involving numerical simulations of water waves use potential flow techniques and interface tracking methods to track the free surface location. In this method, the technique for generating waves involves an accurate calculation of the linear (or non-linear) initial wave field up to the desired order of the calculation involved. In general, these waves do not break within a short period of time which is usually desired in numerical simulations. To force these waves to break, many authors use the method detailed by Longuet-Higgins and Cokelet [68] where an artificial pressure force is applied to the wave for a short period of time traveling in phase with the wave. Longuet-Higgins and Cokelet found that if this pressure forcing is applied to a wave which has an amount of energy just below the energy of the Stokes limiting wave, the wave will break shortly after the completion of the forcing period. This type of method is very useful when periodic and small domains of the order of a wavelength are used as it can be applied to force a single

wave to break in a short time.

Other successful studies use the concept of wave focusing as is used in many wavetank experiments. Depending on the implementation, it involves including the presence of a wavemaker on one boundary and simulating the entire length of the tank (c.f. Dommermuth *et al.* [24]). Either the signal of the wavemaker is actually reproduced or an accurate estimation of the flow leaving the wavemaker is calculated as an inlet condition. The generated wave group is allowed to propagate downstream where dispersion causes the group to focus and then break. This technique is used effectively and efficiently for all numerical wavetanks which use potential flow techniques.

While the most straightforward method for generating waves, the numerical wavetank is an inefficient method of generating waves for a viscous flow solver, even one which is only a single fluid. It requires a very large computational domain for which the majority of the fluid is still. Presuming a time-accurate scheme is involved, a lot of computational effort is put into solving for zero. To our knowledge there is only one viscous numerical wave tank in the literature which speaks to the difficult task of attempting this computationally [35].

Section 4.1 details the methods used in this study, their derivation and their effectiveness. Section 4.2 details how surface tension can be used to generate multiple types of breaking waves. Section 4.3 details the actual waves generated for this study and how they were classified as breaking or non-breaking as well as what type of breaking wave. Section 4.4 comments on the consequences of using the methods detailed in this chapter. Finally, section 4.5 highlights improvements which could potentially be used in future work.

4.1 Wave Generation Methods

This section details the four methods used to generate waves of varying types for a multi-fluid, periodic domain. Including the effects of the air volume makes directly implementing many of the potential flow methods detailed in the literature difficult. An initial condition for the air, or at least the air boundary layer, is necessary to elim-

inate extraneous surface vorticity. The periodic domain used in this study precludes the use of a wavemaker. Additionally, the computational effort required to simulate an entire wavetank with both the air and water volumes is significant.

The first of the four methods discussed is what we term an "impulsively" started Airy wave, where no solution for the air volume is used. The second method uses a solution of the two-phase Airy wave problem that satisfies all viscous free-surface boundary conditions and thus contains a solution for both the air and water volumes. The third and fourth methods center around using surface forcing to initiate a wave or force an existing wave similar to Longuet-Higgins and Cokelet. Each method has its advantages and disadvantages, which will also be discussed.

4.1.1 Impulsively Started Airy Wave

Previous authors have used a single-fluid third-order Stokes wave solution which is overly steep as an initial condition to produce breaking waves in a viscous multi-fluid simulation [13]. This method does not give any weight to boundary layers in the air and water and their effect on the initial condition. Our experience has shown that this generates a large amount of surface vorticity when the two fluids have the constitutive properties of air and water. Thus excess vorticity must be damped out or it significantly effects the solution.

The impulsively started linear Airy wave used here is similar to that in Chen and Kharif [13]. However, some effort has been made to smooth out the velocity field as it transitions through the air boundary layer. The location of the free surface is given as:

$$z_{fs} = \epsilon_\lambda \cos(2\pi x - \omega t) \tag{4.1}$$

In the water, the velocity field is given as the real part of:

$$\begin{aligned} u_w &= \quad a_1 e^{2\pi(\vec{\imath}x-\omega t)} \cosh 2\pi(\hat{h}+\delta) \\ w_w &= -a_1 \vec{\imath} e^{2\pi(\vec{\imath}x-\omega t)} \sinh 2\pi(\hat{h}+\delta) \end{aligned} \tag{4.2}$$

where the amplitude and depth are given as

$$\begin{aligned} a_1 &= \frac{2\pi\epsilon_\lambda}{\omega \cosh(2\pi\delta)} \\ \widehat{h} &= \frac{(z-z_{fs})\ell}{(z_{fs}+\ell)} \end{aligned} \tag{4.3}$$

Note that the scaling used in this study is based on the wavelength verses the wavenumber. Thus, $\epsilon_\lambda = ak/2\pi$. In equations 4.1-4.2, the notation used is $\vec{\imath} = \sqrt{-1}$ and ℓ is the undisturbed water depth.

The reason why this is termed "impulsively" started is that, from the air volume's point of view, it sees an impulsively started water volume underneath it. If this remains so using a smoothed level set boundary layer as done in this study, a strong sheet of vorticity is formed at the air-water interface which can affect the solution. It is not clear if the work of Chen and Kharif [13] experiences this vorticity as it is not discussed. To reduce this effect without determining the air boundary layer profile, the water velocity at the free surface is exponentially decayed into the air boundary layer over a small distance using the following decay rate:

$$\begin{aligned} u_a &= u_{fs} e^{(-10\hat{h})} \\ w_a &= w_{fs} e^{(-10\hat{h})} \end{aligned} \tag{4.4}$$

To demarcate the air-water boundary from the surface elevation, the level-set function is initialized from the free surface location as

$$\phi = z_{fs} - z \tag{4.5}$$

While this is not sufficient as a distance function, the level set function can be reinitialized before the start of the computation to obtain a proper distance function based on this estimated one. It should be acknowledged that this flow field does not preserve continuity in the entire volume because of the treatment at the air boundary layer. However, the initial pressure field is solved at the first time step to ensure that the velocity field following satisfies continuity. Practice has shown that the velocity field satisfies continuity within one to two time steps.

Providing that the slope of the wave (ak) is sufficiently small for linear theory to apply, waves generated with this method do not break. The slope associated with the breaking threshold for this method lies between $0.2 < ak < 0.3$. The waves generated by this initial condition tend to be overly energetic in terms of kinetic energy as the wave steepness increases. Whether or not this is due to applying linear theory to waves which are outside the application of the theory is not clear. A third-order Stokes wave was also briefly tested with essentially the same results.

4.1.2 Two-Fluid Airy Wave Solution

Another method for generating an initial condition for a wave in a multi-fluid domain is to include a solution for the air. Initial work was done by Dore [27]. Similar work in the realm of soft waves over mud has been done by Dalrymple and Liu [17] and Wen and Liu [123] where the domain consisted of water with a free-surface over soft mud as another wavy interface. Finally, Mei and Liu [72] looked at the damping of surface gravity waves using a boundary-layer-Poincaré technique where a rotational boundary layer (for the horizontal velocity only) was added to the linear wave solution at the surface to account for viscous damping. None of these applications provide the solution that is needed for this work.

For this solution, the flow field is separated into an irrotational (φ) and a rotational (ψ) part for both fluids. There are commonalities and assumptions which simplifies the solution: (i) the free-surface elevation is known *a-priori*; (ii) the inviscid wave number k is the same in both fluids; (iii) the solution is for deep water; (iv) the equations and boundary conditions are linear and applied at the linearized free surface

$z = 0$. For simplicity, the equations will be non-dimensionalized with respect to the wavelength before the solution is presented.

The irrotational part of the solution can be found as the real part of:

$$\begin{aligned} \varphi_w &= \epsilon_\lambda A_1 e^{\vec{\imath}(2\pi x - \omega t)} e^{(2\pi z)} \qquad \text{in the water } (z < 0) \\ \varphi_a &= \epsilon_\lambda A_2 e^{\vec{\imath}(2\pi x - \omega t)} e^{(-2\pi z)} \qquad \text{in the air } (z > 0) \end{aligned} \tag{4.6}$$

As in section 4.1.1, $\vec{\imath} = \sqrt{-1}$ and ϵ_λ is the wave slope nondimensionalized by the wavelength. To determine the rotational solution, we will define a stream function $\psi_{w,a}$ that satisfies the following linear form of the Navier-Stokes equations:

$$\begin{aligned} \frac{\partial \psi_w}{\partial t} &= \frac{1}{\mathcal{R}e_w} \nabla^2 \psi_w \qquad \text{in the water } (z < 0) \\ \frac{\partial \psi_a}{\partial t} &= \frac{\gamma}{\mathcal{R}e_w} \nabla^2 \psi_a \qquad \text{in the air } (z > 0) \end{aligned} \tag{4.7}$$

Here, $\gamma = \eta/\lambda$ is the ratio of the viscosity ratio (η) and the density ratio (λ) defined in section 2.2. The velocity field is calculated from the stream function in the standard way: $(u, w) = (-\frac{\partial \psi}{\partial z}, \frac{\partial \psi}{\partial x})$. The stream function is assumed to have the form:

$$\begin{aligned} \psi_w &= \epsilon_\lambda A_3 e^{\vec{\imath}(2\pi x - \omega t)} e^{2\pi k_3 z} \qquad \text{in the water } (z < 0) \\ \psi_a &= \epsilon_\lambda A_4 e^{\vec{\imath}(2\pi x - \omega t)} e^{-2\pi k_4 z} \qquad \text{in the air } (z > 0) \end{aligned} \tag{4.8}$$

Unlike the irrotational wave number k, the viscous or rotational wave numbers k_3 and k_4 can not be assumed equal because the viscosity is different in the two fluids. If the stream functions (eqn 4.8) are substituted into the governing equations (4.7) the viscous rotational wave numbers can be determined.

$$k_3^2 = 1 - \frac{\omega \mathcal{R}e_w}{4\pi^2} \vec{\imath} \tag{4.9}$$

$$k_4^2 = 1 - \frac{\omega \mathcal{R}e_w}{\gamma 4\pi^2} \vec{\imath} \tag{4.10}$$

There are four remaining constants: A_1 through A_4. These can be found through the

application of boundary conditions at the two-fluid interface. In this solution, four boundary conditions are applied at the interface for the total velocity field. They are: (i) the linearized kinematic boundary condition, (ii, iii) continuous horizontal and vertical velocity, and (iv) balanced tangential stress. The results are the following:

$$\begin{aligned}
A_1 &= -\frac{\vec{\imath}\omega}{2\pi}\left(\frac{(1-\eta)+\eta(k_4k_3+k_4+k_3)+k_3^2}{(k_3+\eta k_4+\eta+1)(k_4-1)}\right) \\
A_2 &= \frac{\vec{\imath}\omega}{2\pi}\left(\frac{(\eta-1)+(k_4k_3+k_4+k_3)+\eta k_4^2}{(k_3+\eta k_4+\eta+1)(k_4-1)}\right) \\
A_3 &= \frac{\omega}{\pi}\left(\frac{k_4\eta+1}{(k_3+\eta k_4+\eta+1)(k_4-1)}\right) \\
A_4 &= \frac{\omega}{\pi}\left(\frac{k_3+\eta}{(k_3+\eta k_4+\eta+1)(k_4-1)}\right)
\end{aligned} \tag{4.11}$$

Figure 4-1 shows the velocity field at the crest of the wave. While the rotational and irrotational parts of the solution are not continuous at the interface, the full solution is continuous as required by the interface boundary conditions.

It is interesting to note that the shear layer which exists at the interface for the irrotational solution is countered by the rotational field. In a sense, the rotational velocity field, even though discontinuous itself, is actually decreasing the amount of shear in the fluid near the interface. While counterintuitive, this fact will be discussed in the forthcoming section regarding the damping of gravity waves.

The solution can be simplified for large Reynolds number flows. First and foremost, the viscous wave numbers (4.9 and 4.10) can be simplified if $\mathcal{R}e_w >> 1$.

$$k_3 = \left(\frac{1-\vec{\imath}}{2}\right)\sqrt{\frac{2\omega\mathcal{R}e_w}{4\pi^2}} \tag{4.12}$$

$$k_4 = \left(\frac{1-\vec{\imath}}{2}\right)\sqrt{\frac{2\omega\mathcal{R}e_w}{\gamma 4\pi^2}} = \frac{k_3}{\sqrt{\gamma}} \tag{4.13}$$

Next, because $\mathcal{R}e_w >> 1$, it follows that $k_3 >> 1$ and $k_4 >> 1$. The coefficients A_1

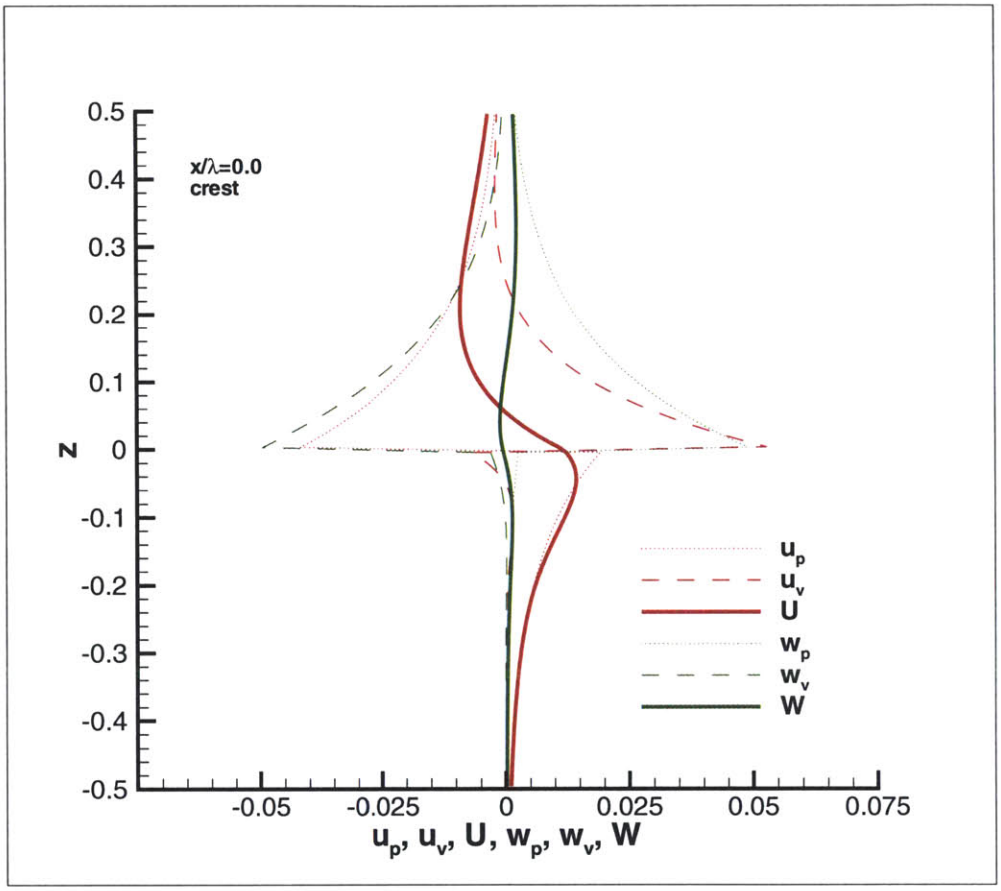

Figure 4-1: Two-fluid Airy wave solution at the crest ($x = 0$) plotted by each component and total velocity field. (u_p, w_p) are the irrotational flow components and (u_v, w_v) are the rotational flow components while (U, W) are the total velocity components.

through A_4 can also be simplified.

$$\begin{aligned} A_1 &= -\frac{\vec{\imath}\omega}{2\pi} \\ A_2 &= \frac{\vec{\imath}\omega}{2\pi} \\ A_3 &= (\vec{\imath}+1)\, f\sqrt{\frac{2\omega}{\mathcal{R}e_w}} \\ A_4 &= -(\vec{\imath}+1)\, f\sqrt{\frac{2\gamma\omega}{\mathcal{R}e_w}} = -A_3\sqrt{\gamma} \end{aligned} \tag{4.14}$$

where f is only a function of the ratio of the constitutive properties η and λ:

$$f = \frac{\sqrt{\eta\lambda}}{(1+\sqrt{\eta\lambda})} \tag{4.15}$$

The dispersion relationship gives the frequency of the wave as a function of the wave number. It comes from balancing the normal stress at the interface between the two fluids with surface tension. For simplicity, only the potential flow solution is used to determine the dispersion relationship here even though the boundary layer should have a small effect on the dispersion relationship. The two fluid dispersion relationship which includes the effects of surface tension, is given by Lamb [56]:

$$\omega = \left(2\pi\frac{1-\lambda}{1+\lambda} + 8\pi^3\frac{\mathcal{F}r}{\mathcal{W}e}\frac{1}{(1+\lambda)}\right)^{1/2} \tag{4.16}$$

With this dispersion relationship, equations 4.6, 4.8, and 4.11 can be used as an initial condition to start a multi-fluid simulation of an Airy wave. While the coefficients in equation 4.14 are available, the full coefficients are used (equation 4.11) in this method. As in the impulsively started Airy wave method, the air-water boundary is demarcated by equation 4.5 and reinitialized to a proper signed distance function before the start of the simulation. For the purposes of initializing the velocity field, the free-surface normalized depth in equation 4.3 is used for z. Unlike the impulsive Airy wave, this flow field does satisfy continuity initially and the initial pressure field is solved after the flow field has been initialized.

The waves generated by this initial condition are similar to the impulsively started case in that providing that the slope of the wave ak is sufficiently small for linear theory to apply, waves generated with this method do not break. The slope associated with the breaking threshold for this method lies between $0.2 < ak < 0.3$. However, the waves generated by this initial condition have a better balance between kinetic and potential energy. This does degrade as the initial wave steepness increases. Again, the reasons behind this are not clear.

Damping of Gravity Waves between Two Fluids

At this point in the discussion on wave generation techniques, we will deviate from the topic to derive the laminar damping rate of gravity waves between two fluids. This damping rate is used extensively in forthcoming chapters. As the two-fluid Airy wave solution has just been derived, this is an opportune time to perform this derivation.

The derivation is based on an estimate outlined in Lamb [57] for a potential flow solution of a wave in a single fluid with a free surface. The basic concept behind the Lamb method is that the change in total energy per unit area is equal to the average rate of work done by the surface forces if the potential flow were actually viscous.

$$\frac{d}{dt}E = -\overline{W} \tag{4.17}$$

In general, this approach applied to linear waves yields an equation for the amplitude decay of the form:

$$\frac{d}{dt}a = -\Gamma a \tag{4.18}$$

The first step is to calculate the rate of work done by surface forces due to the flow field in the water. Here, the surface stresses σ are chosen to be viscous stresses.

$$\begin{aligned} \mathcal{D}_w &= \left(\sigma_{33}w + \sigma_{13}u\right)_w \\ \mathcal{D}_w &= \mathcal{R}_{w1} + \mathcal{R}_{w2} \end{aligned} \tag{4.19}$$

The work done by the air on the water is similar but has a negative sign due to the

direction of the normal vector.

$$\mathcal{D}_a = -\left(\sigma_{33}w + \sigma_{13}u\right)_a$$
$$\mathcal{D}_a = \mathcal{R}_{a1} + \mathcal{R}_{a2} \tag{4.20}$$

In calculating the total work done at the surface by the air and water ($W = \mathcal{D} = \mathcal{D}_w + \mathcal{D}_a$), it is noted that there are terms proportional to $\cos(2\pi x - \omega t)$ and $\sin(2\pi x - \omega t)$ in the velocity field. Thus, the total work terms will contain terms of the form $\cos^2$, $\sin^2$ and $\sin \cdot \cos$. As we need $\overline{W}$, these terms will be averaged over a wavelength. Thus, only the terms proportional to $\cos^2$ and $\sin^2$ will be retained and shown in this derivation. The terms for the work done by the water and the air become:

$$\overline{\mathcal{R}}_{w1} = \frac{2}{\mathcal{R}e_w}\left(2\pi\epsilon^2\omega^2 - 4\pi^2\epsilon^2\omega f\sqrt{\frac{2\omega}{\mathcal{R}e_w}} - 4\pi\epsilon^2\omega^2 f + 8\pi^2\epsilon^2 f\frac{\omega}{\mathcal{R}e_w}\sqrt{2\omega\mathcal{R}e_w}\right) \tag{4.21}$$

$$\overline{\mathcal{R}}_{w2} = \frac{4\pi\epsilon^2\omega^2}{\mathcal{R}e_w} - 2\epsilon^2\omega^2 f\sqrt{\frac{2\omega}{\mathcal{R}e_w}} - \frac{8\pi\epsilon^2\omega^2 f}{\mathcal{R}e_w} + 4\epsilon^2 f^2\omega^2\sqrt{\frac{2\omega}{\mathcal{R}e_w}} \tag{4.22}$$

$$\overline{\mathcal{R}}_{a1} = \frac{\eta}{\mathcal{R}e_w}\left(-4\pi\epsilon^2\omega^2 - 8\pi^2\epsilon^2 f\omega\sqrt{\frac{2\omega}{\mathcal{R}e_w}}\sqrt{\gamma} - 8\pi\epsilon^2 f\omega^2 - 16\pi^2\sqrt{\gamma}\omega\sqrt{\frac{2\omega}{\mathcal{R}e_w}}\epsilon^2 f^2\right) \tag{4.23}$$

$$\overline{\mathcal{R}}_{a2} = \frac{\eta}{\mathcal{R}e_w}\left(-4\pi\epsilon^2\omega^2 - 8\pi\epsilon^2\omega^2 f - \pi\epsilon^2\omega^2 f\sqrt{\frac{2\omega\mathcal{R}e_w}{\gamma}} - 4\pi\epsilon^2 f^2\sqrt{\frac{2\omega\mathcal{R}e_w}{\gamma}}\right) \tag{4.24}$$

Combining equations 4.21 through 4.24 yields the following equation for the average rate of work done by the surface stresses:

$$\begin{aligned}\overline{W} = {} & \frac{4\pi\epsilon^2\omega^2}{\mathcal{R}e_w}(1+\eta) - \frac{8\pi\epsilon^2\omega^2 f}{\mathcal{R}e_w}(1-\eta) \\ & + \frac{1}{2}\left[\epsilon^2\omega^2 f\sqrt{\frac{2\omega}{\mathcal{R}e_w}}\left(\sqrt{\eta\lambda} - 2\right) + 2\epsilon^2\omega^2 f^2\sqrt{\frac{2\omega}{\mathcal{R}e_w}}\left(\sqrt{\eta\lambda} + 2\right)\right. \\ & \left. + 8\pi^2\epsilon^2 f\frac{\omega}{\mathcal{R}e_w}\sqrt{\frac{2\omega}{\mathcal{R}e_w}}(\eta\sqrt{\gamma} - 1) + 16\pi^2\epsilon^2 f^2\frac{\omega}{\mathcal{R}e_w}\sqrt{\frac{2\omega}{\mathcal{R}e_w}}(\eta\sqrt{\gamma} - 1)\right]\end{aligned} \tag{4.25}$$

The kinetic energy per unit area of the wave is given by:

$$\kappa = \int_{Aw} \frac{1}{2}\left(U_w^2 + W_w^2\right) \mathrm{d}Aw + \int_{Aa} \frac{\lambda}{2}\left(U_a^2 + W_a^2\right) \mathrm{d}Aa \tag{4.26}$$

If the total velocity field for both the air and the water is substituted into equation 4.26 and only the dominant term is kept, the total kinetic energy per unit area (or volume) is:

$$\kappa = (1+\lambda)\frac{\epsilon_\lambda^2 \omega^2}{8\pi} \tag{4.27}$$

The total energy per unit volume is twice equation 4.27 using equipartition. To determine the damping rate of the wave, we substitute the average rate of work done by the surface forces (equation 4.25) and the total energy per unit volume (equation 4.27) into equation 4.17. After some manipulation, the damping rate of the amplitude of the wave can be determined following equation 4.18.

$$\begin{aligned}\Gamma = {} & \frac{8\pi^2}{\mathcal{R}e_w}\left(\frac{1+\eta}{1+\lambda}\right) + \frac{\pi}{1+\lambda} f\sqrt{\frac{2\omega}{\mathcal{R}e_w}}\left(-2 + \boxed{3\sqrt{\eta\lambda}}\right) \\ & - \boxed{16\pi^3 \frac{f}{\mathcal{R}e_w}\left(\frac{1-\eta}{1+\lambda}\right)} - \boxed{\frac{\pi}{1+\lambda}\frac{f^2}{\sqrt{\eta\lambda}}\sqrt{\frac{2\omega}{\mathcal{R}e_w}}} + O(\mathcal{R}e_w^{-3/2})\end{aligned} \tag{4.28}$$

The boxed terms are associated with the effect of the air on the water. They originate from evaluation of the surface stresses on the water by the air (equation 4.20). If the damping rate is evaluated for water waves in the absence of air, ($\eta = 0$ and $\lambda = 0$), then Lamb's result is recovered.

We can examine the relative magnitudes of each term for the damping rate at the Reynolds number of interest for this problem ($\mathcal{R}e_w = 2000$) for a range of Weber numbers. Table 4.1 contains the value of each term in equation 4.28 including the terms proportional to $\mathcal{R}e_w^{-3/2}$ for an air-water interface problem. The dominant term in the damping rate is the first term. This term is due to the irrotational flow. The second term makes a minor adjustment to decrease the damping rate. This second term is a function of the rotational field. As discussed in the derivation of the two-fluid Airy wave solution, the purpose of the rotational field is to actually decrease

the shear rate at the air-water interface caused by the discontinuous irrotational flow field. Thus, its affect on the damping rate is to decrease it.

The third through fifth terms of equation 4.28 are the effects of the work done by the air on the surface. As can be seen in table 4.1, these terms (in particular term 4 and 5) are one order of magnitude less than the second term. They are also negative. Thus, they reduce the damping rate of the irrotational flow but very little due to their size. The terms which are proportional to $\mathcal{R}e_w^{-3/2}$ are inconsequential.

The amplitude reduction of the various terms is also shown in table 4.1. The amplitude reduction is calculated as the reduction of the initial amplitude at $t = 1$ or

$$\frac{\eta}{\eta_0} = e^{-\Gamma} \tag{4.29}$$

While terms associated with the air work (terms 3 through 5) are important, their effect is to change the amplitude reduction by only 0.1%. Thus for the purposes of this study, the damping rate used in estimating laminar losses in subsequent chapters only includes the first two terms. Namely,

$$\Gamma = \frac{8\pi^2}{\mathcal{R}e_w}\left(\frac{1+\eta}{1+\lambda}\right) - \frac{2\pi}{1+\lambda}f\sqrt{\frac{2\omega}{\mathcal{R}e_w}} \tag{4.30}$$

Chen and Kharif have a similar equation for the damping of gravity waves between two fluids (their equation 11) [13]. The only difference between it and this simplified damping rate is that the second term has a positive sign where this one is negative. Based on the discussion regarding the purpose of the second term, the negative sign is correct. Investigation of their paper, in particular their figure 3b, shows that it is likely a typographical error as the damping line on their figure is more representative of a minus sign verses a positive sign.

Table 4.1:

Relative magnitude of damping rate terms (eqn 4.28) for $\mathcal{R}e_w = 2000$.

$\mathcal{W}e$	ω	Term 1	Term 2	Term 3	Term 4	Term 5	Term 6	Term 7
7.38	6.312	0.03983	-0.001572	7.457E-06	-0.0007733	-0.0007835	-3.0050E-05	2.0183E-07
738	2.570	0.03983	-0.001003	4.758E-06	-0.0007733	-0.0004999	-1.9175E-05	1.2878E-07
73,868	2.504	0.03983	-0.000990	4.697E-06	-0.0007733	-0.0004935	-1.8929E-05	1.2713E-07
738,684	2.504	0.03983	-0.000990	4.696E-06	-0.0007733	-0.0004935	-1.8927E-05	1.2712E-07
∞	2.504	0.03983	-0.000990	4.696E-06	-0.0007733	-0.0004935	-1.8926E-05	1.2711E-07

$\mathcal{W}e$	ω	$\Gamma_{1:2}$	$\Gamma_{1:5}$	$\Gamma_{1:7}$	% Amp Red$_{1:2}$	% Amp Red$_{1:5}$	% Amp Red$_{1:7}$
7.38	6.312	0.038261281	0.036711834	0.036681985	96.25%	96.40%	96.40%
738	2.570	0.038830218	0.037561644	0.037542598	96.19%	96.31%	96.32%
73,868	2.504	0.038843083	0.03758086	0.037562058	96.19%	96.31%	96.31%
738,684	2.504	0.038843202	0.037581038	0.037562238	96.19%	96.31%	96.31%
∞	2.504	0.038843215	0.037581058	0.037562258	96.19%	96.31%	96.31%

4.1.3 Surface Forcing I

It is not necessary to use a solution of the wave field to generate plane progressive waves for an initial condition. Another method uses surface forcing on a flat, quiescent fluid. Using a normal pressure force on the surface which moves with a given speed, a progressive wave can be produced. Depending on the initial amount of energy input by the surface force, the resulting wave will either progress as a non-breaking wave or form a breaking wave shortly after the forcing has been removed.

Forcing the surface in a multi-fluid volume is applied in a similar manner as the surface tension is applied as discussed in section 2.2.2. The smoothed delta function is used to locate the interface in the volume and apply a force in the normal direction. The surface force applied is:

$$\vec{\mathcal{F}}_s = p(x,t)\vec{n}\delta(\phi;\epsilon) \tag{4.31}$$

The normal vector is calculated from the level set function as in equation 2.12 and the smoothed delta function is the same function which is used in the calculation of the surface tension, i.e. equation 2.22. The "pressure" forcing $p(x,t)$ can be any desired function providing it moves with a phase speed so that it imparts a phase speed to the water. The one chosen for this work is a simple sine wave.

$$p(x,\hat{t}) = \frac{p_0}{2}(1+\cos(\pi\hat{t}-\pi))\sin(2\pi x - \pi\hat{t}) \tag{4.32}$$

where p_0 is a tunable constant to control the magnitude of the forcing. The time $\hat{t}$ is given such that the forcing is ensured to turn off after a half-period of the forcing:

$$\hat{t} = \begin{cases} t & 0 \le t \le 2\pi/3 \\ 0 & t \ge 2\pi/3 \end{cases} \tag{4.33}$$

or

$$\hat{t} = \min\left(\frac{t}{\pi/3}, 2\right) \tag{4.34}$$

This forcing is added to the momentum equations (eqn 2.28). To keep the effect of this term separate from the pressure field, it is solved separately using the same process for the pressure field (section 2.5).

$$\nabla \cdot \frac{1}{\rho(\phi)} \nabla \mathrm{F}_s = \vec{\mathcal{F}}_s \tag{4.35}$$

The gradient of F_s is also added to the momentum equations. It is not necessary to keep the effect of this term separate from the pressure field. It is sufficient to add equation 4.31 to the momentum equations and solve for the pressure field.

As stated previously, this forcing is applied to a flat, quiescent surface. The initial velocity and pressure field are zero and the level set function is given as:

$$\phi = -z \tag{4.36}$$

where $z = 0$ represents the water line.

A potential drawback to this method is the inclusion of surface tension at the start of the wave forcing. As the surface begins to develop curvature from the surface forcing, the surface tension force which is proportional to the curvature fights this and flattens the surface out. Thus, for cases where this wave generation method is used and it is desirable to include surface tension effects, the surface tension force is turned on slowly such that the surface is allowed to deform before the surface tension can remove it. This is accomplished by slowly increasing the reciprocal of the Weber number such that it reaches its intended value $\mathcal{W}e_t$ before the surface forcing

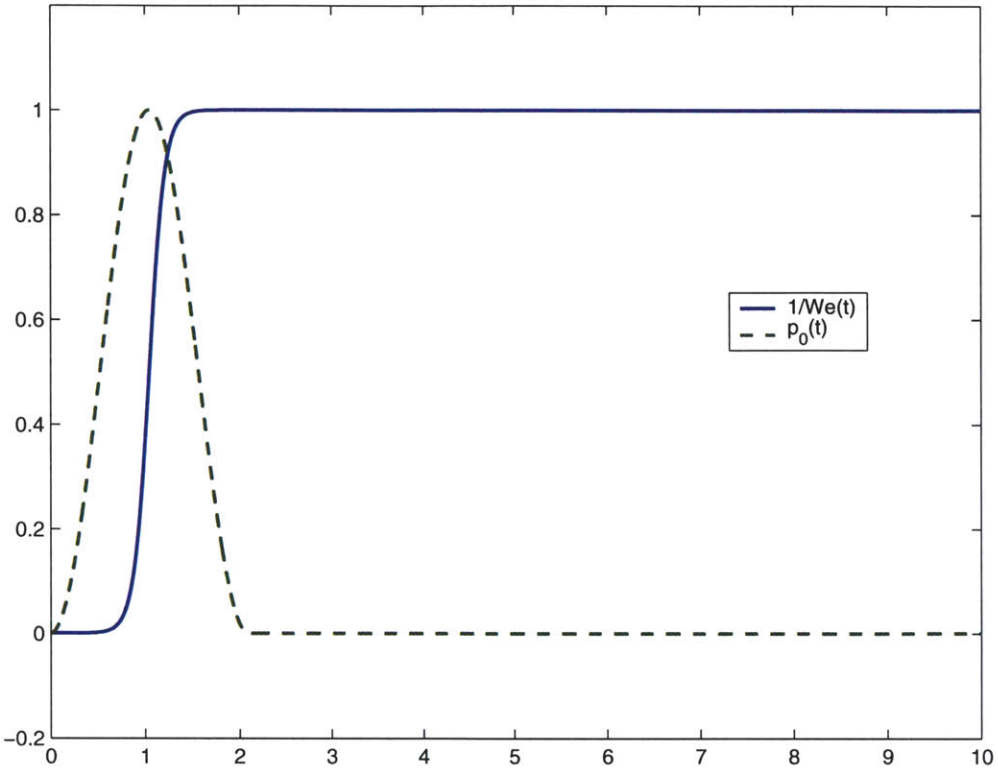

Figure 4-2: Ramp-up of surface tension coefficient (-) and forcing amplitude (- -), normalized by their peak values.

is complete. This is shown in figure 4-2.

$$\frac{1}{\mathcal{W}e}(t) = \frac{1}{2\mathcal{W}e_t}(1 + \tanh(6\hat{t}_1 - 5\pi) \tag{4.37}$$

$$\hat{t}_1 = \begin{cases} t & 0 \leq t \leq 5\pi/12 \\ 0 & t \geq 5\pi/12 \end{cases} \tag{4.38}$$

or

$$\hat{t}_1 = \min(5\pi, t) \tag{4.39}$$

The benefit of this wave generation method is that the initialization is clean in terms of the initial velocity and pressure fields for both fluids. Over a range of forcing

amplitude, $0.025 \leq p_0 \leq 0.05$, this method creates a range of non-breaking and breaking progressive waves. The difficulty lies in the fact that this method relies solely on surface forcing to generate a full-fledged progressive wave. The plunging breaking waves generated in these cases tend to have an excess of horizontal momentum and be more jet-like compared to the plunging breaking waves seen through wave focusing or waves generated with the linear Airy wave solution (one or two fluids). Despite this fact, this method is robust in generating plane progressive waves.

4.1.4 Surface Forcing II

Another method of wave generation which uses surface forcing is in the spirit of the pressure forcing used by Longuet-Higgins and Cokelet. A pressure force similar in nature to what is detailed in section 4.1.3 is applied to a field which already has a plane progressive wave in it. As the wave surface is already developed, the difficulty of including surface tension effects addressed in section 4.1.3 does not arise.

The method centers around applying a sinusoidal pressure forcing which is 90° out of phase with the wave such that the positive pressure forcing is on the back face of the wave $\eta_x > 0$ and negative pressure forcing is on the front face of the wave $\eta_x < 0$. If this is not implemented sufficiently, it is possible to generate waves which move in the opposite direction of the original wave, giving the appearance of a standing wave in the solution. Therefore, it is critical that the forcing move at the same speed of the wave being forced. When this surface forcing is applied in potential flow calculations, the phase speed of the initial wave is easily determined and constant as there are no viscous effects on the wave phase speed.

In this method of (breaking) wave generation, the surface forcing is applied in the same manner as for SFI in terms of methodology. However, instead of a flat, quiescent surface, it is applied to a pre-existing wave field. The difference between SFI and this method is that the force which is applied is a function of the slope of the surface rather than a prescribed shape. To preclude the need for constructing a surface and determining the slope of the interface at every time step, the sign of the forcing is inferred from the sign of the surface normal in the x direction. The normal

is also used to direct the force vector in the surface normal direction and the delta function is utilized to include the surface forcing only in the realm of the smoothed surface.

$$\vec{\mathcal{F}}_s = p(t) n_x \vec{n} \delta(\phi; \epsilon) \tag{4.40}$$

The variation of the amplitude of the surface forcing over time is controlled in the same manner as that for SFI such that the function $p(t)$ is given as:

$$p(t) = \frac{p_0}{2}(1 + \cos(\pi \hat{t} - \pi)) \tag{4.41}$$

and the time is modified as in equation 4.33.

While the magnitude of the forcing in equation 4.41 is generally arbitrary and only for a period of time, this method is similar to what is used in the literature to impart a sustained wind input to a wave field where a surface pressure distribution is added as a function of the local wave slope η_x. Banner and Song [104] use the following surface pressure distribution in their study on the influence of wind forcing on the breaking of deep water waves.

$$p_s(x,t) = \alpha \rho_a u_\star^2 \eta_x(x,t) \tag{4.42}$$

The forcing is a function of the shear stress on the surface imparted by the air $\rho_a u_\star^2$ and a tunable constant α. There is much more meaning to these terms and the interested reader is referenced to the text by Phillips [87] and section 2 of Donelan [26] for a thorough discussion on empirical methods and realistic bounds for these coefficients. Suffice it to say, the forcing method SFII is not without physical meaning.

This method is ideal for taking waves which do not break or break very little and impart energy to them such that they will certainly break. The initial velocity and pressure fields are not necessarily clean in that they have been estimated using linear theory. However, if waves are taken with initial slopes in the range of $0.2 \leq ak \leq 0.3$ and a small amount of forcing is applied (the amount of which is dependant on the initial slope of the wave), a range of breaking waves can be generated consistently.

The method works best when the amplitude is near the limit of the linear theory $ak \approx 0.3$ in that little energy needs to be used to make the wave break.

The drawback of the implementation of this method is that the actual slope of the wave is not used, only inferred from the surface normal. After the forcing period is complete, there is evidence through the presence of a small standing wave that the wave has not been forced at its phase speed. The resulting standing wave energy for this method is relatively small compared to other methods in this work. Section 4.4 discusses the presence of standing wave energy in this work. This small standing wave aside, this method is very capable of generating a range of breaking waves.

4.2 Using Surface Tension to Generate Breaking Waves

This section discusses how modifying the surface tension of the problem being investigated can be used to create a range of types of breaking wave. Using surface tension to control the generation of breaking waves may seem like an *ad-hoc* method. From an experimentalists point of view, the surface tension effects and coefficients are dependant only upon the fluids being used. However when performing direct numerical simulation, these properties can be varied easily. The Reynolds number which are capable of being simulated using direct numerical simulation is moderate $O(10^{3-4})$. Based on the scaling of this study, this represents a physical wavelength of millimeters for the low end and centimeters on the high end. At these length scales, the Weber number is around O(1) to O(10). This is a very strong surface tension effect relative to experimental scales where the Weber number is around $O(10^5)$. While the debate about the scalability of Reynolds number effects in breaking waves is still open, there is no doubt that surface tension effects do not scale.

In his review paper on spilling breaking waves, Duncan [31] details the effect of wavelength and thereby surface tension effects on the breaking process. For relatively long wavelengths, a jet is formed which impinges on the front surface of the wave. For

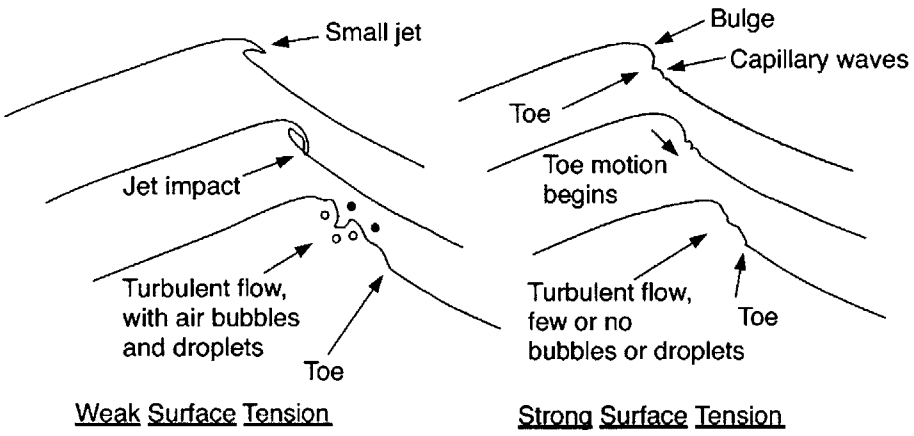

Figure 4-3: Schematic of the effect of surface tension on breaking waves. Reprinted with permission. From [31].

shorter wavelengths, the effects of surface tension suppresses the jet formation and the surface then forms a bulge at the crest with a train of capillary waves at the toe. This is shown schematically in his figure 1 which is reproduced in figure 4-3. Thus by modifying the actual surface tension coefficient, a wavelength which is small due to the Reynolds number restriction of direct numerical simulation can generate spilling but not plunging breaking waves.

An example of such an effect can be seen in figure 4-4 where the only difference between the solutions is the surface tension coefficient. As detailed in Duncan's review paper, the case where the Weber number is $O(10^5)$ forms a plunging breaker. The formation of this jet is suppressed for the cases where the Weber number is $O(10^2)$. The front face of this wave forms a bulge and toe. The capillary waves that Duncan describes which should appear at the toe of the bulge are not resolved and thus not seen. It is quite useful in direct numerical simulation which is limited to moderate Reynolds numbers to use the surface tension coefficient as an additional controlling parameter to generate a variety of breaking waves.

In general, the formation of the bulge in lieu of a plunging jet can be a factor of the energy prior to breaking and the strength of surface tension effects [31]. In the context of this study, the formation of the bulge verses a jet is primarily a function

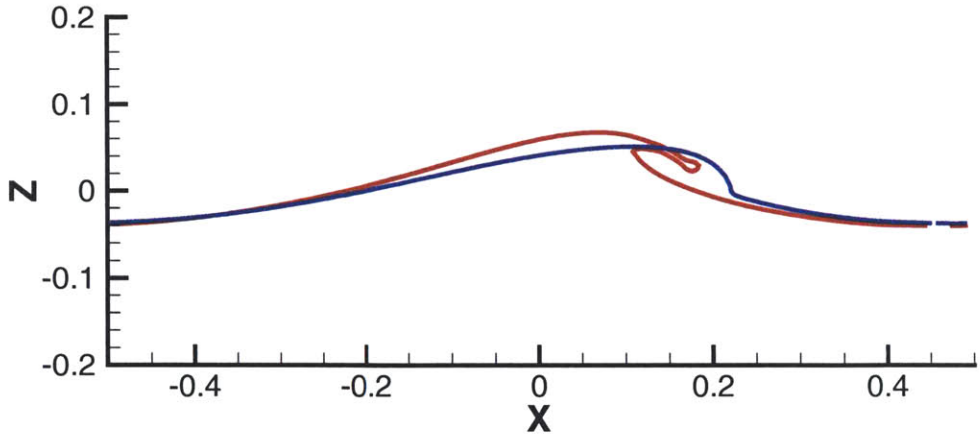

Figure 4-4: Two waves generated by the same amount of surface forcing (SFI) using two different Weber numbers. (red) $\mathcal{W}e = 73,868$; (blue) $\mathcal{W}e = 738$

of surface tension effects and the amount of energy in the wave prior to breaking. A threshold Weber number was not directly investigated as a part of this study and a review of the cases in this study does not reveal a clear transition from bulge to jet. Table 4.2 compiles a sample of the waves in this study which formed bulges and jets along with their Weber number and energy prior to breaking. The strongest conclusion which can be made from table 4.2 and the other waves in this study is that waves which have Weber numbers less than $O(10^3)$ do not form jets. This is consistent with physical expectations as this Weber number is closer to the physical Weber number of the waves being simulated which is $O(10)$. At these small scales, the surface tension effects suppresses the jet formation [31, 119, 63].

For waves with a Weber number greater than $O(10^3)$, the evolution of the surface into a bulge or jet becomes dependant upon the energy in the wave as well. Unfortunately, within the context of this study, it can not be said that, for a given Weber number, the formation of the jet is then only dependant upon the amount of energy in the wave prior to breaking. For example, in table 4.2, consider the four waves which have a fixed Weber number of 73,868. Two form spilling breakers with bulges and the other two form jets. For the cases which have very little standing wave energy in the computational domain (all cases which are not IAW), there appears to be a threshold

between 0.51 and 0.64. Case IAW-08, which has a considerable amount of standing wave energy, forms a strong-spilling breaking wave with an initial energy at 0.6779 of the limiting Stokes wave. The presence of the standing wave and general sparsity of data at different Weber numbers makes it difficult to draw a firm conclusion. Another criteria related to the growth rate of the wave (see section 7.4) or particle speed relative to group or phase speed may also be key.

Table 4.2:

Bulge and Jet Formation as a function of Weber number and energy prior to breaking.

Bulge Formation				Jet Formation			
Case	Class	We	E_w/E_{Stokes}	Case	Class	We	E_w/E_{Stokes}
IAW-04	SS	738	1.1704	A2P-17	JT	73,868	0.6405
IAW-03	SS	738	0.6627	A2P-18	JT	73,868	0.6900
A2P-02	GS	738	0.4765	IAW-09	AE	73,868	1.2005
IAW-08	GS	73,868	0.6779	A2P-14	JT	738,684	0.5893
A2P-06	GS	73,868	0.5119	A2P-16	JT	738,684	0.6411
A2P-09	GS	738,684	0.5178	SFI-04	JT	∞	0.6788
SFI-02	GS	∞	0.5459				

Classification: Non-breaking (NB), Incipient Breaking (IB), Gentle Spilling (GS), Strong Spilling (SS), Jet Formation (JT), Air Entrainment (AE)

4.3 The Waves Generated

The four wave generation methods detailed in section 4.1 were used to generate a variety of waves which are of breaking and non-breaking types. This section details the simulations which were completed, the waves they generated and how they were

classified.

This study entailed the generation of 36 different waves through the four different wave generation methods. Table 4.3 includes all of the relevant information regarding the 36 different waves, including physical and numerical parameters as well as how they were classified. As discussed in chapter 1, there are three classifications used in the literature regarding waves: non-breaking, spilling and plunging. This work takes the spilling breaking wave and divides it into two subcategories: gentle and strong. The same with the plunging breaking waves: jet-forming and air-entraining. Thus, the five wave classifications defined in this work are: non-breaking, gentle-spilling, strong-spilling, jet-forming, and air-entraining.

Classifying waves as breaking or non-breaking is a relatively straight forward process. It involves visually inspecting the surface for signs of breaking, looking at the damping of the wave amplitude compared to that expected by laminar damping effects and finally, consulting the dissipation rate to ensure it experienced no significant relative increase for cases which are determined to be non-breaking. To discern between spilling and plunging breaking waves is also straight forward. Providing that the surface does not form a jet or re-enter itself, then it is classified as a spilling breaking wave. If a plunging jet entrained air, then it was classified as an air-entraining breaking wave.

The only subjective classification was the difference between gentle-spilling and strong-spilling breaking waves. For this study, once a wave was determined to be a spilling breaking wave, the dissipation rate (see chapter 7) was considered next. Waves which saw a mild increase in dissipation rate in the water volumes were first categorized as gentle-spilling breakers. Those that saw a much larger relative increase were labeled strong-spilling breakers. Each case was then reviewed in terms of looking at the balance between the relative increase in dissipation rate between the air and water volumes. As a final check, the evolution of the surface was revisited and the strength of the bulge (and the time it persisted before traveling down the wave crest) were also considered.

Table 4.3: Waves Generated in this Study

Classification: Non-breaking (NB), Incipient Breaking (IB), Gentle Spilling (GS), Strong Spilling (SS), Jet Formation (JT), Air Entrainment (AE)												
Case Name	WGM	$\mathcal{R}e_w$	$\mathcal{F}r$	$\mathcal{W}e$	ak_0	p_0	γ	N_x	N_z	L_x	L_z	Class
SFI-01	SFI			∞	0.0	0.025	3.0					NB
SFI-02	SFI			∞	0.0	0.04	3.0					GS
SFI-03	SFI			∞	0.0	0.03	3.0					NB
SFI-04	SFI			∞	0.0	0.05	3.0					JT
SFI-05	SFI			∞	0.0	0.035	3.0					NB
SFI-06	SFI	2,000	1	∞	0.0	0.045	3.0	320	320	1.0	1.0	JT
SFI-07	SFI			∞	0.0	0.03	2.0					NB
SFI-08	SFI			738	0.0	0.03	3.0					NB
SFI-09	SFI			∞	0.0	0.05	2.0					JT
SFI-10	SFI			738	0.0	0.05	3.0					SS
SFI-11	SFI			73,868	0.0	0.05	2.0					JT

continued on next page

continued from previous page

Case Name	WGM	$\mathcal{R}e_w$	$\mathcal{F}r$	$\mathcal{W}e$	ak_0	p_0	γ	N_x	N_z	L_x	L_z	Class
IAW-01	IAW	2,000	1	738	0.1	0.0	2.0	256	256	1	1	NB
IAW-02	IAW			738	0.2	0.0	2.0					NB
IAW-03	IAW			738	0.3	0.0	2.0					SS
IAW-04	IAW			738	0.4	0.0	2.0					SS
IAW-05	IAW			738	0.5	0.0	2.0					SS
IAW-06	IAW	2,000	1	73,868	0.1	0.0	3.0	320	320	1	1	NB
IAW-07	IAW			73,868	0.2	0.0	3.0					NB
IAW-08	IAW			73,868	0.3	0.0	3.0					GS
IAW-09	IAW			73,868	0.4	0.0	3.0					AE
IAW-10	IAW			73,868	0.5	0.0	3.0					AE
A2P-01	A2P	2,000	1	738	0.2	0.0	2.0	256	256	1	1	NB
A2P-02	A2P			738	0.2	0.125	2.0					GS
A2P-03	A2P			738	0.3	0.0	2.0					IB
A2P-04	A2P			738	0.3	0.04	2.0					GS
A2P-05	A2P			73,868	0.3	0.04	2.0					GS
A2P-06	A2P			73,868	0.2	0.125	2.0					GS

continued on next page

continued from previous page

Case Name	WGM	$\mathcal{R}e_w$	$\mathcal{F}r$	$\mathcal{W}e$	ak_0	p_0	γ	N_x	N_z	L_x	L_z	Class
A2P-07	A2P	2,000	1	73,868	0.25	0.0	2.0	256	256	1	1	NB
A2P-08	A2P			738,684	0.3	0.04	2.0					GS
A2P-09	A2P			738,684	0.2	0.125	2.0					GS
A2P-10[1]	A2P			7.38	0.2	0.0	2.0					NB
A2P-11[2]	A2P	2,000	1	738,684	0.2	0.125	3.0	1024	1024	1	1	–
A2P-12[3]	A2P	10,000	1	63,156	0.2	0.125	3.0	1280	1280	1	1	–
A2P-13[4]	A2P	2,000	1	7.38	0.3	0.0	2.0	256	256	1	1	–
A2P-14	A2P	2,000	1	738,684	0.3	0.04	3.0	320	320	1	1	JT
A2P-15	A2P			738,684	0.3	0.045	3.0					GS
A2P-16	A2P			738,684	0.3	0.06	3.0					JT
A2P-17	A2P			73,868	0.3	0.06	3.0					JT
A2P-18	A2P			73,868	0.3	0.07	3.0					JT

[1]Poorly resolved LSBL, removed from study
[2]Not complete in time to be included in study
[3]ibid
[4]ibid

4.4 Comment on Presence of Standing Waves

Despite considerable effort to develop a wave generation method which had zero standing wave component in the computational domain, standing waves existed for all of the methods considered. In general, an undesired standing wave in a computational domain can result for a variety of reasons. The first is a result of the mismatch of using a linear solution as an initial condition for a simulation which involves a nonlinear free-surface boundary condition [23]. A second is the use of a linear solution outside the bounds of its applicability. A third reason occurs when the free surface is being forced. If the surface forcing is out of phase such that waves are generated progressing in the opposite direction of the initial progression, the result will be a standing wave component. Unfortunately, all three of these reasons appear in the wave generation methods detailed in this chapter. This section addresses their presence in this study as well as quantifies their magnitude and effect on the results shown.

The range of strength and frequency of the standing waves which resulted for each type of wave generation mechanism is shown in table 4.4. The strength and frequency were determined by considering the fraction of total energy that the potential energy (in the water) fluctuated at a given time. For cases with wave breaking or where surface forcing was involved, times well away from both regions (breaking and forcing) were used to determine the fluctuation amplitude and period.

Table 4.4: Percent energy and oscillation period for standing wave for various wave generation methods

Wave Generation Method	% E	Period
Airy Two Phase (A2P)	1.2-1.5	1.28-1.54
Airy Two Phase with Forcing (SFII)	2.6-8.5	1.28-1.53
Impulsive Airy Wave (IAW)	31-49	1.22-1.35
Surface Forcing I (SFI)	4.6-9.1	1.21-1.50

In terms of generating minimal standing waves in the domain, the two-phase Airy

wave is the most reliable with the amplitude of the standing wave energy only about 1% of the total energy of the wave. This standing wave energy is believed to be a function of the linear/non-linear mismatch as well as using the linearized solution on a surface which is not $z = 0$. The amount of energy in the standing wave increases when forcing (SFII) is applied, the amount of which is dependent upon how strong the forcing is. The increase can be 7-8% of the total energy of the wave for cases with the strongest amount of forcing. This result can be for two reasons. The first is from the surface forcing itself. If the forcing is not precisely in phase with the wave, waves moving in the opposite direction can be formed. Also, as the surface force is applied using the smoothed delta function, the forcing is acting over a distance of 3ϵ into both fluids. It is believed that this forcing into the fluid domain verses the exact surface may also cause a wave to travel in the opposite direction. Yet, it is not considered a large effect. In cases where the surface tension was turned on over time, there was no visible increase in standing wave energy. As the surface forcing technique is modeled in the same manner as the surface tension, any standing wave which is a result of forcing the interface over a thickness is considered to be very small.

For cases which the surface forcing (SFI) is used to generate the plane progressive wave, the standing wave energy is 4-9% of the energy in the water volume. The cause of this standing wave can be discerned by inspecting the mechanics of this forcing method. The surface forcing method slowly presses down on the surface as a sine wave which travels. As the surface is initially flat, there is a delay in which the free surface becomes deformed. Once it has deformed, the forcing is able to impart a horizontal energy to the surface which then makes the wave travel. Thus, one reason for the standing wave is the initial deformation of the surface before the wave begins to progress. The other is because, as the surface forcing function is prescribed verses a function of the free-surface slope as in SFII, there is now a phase difference in the forcing function and the slope of the free surface. This phase difference now allows the forcing function to impart energy in the wrong direction.

The cases which use the impulsively started Airy wave incur the largest amount of standing wave energy (31-49%). The largest amount of energy in the standing

wave component corresponds to the cases with the largest initial slope which is well beyond what linear theory would allow. The reason for the standing wave energy in these cases is two-fold. The first is using a linear theory well outside the bounds of its applicability and off of $z = 0$. The second is the shock to the air that the impulsively started wave field gives. This is evident when cases which use the two-phase Airy wave solution are compared to impulsively started waves of the same slope. In the two-phase case, the standing wave energy is no more than 1.5 % while the same cases using the impulsively started wave field have 32-37%. The cases in the literature which use this method do not appear to address this issue nor mention it with any regularity.

For all of the cases, the period of the standing wave is $\sim 1.2-1.5$. This corresponds to a wave number of 3 or 4 depending on the the Weber number based on an inviscid dispersion relationship for an interface between two fluids with surface tension effects (eqn. 4.16). Additionally, there appears to be a connection between the period and the amplitude of the wave but this could not be quantified. The only cases where the standing wave may affect the results in this thesis are the impulsively started cases which have by far the largest standing wave energy. The waves generated on this method appear to ride over the standing wave crests. As some breaking mechanisms are a function of wave focusing, there is nothing which indicates that the breaking mechanism for these cases is not partly to do with a sudden convergence of energy as the progressive waves ride over the standing waves. However, as stated in section 4.1.1, it is more likely that these waves have such an excess of kinetic energy that the waves break to disperse this energy rather than focusing.

In summary, the wave generation methods used in this study are generally well suited for creating breaking and non-breaking waves with little (less than 10%) of the total wave energy existing in the standing wave. Only the cases where the impulsively started method was used does this standing wave energy become significant and potentially affects the solution. The period for the standing wave is consistent for all cases.

4.5 Future Improvements

The wave generation methods discussed in this chapter are by no means the only methods available. However when a multi-fluid domain is present, the number of robust methods with few side effects is fairly small. When a periodic domain is used as in this study, the options are limited further. The two-phase Airy wave method (with and without surface forcing) was found to be the best method of the methods explored here. Yet, while very useful in generating an array of breaking waves, the method is limited in its scope of application.

In general, the four methods used in this study are not useful in studying wave groups or broadband spectrums. The waves generated using these methods essentially had a single frequency represented. It may be possible to extend the two-phase Airy method and use it for multiple wave components to study wave groups. Yet, the design of the wave group must be done carefully in the context of periodic boundary conditions. Without a robust capability for generating and evolving wave groups efficiently, the entire study of wave focusing which is used widely in experiments can not be investigated. Additionally, none of these methods are suitable for the study of steady breaking waves that is another rich area of wave breaking which has not been sufficiently studied numerically in the literature. This section briefly discusses two methods which were developed as additional wave generation methods to address the study of additional unsteady and steady breaking waves.

4.5.1 "Wavemaker Push"

Using a Navier-Stokes flow solver to simulate the entire length of a wavetank is not a trivial computational undertaking, even if only a single fluid is simulated. Additionally, most numerical wavetanks are used to generate information regarding wave-body interactions of which the viscous component is fairly small. Thus, the computational effort may significantly outweigh the amount of useful data which is gained. Outside of trying to replicate wave focusing experiments to do a one-on-one comparison which includes the effects of viscosity and wave-overturning, it is difficult to imagine where

a viscous numerical wavetank would serve a purpose.

Recent experiments by Duncan [32] detailed an interesting set of experiments in which a flexible wavemaker is used to impulsively push water down a channel. It is controlled in such a manner so that the profile of the wavemaker mimics that of a ship hull passing through a plane. This "2D+T" wavemaker is capable of producing waves with a broadband spectrum which break relatively near the wavemaker. Using this type of wavemaker for breaking wave studies is not necessarily a new idea. However, it was abandoned long ago for the wave-focusing techniques which are much easier to control and characterize. Yet, within the context of ship breaking waves, it is much more plausible that an impulsive push more closely mimics the mechanism involved than a wave-focusing technique.

This type of wavemaker and study is well suited to a multi-phase viscous numerical wavetank as the domain requirements are significantly less than wave-focusing techniques. Because of its impulsive nature, it creates waves with a broad spectrum which will allow for nonlinear effects to become more apparent than narrow banded or single-frequency spectrums could attempt.

The most feasible method for numerically representing a wavemaker push of this type is to use a free-slip boundary condition at the boundary which represents the wavemaker. This entails using the following boundary conditions at the wavemaker for the velocity field:

$$u(z,t) = U(z,t) \tag{4.43}$$

where the prescribed velocity field can be made a function of z to allow a flexible wavemaker to be used to mimic a ship bow as in Duncan's experiments. The vertical velocity is allowed to slip in an inviscid manner.

The pressure boundary condition at the wavemaker must be chosen to ensure that the flow satisfies continuity at that point. This means that the pressure gradient on that boundary must include the acceleration term from the wavemaker, namely:

$$\frac{1}{\rho(\phi)}\frac{\partial P}{\partial x} = -\frac{\partial U}{\partial t} - \mathbf{F_x} \tag{4.44}$$

where the forcing $\mathbf{F_x}$ is the x-component of the Navier Stokes equation as defined in equation 2.71.

To keep the numerical domain small, the outlet boundary conditions for the velocity and pressure field must be done with a degree of care to ensure continuity is satisfied, there are no reflections at the boundary and the solution only grows with time if the forcing grows with time [49, 48]. Johansson [49] suggests outlet conditions of the form:

$$\begin{Bmatrix} \frac{\partial^j u}{\partial x^j} \\ \frac{\partial^q w}{\partial x^q} \\ p \end{Bmatrix} (\text{outlet}, z, t) = \begin{Bmatrix} 0 \\ 0 \\ p_0 \end{Bmatrix} \tag{4.45}$$

Providing that $j = q + 1$, Johansson proves that the outlet condition is divergence free. However, if $j \neq q + 1$ and the viscous effects are small, the divergence will be confined to an outflow boundary layer. To ensure that the outlet is divergence free, q is chosen to be 1 making $j = 2$. The prescribed outlet pressure field is $p_0 = 0$ as this is only referring to the dynamic pressure and hydrostatic considerations are not important.

Both the work by Johansson and others deal with grids which are collocated, in that the velocity and pressure points exist at the same point in space and thus are all well defined on the boundary. However, the numerical implementation used in this work uses a staggered grid such that only the velocities are well defined on the boundaries. Thus, to ensure that the flow is divergence free at the outlet boundary condition, the pressure boundary condition is chosen to help enforce continuity as in equation 4.44.

$$\frac{1}{\rho(\phi)} \frac{\partial P}{\partial x} = -\frac{\partial u}{\partial t} - \mathbf{F_x} \tag{4.46}$$

The difficulty in implementing this wave generation method in the context of the numerical capabilities of this study is that the term $\frac{\partial u}{\partial t}$ is not known *a-priori* in an explicit time-stepping scheme. Either an implicit time integration scheme should be included or a scheme which uses collocated grids is necessary such that equation 4.45

can be applied directly. We suggest an implicit time integration scheme be included in future implementations. Unfortunately, this is not a trivial matter because an implicit time integration scheme with a moving free-surface that also includes surface tension effects becomes a nonlinear problem.

4.5.2 Influence of a Submerged Body

Another method of wave generation which was considered deals with the subject of quasi-steady breaking waves. A series of papers by Duncan [29, 30] as well as a paper by Lin and Rockwell [59] show that a train of waves will develop on the free surface behind a submerged object moving with constant velocity. Depending on the speed of the submerged object and its submergence depth, the first crest of this wave will form a breaker. Within the reference frame of the object, this is a quasi-steady breaking wave.

Quasi-steady breaking waves are thought to be yet another class of breaking waves with their own associated dissipation characteristics [29, 74]. Additionally, it is thought that, within the reference frame of a surface ship moving with constant velocity, the bow wave of a ship could be considered quasi-steady after it has broken off the bow and has entered the near-field flow. The validity of this point is in some contention after recent field experiments have shown that even in very calm seas there is an inherent unsteadiness in breaking ship waves [108]. This aside, there is an abundance of experimental and theoretical work on steady breaking waves with a few numerical works available. Thus, the capability of generating quasi-steady breaking waves in a small computational domain would be useful.

In developing this wave generation method, we propose that the actual object itself is not important to the wave generation. Only its influence on the surrounding fluid is important. Other numerical works have put significant effort into replicating the foil geometry used in Duncan's experiments and ensuring that the boundary layer was fully resolved around the foil in addition to the free-surface boundary [46]. This places a large number of points near the foil which could be used near the free-surface. Additionally, using a grid around the foil which accurately resolves the boundary layer

around the foil and adequately resolves the free surface is difficult.

One of the benefits of this numerical implementation is that the grid is Cartesian and the interface is captured in an Eulerian manner. Thus, including an exact replica of the foil geometry and ensuring that the foil boundary layer is adequately resolved would entail changing the grid or using body force techniques [109] to ensure a no-slip condition at the boundary. Even satisfying a free-slip condition about a geometry on a Cartesian grid is not a trivial manner [21]. If only the influence of the geometry is necessary to generate a quasi-steady breaking wave, than we propose that only the influence of the body is necessary to be modeled. Similar work by Iafrati and Campana [45] use a matched method where a viscous free-surface (level set) solver is matched to a boundary element method which then solves the potential solution for a submerged geometry. Within the boundary element method domain, there is no free surface making the solution relatively quick and the influence of the geometry is transmitted through the matching condition at the boundary.

A second approach to this method is one in which a distributed disturbance is placed in the viscous flow domain, beneath the free surface. No effort is needed to resolve the no-slip boundary condition on the geometry or to satisfy even a free-slip boundary along the geometry. This is done through the use of a distribution of Gaussian sources and sinks which mimic the presence of the body.

To add the disturbance to the flow field, the continuity equation is modified such that:

$$\nabla \cdot \vec{\mathbf{u}} = \sigma_d \tag{4.47}$$

where σ_d represents the effect of the disturbance. The (dynamic) pressure field is then decomposed into two parts. The first is the pressure field which would satisfy the continuity equation without the disturbance. The second is the correction which includes the disturbance.

$$P_d = p_1 + p_2 \tag{4.48}$$

Depending on the choice of implementation, the total dynamic pressure can be solved using a single Poisson equation or two separate Poisson solvers can be solved for each

part of the decomposed pressure. To keep the effect of the disturbance separate, we choose to solve two Poisson equations. The first is that given in equation 2.72 which satisfies a divergence-free velocity field. The second is simply:

$$\nabla \cdot \frac{1}{\rho(\phi)} \nabla p_2 = \sigma_d \tag{4.49}$$

The momentum equations are updated with both pressure fields as part of the time integration scheme.

$$\frac{\partial \vec{\mathbf{u}}}{\partial t} = \vec{\mathbf{F}} - \frac{1}{\rho(\phi)} \nabla (p_1 + p_2) \tag{4.50}$$

The choice of the disturbance is generally arbitrary since it is the effect of which we are looking to capture. As the disturbance is in the domain, something which is non-singular or desingularized is a prudent choice. To mimic the effect of a submerged geometry, a distribution of desingularized sources and sinks were used with variable strength. Borrowing from thin airfoil theory, the strength of the source/sink is made proportional to the slope of the thickness of a desired geometry. In this case, an ellipse was chosen yielding the following for the strength of the gaussian sources and sinks.

$$m(x) = -m_0(t) \frac{d}{dx} t(x) \tag{4.51}$$

where

$$t(x) = b \sqrt{1 - \frac{x^2}{a^2}} \tag{4.52}$$

The constant $m_0(t)$ is a scaling constant which can be used to determine the strength of the disturbance. The function of time is to allow the disturbance to be slowly "turned on". If this disturbance is placed in a free stream, it will create a wave train behind it similar to that seen in Duncan's experiments. Depending on the strength of the disturbance, it is possible to make the first wave break. Figure 4-5 shows a representative test simulation using this disturbance technique. This particular case

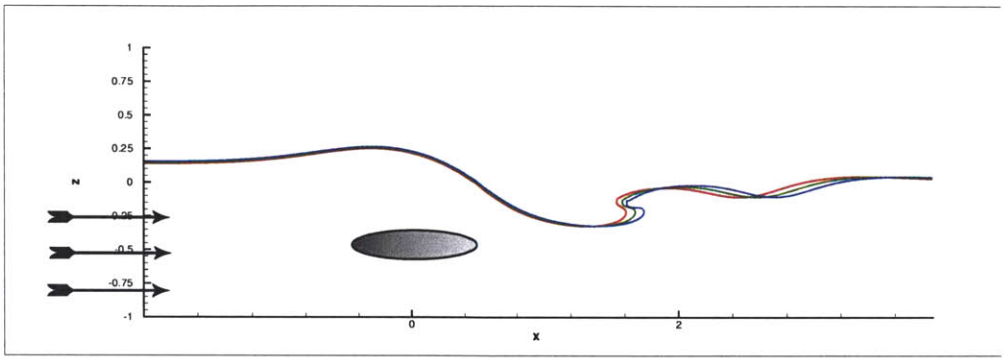

Figure 4-5: Successive free-surface profiles of the formation of a quasi-steady breaking wave in a wave train following a submerged disturbance using the body force technique. Flow is from left to right, ellipse is representation of mimicked ellipse geometry. $\mathcal{R}e_w = 500$, $\mathcal{F}r = 1$, $\mathcal{W}e = \infty$.

is at the start of forming a breaking wave on the first crest of the wave train behind the body. This body force technique has shown to be robust in generating a wave train behind it and shows promise in attaining a quasi-steady breaking wave train for the study of the characteristics and turbulent qualities of this type of wave.

4.6 Conclusions

In general, the method of initiating breaking waves for a computational study is a fairly undocumented process compared to experimental studies. This process is directly tied to the computational techniques involved and some methods may or may not translate well. As the technique used in this study entails a multi-fluid domain, additional complexity is involved as it is not well known how to initialize the air volume.

The techniques developed as a part of this study ranged from using no solution for the air volume and allowing it to react to the water volume to determining a solution for both volumes. Both methods generated breaking waves; however, the method which used some type of solution in the air was more reliable in decreasing the "noise" (or standing wave) in the simulation. Methods which used surface forcing to generate breaking waves were also robust in decreasing the influence of the standing

wave compared to the impulsively started Airy wave. However, the surface forcing technique can introduce standing wave components to solutions which have very little before the forcing is initiated. The surface forcing methods also simulate the effect of energy input to the progressive waves similar to that used to simulate wind forcing.

In addition to using surface forcing on progressive waves to generate wave breaking, the surface tension force is a reliable method for generating different types of wave breaking. By modifying the effective surface tension coefficient (modifying the Weber number while keeping all other parameters the same), waves which form spilling breaking waves will form plunging breaking waves instead. This allows a wider range of breaking waves to be studied using a single wave generation method.

In all, 36 waves were generated using the techniques described in this chapter. They ranged from non-breaking to plunging breaking waves with air entrainment. The benefits and limitations of the techniques were also discussed. In addition to the already cited standing wave "noise" which exists, the waves generated in this study are narrow banded in terms of spectrum and are only unsteady breaking waves. To address these last two limitations, a method which creates a broadband spectrum within a smaller domain such that simulating an entire wave tank is not necessary was outlined as was a method which can be used to simulate quasi-steady breaking waves. A preliminary result for a quasi-steady breaking wave was shown. These wave generation methods, including the future improvements outlined, should facilitate a wide-ranging (direct numerical) investigation of breaking wave kinematics and dynamics which includes viscous as well as air effects in the domain.

Chapter 5

Validation of the Level Set Method

This chapter details the validation effort for this numerical study. It verifies the robustness of the method for simulating surface impact and fluid re-entry problems. Once the method has been verified as robust for this class of problems, the volume, mass and energy conservation are detailed.

The volume conservation of the numerical method is defined as the conservation of the water volume throughout the simulation. The numerical method is found to conserve volume to within 0.2% which is an order of magnitude better than published level set studies. The mass conservation is determined as the amount of divergence in the flow field. For the entire domain, the numerical method conserves mass to machine accuracy. Point-by-point, the mass is conserved to the tolerance of the iterative Poisson solver for the pressure field.

Energy conservation is determined through two tests. The first is a standard test of comparing the viscous damping rate of a linear Airy wave to theoretical values. The numerical method was shown to agree with theoretical values. Because the viscous damping rate is relatively insensitive to the presence of surface tension and the presence of a second fluid, it was determined that this test was inadequate to confirm energy conservation. The second test includes the direct calculation of the energy equation to determine any residual energy losses. Through this second test, the energy conservation of the numerical method was found to be within 10% of the energy in the entire volume.

5.1 Surface Impact and Fluid Re-entry

The purpose of this set of validation tests focuses on the robustness of the level set method in handling surface re-entry problems. As plunging breaking waves are composed of a jet re-entry event, knowledge of the robustness of the method in the context of water impacting and re-entering a surface as well as the phenomena of droplet formation via pinch-off is essential.

This surface impact and re-entry test centered around the impact of a water droplet on a flat free surface. The physics of this canonical problem include all of the relevant issues of interest for this validation such as a moving bulk of water impacting the surface, entry of the impacting water into the bulk below, splash-up of the water surface after the impact event and droplet formation through pinch-off of the resulting splash. The impact of a water droplet on a quiescent surface has been the topic of a variety of studies for over a century [117]. The impact of a drop on a pool of fluid is the source of many high speed photography studies. The formation of the crown with droplets pinching off is a widely sought after picture amongst high speed photographers. The resulting sheet which splashes up after the drop impact contains tiny capillary waves and also ejects droplets back into the air. The ejected droplets are not only nice to look at, but have considerable effect on fluid transfer on the ocean surface during rain. Of particular scientific interest has been the formation of a vortex ring underneath the impact region as vorticity near the air-water interface effects a wide range of topics from the acoustic noise generated by rain to the effect on the gas-transfer rate at the ocean surface.

The purpose of this study was not to try and answer any of the questions posed in the available literature about this scientifically interesting and technically challenging problem. It was only to gauge the capabilities of the level set in modeling this problem. This problem was investigated using two formulations. The first uses the two-dimensional formulation and implementation outlined in chapters 2 and 3. The second is a basic implementation of an axisymmetric formulation based on the work of Sussman and Smereka [112]. The canonical problem begines as a circular drop

Simulation Parameters							
L	λ	η	$\mathcal{R}e_w$	$\mathcal{F}r$	$\mathcal{W}e$	γ_w	Δ
0.25	0.001	0.01	10,000	4	∞	~ 1	0.006

Equivalent Physical Parameters in Air and Water	
Diameter	Impact Velocity
$\sim$ 12.5cm	1.2 m/s

Table 5.1: Numerical parameters for the simulation of water droplet impact.

released from rest two diameters above the pool of still water which has a depth of only a diameter. The parameters involved for the flow are given in table 5.1. The boundary conditions for two-dimensional case are the same as the periodic wave tank described in chapter 2 in that periodicity is used horizontally and free-slip conditions are used on the vertical boundaries. For the axisymmetric case, the horizontal boundaries are represented by symmetry planes and the vertical boundaries are free-slip boundaries.

A time history of the two-dimensional case is shown in figure 5-1. As the drop begins to fall under the effect of gravity, vorticity begins to form in the air about the droplet which is seen in figure 5-1a. At this Reynolds number, it is not expected that the drop will deform any during its free fall. Thus, as it impacts the surface as in figure 5-1b, it is essentially circular. The vorticity in the air flow about the droplet shows signs of the formation of a separation bubble behind the droplet. The motion of the droplet towards the air-water interface causes vorticity to form just above the air-water interface. This vorticity is signed opposite of the vorticity which is along the surface of the droplet. The impact of the droplet on the surface causes this vorticity which formed at the air-water interface to be ejected horizontally. This ejection strengthens it considerably. The impulse of the droplet impact on the surface can be seen by the significant magnitude of the vorticity in the water at the impact point. The splash-up after the drop has entered the water surface can be seen in figure 5-1c. There is some amount of pinch off and droplet formation at the tips of the splash sheet (not shown). The large vortices which have curled over the splash sheet are from the vorticity which formed about the drop as it fell towards the water surface. The vorticity which lies along the inside of the sheet are the vortices which

formed just above the water surface as the drop moved towards the interface. Finally, in the water volume signs of paired vortices being injected into the bulk flow can be seen. However, as the tank depth was only a few diameters of the drop, these vortices do not penetrate very deep. The depth of the tank also contributes to the relatively high sheet splash-up verses the formation of waves propagating away from the impact area.

A time history from the axisymmetric case is shown in figure 5-2. In this case, the vorticity is not shown but two views of the air-water interface are shown. As the droplet impacts the surface, transverse waves can be seen to propagate away from the impact region. The surface begins to form a jet ejection at the impact point. However, the limited tank depth interferes again with the formation of the jet ejection.

Through the simulation of this canonical problem for water impact, the level set method proved to work exceptionally well for water re-entry problems without any special treatment of the surface at the point of re-entry. Sheet pinch-off and droplet formation were also evolved naturally without out any *ad-hoc* assumptions regarding the treatment of the surface in these cases. While the simulations are two-dimensional and without the effects of surface tension, the qualitative comparison to physical experience is good.

5.2 Volume and Mass Conservation

In the literature pertaining to the level set method, there is a large focus on "mass conservation". This mass conservation is related to the reinitialization of the level set function to a signed distance function minimizing the drift of the zero level set. In incompressible flows, mass conservation is related to satisfying the continuity equation as discussed in section 2.2.1. To avoid confusion in this work, we have called the mass conservation used in the level set community volume conservation as it is really is about maintaining the volume of each fluid throughout the simulation. The techniques used to conserve volume during the reinitialization process were discussed in detail in section 3.8. We will retain the definition of mass conservation as satisfying the

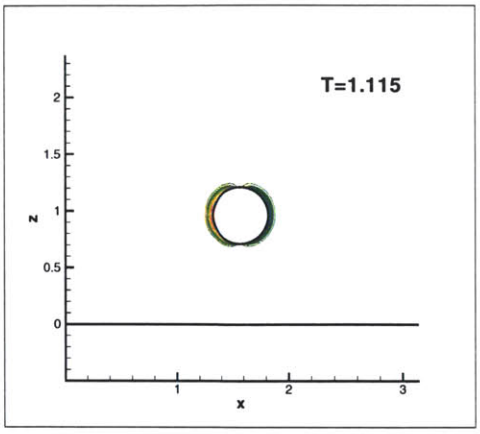

(a)

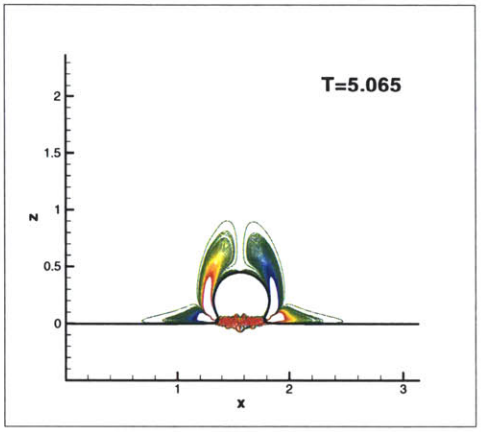

(b)

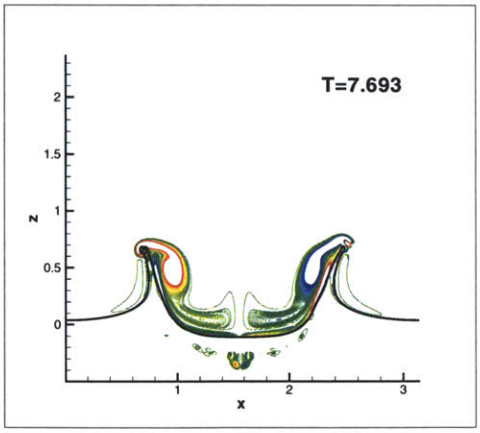

(c)

Figure 5-1: Time series of two-dimensional simulation of water droplet impacting flat surface. Black line represents the air-water interface. Color contours are transverse vorticity $-5 \leq \omega_y \leq 5$ from blue to red.

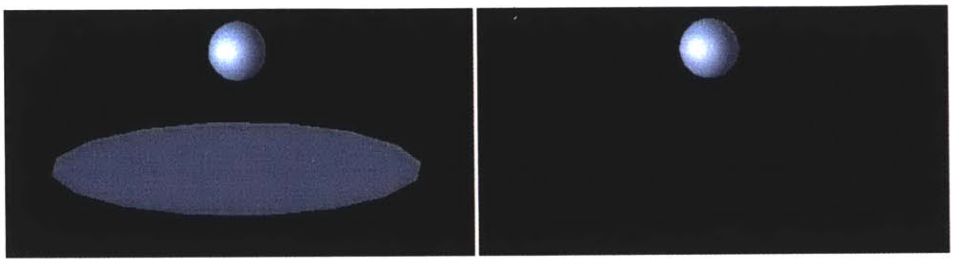

(a) T=0.000

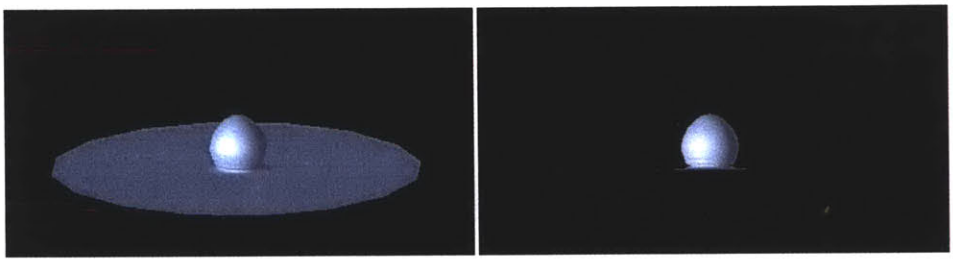

(b) T=5.029

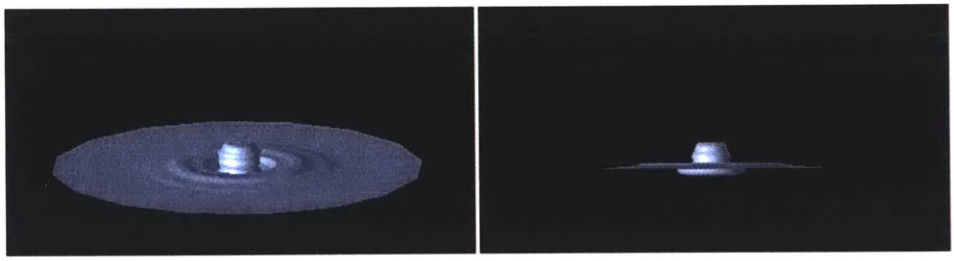

(c) T=6.138

Figure 5-2: Time series of axisymmetric simulation of water droplet impacting flat surface. Each pair is for the same time from a slightly different viewing angle.

continuity equation. This section reports the volume and mass conservation for the waves in this study.

As reported in section 3.8, techniques garnered from various authors regarding the reinitialization of the level set function were combined to provide superior volume conservation. It was reported there that this improvement reduced the amount of volume gained or lost by an order of magnitude. A representative spilling and plunging event were shown against the method generally used in the literature pertaining to the level set method in figure 3-10. Figure 5-3 contains the volume conservation for half of the waves done in this study. While not all of the cases are shown, the volume conservation for all of the waves in this study remains within the 0.2% cited in section 3.8. Careful study of figure 5-3 shows an oscillation in the volume conservation. The frequency of this oscillation is due to the fact that the reinitialization is only done after a number of time steps O(50-100). As stated earlier, the reinitialization is not done every time step only as a concession to balancing code performance with quality of volume conservation. Unfortunately, it is not possible to compare this volume conservation with the literature as the volume conservation is rarely reported. If it is reported it is generally on the order of 2-3%.

Figure 5-4 shows the maximum and total divergence of the flow field for the same waves shown in figure 5-3. The convergence tolerance of the pressure Poisson equation will be a factor of the maximum divergence in the entire flow field (water and air volumes) will be a factor of the convergence tolerance of the Poisson equation. This is because the solution of the pressure Poisson equation dictates the amount of divergence permissible in the flow field. If the Poisson equation was solved exactly for the pressure field, then the maximum divergence in the flow field would be to machine accuracy. However, as an iterative solver is used in this implementation, it will be dictated by the accuracy to which this is solved. The total divergence of the flow should be zero at every time step. This is because of the use of the compatibility condition in the solution of the Poisson equation dictates zero divergence in the integral sense. As seen in figure 5-4, the maximum divergence in the flow field is generally $O(10^{-7})$ for all of the cases considered. As the tolerance for convergence

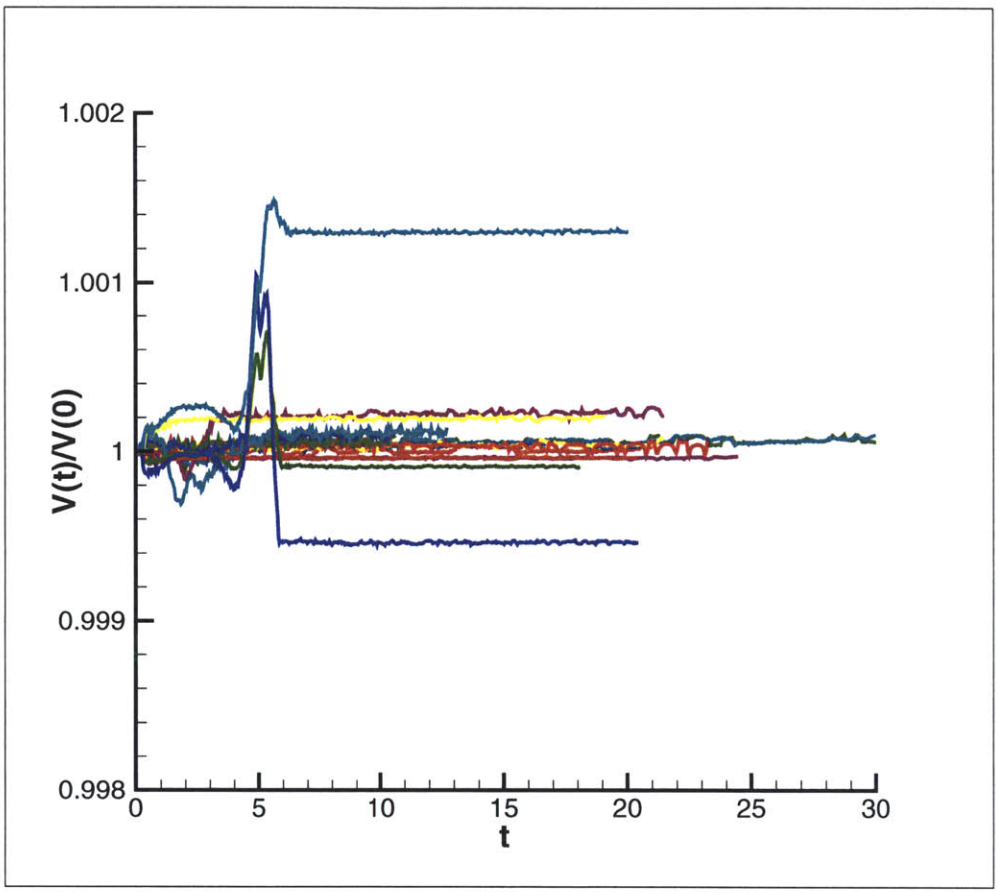

Figure 5-3: Volume conservation for the waves in this study over the entire length of the simulation. Outliers are case SFI-04 (upper) and SFI-11 (lower).

criteria of the pressure Poisson equation is the L_∞ norm of 10^{-8}. This is quite acceptable. The total divergence in the field for all of the cases considered is essentially machine accuracy.

5.3 Damping of Linear Waves

The purpose of this test is to provide validation for the damping of linear waves by viscosity as an initial measure of the numerical dissipation of the numerical implementation of this study. The method used here is a common method used for viscous flow solvers which include free surfaces. In the absence of surface tension and air, the amplitude of a linear wave will be damped out by only viscosity. An approximation of the damping coefficient using linear Airy waves appears in Lamb [57] and a modal analysis appears in Landau and Lifshitz [58]. Both show that the amplitude will behave as:

$$\epsilon(t) = \epsilon_0 e^{-\Gamma t} \tag{5.1}$$

where ϵ_0 is the initial wave amplitude and Γ is known as the damping coefficient. The non-dimensional damping coefficient for waves in a single fluid, using the wavelength as a length scale is:

$$\Gamma = \frac{8\pi^2}{\mathcal{R}e_w} \tag{5.2}$$

Chapter 4 includes a derivation for the two-fluid Airy wave solution which was derived in section 4.1.2. The simplified form of the damping rate (equation 4.30) is given here for reference.

$$\Gamma = \frac{8\pi^2}{\mathcal{R}e_w}\left(\frac{1+\eta}{1+\lambda}\right) - \frac{2\pi}{1+\lambda} f \sqrt{\frac{2\omega}{\mathcal{R}e_w}} \tag{5.3}$$

Equation 5.1 defines the amplitude envelope of the damped gravity wave. This damping rate is used in many of the forthcoming chapters to determine the laminar damping rate of the waves in this study. Thus, its applicability should be tested.

For this validation test, a non-breaking wave with little standing wave energy in the domain was chosen (case A2P-01). The Reynolds number for this case is, as it is for all cases in this study, 2000. Using the inviscid frequency of the wave as calculated

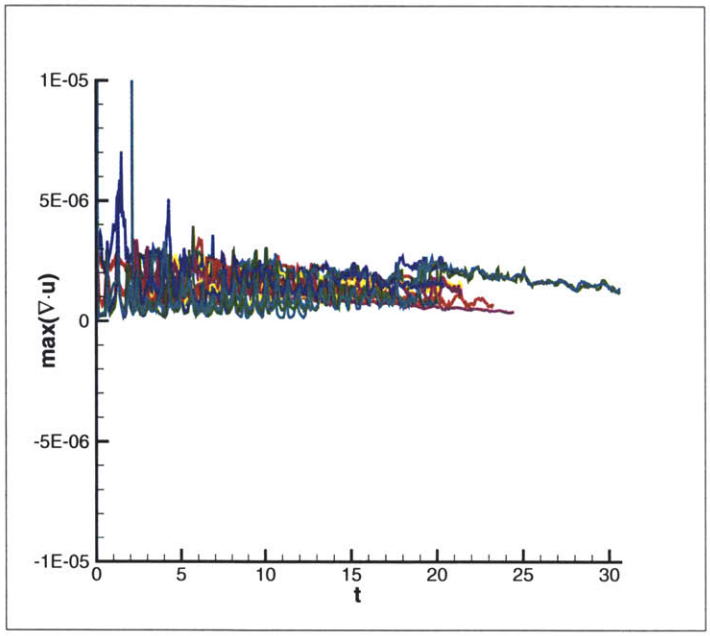

(a) Maximum divergence in volume

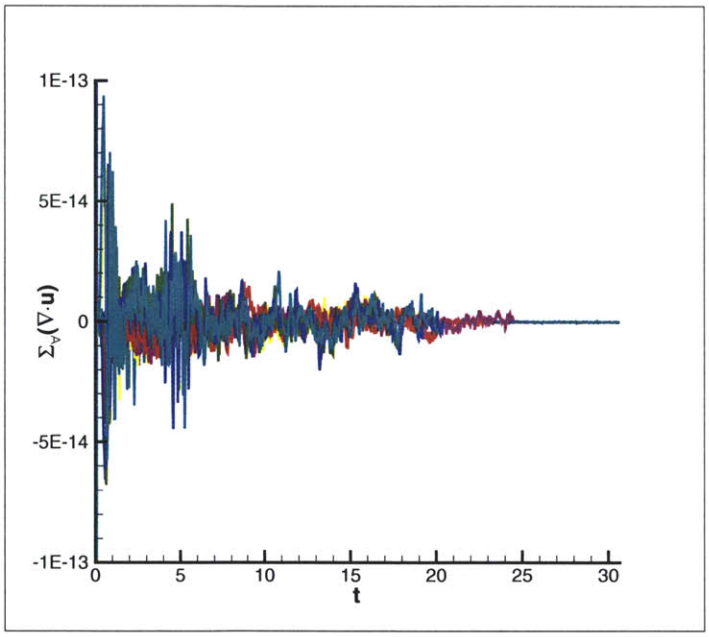

(b) Total divergence in volume

Figure 5-4: Maximum and total divergence of entire flow field for the waves in this study over the entire length of the simulation.

by equation 4.16, the damping rate for the two-fluid Airy wave is 0.0388. The damping rate for a single-fluid Airy wave based on equation 5.2 is 0.0395. The wave amplitude at a given point in the domain over time as a wave probe would measure a train of waves is shown in figure 5-5 along with the amplitude envelopes using both damping rates. It should be noted that the amplitude envelopes essentially lie on top of each other. Additionally, very little difference is seen if the actual frequency of the wave is used as calculated through a Fourier transform of the wave (not shown). However, the difference in the actual frequency of the wave and that given through the inviscid dispersion relationship is 0.9%. The small effect of the standing wave can be seen in the modulation of the amplitude during the decay of the wave in figure 5-5. This particular wave has a standing wave which represents 1.22% of the total energy in the wave. Despite the modulation by the standing wave, the damping of this two-fluid Airy wave is as predicted by theory.

The results of this validation test show that while the comparisons are good, the damping envelope is fairly insensitive to small changes in Γ. The Γ for a single fluid predicts the damping envelope as well as the first and second terms of the two-fluid solution. Thus, using this type of validation test for a rigorous check on energy conservation is not prudent. Another method is presented in section 5.4.

5.4 Energy Conservation

As discussed previously, the common method of gauging numerical verses viscous dissipation by studying the amplitude damping of a linear Airy wave is inadequate for multi-fluid flows. The issue revolves around the dominance of the term which is due to the water volume and inversely proportional to the Reynolds number. Unless the second fluid has a density and viscosity near that of the water, the amplitude envelope of the waves is fairly insensitive to the presence of the second fluid. Thus, to better understand the energy conservation of the numerical implementation in this study, a more rigorous check on the energy conservation is needed.

The method chosen for validating energy conservation was to begin with the equa-

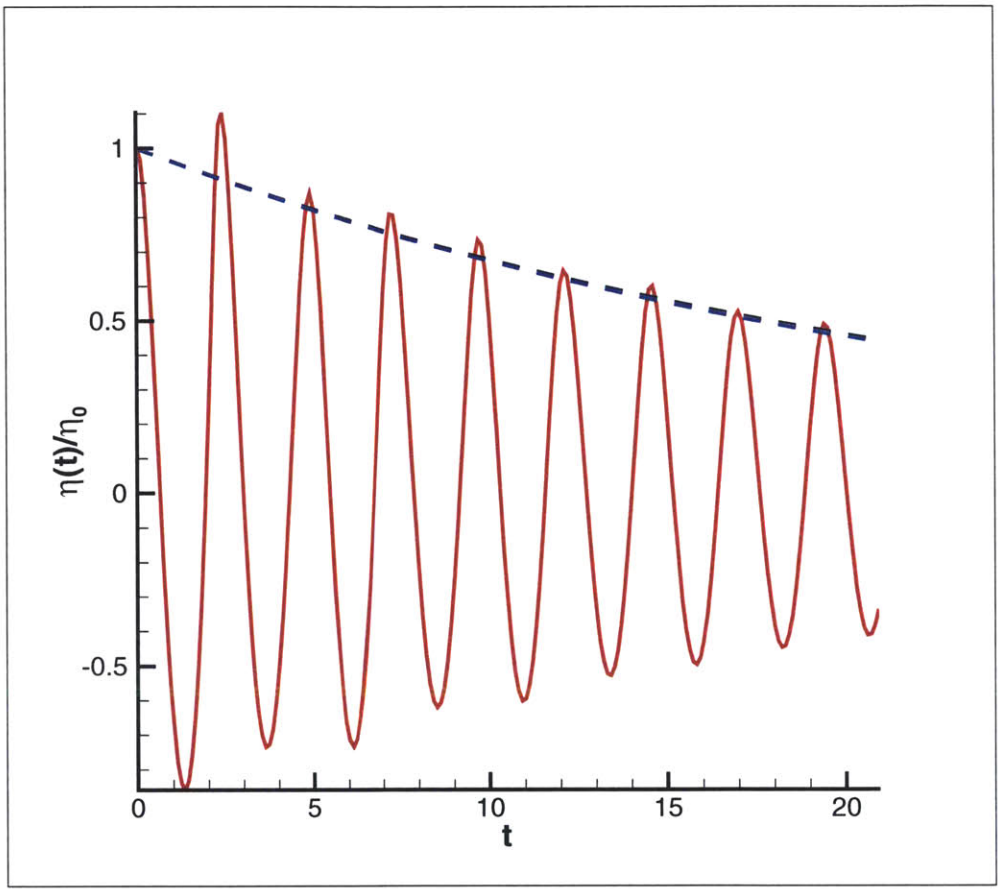

Figure 5-5: Amplitude of two-fluid Airy wave (case A2P-01) at $x = 0$ over the time of the simulation. Black line represents amplitude envelope using the two-fluid solution (equation 5.3). Blue line represents amplitude envelope using single-fluid solution (equation 5.2). Note that the blue and black lines lie on top of each other.

tion which governs the conservation of mechanical energy in the control volume. This was derived in section 2.4. The change in total energy per unit volume was defined in equation 2.61 using notation prevalent in the literature. It is given here for reference.

$$\frac{\partial E}{\partial t} + \nabla \cdot \vec{F} = \frac{1}{\mathcal{R}e_d}\left(\nabla \cdot \vec{\Sigma} - \varepsilon\right) + \vartheta \tag{5.4}$$

Integration of equation 5.4 over the control volume of interest, namely the entire computational domain yields:

$$\frac{\partial \overline{E}}{\partial t} = -\frac{\overline{\varepsilon}}{\mathcal{R}e_d} + \overline{\vartheta} \tag{5.5}$$

where the periodic and free-slip boundaries have been used to simplifity the equation and

$$\overline{\{\cdot\}} = \int_{\forall} \{\cdot\} \mathrm{d}\forall$$

To determine the energy conservation of the numerical method, a residual is defined based on equation 5.5 such that when zero, the numerical method conserves energy perfectly.

$$\frac{\partial \overline{E}}{\partial t} + \frac{\overline{\varepsilon}}{\mathcal{R}e_d} - \overline{\vartheta} = \mathbf{R} \tag{5.6}$$

The residual will include not only any energy losses due to the numerical implementation, but it will also include any numerical errors associated with the calculation of equation 5.6. This residual is the rate that energy is (or is not conserved). To equate this to an actual amount of energy lost throughout the simulation, the residual must be integrated in time using a cumulative integration:

$$\underline{\mathbf{R}}(t) = \int_{t_{ref}}^{t} \mathbf{R} \mathrm{d}t \tag{5.7}$$

Figure 5-6 shows the cumulated residual for all of the waves in this study over the

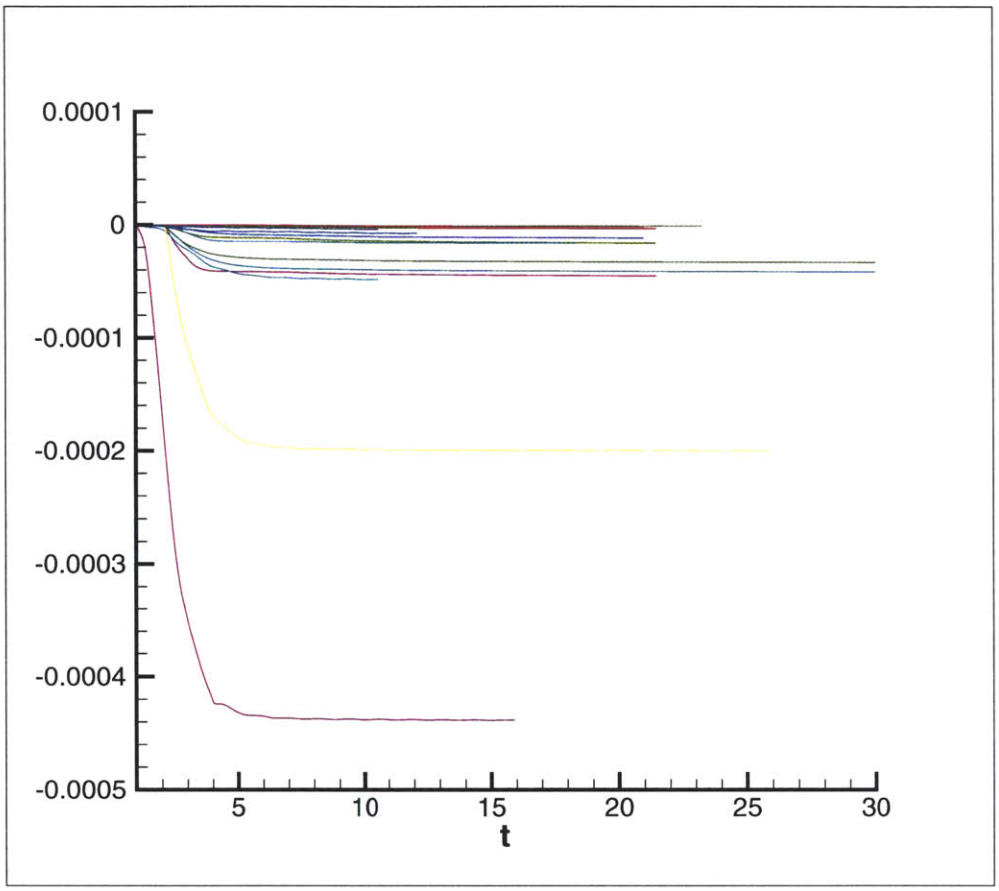

Figure 5-6: Cumulative energy lost over the entire simulation for the waves in this study.

entire life of the simulation. For all of the non-breaking cases, this residual is extremely small and relatively constant. As the breaking event becomes more violent, the residual increases with the maximum amount of energy lost to numerical effects occurring for cases where there is significant air entrainment.

The actual amount of energy lost during the entire simulation is only significant when considered against the amount of energy lost to the physics being modeled. Figure 5-7 shows the cumulative energy lost over the entire simulation as a fraction of the total energy lost in the volume over the same time period. It is shown against the amount of energy in the wave before breaking non-dimensionalized by the energy in the Stokes limiting wave. This is chosen as it is a useful measure of the breaking

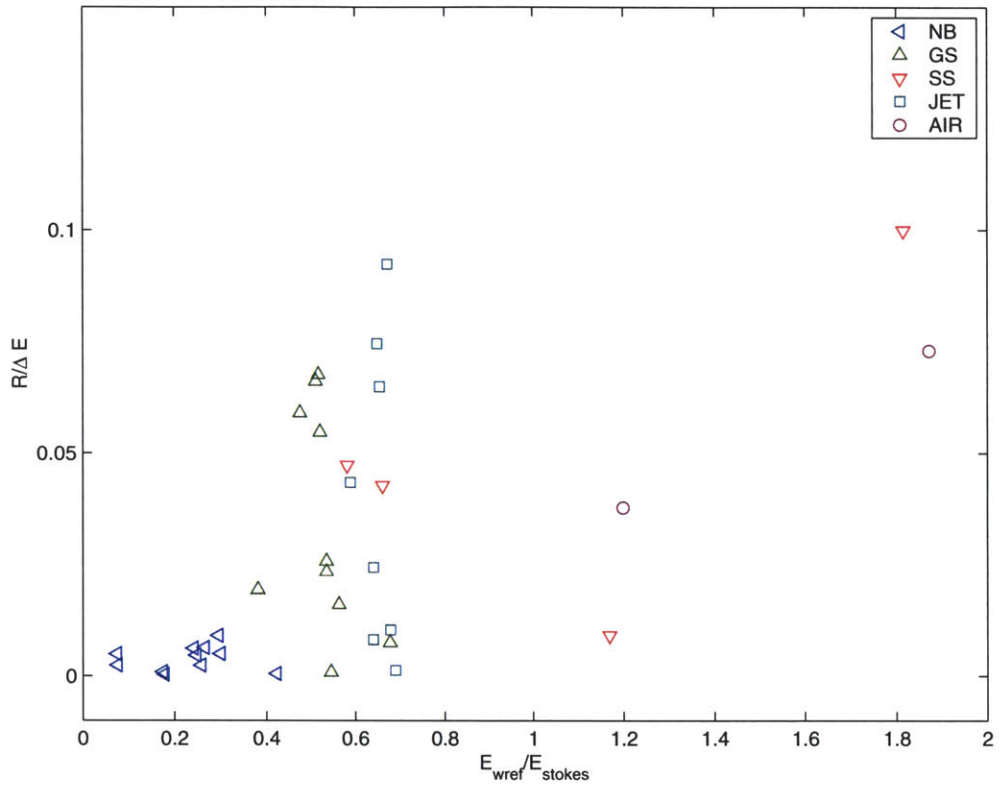

Figure 5-7: Cumulative energy lost over the entire simulation as a fraction of the energy lost to breaking during the simulation for all of the waves in this study. Plotted against amount of energy in the wave before the breaking event. ($\triangleleft$) non-breaking, ($\triangle$) gentle-spilling, ($\triangledown$) strong-spilling, ($\square$) jet formation, and ($\circ$) air entrainment.

strength of the wave in subsequent chapters. For all of the waves in this study, this is less than 10% meaning that the energy in the entire volume is conserved to within 10%.

A similar technique can be used to address the conservation of energy for a single fluid in the domain. In the case of the water volume, the residual is defined from equation 2.67. Integrating over the same control volume as before, the equation for the residual of the energy conservation in the water volume is:

$$\frac{\partial \overline{E}_w}{\partial t} + \frac{\overline{\varepsilon}_w}{\mathcal{R}e_w} - \overline{\vartheta}_w - \overline{\chi} = \mathbf{R_w} \tag{5.8}$$

Chapter 8 discusses the calculation of $\overline{\chi}$ extensively. In this chapter, it is determined

that direct calculation of $\overline{\chi}$ in this study has been polluted through the double booking of surface tension and surface forcing effects. Thus, because the residual in the water (and air) volumes is dependent upon the calculation of $\overline{\chi}$, the calculated residual for these volumes degrades for many of the waves in this study. The residual for the water volume using the direct calculation of the energy transfer rate at the interface is shown in figure 5-8 as a fraction of the total energy lost in the water volume over the breaking event. For many of the waves where there are stronger surface tension effects, such as the spilling breaking waves, the amount of energy lost to numerical error almost doubles. Thus, while less than 10% of the total energy lost in the entire volume, because of the poor calculation of the energy transfer at the interface using direct methods, the conservation of energy in the water volume during the breaking event is only to within 16%. This does not mean that the energy conservation for the water volume is poor. As the energy conservation of the entire volume is to within 10%, the water and air volumes are also conserved to within this amount. The significant residual calculation shown here only points to the poor calculation of the energy transfer between the two volumes.

5.5 Convergence

This section discusses the convergence of the numerical method. The grid convergence rate for a non-breaking and breaking wave in which all parameters are kept the same, except the grid resolution is discussed. As discussed in section 2.7, this includes the ratio of the viscous boundary layer to the level set boundary layer γ_w.

One must be careful in performing a grid convergence using a smoothed interface level set implementation. In section 2.7.1, we showed that the governing equations were a function of the level set boundary layer thickness (ϵ) or its relationship to the viscous boundary layer thickness (γ_w). The difference between the smoothed and sharp solution is a fixed quantity once a smoothed interface is chosen. The question becomes, what is the convergence of the smoothed governing equations? To this end, grid convergence tests must be done with a fixed interface thickness verses a fixed

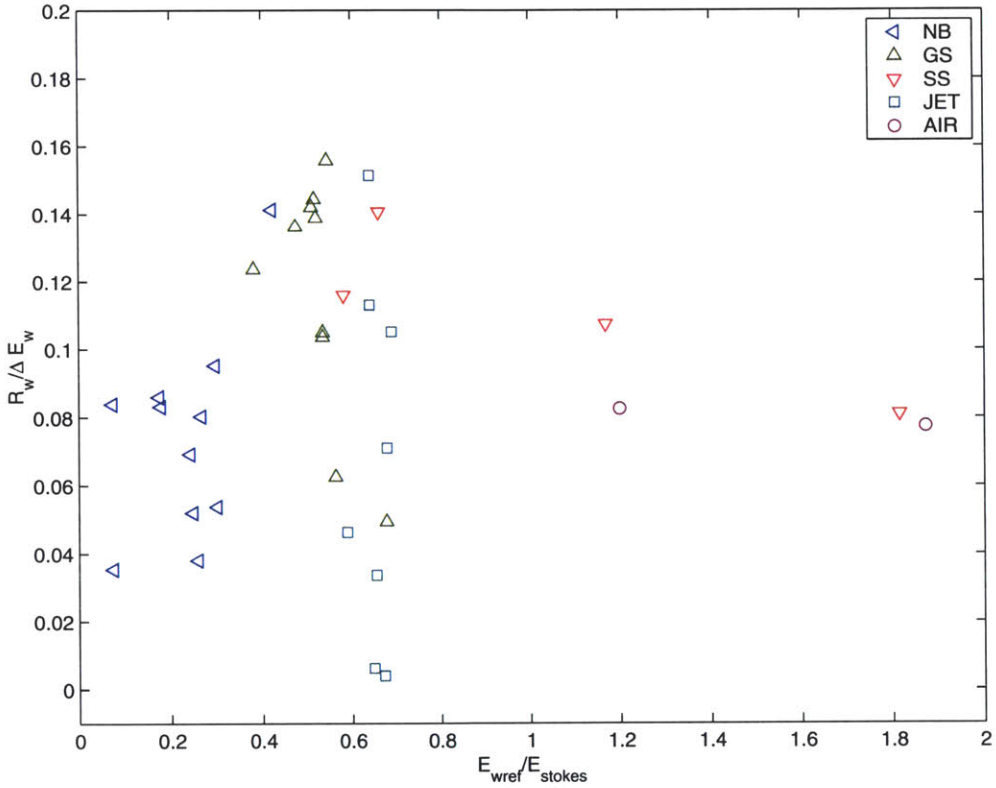

Figure 5-8: As in figure 5-7 except for the water volume only.

	Grid 1	Grid 2	Grid 3
N	65,536	102,400	262,144
% Volume Conserved	0.0043%	0.0033%	0.0005%
Slope Parameter	0.3345	0.3315	0.3272
Fraction E_w lost due to breaking	0.0140	0.0148	0.0154
Fraction viscous losses which are laminar	1.059	1.063	1.065
Fraction of energy lost transferred through interface	0.0428	0.0458	0.0489
Fraction of energy lost due to numerical error	0.00656	0.00453	0.00262

Table 5.2: Grid convergence for a non-breaking wave.

number of points in the interface. In the literature, the number of points over which the interface is smoothed is usually given as a fixed parameter. Thus, only modifying the grid spacing with a fixed number of points in the smoothed region as part of the grid convergence test actually poses different problems instead of trying to converge a single solution.

The first example of grid convergence can be seen in section 2.7 in the canonical problem of the vortex pair rising to the interface. Figures 2-9 and 2-10 show a grid convergence test which involved the modified level set function. The ratio between the level set boundary layer and viscous boundary layer is kept constant as the grid is refined and convergence can be seen in the profile of the interface and the vorticity at the interface.

The convergence for the non-breaking wave is performed as follows. Case SFI-07 is run at three resolutions. This case is a non-breaking wave at Reynolds number 2000 and an infinite Weber number. Various quantities are given for the respective resolutions in table 5.2. All of the quantities improve as the grid resolution increases. In particular, the volume conservation increases drastically and the residual energy lost throughout the simulation decreases as the grid is resolved.

The convergence for the breaking wave is performed in a similar manner for case SFI-09. This case is also at a Reynolds number 2000 and an infinite Weber number. In fact, case SFI-09 is case SFI-07 with a slightly larger surface forcing amplitude. The same quantities shown for the non-breaking wave in table 5.2 are given for the breaking case in table 5.3. As in the non-breaking case, volume conservation increases

	Grid 1	Grid 2	Grid 3
N	65,536	102,400	262,144
% Volume Conserved	0.131	0.055%	0.050%
Slope Parameter	0.7076	0.6938	0.6785
Fraction E_w lost due to breaking	0.2470	0.2278	0.2095
Fraction viscous losses which are laminar	0.5093	0.5756	0.6517
Fraction of energy lost transferred through interface	-0.2811	-0.3180	-0.3667
Fraction of energy lost due to numerical error	0.05514	0.0648	0.0845

Table 5.3: Grid convergence for a breaking wave.

with increasing grid resolution. In fact, except for the energy lost due to numerical error all of the quantities shown improve with increasing resolution. The numerical error increases for each increasing resolution of the breaking wave. The exact reasons behind this are not clear. One possible reason is that, while the parameters of the simulation (γ_w and wave forcing), the resulting wave slopes before breaking are different. Thus, each breaking wave is slightly different and convergence is hard to judge.

5.6 Conclusions

The validation of the numerical method was presented in this chapter. First, the robustness of the numerical method for simulating a water drop impacting a flat free surface was considered. This test was used to determine the capability of the level set method for flows with surface re-entry. Robustness in this area is critical for the simulation of plunging breaking waves. The method proved to be highly adept at simulating this phenomenon without any special treatment at the impact point.

Once the robustness of the method was established the volume and mass conservation of the implementation was established for all of the waves in this study. The numerical method proved to conserve mass for the domain to within machine accuracy. The volume of water simulated was also conserved to within 0.2% for all of the waves considered. This volume conservation is an order of magnitude less than what is established in the literature.

The numerical dissipation of the implementation was also established. The first attempt to determine this was done through the simulation of a plane progressive wave which does not break. The damping of the amplitude of the wave was compared to theory developed in chapter 4. However, it was determined that while this type of validation may be adequate for single fluid simulations, the effects of the air have little effect on the amplitude envelope derived from theory. Thus, it would be difficult to tell whether or not the energy conservation of both fluids is sufficient.

A second method involved the calculation of the energy equation for the entire volume. The residual of this calculation (left-hand side minus right-hand side) presents the amount of energy lost during the simulation to numerical dissipation and any errors associated with the energy calculation itself. The residual was shown as a fraction of the total amount of energy lost in the volume. For all of the waves in this study, this quantity was less than 10%. A similar residual calculation was shown for the water volume only. This residual calculation is dependent upon direct calculation of the energy flux rate term discussed in chapter 8. As discussed in chapter 8, there are issues regarding direct calculation of this term at this time. Thus, the energy conservation calculation for the water has more associated errors which is reflected in the larger residuals for this volume. However, as the total volume calculation shows an energy conservation of over 90% for all of the waves in this study, the numerical implementation is considered to have adequate energy conservation.

Finally, a grid convergence study was presented. For the canonical problem of a vortex pair interacting with a free surface, the convergence of the implementation was established. The convergence rate for a single breaking and non-breaking wave was also discussed.

Chapter 6

Kinematics and Dynamics of Breaking Waves

This chapter focuses on the kinematics and dynamics of breaking waves. While this is a large field of study encompassing many relevant length and time scales, this work focuses on the geometry, velocity field and surface stresses as they pertain to the moderate length scales in this study. Of all of the areas of study, crest geometry has received the most attention in the literature over the past two decades due to its ease of measurement. Information regarding the velocity field is significantly sparser, especially near the surface and in the free-surface boundary layer as well as in the breaking region itself. This is particularly the case for plunging breaking waves where very little about the kinematics is known after the plunging event where the entrainment of air and three-dimensional turbulent nature of the field makes measurements difficult.

For crest geometry, the most cited body of work is that by Bonmarin [8] which uses multiple breaking wave generation techniques to generate an ensemble of breaking waves and reports the evolution of seven geometric parameters up to breaking and, if possible, during the breaking event for both spilling and plunging breaking waves. The work of Duncan *et al.* [28] also details the crest evolution up to and through the breaking event for gentle-spilling breaking waves.

While the geometry of breaking waves through the breaking event is relatively well

documented, until just recently, very few experiments have tackled the difficult task of measuring the velocity field in the breaking region. For gentle-spilling breaking waves, Qiao and Duncan [90] provide a clear description of the velocity field throughout the breaking event. Perlin *et al.* [85] provide velocity measurements of a plunging breaking wave prior to breaking and recent velocity field measurements by Melville *et al.* [77] look at the large scale effects of breaking waves on turbulence and the formation of coherent structures. While it is not part of this study, it should be noted that more progress has been made in measuring the velocity field of steady breaking waves [59, 16].

In general, most experimental studies focus on the spectral evolution of the breaking waves to deduce information regarding the kinematics of wave breaking. Because of the Reynolds numbers involved at the laboratory scale, the spectrum gives a fairly accurate idea of the flow field and energy providing assumptions regarding equipartition of the energy and linear flow apply. In the context of pre-breaking build-up and well after post-breaking, this technique is sound for wave groups in the laboratory setting.

In theory, numerical simulations have the capability of providing both the surface and velocity field evolution of breaking waves. Yet until recently, the methods have been limited by either the physics being modeled (inviscid flows) or the numerical method employed (surface re-entry). Numerical efforts which use inviscid techniques include Dommermuth *et al.* [24], Longuet-Higgins and Cokelet [68, 69], and Tulin *et al.* [122, 115, 119]. Because simulating the surface re-entry problem is so difficult, there are relatively few simulations which go past the breaking event for plunging breaking waves.The recent techniques which include viscous effects and surface re-entry are Iafrati and Campana [45] and Chen and Kharif [13].

This chapter uses the waves in this study to address the kinematics and dynamics of spilling and plunging breaking waves. Section 6.1 details the spilling breaking waves in this study by considering a representative case of a gentle-spilling and strong-spilling breaking wave as defined in chapter 4. The evolution of the free-surface is detailed along with the characteristic velocity, vorticity field, and vorticity flux. De-

tailed comparisons to what is expected from experimental measurements is discussed. The stresses in the wave throughout the breaking event are shown. The sources of vorticity and stresses in the wave are shown to be essentially curvature effects due to the deformation of the surface during the breaking event.

Section 6.2 deals with the plunging breaking waves in this study by focusing on the formation of the jet, its breakup and re-entry into the front of the wave crest, and the entrainment of air when applicable. It also details the velocity, vorticity and stresses of the wave during the jet formation and the jet re-entry/breakup phases. The air entrainment is briefly discussed within the context of the bounds of this study. As the waves in this study are purely two-dimensional and the air is incompressible, quantifying the concepts of bubbles and bubble dynamics is outside the scope of this work. However, general comments and a qualitative discussion on the air entrained is included at the end of this section.

Section 6.3 details the spectral evolution of a variety waves in this study. It includes a comparison between non-breaking and breaking waves from incipient to plunging. Qualitative comparison to the generally accepted results in the literature is included. As wave focusing experiments generally contain broadband spectrums, the comparison is qualitative mainly due to the narrow bandwidth of the waves in this study. We have found that, in general, there is a shift in energy from low to high wavenumbers in the pre-breaking buildup. This shift of energy is represented by the steepness in slope developed before the breaking event. Within a few wave periods after the breaking event, there is a loss of energy at all wavenumbers. The loss of energy is much more significant at the higher wavenumbers.

6.1 Spilling Breaking Waves

A comprehensive review of spilling breaking waves is contained in a review paper by Duncan [31]. During a spilling-breaking event, a "bulge" generally forms on the front face of the wave surface. This bulge is accompanied by a train of small capillary waves located at the bottom of the bulge on the wave face (or toe). Shortly after the

bulge forms, it separates from the crest of the wave and moves down the face. This motion of the bulge leaves a region of surface turbulence in its wake as well as the presence of larger capillary waves.

The train of capillary waves at the toe of the bulge has received considerable attention in the literature. In particular, Longuet-Higgins postulates that the capillary waves generate a shear flow at the toe of the bulge [66, 65]. This shear flow quickly becomes unstable and causes the bulge to separate from the wave crest and move down the face. According to Longuet-Higgins theory, the presence of the capillary waves at the toe is essential for the bulge to move along the face of the wave unless the velocity field separates from the front face of the wave due to surface curvature effects. In fact, it has been reported that there is no flow reversal (or separation) in the wave up until the bulge moves along the face of the wave [90]. The only cases reported in the literature in which flow reversal exists and the bulge did not move relative to the wave crest were waves which were quasi-steady in nature, such as the wave train behind a towed submerged hydrofoil [30].

In chapter 4, we classified spilling breaking waves into two types – gentle and strong. Both types of spilling breaking waves are characterized by a steepening of the surface and a localized region of increased energy at the crest. In a predominance of the spilling breakers in this study, the steepening of the surface results in the formation of the bulge on the wave crest as reported in the literature.

Figures 6-1, 6-2, and 6-3 show three stages of breaking for a spilling breaking wave in this study. Also included in the figures are contours of transverse vorticity. The first stage is a developmental stage (figure 6-1) where the bulge forms on the front face of the wave. While it is not necessary for surface forcing to generate the breaking wave, it is noted that in this particular case, the bulge forms during the forcing phase. Before the bulge forms, there is little or no vorticity in the water flow and a small amount of vorticity in the air due to the flow over the crest and trough. As the bulge forms on the front face of the wave, a region of positive vorticity in the water flow forms at the toe and significant vorticity develops in the air flow at the crest.

The second stage is the breaking stage (figure 6-2). During this sustained breaking

stage, the bulge and toe are relatively stationary on the wave face and there is little change in the vorticity in either fluid. Recalling the descriptions by Duncan and Longuet-Higgins, the lack of motion by the bulge is different than what is seen in experiments where the bulge separates from the crest and moves down the face of the wave. At this point, it is not entirely clear why this is the case. However, the reasons which may be responsible for this phenomena are discussed in detail later in this section.

The third stage is a "dissipating" stage (figure 6-3) where the wave is returning to a less energetic wave with little vorticity and curvature to the surface. This stage sees a decrease in strength of the vorticity in the bulge and on the wave face. The air-water interface begins to lose its characteristic bulge until it returns to a symmetric plane progressive wave with an overall decreased amplitude. As the bulge did not separate from the wave face and move relative to the wave crest, there is very little turbulence or vorticity in the flow field after the breaking event.

With figures 6-1 through 6-3 in mind, this section discusses the evolution of the air-water interface for both gentle- and strong-spilling breaking waves. The velocity and normalized stress profiles are considered to elucidate the characteristic kinematics and dynamics of the field. The vorticity field is examined as well as the sources of vorticity through consideration of the vorticity flux at the surface.

6.1.1 Evolution of the Air-Water Interface

This section discusses the evolution of the air-water interface for the spilling breaking waves in this study. The formation of the bulge in the spilling breaking waves is shown in figure 6-4 for both gentle-spilling and strong-spilling breaking waves. From a typical sinusoidal profile, there is an increase in crest elevation and decrease in the trough depth prior to the bulge formation. The formation of the bulge is apparent in both profiles during the breaking event; yet the strong-spilling waves have a more pronounced bulge with larger curvature which lasts longer than the gentle-spilling waves.

Bonmarin [8] also notes a change in crest elevation and trough depth prior to wave

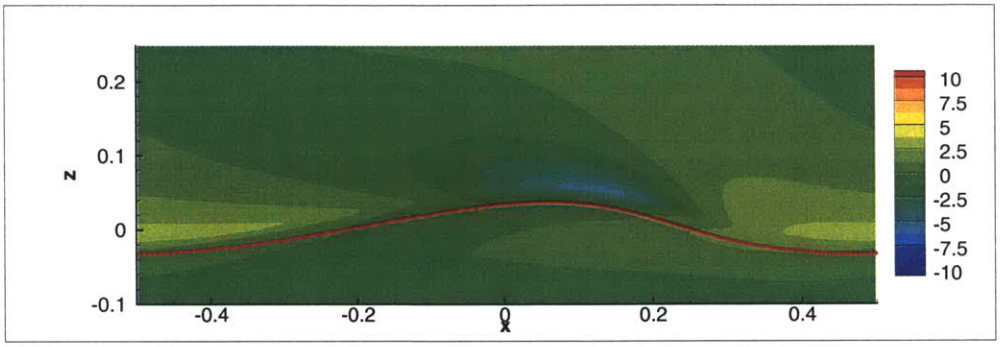

(a) $t = t_1$

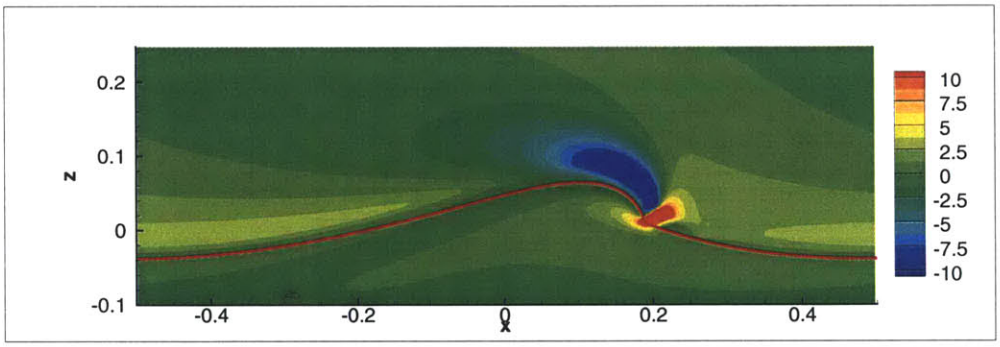

(b) $t = t_1 + 0.35T$

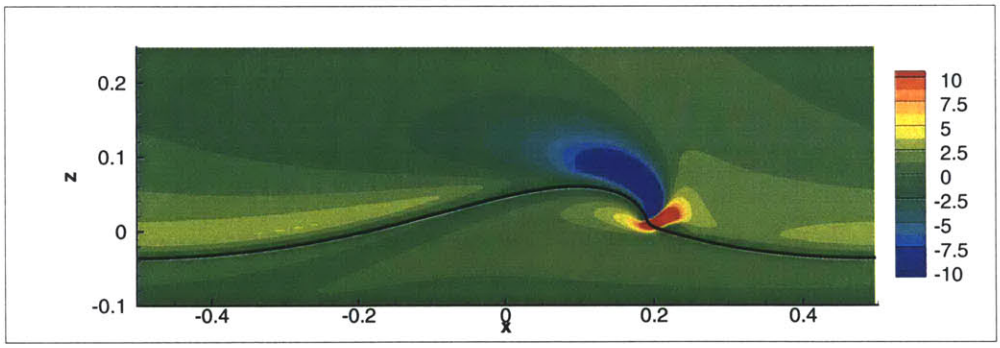

(c) $t = t_1 + 0.47T$

Figure 6-1: Time evolution (development) of a spilling breaking wave (case A2P-02) with transverse vorticity contours shown. Interface is represented by red line if surface forcing exists and black line if it does not. Nondimensional theoretical wave period (T) is 2.57.

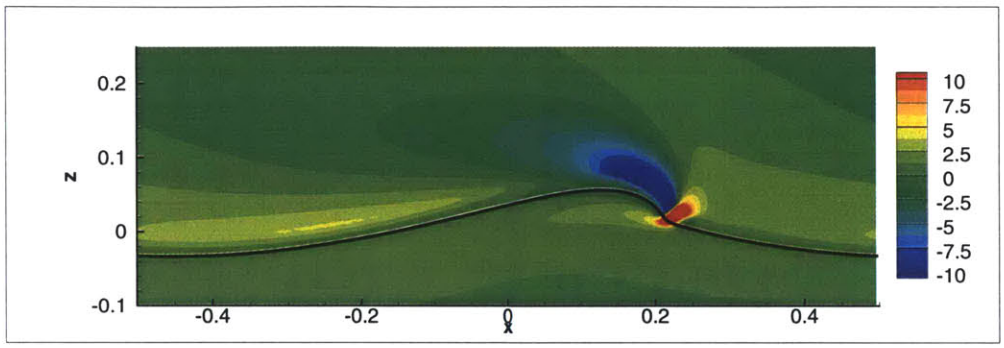

(a) $t = t_1 + 0.85T$

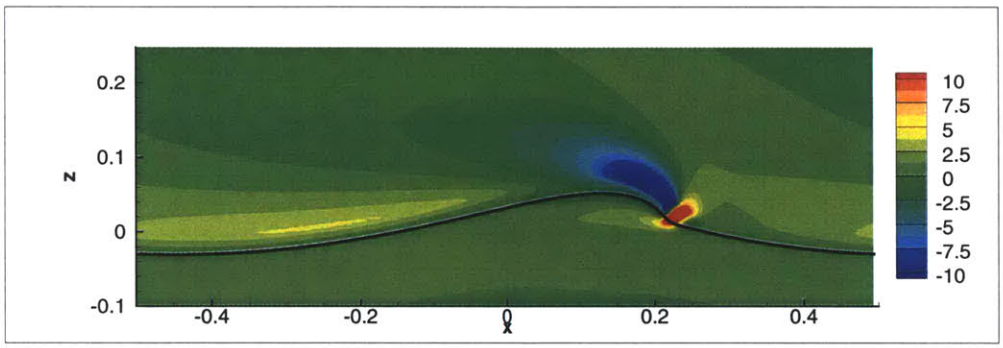

(b) $t = t_1 + T$

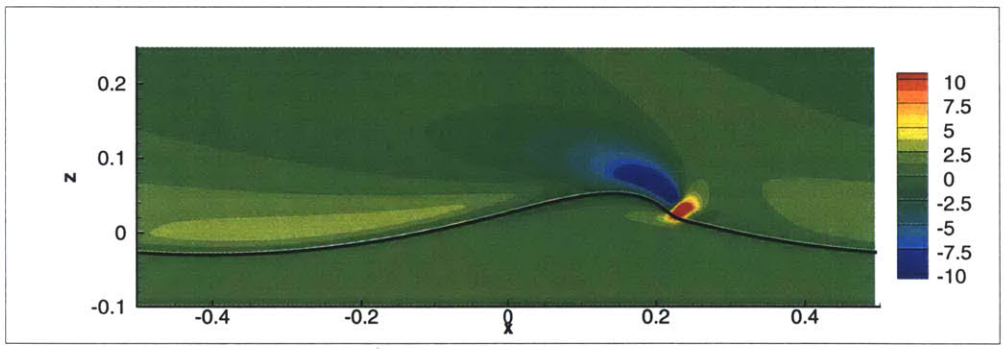

(c) $t = t_1 + 1.24T$

Figure 6-2: Time evolution (breaking event) of a spilling breaking wave (case A2P-02) with transverse vorticity contours shown. Interface is represented by red line if surface forcing exists and black line if it does not. Nondimensional theoretical wave period (T) is 2.57.

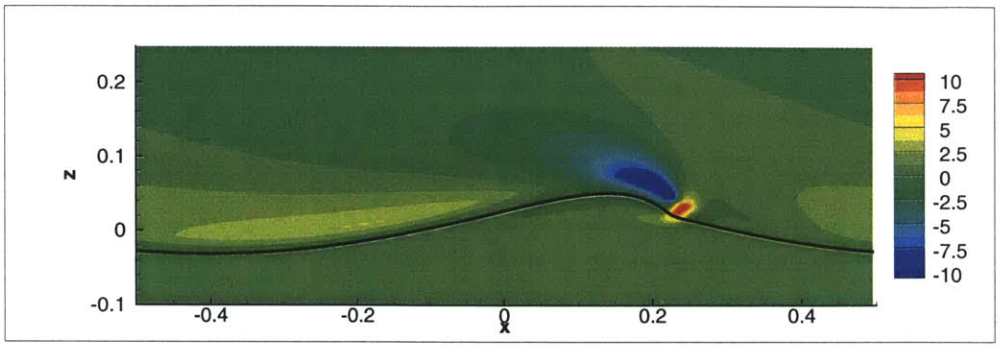

(a) $t = t_1 + 1.40T$

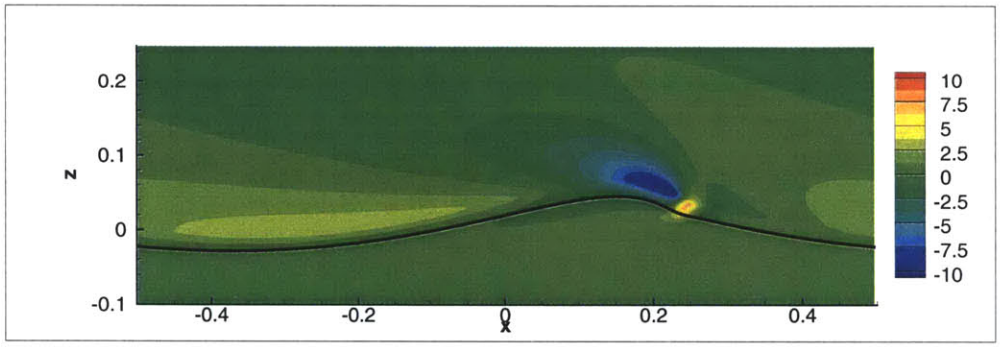

(b) $t = t_1 + 1.63T$

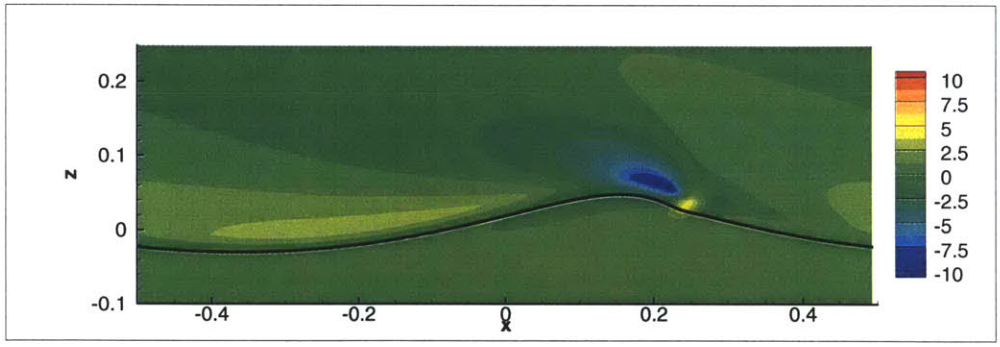

(c) $t = t_1 + 1.79T$

Figure 6-3: Time evolution (dissipating) of a spilling breaking wave (case A2P-02) with transverse vorticity contours shown. Interface is represented by red line if surface forcing exists and black line if it does not. Nondimensional theoretical wave period (T) is 2.57.

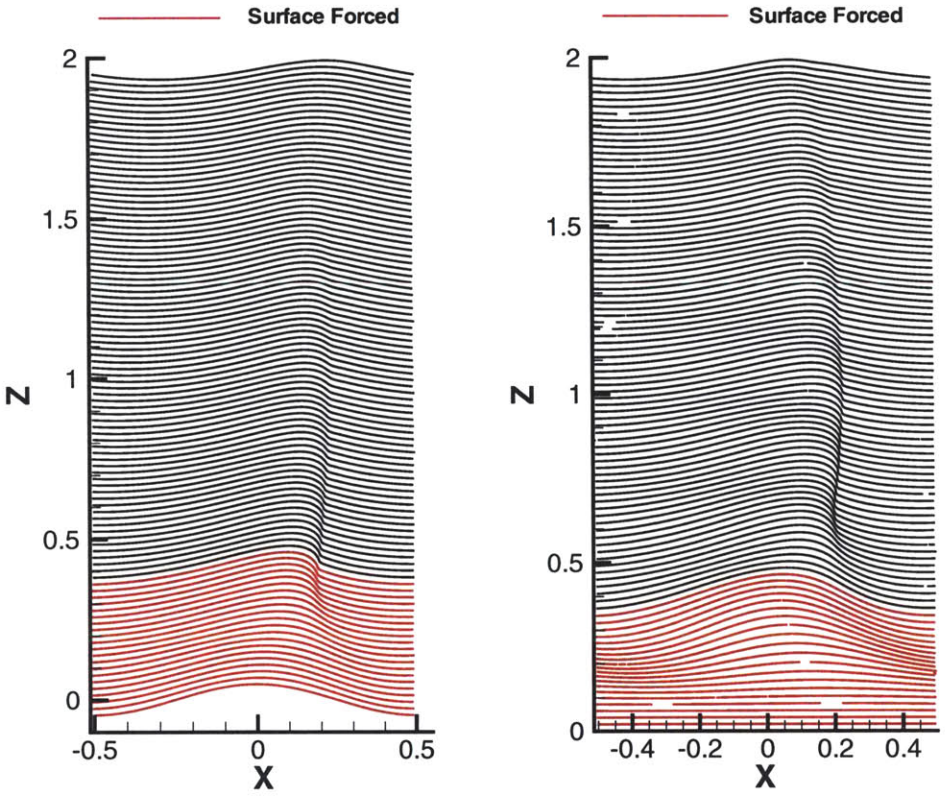

(a) gentle-spilling

(b) strong-spilling

Figure 6-4: Waterfall profiles of gentle-spilling (case A2P-04) and strong-spilling breaking waves (case SFI-10). Successive vertical profiles (every $\Delta t = 0.1$) are offset by $\Delta z_{off} = 0.02$. Red surface profiles are times when surface is being forced.

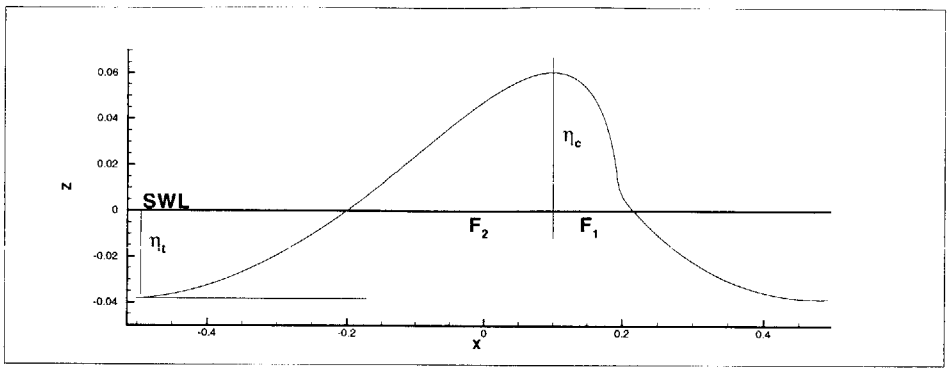

$$H = \eta_c + \eta_t; \quad \mu = \eta_c/H; \quad \lambda = F_2/F_1; \quad \epsilon = \eta_c/F_1; \quad \delta = \eta_c/F_2$$

Figure 6-5: Definitions for four asymmetry parameters.

breaking. Longuet-Higgins and Cokelet [69] showed approximately 20% increase in crest elevation and decrease in trough depth for a wave of initial steepness of 0.28 just prior to breaking onset. This is also seen in the waves in this study. For example, the gentle-spilling breaking wave shown in figure 6-4a has a 25% increase in crest height and 20% decrease in trough depth just prior to the breaking event.

In addition to the change in height and depth of the crest and trough of the wave, the wave evolves from an initially symmetric sinusoidal shape to an asymmetric shape. The asymmetric shape appears before the bulge formation. Kjeldsen and Myrhaug [50] defined four parameters to describe the asymmetry of a wave profile: a horizontal asymmetry factor μ, a vertical asymmetry factor λ, and a crest front and rear steepness ϵ and δ, respectively. Figure 6-5 defines these parameters. Bonmarin [8] reports a range of these parameters for the breaking waves in their experimental study. The waves in this study fall within the ranges of what is seen in Bonmarin's study for all four parameters. This is shown in table 6.1.

Table 6.1:

Comparison of wave asymmetry parameters to experimental data.[1]

Parameter	Minimum	Maximum	Mean	Value
(a) μ: Horizontal asymmetry				
Experiment	0.59	0.91	0.75	-
Gentle-spilling Wave				0.61
Strong-spilling Wave				0.58
(b) λ: Vertical asymmetry				
Experiment	0.78	2.37	1.38	-
Gentle-spilling Wave				2.43
Strong-spilling Wave				2.40
(c) c: crest front steepness				
Experiment	0.24	0.68	0.41	-
Gentle-spilling Wave				0.49
Strong-spilling Wave				0.54
(d) δ: crest rear steepness				
Experiment	0.19	0.42	0.31	-
Gentle-spilling Wave				0.20
Strong-spilling Wave				0.22

[1] Experimental data from Bonmarin [8] table 4; Gentle-spilling wave (A2P-04); Strong-spilling wave (SFI-10).

What is not seen in the free-surface profiles in figures 6-1 through 6-4 or any of the spilling breaking waves in this study is the train of capillary waves at the toe of the bulge. Nor does the bulge appear to separate from the crest and move down the front face of the wave. In all of the spilling breaking waves in this study, the bulge forms and then dissipates without any relative motion to the wave crest.

There are a few possible reasons as to why the capillary wave train appears in experiments and some simulations but does not appear in this study. The first is that

the physical length scale of the waves considered in this study is relatively small (0.1 cm) compared to the experiments (1 m). Longuet-Higgins [66] reports, that for waves which the wavelength is on the order of 1 m, the capillary wavelength is on the order of 5-50 cm . This reported capillary wavelength is well above the primary wavelength of the waves in this study by at least an order of magnitude. There are no published experimental results of waves at this wavelength. Thus, it is not clear if waves of this size see a wave train at the toe near the bottom of the bulge.

Second, if such a wave train were to exist for waves of this scale, it is uncertain if the simulations performed in this study would resolve them. Consider the waves generated by Duncan [28]. The primary wavelength of the generated wave was 0.789 m which resulted in a capillary wavelength of 0.38 cm. Relatively speaking, based on the wavelength of the main wave in the simulations, the capillary wavelength which would result would be about 35 μm. This wavelength is unfortunately smaller than the smallest resolved wavelength (45 μm) in this study. Thus, if waves of primary wavelength on the order of 0.1 cm do indeed form a secondary wave train near the bulge during the breaking event, the resolution of these simulations was not sufficient to detect their presence.

Third, the moderate Reynolds number of the waves in this study ($\mathcal{R}e_w = 2000$) damps out the small capillary waves before they are formed. Consider the wavelength seen in Duncan's experiments of 0.789 m. A pseudo-viscosity for this wavelength at a Reynolds number of 2000, is $O(10^{-3})$. The capillary waves in Duncan's experiment are 0.38 cm. Using this pseudo-viscosity, the Reynolds number for the capillary wave is $O(10^{-1})$. Based on equation 4.30, the damping rate of these capillary waves is O(100) which is four orders of magnitude larger than the primary wave. Based on the wavelength and frequency of the capillary waves, the waves would be damped out in a single capillary period because of the increased dissipation from the pseudo viscosity.

The fourth reason is purely numerical. It is not clear if the smoothed interface has an effect on the formation of the capillary waves. Based on these four arguments, the characterization of the presence and effect of the capillary wave trains seen in

experiments is considered outside the scope of this study.

The evolution of the free-surface during the spilling breaking event up until the bulge movement compares well to what has been presented in the literature in terms of the geometry and behavior. The absence of a capillary wave train is disappointing as no direct comparison can be made to existing experiments. However, its absence, combined with the lack of movement of the bulge, is an indirect correlation to what is proposed in the literature.

6.1.2 Characteristic Velocity Field

Within the reference frame fixed with the crest, the flow field for a plane-progressive wave consists of a surface parallel current in the opposite direction of the crest motion. As the surface deforms during the bulge formation, the velocity field can either follow the surface or separate from the surface, forming a dividing streamline with the flow in the bulge above it. In experiments on gentle-spilling breaking waves performed by Qiao and Duncan [90], the flow field has been observed to follow the surface providing the bulge is not moving along the surface relative to the crest. This is also seen in the gentle-spilling breaking waves in this study. Figure 6-6 shows an instantaneous characteristic velocity profile for a gentle-spilling breaking wave during the breaking phase as seen in figure 6-2. Also included is the air-water interface and a select number of streamlines in the water and air volume near the surface. At this instant and throughout the breaking event, the velocity field in both fluids is able to follow the curvature of the surface and no flow separation exists. This is the case throughout the breaking event for the spilling breaking waves in this study. However, in general some flow reversal is seen in experiments during the period of bulge movement [90]. As the bulge does not move nor does the shape of the bulge increase such that the flow can not follow the surface, no flow reversal is seen or expected.

The normalized stress components $\tau_{ij}/\mu(\phi;\epsilon) = 2S_{ij}$ are shown in figure 6-7. While the normal stress are equal and opposite due to continuity, both the normal stresses τ_{11} and τ_{33} are shown for completeness along with the shear component, τ_{13}. The toe of the bulge and the bulge itself contains a localized region of increased

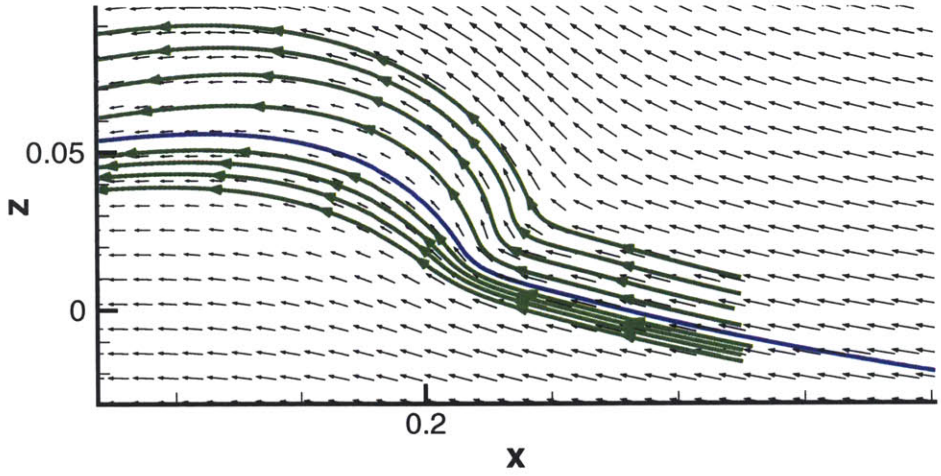

Figure 6-6: Instantaneous velocity vectors of gentle-spilling breaking wave (case A2P-02) during the breaking phase. Every second vector is plotted. Blue line is surface location. Green lines are streamlines.

stresses. This equates to a large region of dissipation at the toe and in the bulge. Additionally, as seen in the velocity vectors in figure 6-6, there is no sign of a separation point where the tangential stress along the face of the wave would be zero. The stresses in the air volume are similar in nature in that there are regions of high stress at the bulge due to the curvature, but no separation exists in the air volume. Above the crest of the wave, there is also a region of shear stresses which occurs as the air-flow attempts to follow the curvature of the wave crest.

The normalized stress components can be converted to surface normal and surface shear stresses through the use of the normal and tangent vectors. The transformation is:

$$\begin{aligned} \tau_{nn} &= n_i \tau_{ij} n_j \\ \tau_{ns} &= t_i \tau_{ij} n_j \end{aligned} \tag{6.1}$$

The definition of the normal vector is as in equation 2.12 but with a negative sign

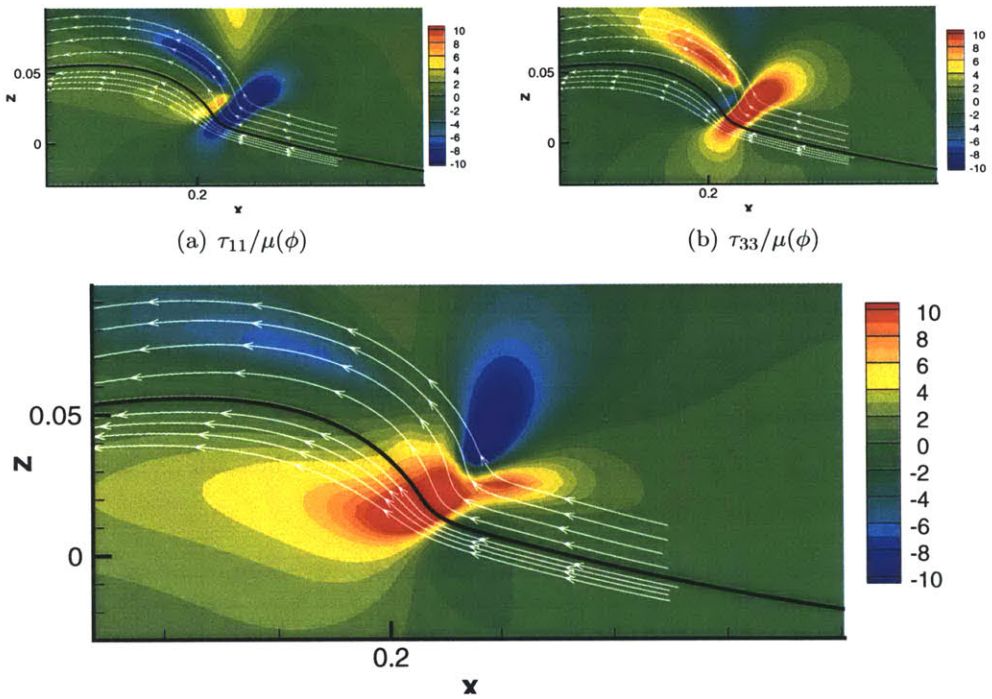

(a) $\tau_{11}/\mu(\phi)$

(b) $\tau_{33}/\mu(\phi)$

(c) $\tau_{13}/\mu(\phi)$

Figure 6-7: Instantaneous normalized stress components for a gentle-spilling breaking wave (case A2P-02) during the breaking phase. Black line is surface location. White line are streamlines as in figure 6-6.

such that it points out of the water into the air volume. Thus,

$$\vec{\mathbf{n}} = -\frac{\nabla\phi}{||\nabla\phi||}$$
$$\vec{\mathbf{t}} = \frac{(\phi_z, -\phi_x)}{||\nabla\phi||} \tag{6.2}$$

are the normal and tangents used in equation 6.1. The normalized surface normal and shear stresses are shown in figure 6-8. As is seen in figure 6-7, the toe region has a localized region of large stresses, both normal and shear, in both the air and water volumes which will contribute to significant dissipation. The crest itself is essentially stress free in both fluids. Yet, above the front face of the crest in the air volume, there is significant amount of positive surface shear stress as the air flow adjusts for the curvature of the surface. Also, just above the toe area, there is a small point of negative normal stresses in the air. In the bulge area, the water volume has a small region of negative shear stresses just following the positive region in the toe. The air flow also sees regions of negative shear stress around the toe region. Thus, while no separation exists in the flow, there are regions where, in the surface coordinates, the shear stresses have become zero.

For the waves which are strong-spilling breaking waves, the bulge on the front face of the wave is more pronounced (see figure 6-4). Thus, flow reversal and separation in these cases is more likely as the surface parallel velocity has a sharper change in curvature to follow than in the gentle-spilling cases. Figure 6-9 shows the velocity field in the reference frame of the crest for a strong-spilling breaking wave during the breaking event. Compared to the gently-spilling breaking wave in figure 6-6, there is an increase in curvature of the surface at the toe of the bulge; however, there is no significant flow reversal in the water volume for this case. As it has been established that bulge movement relative to the crest generates a separated field for unsteady spilling breaking waves [90], this is not unexpected. In fact, the cases in the literature where there exists a definitive separated bulge region which does not move are cases of quasi-steady breaking waves where a detached bulge rides above the dividing streamline [15, 59]. The flow in the air above the wave has a distinct

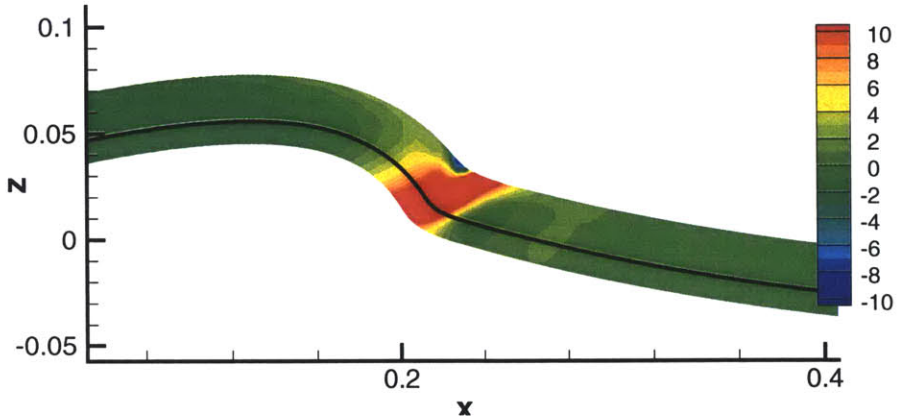

(a) $\tau_{nn}/\mu(\phi)$

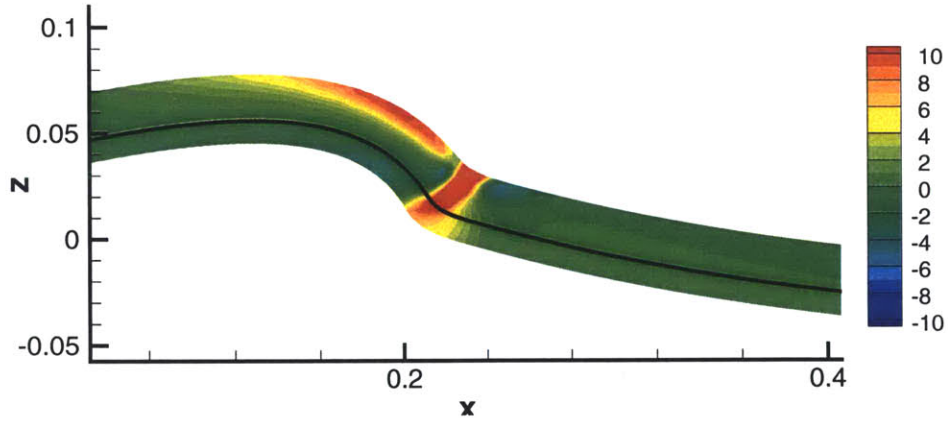

(b) $\tau_{ns}/\mu(\phi)$

Figure 6-8: Instantaneous normalized stress components in surface coordinates for a gentle-spilling breaking wave (case A2P-02) during the breaking phase. Black line is surface location.

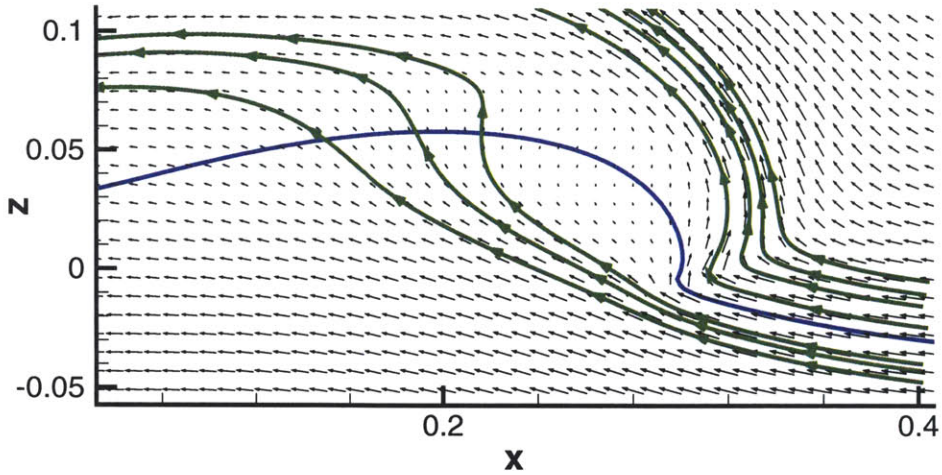

Figure 6-9: Instantaneous velocity vectors of strong-spilling breaking wave (case SFI-10) during the breaking phase. Every second vector is plotted. Blue line is surface location. Green lines are streamlines.

flow reversal at the toe of the bulge like an interior corner flow. Based on the velocity field and streamlines, there is evidence of a separated region in the air volume above the wave crest like an exterior corner flow. This is very much like what is seen in studies of flow over wavy surfaces or mountains. Note in figure 6-9 the streamlines go through the interface. At this instant in time, there is an upward motion of the surface due to the presence of a standing wave in the computational domain.

As in the gentle-spilling case, the normalized stress components are shown in figure 6-10 for the strong-spilling breaking wave. In general, compared to the gently-spilling waves, the normal stresses in the water volume are fairly similar in nature, albeit stronger, and again balance out as continuity demands. The shear stresses are much stronger and less localized at the bulge region, reaching back into the wave. The larger magnitude of the stresses indicate a larger dissipation rate in these types of waves, which is confirmed in chapter 7. The shear region in the wave crest begins at the toe location and practically extends the entire width of the wave crest, in-line with the surface parallel velocity as it approached the toe. This reveals the existence of a shear layer between the bulk fluid and the fluid in the crest of the wave. While no flow reversal exists in the water volume in these strong spilling breaking waves,

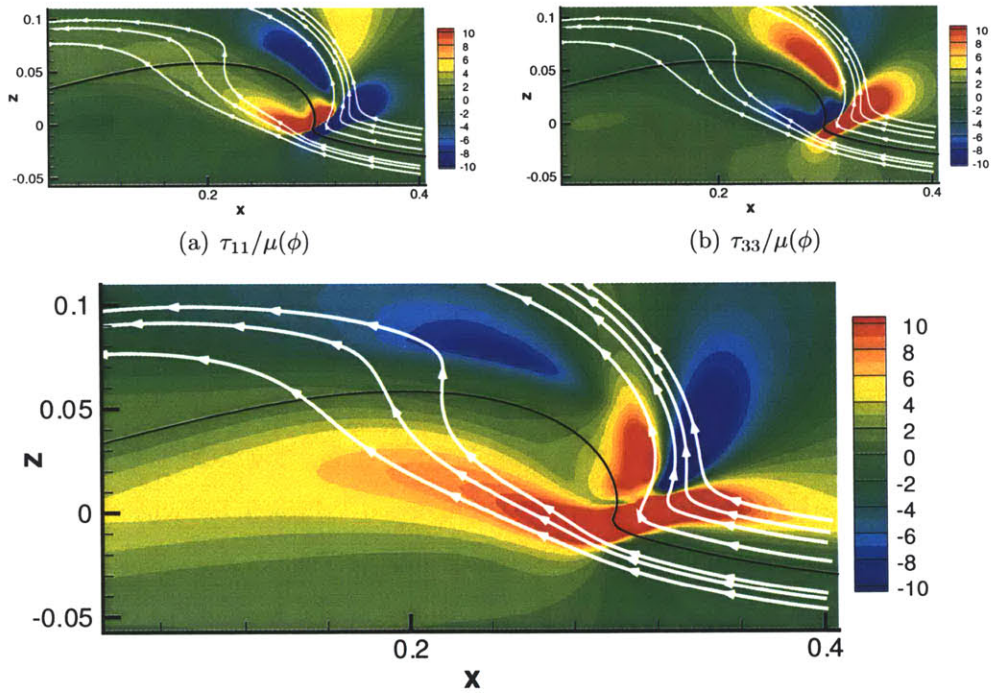

(a) $\tau_{11}/\mu(\phi)$ (b) $\tau_{33}/\mu(\phi)$

(c) $\tau_{13}/\mu(\phi)$

Figure 6-10: Instantaneous normalized stress components for a strong-spilling breaking wave (case IAW-04) during the breaking phase. Black line is surface location. White line are streamlines as in figure 6-9.

a fairly strong shear layer does as the flow adjusts to the free-surface profile. The air volume shows the greatest difference between gentle- and strong-spilling breaking waves. While there is no sign of separation in the air volume for gentle-spilling breaking waves, there exists a small region right near the toe of the bulge where zero stress exists. The shear layer above the wave crest in the air flow still exists and as expected is considerably stronger than in gently-spilling waves.

Figure 6-11 shows the normalized stresses in surface coordinates calculated as in equation 6.1. As in figure 6-10, there is a strong localized region of positive surface normal and shear stresses at the toe. The normal stresses have a small point of negative stresses in the air above the toe which was seen in the gentle spilling breaking wave. The surface shear stresses in the water volume are dominated by the toe location without evidence of any other significant regions of activity. In the air

volume, however, the area above the crest of the wave has significant positive shear stresses and just before the toe region a negative shear stress. Again, the shear stresses change sign near the toe region in the air showing a flow reversal and possible separation region.

6.1.3 Vorticity and Vorticity Flux

Through investigation of the velocity and stresses of spilling breaking waves in section 6.1.2, the bulge region of the breaking wave was determined to be the region of interest. Thus, the vorticity in this mainly irrotational flow field is expected to be confined to the bulge region. This is seen in figures 6-1 through 6-3 where the vorticity for each stage of the spilling breaking event is shown. The developmental stage shows the vorticity developing in both fluids as the bulge forms. During the breaking event, the vorticity is relatively unchanged. During the dissipation stage, the strength of the vorticity decreases as the bulge disappears. Figure 6-12 shows the vorticity for both the gentle- and strong-spilling breaking waves during the breaking event. The structure of the vorticity is fairly consistent between the two cases. There is a strong positive vortex at the toe of the bulge in both the air and water volumes. Note that positive vorticity is clockwise in these figures. There is also secondary weaker vortex of negative vorticity right above it on the bulge.

In his paper regarding capillary rollers and bores, Longuet-Higgins [65] proves that any curved, free surface (in a steady flow) is a source of vorticity and its strength is proportional to the curvature times the particle speed ($\omega = -2\kappa q$). As the bulge does not propagate, the spilling breaking waves in this study can be considered steady within a reference frame which follows the crest over a short period of time. However, because this study includes the effects of the air volume above the wave, the air-water interface is not a shear-free surface in that its boundary condition is only that of continuous shear between the two volumes. Also, as seen in figures 6-7 and 6-10, the region of the bulge is not a region of minimal shear. Thus, direct comparison to the theory is not applicable. However, when compared to the local curvature and tangential velocity component ($2\kappa\vec{\mathbf{u}} \cdot \vec{t}$), there is qualitative comparison to Longuet-

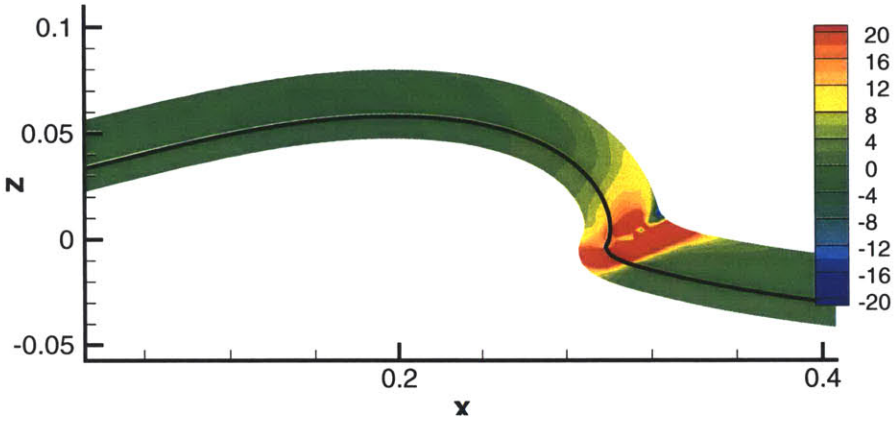

(a) τ_{nn}

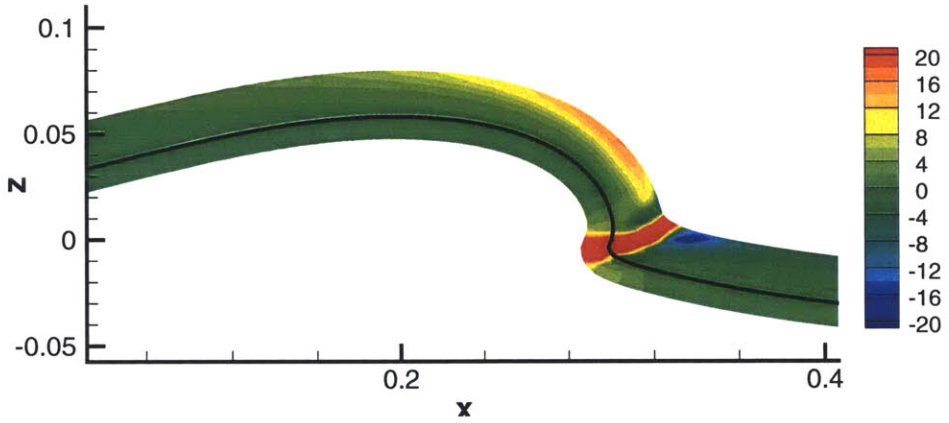

(b) τ_{ns}

Figure 6-11: Instantaneous normalized stress components in surface coordinates for a strong-spilling breaking wave (case IAW-04) during the breaking phase. Black line is surface location. White line are streamlines as in figure 6-9.

Higgins in the sense that the strength (and sign) of the vorticity agrees within 20%. Based on this assessment, the vorticity in the water which appears at the toe of the bulge is believed to be a curvature effect only. For the air, the vorticity in the region is also a curvature effect while the vorticity above the crest is due to separation of the air flow from wave crest.

Following the work of Rood [93, 94], the vorticity flux at the surface is shown in figure 6-13. The vorticity flux which is shown is the two-dimensional version of

$$\frac{1}{\mathcal{R}e_w}\vec{n}\cdot\nabla\vec{\omega}\underbrace{=}_{\text{in 2D}}\frac{1}{\mathcal{R}e_w}\vec{n}\cdot\nabla\omega_y \tag{6.3}$$

In equation 6.3 and figure 6-13, the normal points into the surface. Therefore, from the perspective of the water volume, a negative vorticity flux means a flux of *positive* vorticity *into* the water volume. From the perspective of the air volume, it represents a flux of *positive* vorticity *into* the air volume. This is confirmed with figure 6-12.

To summarize the kinematics and dynamics of spilling breaking waves, it has been determine that the flow in the wave is responding to curvature effects. There is no sign of any flow reversal for the water volume in the velocity vectors and normalized stresses, even for the strong-spilling breaking wave. Therefore, the vorticity in the water is only a function of curvature effects. The flow in the air around the wave presents a different picture. Analysis of the velocity and stress fields shows that as the wave transitions from a gentle- to strong-spilling breaking wave, the air experiences a flow reversal at the toe of the bulge. This reversal is a significant source of vorticity for the air and there is a corresponding increase in the stresses in the fluid (and the dissipation which is discussed in chapter 7). The back face of the wave (or backside of the crest) is generally another point of separation for the air flow around the wave. Depending on how energetic the air flow is as it approaches the crest of the spilling breaking wave, the air separates off of the crest much like the flow off of a backward facing step. This is evident even in the gentle-spilling breakers but certainly predominant in the strong-spilling breakers.

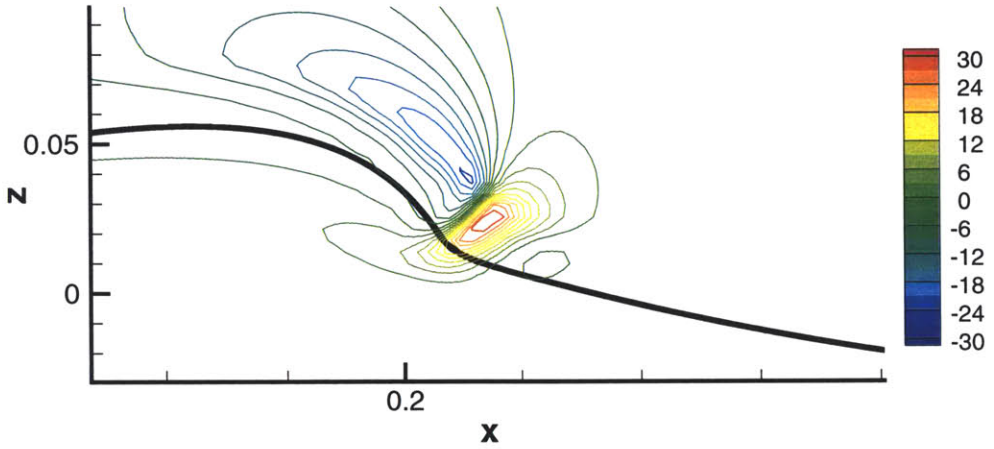

(a) gentle-spilling

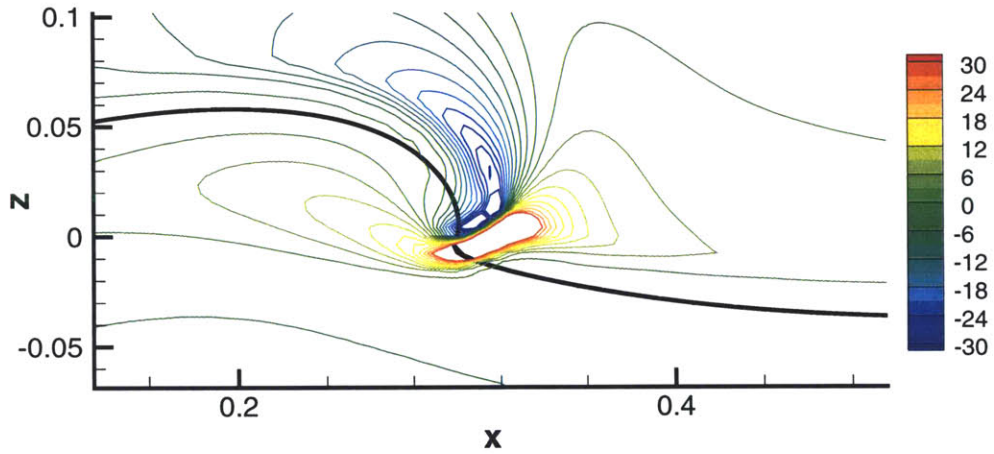

(b) strong-spilling

Figure 6-12: Instantaneous vorticity contours for spilling breaking waves during the breaking event. Gentle-spilling is case A2P-04 and strong-spilling is case SFI-10. Black line is surface location.

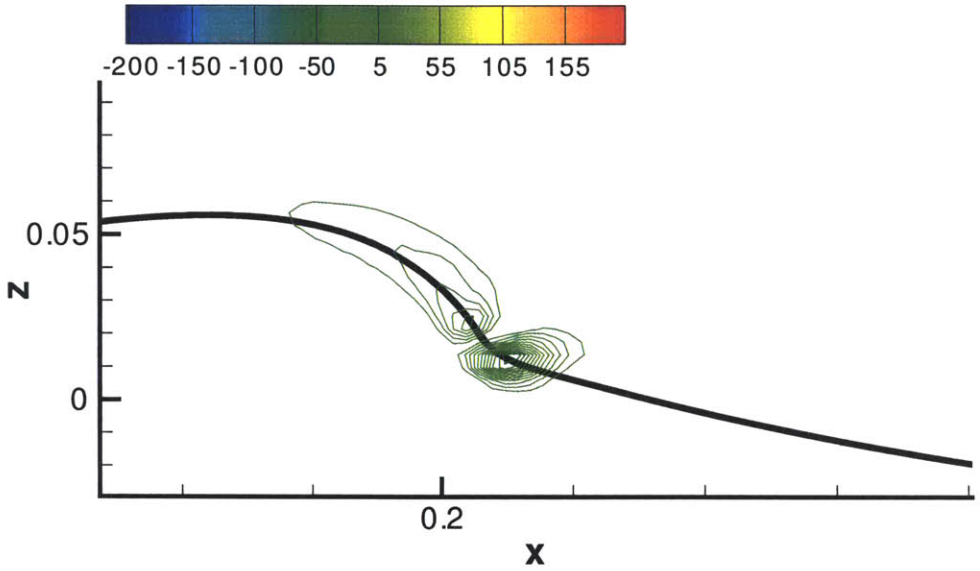

(a) gentle-spilling

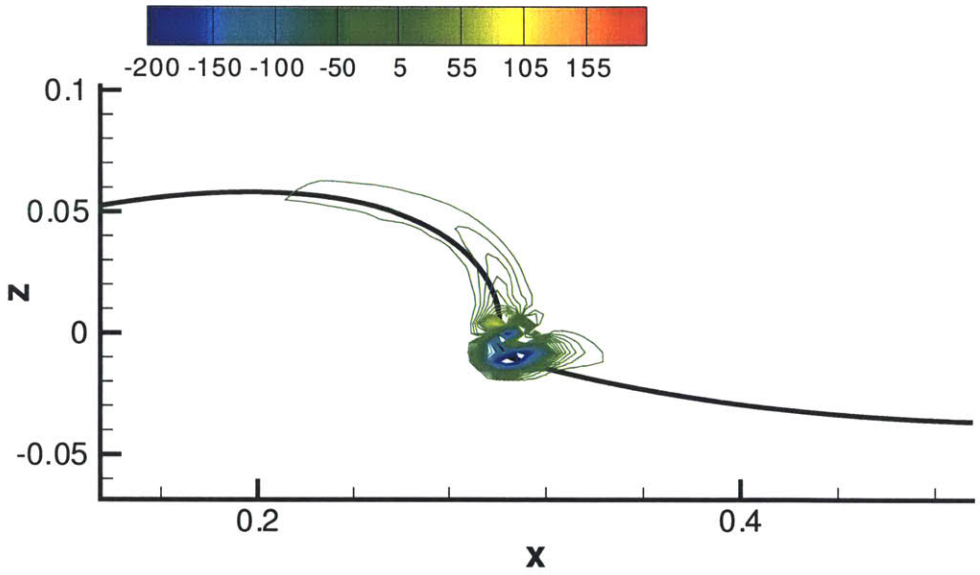

(b) strong-spilling

Figure 6-13: Instantaneous vorticity flux for spilling breaking waves during the breaking event. Gentle-spilling is case A2P-04 and strong-spilling is case SFI-10. Black line is surface location.

6.2 Plunging Breaking Waves

Past studies regarding plunging breaking waves have mainly focused on the topic of waves in shallow water such as shoaling and waves impacting on walls such as sea walls. Deep water plunging breaking waves are less common in nature but have a great effect on offshore structures, air-sea mixing, increased ocean turbulence and wind-wave-current interactions. Experimental measurements of deep water plunging breaking events have appeared within the last few decades [92, 80, 54]. However, the experimental methodology was limited to qualitative measurements *during* the breaking event. As will be discussed in chapter 7, these measurements treat the breaking region like a "black box" where increased turbulence and the entrainment of air makes detailed measurements difficult. Recently, some authors have attempted to make quantitative measurements during the plunging event [77, 85]. Yet because the field of view used for the experiments encompasses the entire wave, the details of the flow at the crest and in the free-surface boundary layer are lacking.

Until recently, the numerical study of plunging breaking events has been limited to two-dimensional simulations using potential flow methods [24, 68]. These works give a detailed view of the crest kinematics and dynamics up until the plunging jet re-enters the water surface. Due to the numerical method employed, they can not simulate past the re-entry event. A recent numerical work by Chen and Kharif [13] is the first viscous simulation of a plunging breaking wave. This work shows the impact of the plunging jet on the surface and subsequent impact events as the jet either bounces along the wave face or causes an ejection from the bulk flow. However, the constitutive properties of the fluids used in the simulation do not have the properties of air and water. In particular, the viscosity ratio is significantly higher (0.4 compared to the actual 0.01) than in reality, thus the applicability of their results has yet to be seen.

Experiments and simulations report that during the development of a breaking wave, the wave develops significant asymmetry. In a spilling breaking wave, the asymmetry gives way to the bulge as discussed in section 6.1.1. For a plunging

breaking wave, the asymmetry develops into a near vertical region on the crest of the wave. In general, during a plunging event, a jet forms at this point shortly after it becomes near vertical. This event is usually associated with a particle velocity speed which is greater than the phase speed of the wave and a large pressure gradient at the location of the jet formation which then accelerates the flow forward [67]. In the literature, the jet which forms curves and stays intact during the plunging event where it re-enters the front face of the wave [8, 92]. This forms an initial air pocket which is responsible for most of the air entrainment. The plunging jet then causes subsequent splash-up and re-entry events. Each event is decreased in amplitude and the amount of air entrained.

Chapter 4 discusses how surface tension is used to create plunging breaking waves at the length scale relevant for this study. By reducing the surface tension effects, the jet formation is allowed to occur. All of the plunging breaking waves generated in this study have been generated using a relatively weak surface tension coefficient and either a surface forcing technique or over-energetic wave field. In chapter 4, the plunging breaking waves were separated into two types: those that form jets and those that entrain air. In the jet-forming events, the jet which forms is ejected from the near vertical wave face. The jet impacts the wave surface and then has subsequent ejection and re-entry events. However, because of the thinness of the jet which forms in these cases, the jet pinches off of the wave face at the ejection point before the air pocket collapses and entrains air into the bulk flow. The waves which entrain air have a thicker jet which forms and stays intact as the air pocket collapses.

The majority of the plunging breaking waves in this study have been classified as jet-forming with only a few waves entraining air. Figures 6-14, 6-15 and 6-16 show the time evolution of the air-water interface and the transverse vorticity for a plunging breaking wave which has a jet ejection. The breaking event has three main stages. The first is the development stage (figure 6-14) in which the surface of the wave becomes near vertical. Up until this time, there is no vorticity in the water except for a very thin region on the front face of the wave. The air flow has relatively strong vorticity near the crest and trough of the wave.

As the jet forms and the curvature of the air-water interface becomes significant (figure 6-15), the vorticity in the water becomes stronger in this area but is still limited to a thin region near the interface. The air sees significant vorticity as it is trapped underneath the jet and the air pocket is formed. When the re-entry event occurs (figure 6-15c), there is a region of positive vorticity in the water beneath the impact point which is the result of the impulse of the jet on the wave face.

The third stage of breaking for the jet-forming cases is a jet disintegration (figure 6-16) stage. Here the jet becomes thin and pinches off. There is very little change in the vorticity field for during the jet disintegration phase as most of the vorticity is in a thin region near the surface of the wave.

The other type of plunging breaking wave in this study is the case where there is significant air entrainment. These cases were formed through over-energetic waves as initial conditions and have the most standing wave energy associated with them. Figures 6-17, 6-18 and 6-19 show the interface evolution and transverse vorticity contours for one such wave. This type of plunging breaking wave has four main stages associated with it. The first stage is the development stage and is shown in figure 6-17. The effect of the over-energetic wave with the standing wave influence can be seen in the surging motion of the interface. Similar to the jet-forming plunging wave, the surface becomes near vertical which leads to the formation of the jet. The vorticity in the water is also relegated to a very weak and thin region at the interface on the front face of the wave. The air flow sees considerable vorticity in the flow as the overall amplitude of the wave is significantly larger than the jet-forming cases. This causes separation in the air flow at the crest and trough of the wave.

The second stage of this type of wave is the jet formation stage (figure 6-18). Compared to the jet formed in the previous case, a thicker jet forms and curls down towards the front face of the wave. However, while the jet is relatively thicker, the vorticity is similar to that of the jet ejection in that it is still confined to a thin region near the surface for the water and relatively large in the air flow as the air pocket forms.

The third stage of this type of breaking wave is the jet re-entry phase. The jet

re-entry phase is shown in figure 6-19 with the air entrainment phase reserved for discussion section 6.2.3. During the jet re-entry phase, there is localized regions of strong vorticity at the points where the jet impacts the front face of the wave as well as points of extreme curvature where the jet has curled over. The re-entry phase has multiple impact events before the jet has thinned enough to disintegrate. The vorticity in the air flow during this phase remains strong. The fourth stage is the air entrainment phase which is reserved for discussion in section 6.2.3.

6.2.1 Jet Formation

The formation of the plunging breaking wave is shown for two cases in figures 6-20 and 6-21. The first case is where a packet of fluid is ejected from the water surface at the crest, which has been termed jet-forming in this study. Due to the nature of the jet, it disintegrates before the air pocket collapse can entrain air into the flow. Thus, there is little or no air entrainment in these types of waves. The second case is where the jet remains intact long enough for the air pocket to collapse and entrain air.

For both cases, the formation of the jet is similar to that reported in literature in that right before the jet formation there is a point where the crest becomes essentially vertical. As the jet forms, the surface takes on a blunt curved appearance and re-enters the surface. For the cases where the plunging event represents a fluid ejection, the jet is generally very thin and pinches off at the point from where it ejected. What is left of the jet impacts the front face of the wave. This impact happens one or two more times in something akin to a skipping motion verses secondary and tertiary ejection events.

For the cases where the plunging event is more violent and entrains air, the jet which forms is thicker at the point of formation and does not break up quickly. In fact, the jet remains in tact through the first and second re-entry event. This type of plunging event is more representative of the plunging events seen in wave focusing experiments and some numerical simulations verses the jets which pinch off as in the ejection case discussed previously.

Description of the crest overturning phase of the plunging event has received recent

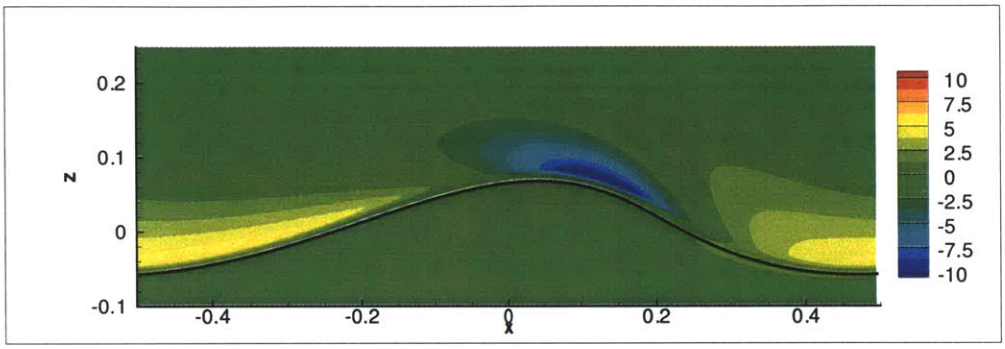

(a) $t = t_1$

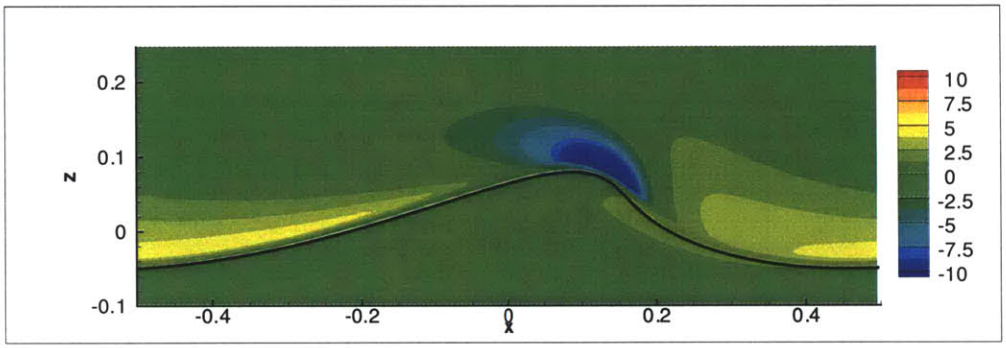

(b) $t = t_1 + 0.28T$

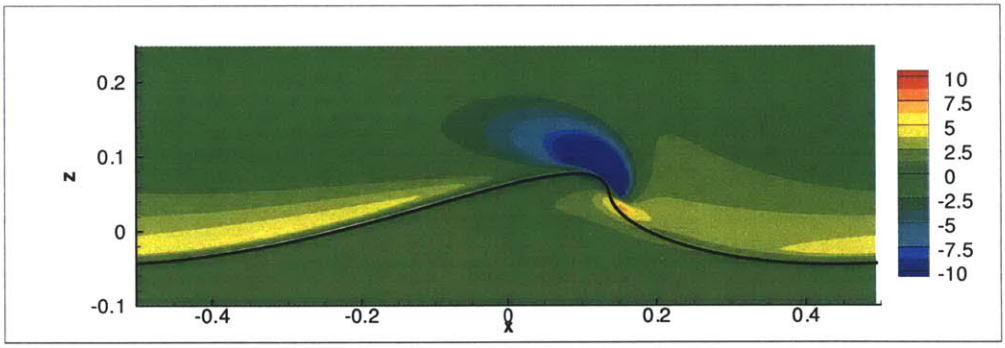

(c) $t = t_1 + 0.52T$

Figure 6-14: Time evolution (development) of a plunging breaking wave (case SFI-04) with vorticity contours shown. Black line represents air-water interface. Nondimensional theoretical wave period (T) is 2.51.

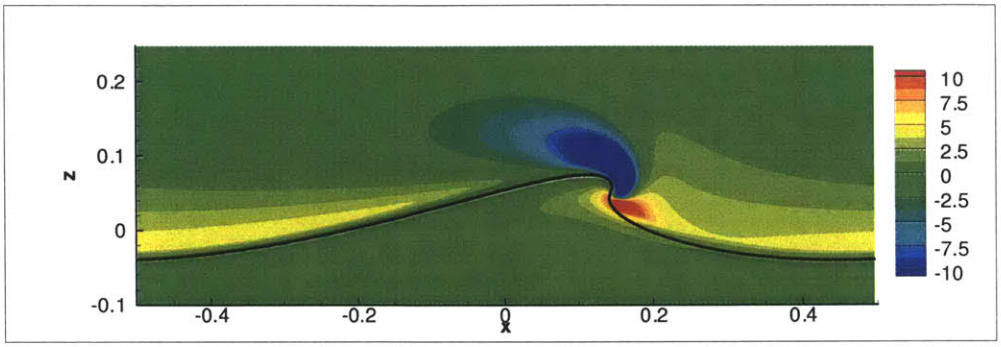

(a) $t = t_1 + 0.64T$

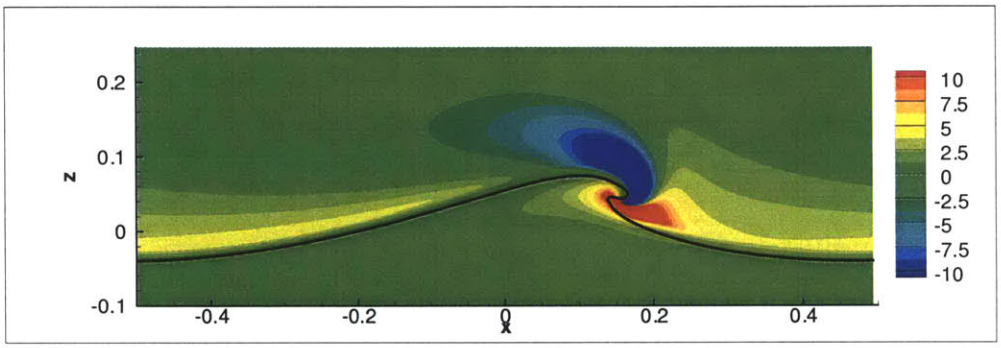

(b) $t = t_1 + 0.76T$

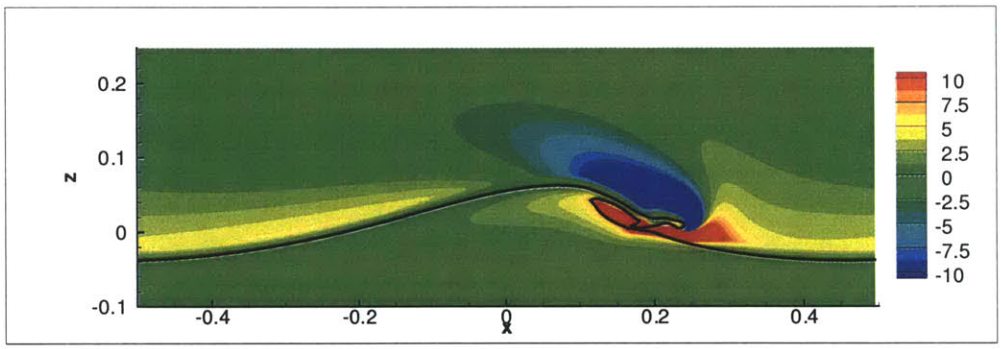

(c) $t = t_1 + T$

Figure 6-15: Time evolution (jet formation) of a plunging breaking wave (case SFI-04) with vorticity contours shown. Black line represents air-water interface. Nondimensional theoretical wave period (T) is 2.51.

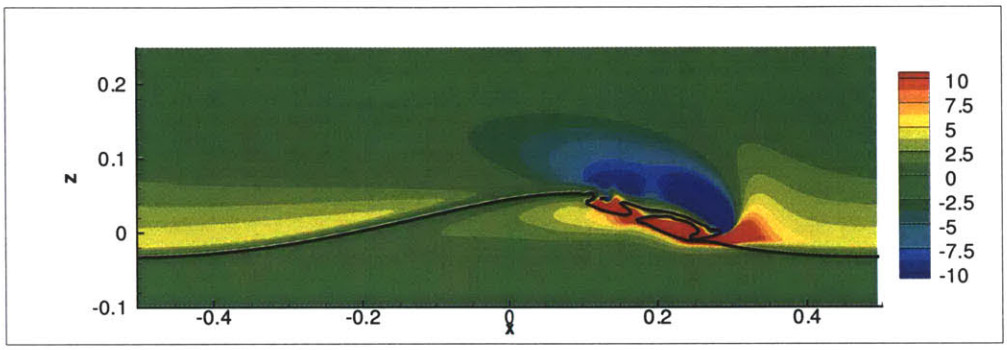

(a) $t = t_1 + 1.16T$

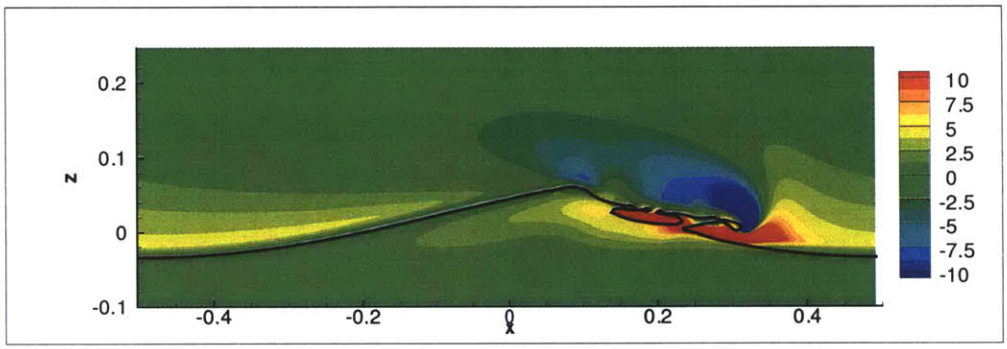

(b) $t = t_1 + 1.32T$

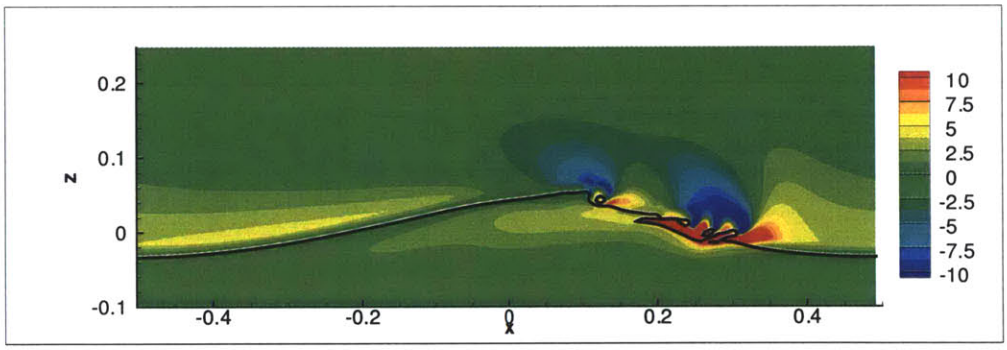

(c) $t = t_1 + 1.48T$

Figure 6-16: Time evolution (jet disintegration) of a plunging breaking wave (case SFI-04) with vorticity contours shown. Black line represents air-water interface. Nondimensional theoretical wave period (T) is 2.51.

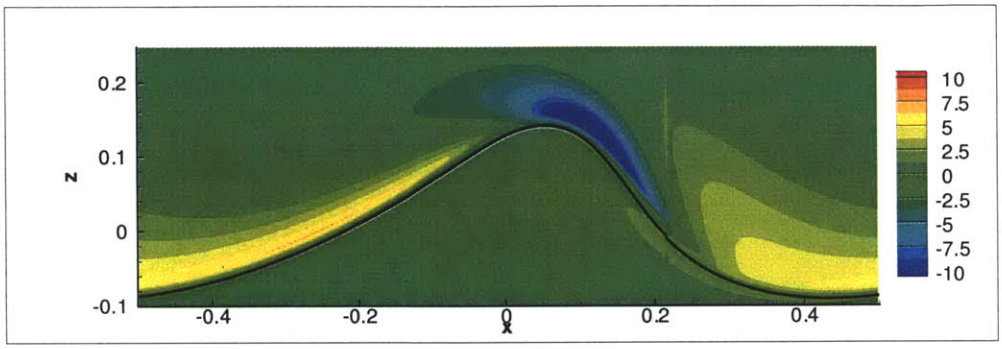

(a) $t = t_1$

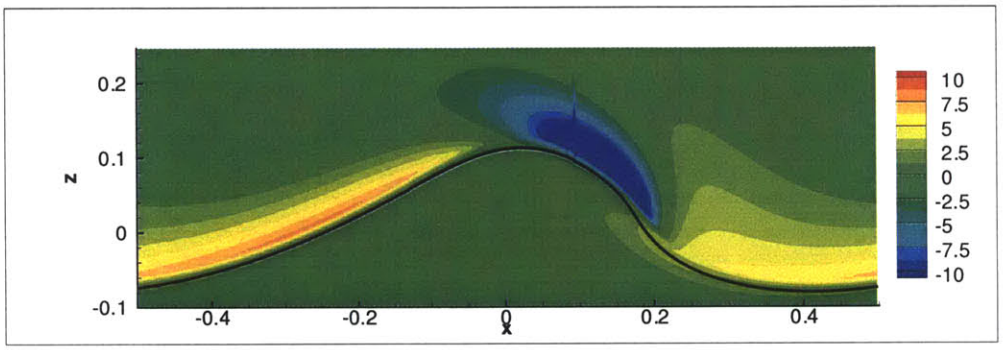

(b) $t = t_1 + 0.12T$

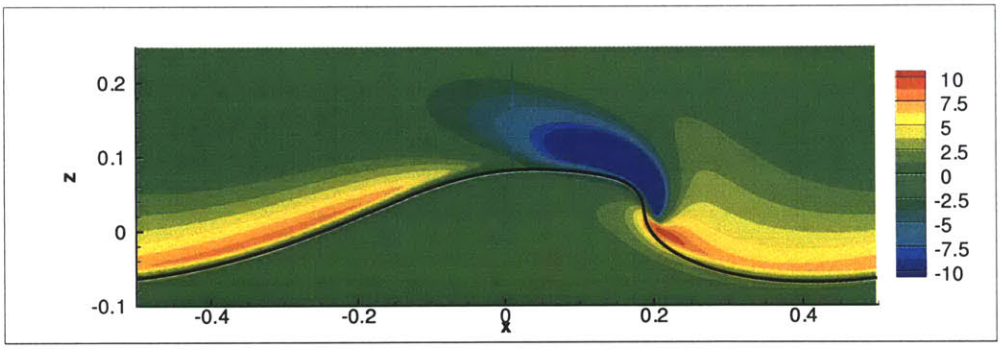

(c) $t = t_1 + 0.20T$

Figure 6-17: Time evolution (development) of a plunging breaking wave (case IAW-10) with vorticity contours shown. Black line represents air-water interface. Nondimensional theoretical wave period (T) is 2.51.

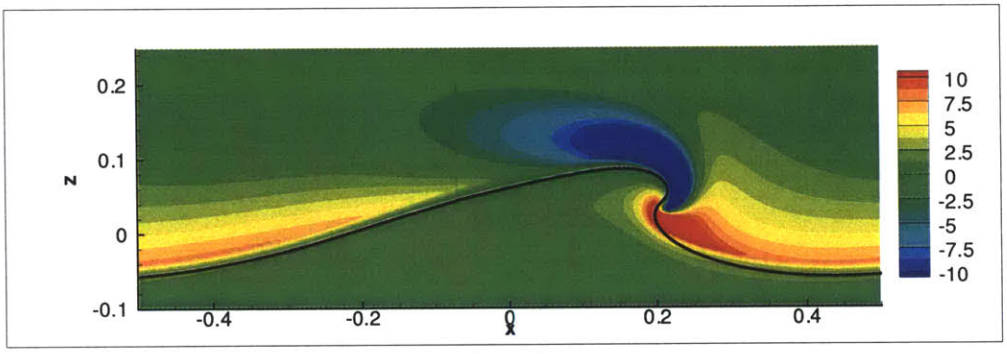

(a) $t = t_1 + 0.28T$

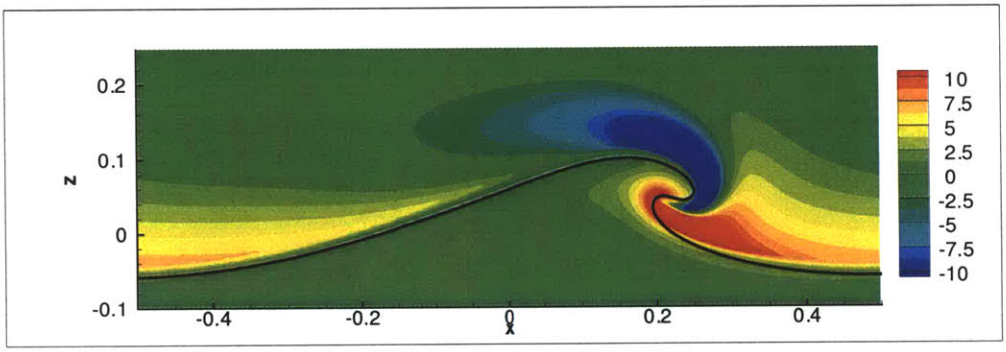

(b) $t = t_1 + 0.36T$

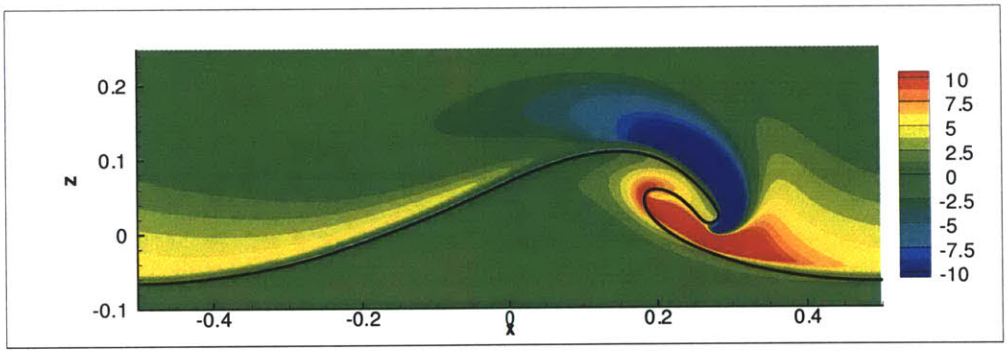

(c) $t = t_1 + 0.44T$

Figure 6-18: Time evolution (jet formation) of a plunging breaking wave (case IAW-10) with vorticity contours shown. Black line represents air-water interface. Nondimensional theoretical wave period (T) is 2.51.

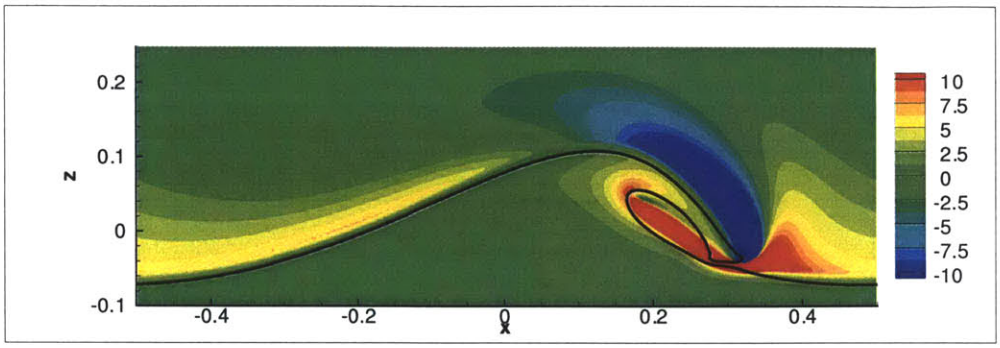

(a) $t = t_1 + 0.52T$

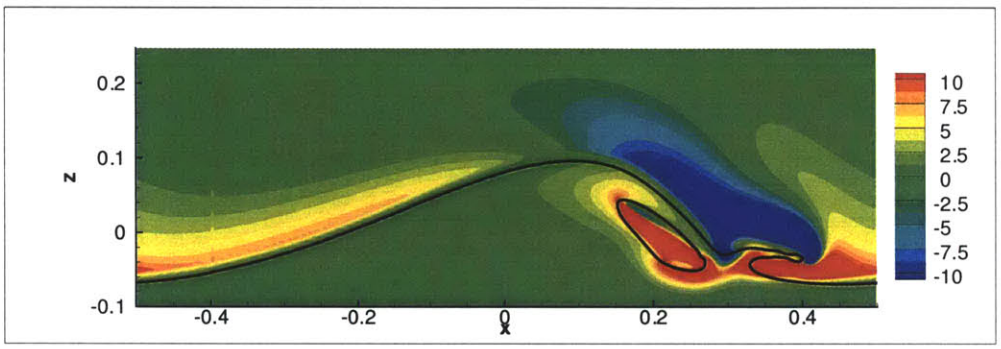

(b) $t = t_1 + 0.60T$

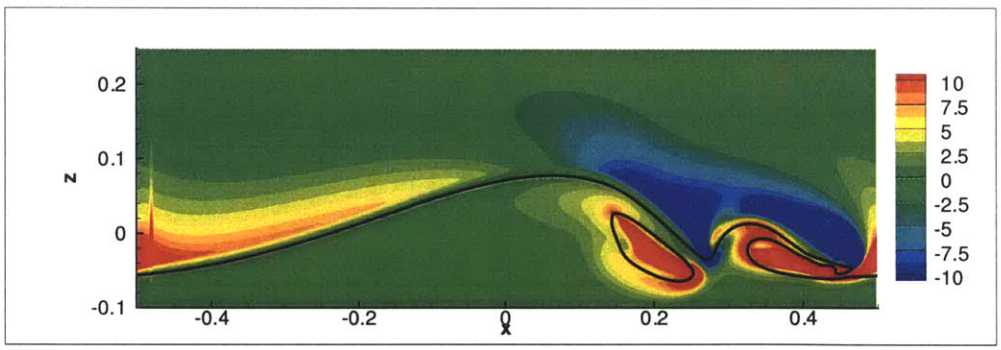

(c) $t = t_1 + 0.68T$

Figure 6-19: Time evolution (jet re-entry) of a plunging breaking wave (case IAW-10) with vorticity contours shown. Black line represents air-water interface. Nondimensional theoretical wave period (T) is 2.51.

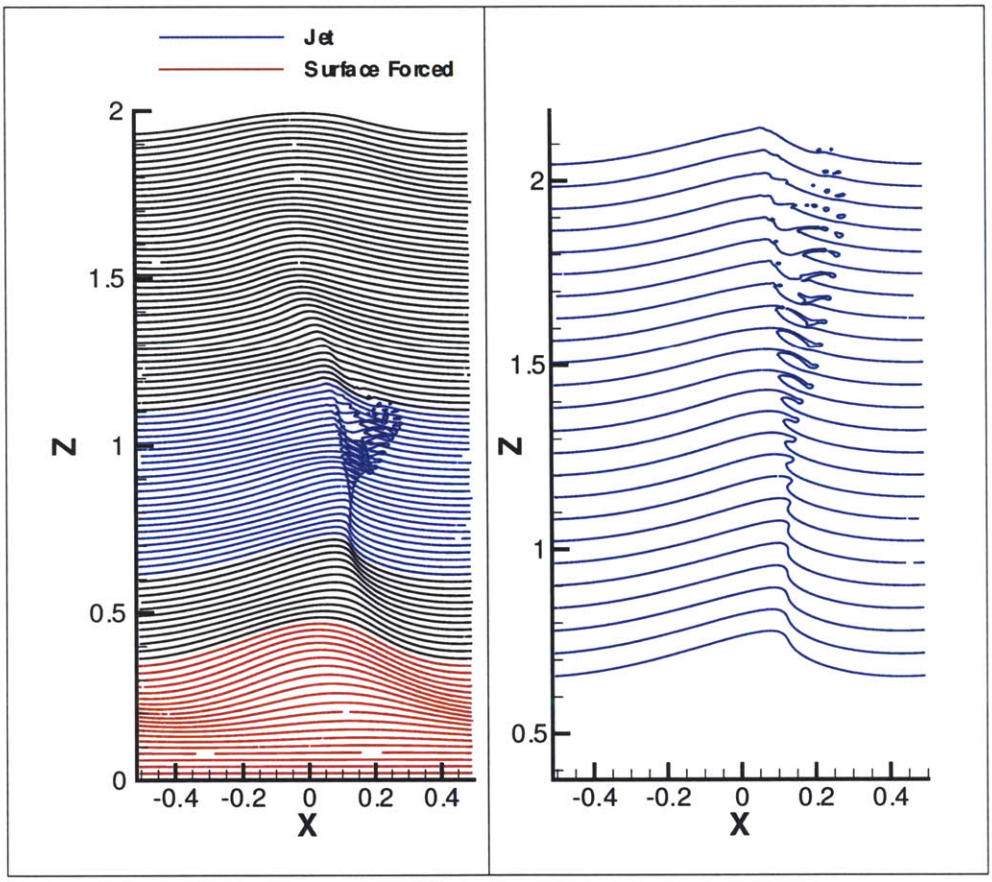

Figure 6-20: Waterfall profiles of a jet-forming plunging breaking wave (case SFI-11). Red surface profiles are times when surface is being forced. Blue surface profiles are the time of jet formation, re-entry and breakup. Left is successive vertical profiles (every $\Delta t = 0.1$) offset by $\Delta z_{off} = 0.02$. Right is jet event where successive vertical profiles (every $\Delta t = 0.1$) are offset by $\Delta z_{off} = 0.06$

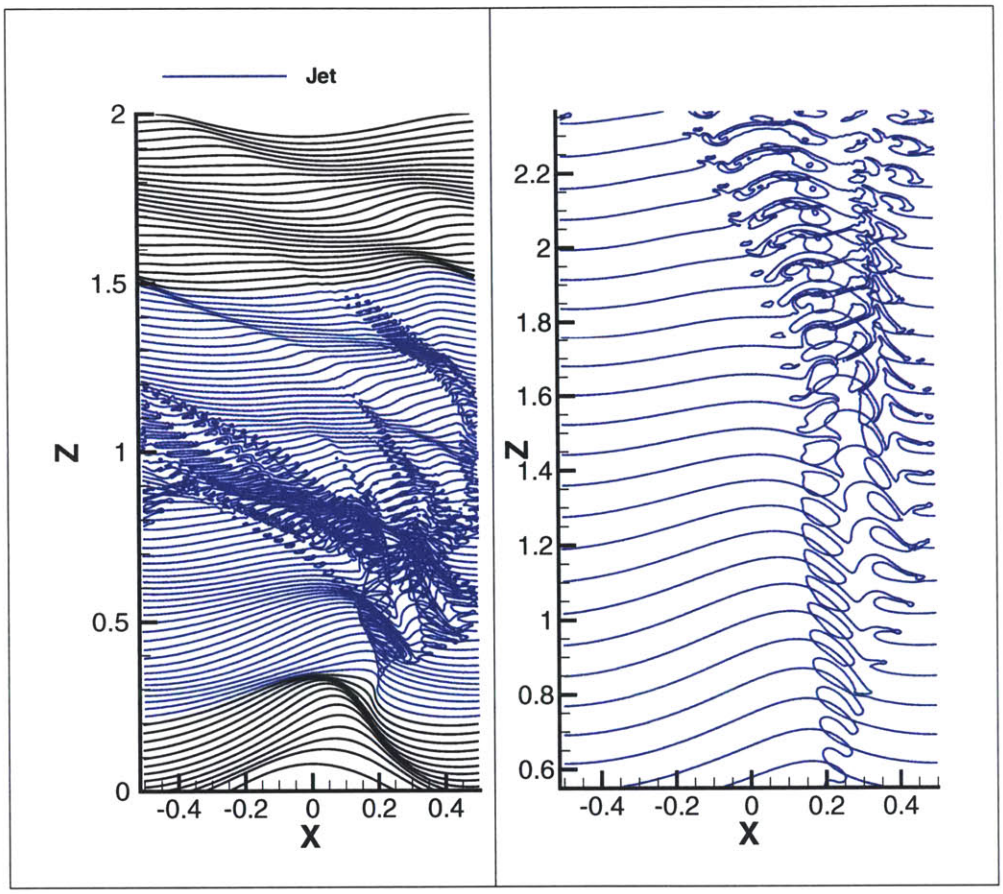

Figure 6-21: Waterfall profiles of a plunging breaking wave with air entrainment (case IAW-10). Left is successive vertical profiles (every $\Delta t = 0.1$) offset by $\Delta z_{off} = 0.02$. Right is plunging event where successive vertical profiles (every $\Delta t = 0.1$) are offset by $\Delta z_{off} = 0.08$

attention mathematically by Longuet-Higgins [64], New [81] and Greenhow [38]. The theory of New states that the inside profile of the overturning jet of a plunging breaking wave was approximated by an ellipse with a major-to-minor axis ratio of $\sqrt{3}$. Bonmarin [8] considers the ellipse solution of New to one plunging breaking wave by inscribing the $\sqrt{3}$ ellipse on the interior of the jet as well as the best fit ellipse. For the wave discussed, it was found that shortly after the jet formed, the ratio started on the order of 2, decreased to 1.3 and then increased to 1.6 by the jet impact. Figure 6-22 shows three moments in the plunging event for a wave which has air entrainment. In all three cases, an ellipse which is the "best fit" to the interior curvature of the wave is shown. The $\sqrt{3}$-ellipse is also shown for comparison. For this particular wave, the best-fit ellipse begins with the theoretical $\sqrt{3}$-ellipse. At the moment of impact in figure 6-22c, the ellipse has a major-to-minor axis ratio of 2.3. Table 6.2 contains a comparison of the wave in figure 6-22 and Bonmarin's experimental results. Both show similar trends in that the ratio begins larger than the theoretical value, drops to lower the value and then increases again. Otherwise there is variability in the ratio throughout the breaking event.

Table 6.2: Major-to-minor axis ratios of best-fit ellipse for a plunging breaking wave (case IAW-10) and experimental results.

Level Set Simulation		Experimental Results [8]	
t	a/b	t	a/b
t	1.73 [1]	t	2.33
$t + 0.04T$	1.97		
$t + 0.08T$	2.09	$t + 0.10T_0$	1.36
$t + 0.12T$	1.67		
$t + 0.16T$	1.86 [2]	$t + 0.12T_0$	1.49
$t + 0.20T$	1.86		
$t + 0.24T$	2.09		
$t + 0.28T$	2.32 [3]	$t + 0.14T_0$	1.61

[1]figure 6-22a;[2]figure 6-22b; [3]figure 6-22c

The velocity field in the reference frame of the crest of both types of plunging events as the jet forms is shown in figure 6-23. For the ejection case, the horizontal velocity is just slightly greater than the speed of the crest with very little vertical velocity. This is in stark contrast to the case with air entrainment where, while the horizontal velocity in the jet is still greater than the crest speed, the vertical velocity is significant. It should be noted that no comparison between the magnitude of the velocity field between the two figures should be made as the velocity vectors are scaled differently. Also note that as in the discussion of the velocity field for spilling breaking waves, the streamlines which go through the interface are a function of the presence of the standing wave. At the instant in time shown, there is an upward motion of the interface due to the standing wave in the computational domain.

It has become accepted in the literature that when a jet forms on the crest of the wave the velocity at that point is greater than the phase speed of the crest. This is seen in numerical simulations and experiments [68, 85]. Additionally, Longuet-Higgins states that there is a significant pressure gradient at the point of the jet formation which accelerates the fluid and propels the jet forward [67]. This type of behavior is seen in both types of plunging events. Figure 6-24 shows the pressure field inside the wave for the ejection case. The gradient of the pressure field is represented by the vector field in this figure. The range of the contours has been limited to highlight the jet region. The gradient of the pressure field is very strong horizontally at the point of ejection.

Perlin *et al.* [85] state that up to the point of jet formation, the flow is essentially irrotational. However, this claim is fairly weak based on the resolution of their measurement techniques. As discussed in section 6.1.3, any curved surface (shear-free or not) is a source of vorticity in the flow. As the free-surface elevations in figures 6-20 and 6-21 show, there should be a certain amount of vorticity in the flow near where the jet begins to form as the surface experiences a significant change in curvature. The evolution of the vorticity during the jet formation and breakup is shown in figure 6-25. In the vertex of the jet, a positive vorticity exists beginning at the jet formation throughout the ejection event. The tip of the jet also has a small amount of negative

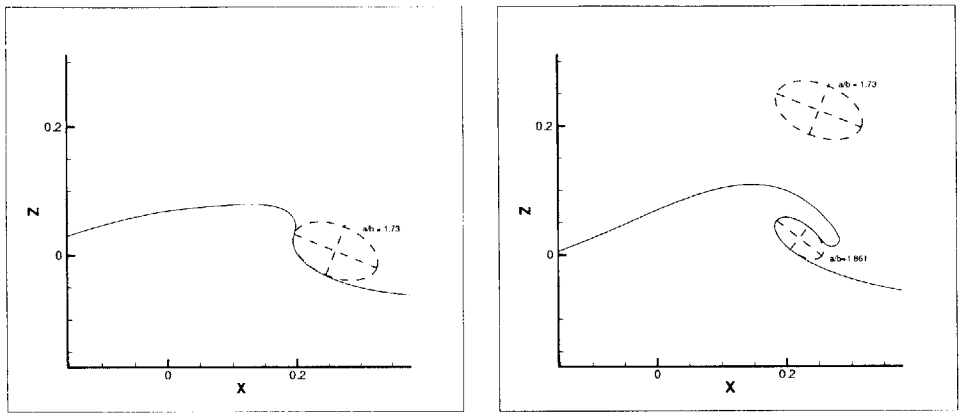

(a) Jet formation t

(b) Curl of jet $t + 0.16T$

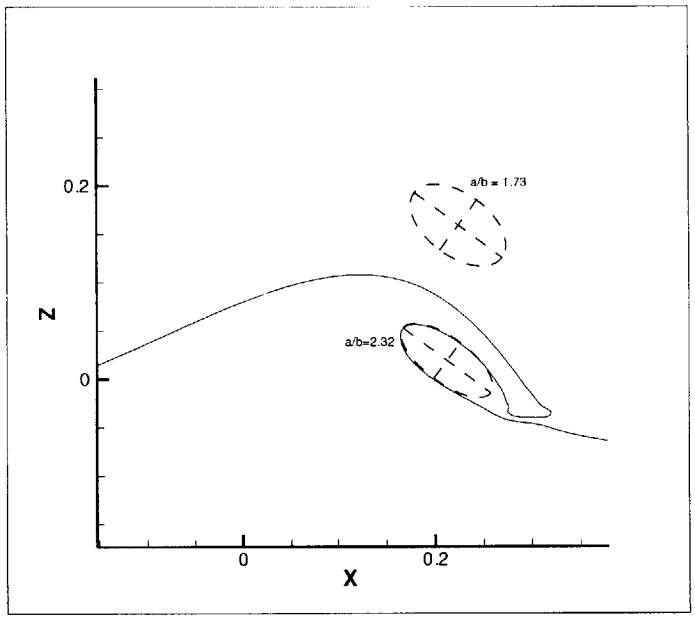

(c) Jet re-entry $t + 0.28T$

Figure 6-22: Best-fit ellipses for the inside curvature of a plunging breaking wave (case IAW-10). Also shown are the $\sqrt{3}$-ellipse from theory for reference.

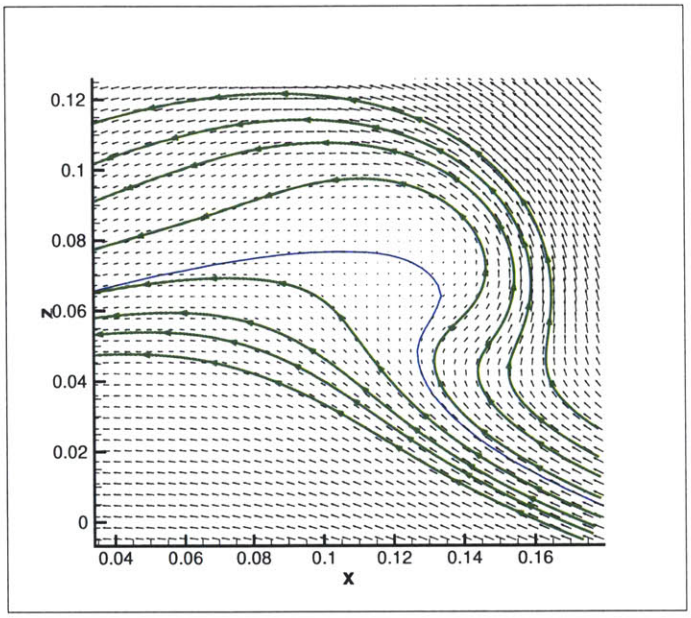

(a) Ejection (case SFI-11). Every vector plotted.

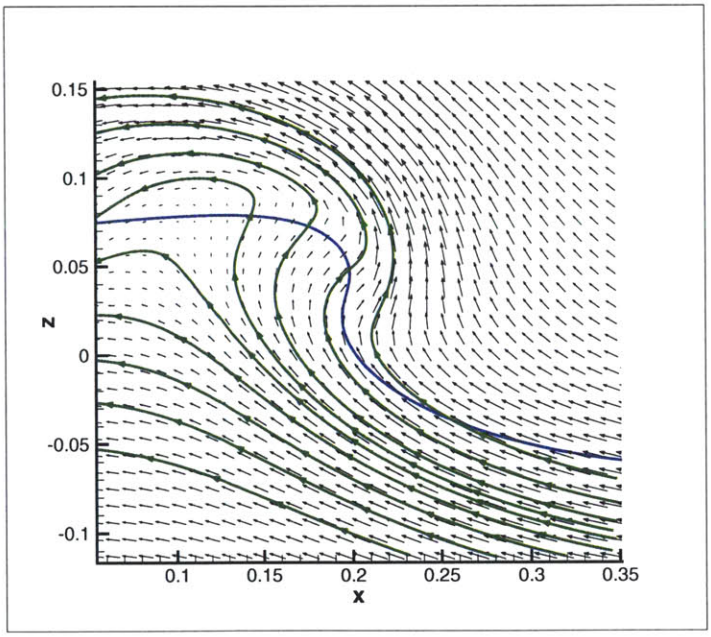

(b) Air Entrainment (case IAW-10). Every other vector plotted.

Figure 6-23: Instantaneous velocity field of two types of plunging events in the reference frame of the crest as the jet is forming. Blue lines represent surface location. Green lines represent selective streamlines.

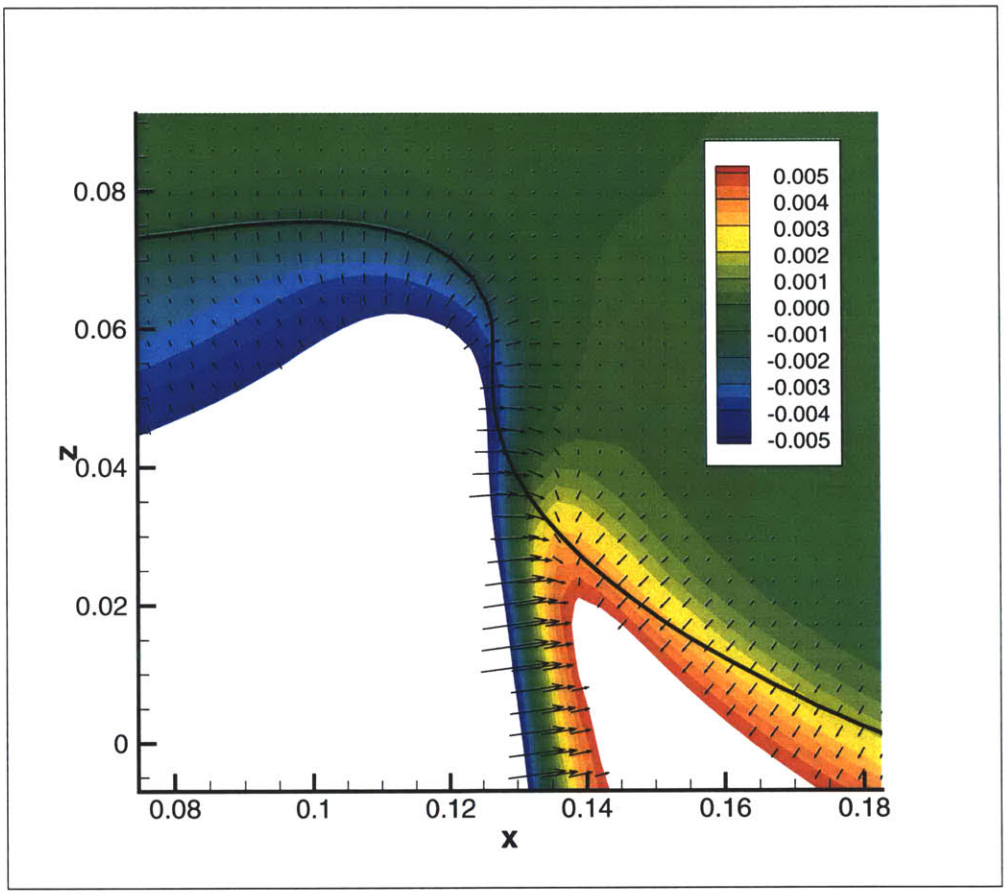

Figure 6-24: Instantaneous contours of the dynamic pressure field as jet is forming. Vectors represent ∇P_d and black line is the surface location.

vorticity due to the opposite sign of the curvature at that location. Throughout the formation of the jet, the vorticity is confined to a very narrow region near the surface and it is unlikely that the experiments by Perlin *et al.* [85] could resolve this vorticity with any accuracy.

It should also be noted that in comparison to the vorticity in the water, the vorticity in the air is significantly larger (by at least an order of magnitude). As discussed within the context of spilling breaking waves, the air generally experiences significantly larger vorticity due the curvature of the water surface and the separation it causes. In figure 6-25 it has been removed to focus on the vorticity in the water volume.

6.2.2 Jet Re-Entry and Breakup

The breakup of the jet in the case of ejection has not been widely studied in the literature. Longuet-Higgins [67] proposes that the disintegration of the jet in a plunging breaker is a two-stage process. The first is an inviscid mechanism which breaks the three-dimensional sheet of water transversely into fingers. This mechanism is caused by a rapid growth of perturbations as the jet becomes thin. According to Longuet-Higgins, this thinning of the sheet is accompanied by a drastic reduction in the normal pressure gradient in the jet. The second stage occurs relatively quickly once the fingers appear. During this stage, the fingers break up and form droplets through thinning.

While Longuet-Higgins theory is for a three-dimensional process (the breakup of sheet to fingers which then form droplets), some similarity between his theory and the breakup of the two-dimensional jets in this study can be seen. Figure 6-26 is a magnified view of the free-surface evolution shown in figure 6-20. Starting at the surface labeled (I), the jet is thin and continues to thin before it pinches off at $II \leq T \leq III$. At profile (II), the jet thickness is just greater than two grid points. Small cylindrical droplets form at the pinch-off point. At the moment before jet pinch-off, there are no perturbations on the surface where the jet is thinning. Thus, the mechanism for the jet breakup at this point is pinch off due to the thinness of the sheet.

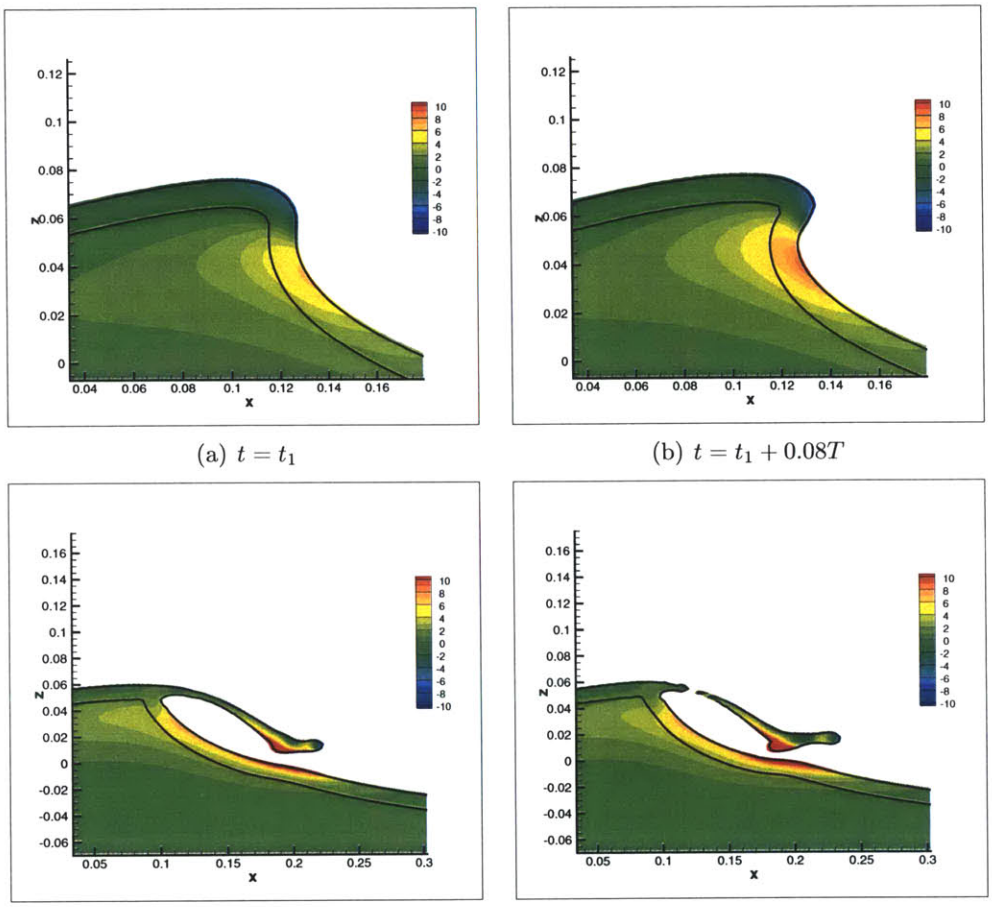

(a) $t = t_1$

(b) $t = t_1 + 0.08T$

(c) $t = t_1 + 0.44T$

(d) $t = t_1 + 0.48T$

Figure 6-25: Evolution of transverse vorticity ω_y for a plunging breaking wave which forms a jet. (case SFI-11) Black lines represent the boundary of the smoothed interface with the centerline the surface.

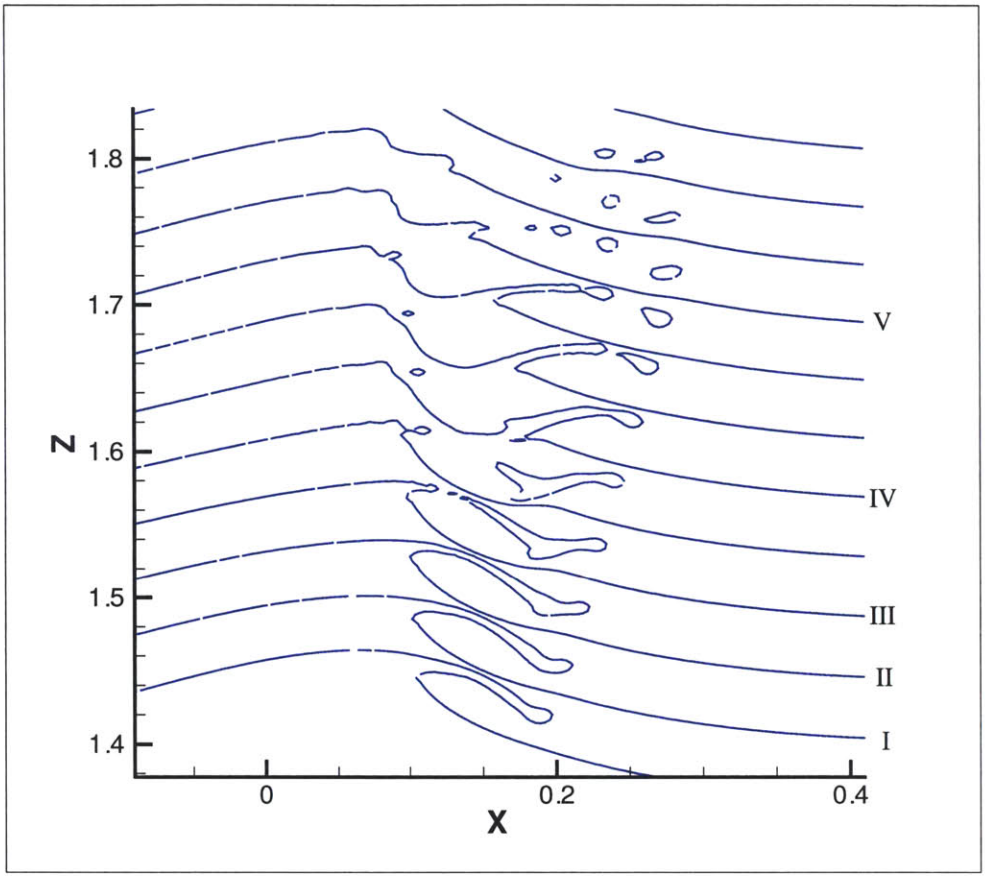

Figure 6-26: Enlarged view of breakup of jet in the ejection case (case SFI-11). Successive free surfaces are at $\Delta t = 0.1$. Vertical offset is $\Delta z_{off} = 0.04$.

One key to the jet breakup as cited in Longuet-Higgins paper [67] is a significant decrease in the pressure gradient within the jet. Figure 6-27 shows contours of the dynamic pressure in successive moments before the jet breakup. The range of the contours have been minimized to highlight the jet area and blanked out in the bulk flow. As the jet forms, there is a substantial decrease in the pressure field in the jet, especially at the pinch-off point. There is essentially no pressure gradient in the jet itself except at the very tip of the jet where curvature effects exist.

Once the jet has impacted the surface and caused a second ejection, the tip of the jet begins to see a perturbation on the upper and lower surfaces (c.f. figure 6-26 profile IV). The surface forms what is described by Taylor [116] (and subsequently

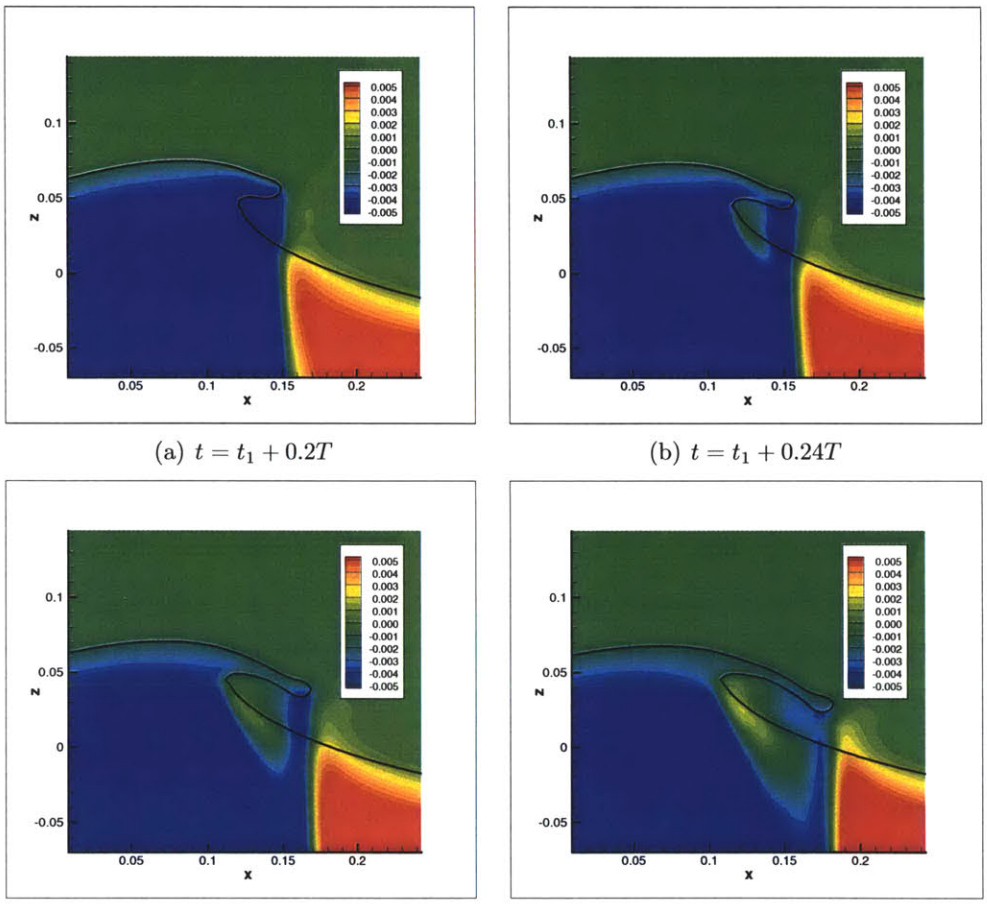

(a) $t = t_1 + 0.2T$

(b) $t = t_1 + 0.24T$

(c) $t = t_1 + 0.28T$

(d) $t = t_1 + 0.32T$

Figure 6-27: Instantaneous contours of dynamic pressure P_d prior to the jet breakup. (case SFI-11) Black line represents surface location.

Longuet-Higgins) as a symmetric perturbation. This symmetric perturbation grows, but not as quickly as the sheet thins. Thus, the sheet will quickly break into droplets. This is seen at profile V where the sheet has broken into four droplets.

For the case where the jet entrains air, this type of pinch off and jet breakup does not occur during the first plunging event. Instead, the jet stays in tact. Figure 6-28 shows the surface evolution during this initial phase for a plunging case which later entrains air. Compared to the ejection in figure 6-26, the jet in this case is considerably thicker and more rounded. It re-enters the water surface and causes a second jet to form. The second jet is somewhat more similar to the ejection jet in figure 6-26. As it lengthens and thins, the tip of the jet begins to show signs of perturbations which later pinch off and form droplets.

Figure 6-29 shows contours of the dynamic pressure shortly after the first impact event and the jet ejection. At the point of impact, there is a region of significant pressure which has resulted from the impact force of the jet on the surface. Inside both the first and second jet there is little pressure gradient except at locations of extreme curvature due to surface tension effects. The beginnings of the initial pinch off of the second jet is also visible in this figure.

Figures 6-30(a) and 6-30(b) show the extent of the jet impact on the flow field. Within the reference frame moving with the crest, there is very little influence of the jet re-entry on the underlying bulk flow beneath $z/\lambda = -0.1$. This compares well to the experimental measurements of Bonmarin [8] where it is stated that the penetration of the jet does not impact the bulk flow significantly.

The evolution of the (normalized) stresses from the formation of the jet through jet breakup is shown in figures 6-31 through 6-34. As the two normal components are equal and opposite due to continuity, only one of the normal components is shown here. At the point of jet formation (figure 6-31), there is a concentration of normal and shear stresses at the concave section below the point where the jet forms. unlike the case of strong spilling breaking waves where the shear region almost reaches the entire extent of the wave crest, the shear region is considered a local region. This localized region persists as the jet impacts on the front face of the wave (figure 6-32).

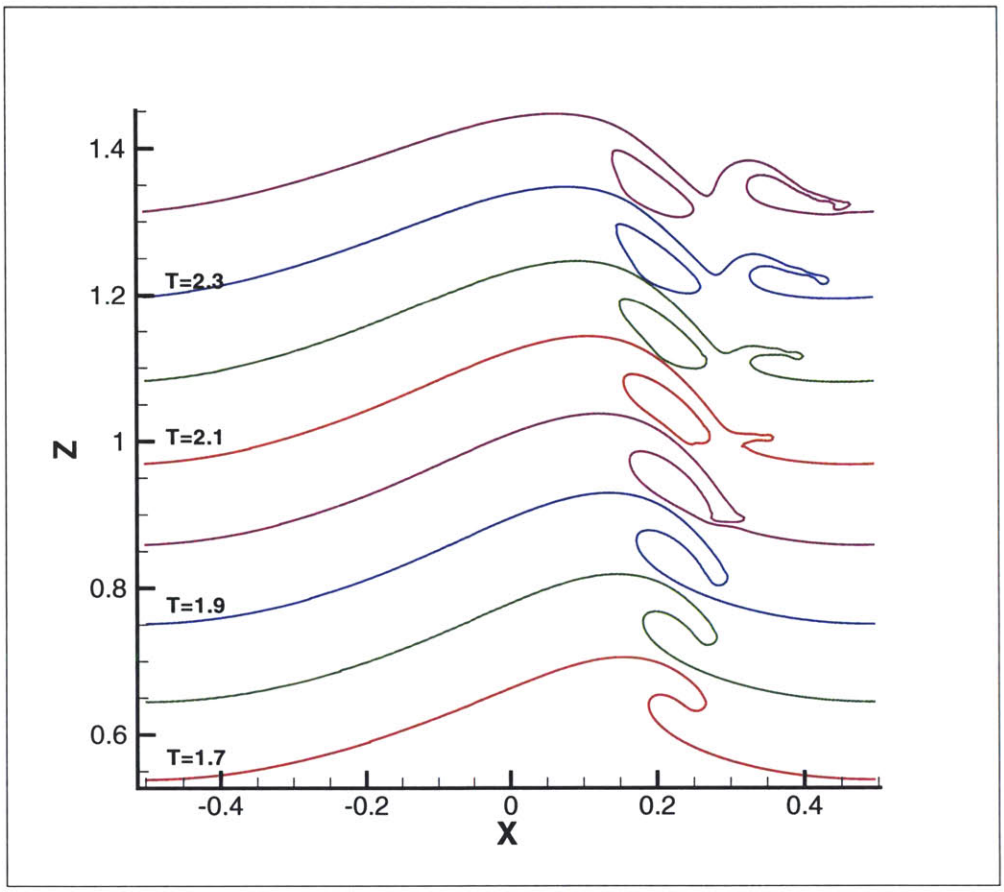

Figure 6-28: Air-water interface during initial plunging event (case IAW-10). Shown at every $\Delta t = 0.1$. Color represents the surface at different times.

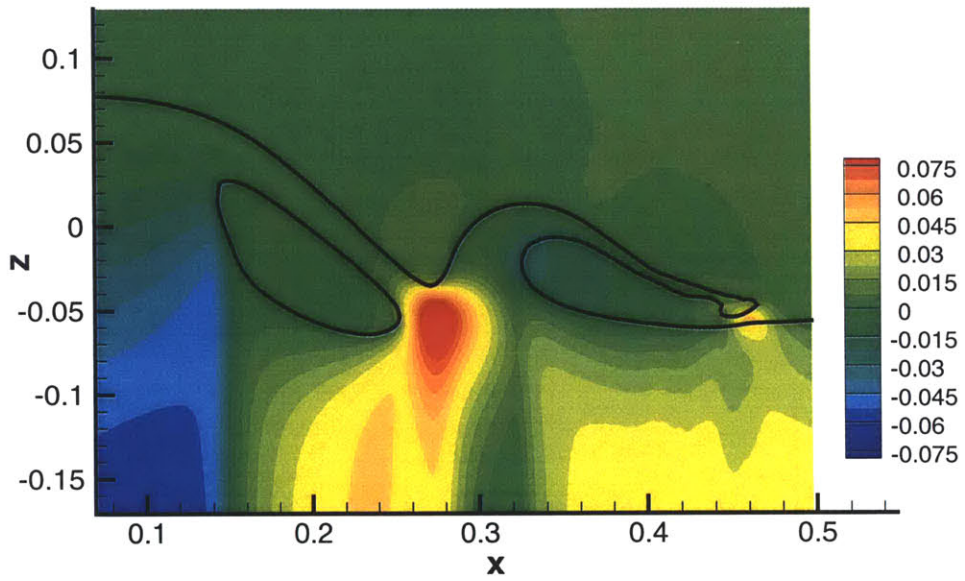

Figure 6-29: Dynamic pressure P_d after first impact event and ejection. (case IAW-10) Black line represents air-water interface.

Additionally, at the point of impact, as is to be expected there is another region of strong stresses (normal and shear). The jet itself is generally free of stresses except near where it has impacted the surface. Shortly after the first impact event (see figure 6-33), the localized region of shear stress at the point of the first jet formation has disappeared. Yet, this region still persists in the normal stresses.

At the point of impact, the character of the normal stresses has changed. Where it was initially a single localized region of positive (for τ_{11}) normal stresses, it now has two distinct regions. Underneath the point of the second ejection, a negative (again for τ_{11}) region of normal stresses has formed. This change in sign is appropriate. As at the point of the first jet formation, there was a strong positive region of $\frac{\partial u}{\partial x}$ showing that the jet formed was generally horizontal. At the point of second ejection, the jet motion is more vertical, thus a strong positive region of $\frac{\partial w}{\partial z}$ is present.

Also of note, unlike the first jet at this point in time, the second jet is not free of normal stresses. The shear stresses in the region of the second jet are similar to the first jet in that there is a localized region at the cusp of the jet and the jet is generally

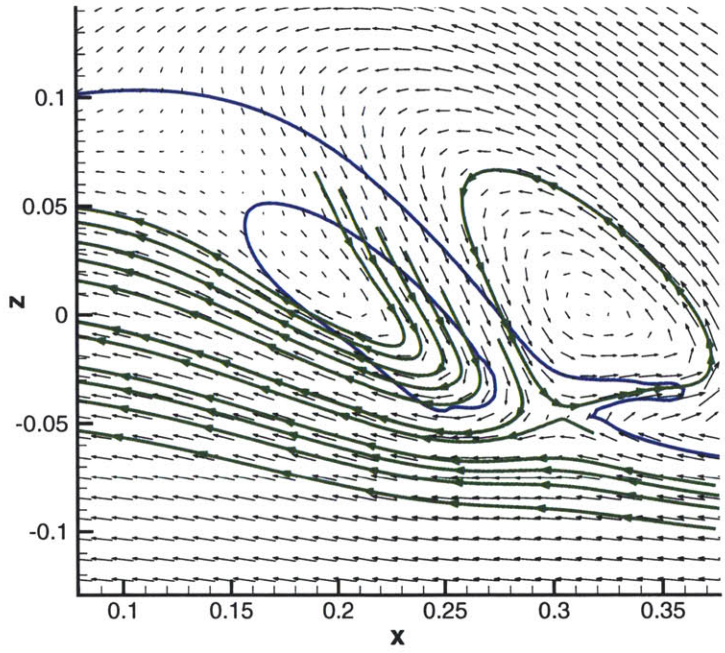

(a)

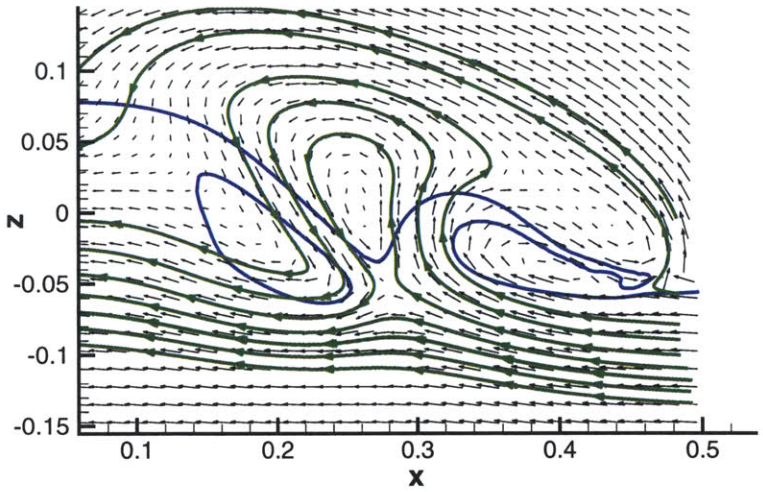

(b)

Figure 6-30: Instantaneous velocity vectors (every 3rd) and stream lines (green) during jet re-entry and second jet ejection in the reference frame of the crest. Blue line represents air-water interface. (case IAW-10)

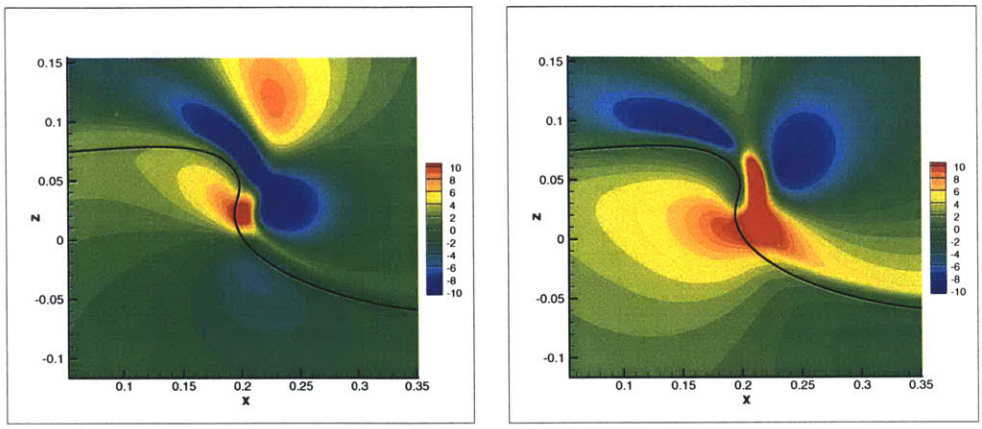

(a) τ_{11} (b) τ_{13}

Figure 6-31: Normalized stress components at jet formation. Black line represents the air-water interface. (case IAW-10)

shear stress free. Well after the jet formation and re-entry/breakup point (see figure 6-34), there are very little normal stresses at the surface while there is a thin layer of increased shear stresses at the surface.

6.2.3 Air Entrainment

This section briefly discusses the air entrainment which occurs in the plunging breakers in this study. In laboratory experiments and the field, plunging breaking waves entrain a significant amount of air as the pocket of air trapped by the plunger collapses. The air entrained is a significant source of noise in the ocean and contributes to the increased dissipation seen in plunging breaking events [55]. Yet, little is known about the entrainment of air during the breaking event as it is a difficult measurement to do accurately. Most experiments center on measuring the void fraction (or amount of air in the volume) after the wave has broken.

Even in experiments where the wave is initially two dimensional, the collapse of the air pocket under the plunging breaking wave is certainly a three-dimensional effect. Additionally, the air in the pocket is actually a compressible fluid. The waves in this study were generated using a two-dimensional model which assumes that both fluids are incompressible. Because of these modeling assumptions, the resulting air

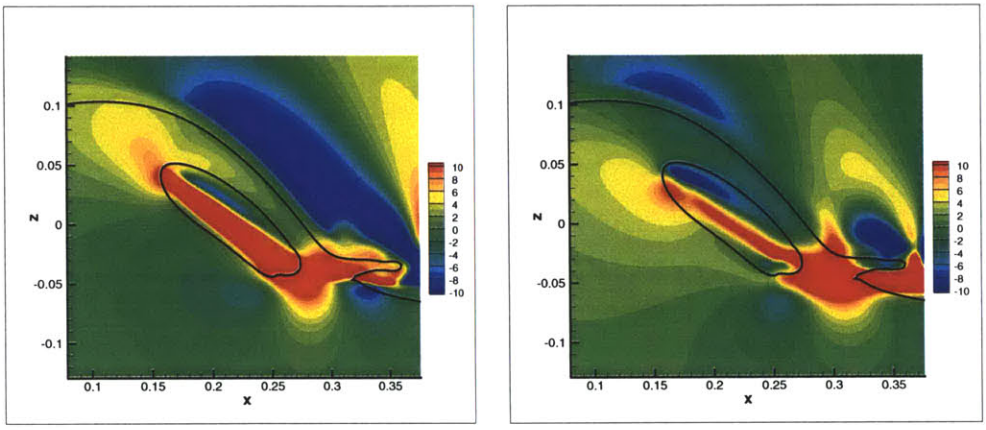

(a) τ_{11} (b) τ_{13}

Figure 6-32: Normalized stress components at jet impact. Black line represents the air-water interface. (case IAW-10)

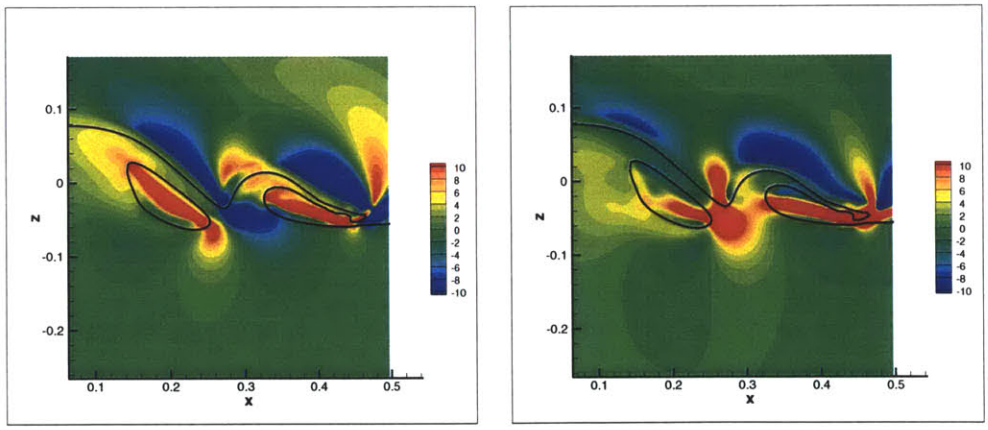

(a) τ_{11} (b) τ_{13}

Figure 6-33: Normalized stress components at jet impact. Black line represents the air-water interface. (case IAW-10)

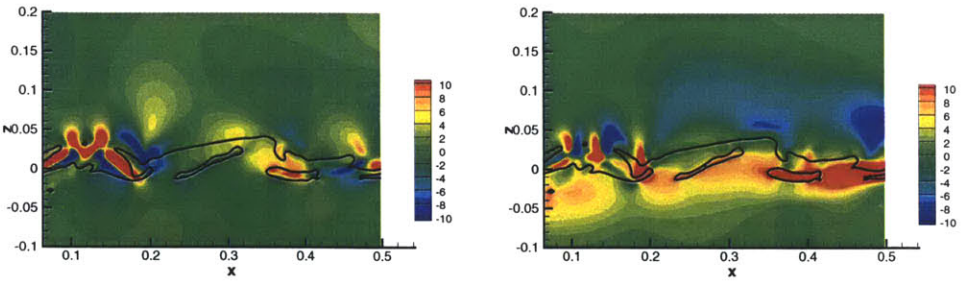

(a) τ_{11} (b) τ_{13}

Figure 6-34: Normalized stress components well after jet re-entry and breakup. Black line represents the air-water interface. (case IAW-10)

pocket and bubbles will be artificially stiffer. As the air pocket collapses, there is no third dimension to allow the air to escape. As bubbles rise to the surface due to buoyancy, there is also no compressibility effect which allows them to change their size naturally. Thus, the air entrainment in the waves in this study must be discussed within the context of these limitations and direct comparisons to the literature and real-life experiences is not appropriate.

Figures 6-35 through 6-37 show the progression of the plunging breaking wave shown in figure 6-28. Firstly, the influence of the standing wave is seen clearly in figure 6-35. It should be noted that this case which has air entrainment is also one of the cases generated by the impulsive airy wave method (see section 4.1) which has over 30% of its energy represented by a standing wave. The decrease in wave amplitude at the crest and the upwelling of the plunging region are signs of the presence of this standing wave. This significantly deforms the shape of the plunging region. However, the formation of a bubble from the collapse of the first air pocket can be seen. It has been labeled "a" in figures 6-35 through 6-37. This bubble can be traced through time as it slowly rises but becomes unresolvable before it reaches the surface.

During the plunging event, the shape of the plunging region has been deformed by the presence of the standing wave such that we have no clean record of the collapse of a plunging region and the secondary jet events. This makes it difficult to compare even qualitatively to what is available in the literature. However, Bonmarin [8] describes the re-entry and ejection event as having two possible modes. The first is where

the rear part of the splash-up flows over the falling crest. The second is where it moves back into the original penetrating crest (see Bonmarin figure 25) affecting the air entrainment. While the motion is clearly affected by the standing wave, the secondary jet can be seen to move back into the original penetrating crest in figure 6-35.

As the air pocket collapses, large bubbles form as the air pocket pinches off from the air volume (see figure 6-36). Some of these bubbles form smaller bubbles as they rise to the surface (such as bubble "b"). Other bubbles simply rise to the surface and burst (such as bubbles "c", "d" and "f"). The sheet which forms after a third impact event (labeled as "e"), finally thins enough where droplets begin to form from it in a similar manner to the jet ejection discussed in section 6.2.2. A period or so after the plunging event, there is very little air which remains beneath the surface.

6.3 Spectrum Evolution of Breaking Waves

In regards to the literature available for breaking waves, many of the experiments look at the evolution of the spectrum prior to and after the breaking event. This is highly desirable as it gives information on how the breaking event effects the spectrum. This type of information is as invaluable to wave forecasting and spectrum evolution as wind input or breaking criteria. The modeling focuses on the frequency spectrum and experiments are well matched to this as at every location they have a wave probe measurement which gives the surface deformation as a function of time. The wave focusing experiments use broadband input spectrums on the order of 30 wave frequencies. This is the case with the top-hat spectrum used by many authors [92, 80, 54]. The energy lost from the input spectrum tends to be near the upper end. This has brought the authors to conclude that low frequency waves persist through breaking.

The waves generated in this study contain primarily 2-3 discrete wave modes. This makes it difficult to draw direct comparisons. However, a common thread in the experimental results which we can see as well is an increase in energy in higher

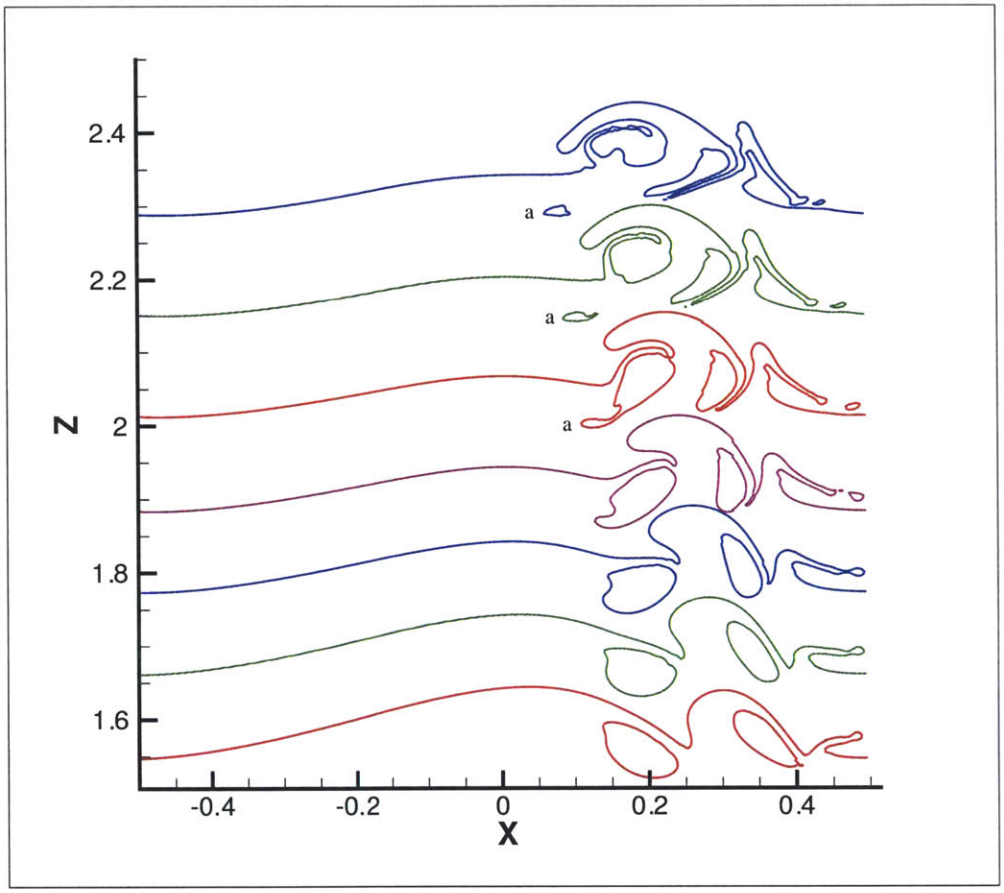

Figure 6-35: Progression of the plunging breaking wave with air entrainment. (case IAW-10). Each color represents the air-water interface at a given time.

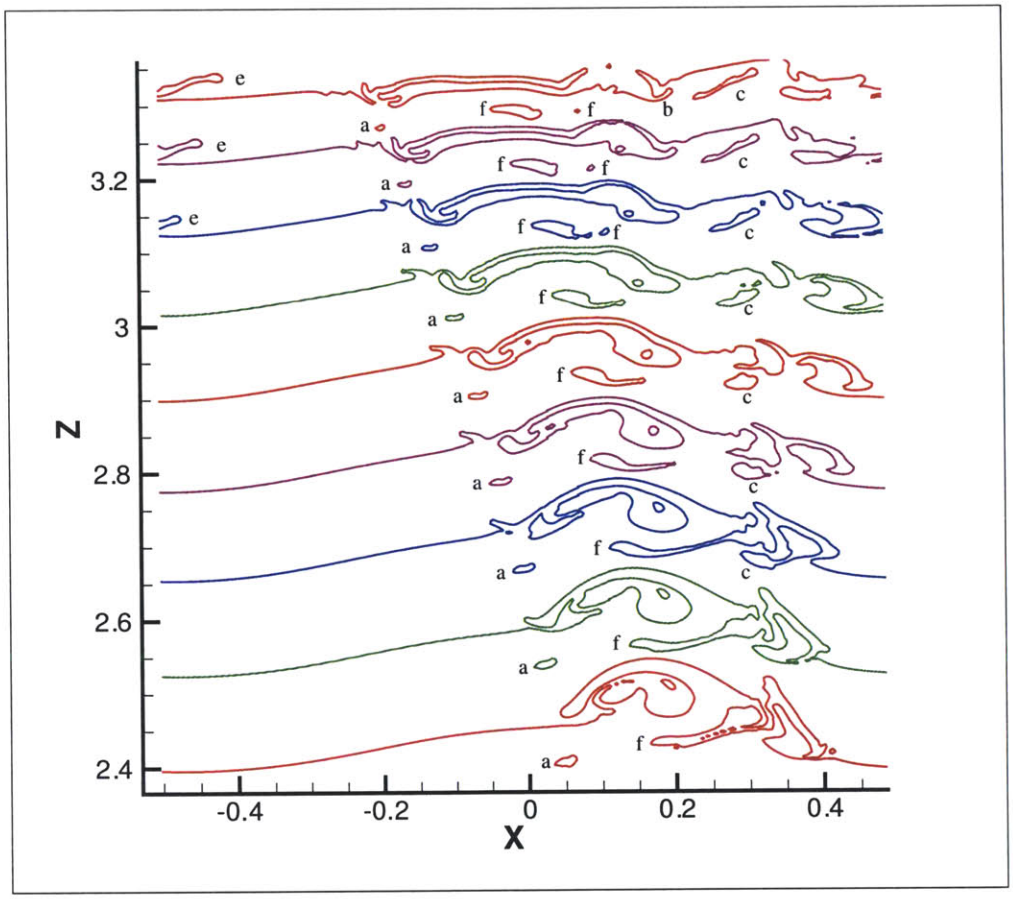

Figure 6-36: Progression of the plunging breaking wave with air entrainment. (case IAW-10). Each color represents the air-water interface at a given time.

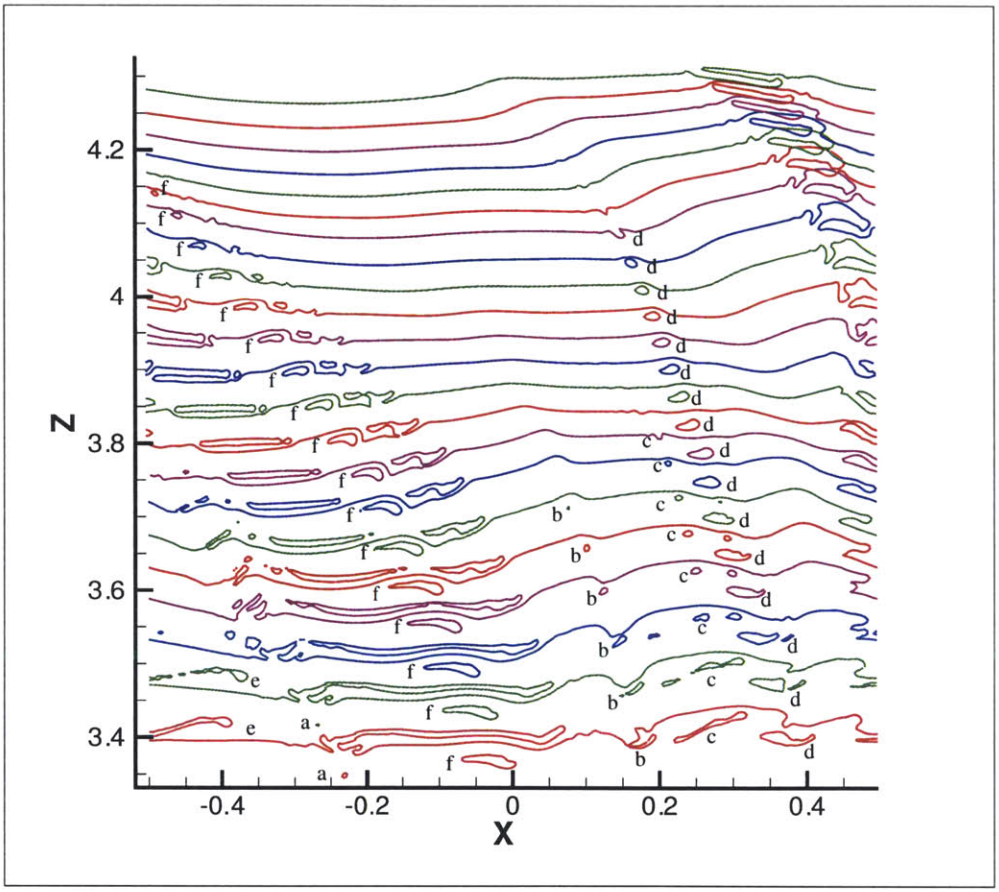

Figure 6-37: Progression of the plunging breaking wave with air entrainment. (case IAW-10). Each color represents the air-water interface at a given time.

frequencies as the breaking event is approached and a decrease in this energy after it has happened. This section discusses the evolution of the spectrum as a function of wavenumber before and after the breaking event as well as throughout (when applicable).

For this analysis, the amplitude spectrum is calculated using a Fast-Fourier Transform (FFTPACK [114]) of an interpolation of the air-water interface at every available time step. No effort is made to stop the transform process if the surface becomes multi-valued. Regions where the Fourier transform are invalid are noted in the respective figures and text as necessary. It should also be noted here that for the waves in this study and in experiments, the spectrum is only a measure of the potential energy in the flow field. As the spectrum is taken throughout the breaking process, arguments regarding the use of equipartition of energy do not apply.

To establish a baseline of comparison, the first investigation of the spectrum evolution is a case between a wave which does not break and one which has been classified as incipient breaking. The incipient breaking case has no surface forcing, thus any change in the energy is due to the wave breaking naturally. The first four modes of the amplitude spectrum are shown as a function of time in figure 6-38.

The incipient breaking event begins between T=1 and T=1.5 and lasts until T=6. The surface never becomes multi-valued in this case thus the spectrum is applicable for the entire time of the simulation. Up until the breaking event, the first and second modes of the non-breaking and incipient-breaking waves are essentially the same. A very small difference appears at breaking onset in the first and second modes. This difference becomes more pronounced in the third and fourth modes. This continues through the breaking event. After the breaking event, there is a small amount of energy lost in the first and second modes and which becomes more significant again in the third and fourth modes. Well after the breaking event, the modes return to a similar behavior as the non-breaking wave. There is a modulation in time for both only in the incipient-breaking case, this modulation has shifted phase compared to the non-breaking case.

Thus, to summarize, even in the incipient breaking case, there is a shift in energy

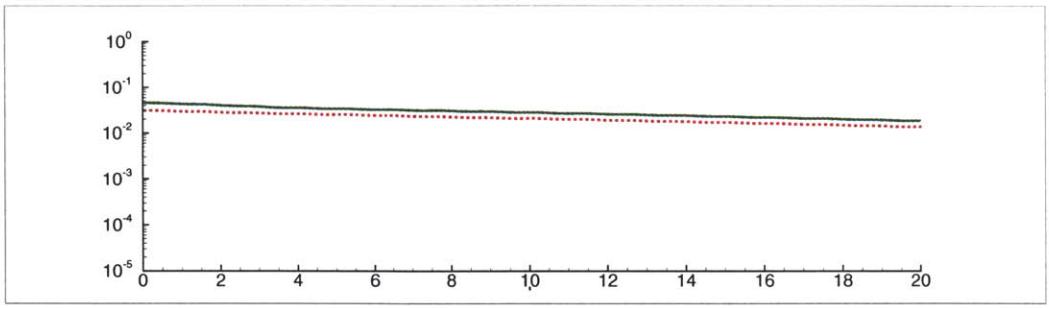

(a) Mode 1

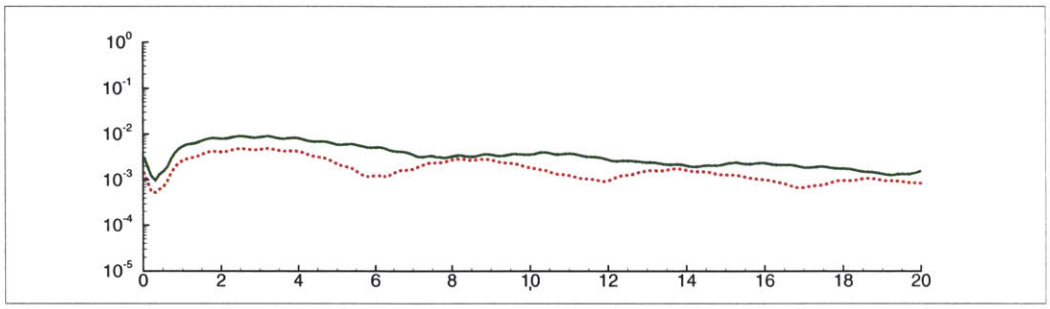

(b) Mode 2

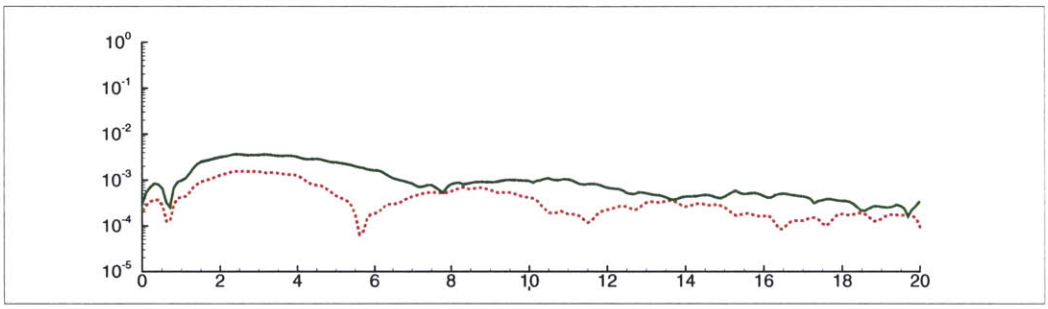

(c) Mode 3

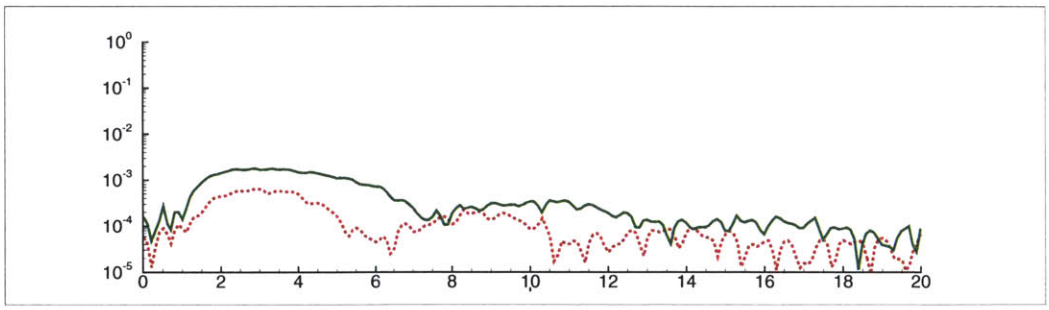

(d) Mode 4

Figure 6-38: Modes for a non-breaking wave (case A2P-01) and an incipient-breaking wave (case A2P-03).

from the lower wave numbers to the higher ones prior to the breaking event. Then, as a certain amount of energy has been lost to breaking, all of the modes see a decrease energy associated with the energy lost to breaking and essentially return to a characteristic behavior similar to a non-breaking wave.

The normalized spectrum amplitudes for the first ten modes of the spectrum for a non-breaking and gentle-spilling breaking wave are shown in figure 6-39 in a different format. Shown are the contours of the normalized energy at each wave number as a function of time:

$$E(k,t) = \frac{A_k^2(t)}{2E(t_{ref})} \tag{6.4}$$

where the normalization is the total energy in the wave at a reference time t_{ref}

$$E(t_{ref}) = \frac{1}{2}\sum_{\text{all k}} A_k^2(t_{ref})$$

The breaking event for the gently spilling case lies within the dashed box. Inspection of the evolution of the free surface for this case yields that there is no multi-valued region of the surface such that the spectrum is valid throughout the simulation. The normalized spectrums are similar for the two types of waves. However, just prior to the breaking event, there is a slight shift in the energy from lower to higher wavenumbers, in particular for modes greater than the second mode. After the breaking event, there is an associated decrease in energy at all wavenumbers and a discernable shift in the phase of the modulation for wave modes greater than 2. Thus, the gentle-spilling waves see the similar behavior as the incipient-breaking case where there is a shift in energy from low to high wavenumbers prior to breaking and an overall loss of energy at all wavenumbers after breaking.

If we consider the amplitude spectrums for a gently spilling breaking wave and a wave which forms a jet, the breaking effect is much more apparent. Figure 6-40 shows the actual amplitude spectrum $A(k,t)$ as a function of wavenumber and time for two cases which originated from surface forcing (SFI). The only difference in the

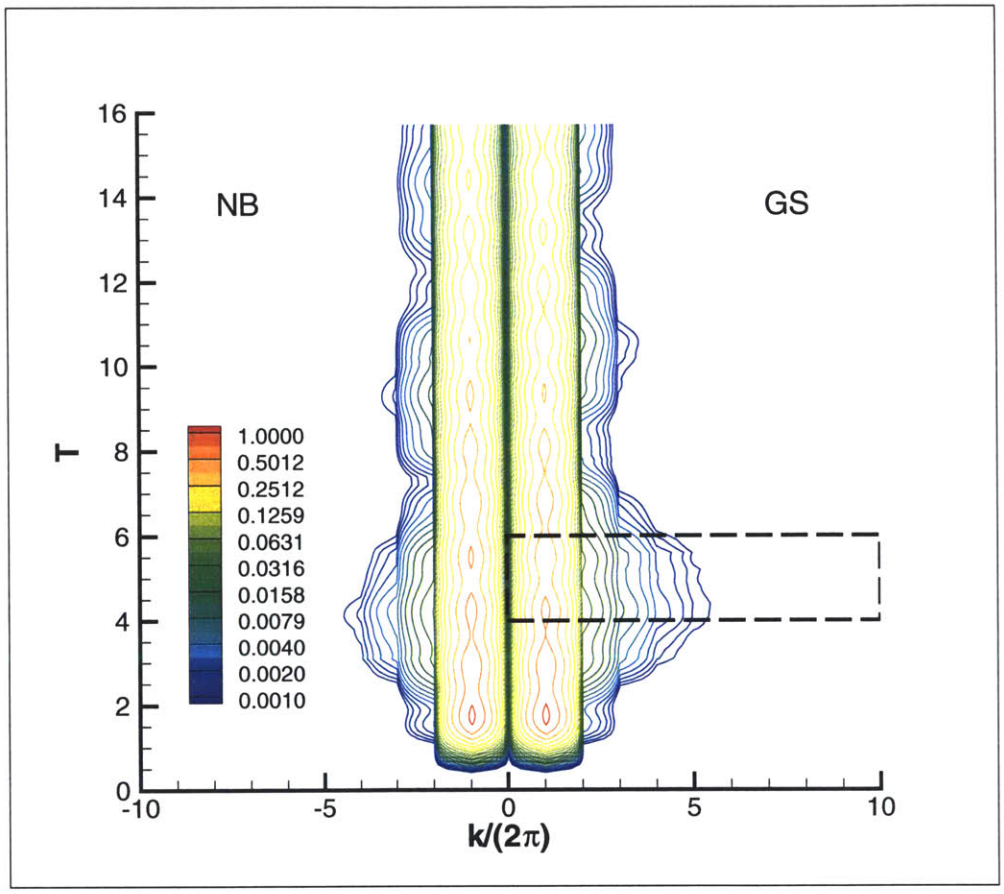

Figure 6-39: Normalized modes (eqn. 6.4) for a non-breaking wave (case SFI-05) and an incipient-breaking wave (case SFI-02).

two cases is the magnitude of the surface forcing (or the amount of energy input into the surface). This is evident at the time the surface forcing has been removed (T=2.09) in which the case which forms a jet has more energy in the first mode. For both cases, the breaking event occurs between $4 \leq T \leq 6.5$. The gentle-spilling case is the same case shown in figure 6-39 and does not generate a multi-valued surface. By definition, the jet formation does. Inspection of the free-surface elevation for this case shows that the spectrum is valid between $4.0 \leq T \leq 6.2$. Prior to the breaking event, the build-up of energy at the higher wavenumbers is considerably more prevalent than in the gentle-spilling case. The primary mode sees a decrease in energy prior to breaking which implies that the energy is being shifted from the lower wavenumber to the higher ones in the period before breaking. After the breaking event, the jet has actually less energy in the first mode than the gentle-spilling case which can be seen in figure 6-40 by judging the width of the band of the contour at T=7. It can be seen in figure 6-41 which shows the energy in the entire spectrum calculated as in equation 6.4 for every available time step. In this figure, it is clear that the jet actually has less overall energy than the gently spilling breaker after the breaking event.

In summary, the spectrum evolution has been considered throughout the breaking event for the waves in this study. For all of the cases, there was a shift in energy from lower wavenumbers to higher wavenumbers. The amount of energy and extent of the shift was highly dependant upon the type of breaking event. This shift of energy from low to high wavenumbers is key in the development of the wave steepness and asymmetry. After the breaking event, the energy lost was distributed across all significant wavenumbers. In particular, for the plunging breaking waves, the amount of energy which remained in the spectrum after the breaking event was less than the amount of energy in the gentle-spilling event.

Comparisons to the literature can only be qualitative. The waves generated in this study are very narrowbanded and have $O(2-3)$ discrete wave modes present whereas the wave groups generated for wave focusing experiments generally include $O(30)$ wave frequencies in their initial wave spectrum. Yet, despite the difference in the number of frequencies represented, there are similarities between the breaking

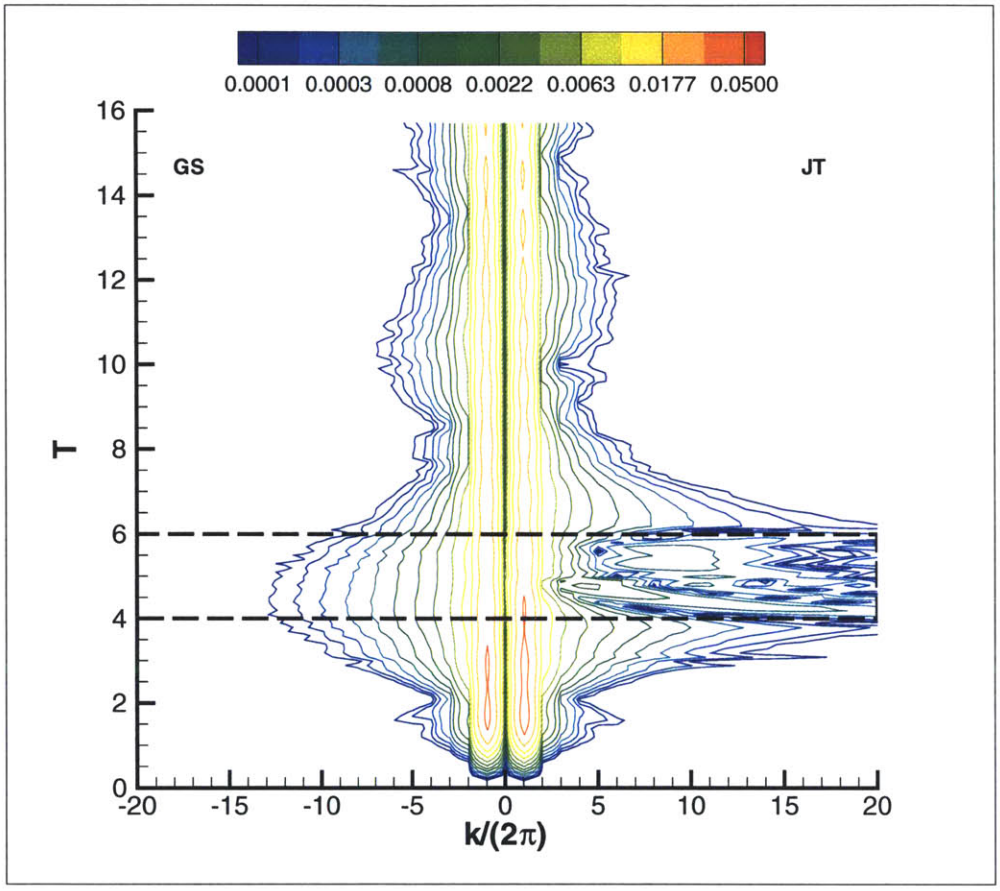

Figure 6-40: Amplitude spectrum $A(k,t)$ as a function of time for a gently spilling breaking wave (case SFI-02) and a plunging-breaking wave which forms a jet (case SFI-06).

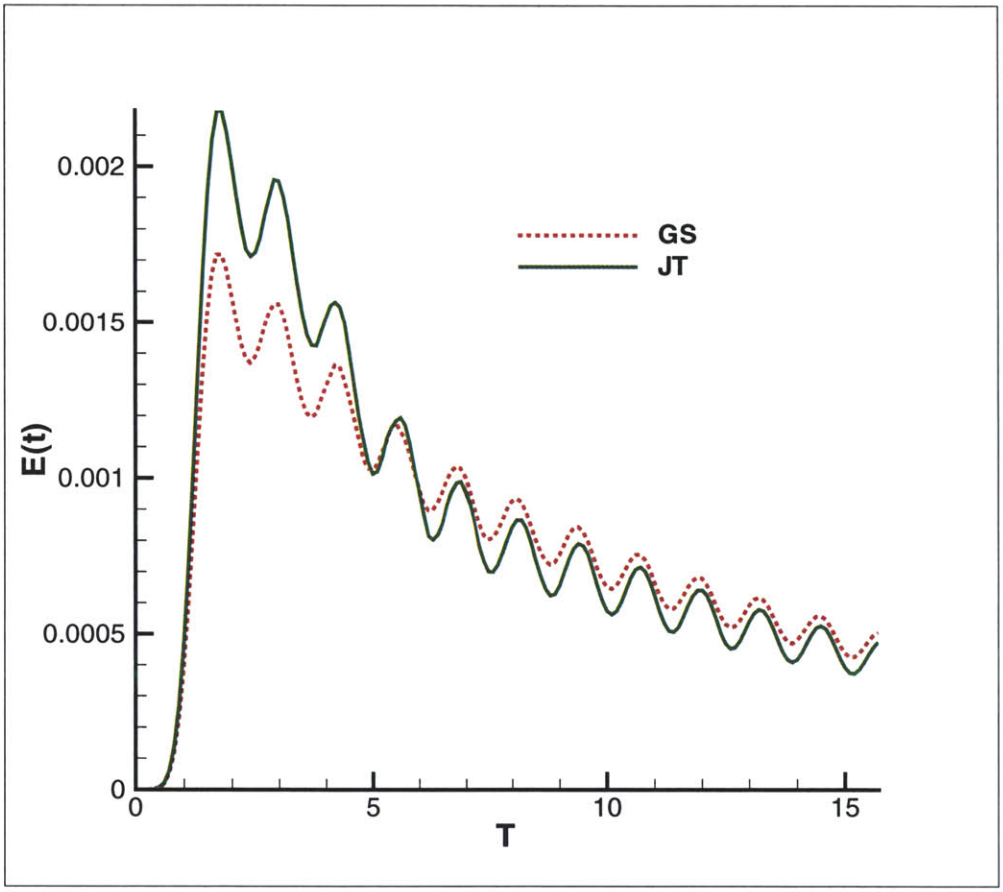

Figure 6-41: Total energy in the amplitude spectrum E(t) from equation 6.4 for a gently spilling breaking wave (case SFI-02) and a plunging-breaking wave which forms a jet (case SFI-06).

waves in this study and that reported in the literature.

In general, prior to the breaking event, there is a notable decrease in energy at the upper end of the primary input spectrum (in many cases this is a top-hat shape). This is coupled with an increase in energy at frequencies above this input spectrum. This can be seen in the waves in this study. In particular, it is evident in figure 6-40 (e.g. $T \sim 3$) where there is an actual decrease in the amount of energy in the first mode near breaking onset and a buildup of energy at much higher wavenumbers.

In wave focusing experiments, after the breaking event, the increased energy at higher frequencies still exists and takes about a period to dissipate. This can also be seen in figure 6-40. The non-dimensional period for the wave on the right of figure 6-40 is approximately 2.5. Within one wave period, the built-up energy in the high wave modes has dissipated to below pre-breaking levels. In Rapp and Melville [92], at a distance well away from the breaking event, the wave had lost about 90% of the energy which had built up in the higher frequencies. They also reported that 24% of the primary input spectrum had been lost as well, almost entirely from the high end of the input top-hat band. While almost all of the energy has been lost from the higher wave modes in the waves in this study, it is difficult to directly compare the amount of energy lost from the primary input spectrum. Yet, as will be seen in chapter 7, the amount of potential energy lost to the breaking event compares well with experiments so it is not a stretch to say that if the waves in this study had a larger input bandwidth that similar results would have been seen.

6.4 Conclusion

In this chapter, we've shown the kinematics and dynamics of the spilling and plunging breaking waves in this study as well as their spectral evolution. For spilling breaking waves, the formation of the bulge was detailed and compared to that in literature. This included comparisons of geometric quantities such as steepness and asymmetry factors.

The velocity field associated with the bulge was also described. Through investi-

gation of the velocity field and stresses in both the air and the water, we determined that the there was no flow reversal in the wave for either gently-spilling or strong-spilling breaking waves. Yet, in the air flow as the wave face became more prominent, the air flow experienced flow separation at the toe of the bulge and the back face of the wave. All of the separation and vorticity in both fluids was attributed to curvature effects as the surface parallel velocity field tried to follow the shape of the wave. The vorticity flux was shown to support this conclusion. It was also found that, unlike the localized shear region seen in gently-spilling breakers at the bulge, a significant shear layer existed in strong-spilling waves that reached almost the extent of the wave crest.

Finally, the capillary wave train seen in experiments for gently spilling breaking waves which were not seen in this study was also discussed. Reasons for their lack of appearance in this study ranging from physical quantities and issues related to scaling to numerical resolution and use of a smoothed surface were discussed. The capillary wave train is attributed to the movement of the bulge down the front face of the wave and an associated flow reversal as this occurs. As these phenomena do not occur in the spilling breaking waves in this study, we are not entirely surprised that the wave train is not seen.

A detailed investigation of the formation of the jet for two types of plunging breaking waves was performed. It was found that a large pressure gradient appeared at the point of the jet formation as well as an increased speed of the crest relative to the phase speed of the wave. These are both consistent with findings in the literature. A region of stresses and vorticity occur at the jet formation location. Unlike the strong spilling breaking waves, this region is very localized. Some experimental results show that plunging breaking waves are irrotational up until the breaking event. We have shown that the region of vorticity which does exist prior to the jet formation is very thin and likely not resolved by current experiments. However, based on arguments regarding curvature effects, the flow must be rotational in the regions where we have found vorticity.

The impact of the jet on the front face of the wave as well as its pinch off and

breakup were also described in detail. For the waves in this study, the re-entry of the jet on the wave surface had little effect on the velocity field in the bulk. The stresses and vorticity associated with this impact are also contained to a very thin region near the surface. While the pinch off of the jet from the wave is caused by a thinning of the surface, the breakup of the jet is similar to what is described in the literature by Taylor and subsequently Longuet-Higgins. The breakup of the jet into cylindrical droplets occurs as a symmetric perturbation on the upper and lower surfaces of the jet forms. The perturbations grow and the jet thins and thus the droplets are formed.

A brief discussion within the context of the limitations of this study of the air entrainment for the waves in this study was also provided. The bubbles are formed as regions in the air pocket pinch off. These bubbles either become unresolvable, breakup into smaller bubbles or burst at the surface. One to two periods after the breaking event, there are essentially no bubbles left in the wave. As the bubbles in this study are considered overly stiff, no comparison to the literature was attempted.

Finally, the evolution of the spectrum throughout the wave breaking event was also discussed. We showed that there was a loss of energy at low wavenumbers prior to breaking which corresponded to an increase in energy at higher wavenumbers. These higher wavenumbers are essential to developing the wave steepness necessary for the wave. The energy remains in the higher wavenumbers for approximately one wave period after the breaking event before it is fully dissipated. This behavior and the potential energy loss is consistent with findings in the literature.

Chapter 7

Energy Loss Due to Wave Breaking

The amount of energy lost due to wave breaking has been a long sought after quantity as it has a wide range of applications. In the context of wave forecasting, determining a breaking criteria and an associated energy dissipation would allow models to better accurately predict the evolution of wave spectrums. In the context of ship wave breaking, the capability of modeling breaking ship waves is critical in accurately predicting the near field flow of a surface ship.

This chapter details the energy loss due to wave breaking by drawing on the waves in chapters 4 and 6. As this study uses direct numerical simulation, no turbulence closure models have been used to assume anything about the dissipation. Additionally, because it has the solutions for both the water and air volume, it provides unique insight to the vortical dynamics and dissipation in the air. In section 7.1 we detail the dissipation rates for both volumes spatially and temporally. To the best of our knowledge, this section provides a first ever look at these quantities *during* the breaking process. Section 7.2 details the total amount of energy lost due to breaking using a control volume approach which is popular in the current literature. Comparison to available experimental data from the literature is detailed in section 7.3. Finally, we briefly explore the existence of a wave breaking criteria based on recent work in the literature which is based on the theory of a local mean convergence in the flow in section 7.4.

7.1 Dissipation Rates

This section details the dissipation rates of breaking (and non-breaking) waves for both air and water, for the various types of waves which are a part of this study (non-breaking, gentle-spilling, strong-spilling, jet-forming and air-entrainment). To our knowledge, this study has provided the first detailed view of the spatial and temporal variation of the dissipation rates *during* the breaking event. While some cases in the literature have attempted to provide global estimates and decay rates for the water volume [74], there is no evidence that this has been done for the air. Through this study, we have found that there is an increase in magnitude of the dissipation rate during the breaking process for both air and water and the amount of increase is dependent upon the type of breaking wave generated. For most cases, the relative increase is more in the air than the water. In fact, for some cases where the surface deformation is large causing significant separation in the air, the dissipation rate in the air is of the order of that of the water during the breaking process. In addition to the highly unsteady nature of the dissipation rate, a correlation to the strong dissipation rates in both fluids and regions of separation as well as a local persistence of increased dissipation post-breaking in some regions are identified.

7.1.1 Calculation of Dissipation Rate

Section 2.4 of this thesis contains the derivation of the energy equation for a volume containing multiple incompressible fluids so the derivation will not be repeated here. The term responsible for the dissipation by viscosity is:

$$\varepsilon = \frac{1}{\mathcal{R}e_w}(\tau \cdot \nabla)\vec{\mathbf{u}} \tag{7.1}$$

The stress tensor is given in equation 3.7 as $2\mu(\phi)S_{ij}$. Putting this into equation 7.1 yields the energy dissipated per unit volume of fluid.

$$\varepsilon = 2\frac{\mu(\phi)}{\mathcal{R}e_w}S_{ij}\frac{\partial}{\partial x_j}u_i \tag{7.2}$$

or using continuity

$$\varepsilon = 2\frac{\mu(\phi)}{\mathcal{R}e_w}S_{ij}^2 \tag{7.3}$$

To calculate the energy dissipated in each fluid, the dissipation per unit volume is multiplied by either the smoothed Heaviside function $H(\phi;\epsilon)$ to extract the water or $1 - H(\phi;\epsilon)$ for the air.

$$\begin{aligned} \varepsilon_w &= H(\phi;\epsilon)\varepsilon \\ \varepsilon_a &= (1 - H(\phi;\epsilon))\varepsilon \end{aligned} \tag{7.4}$$

For consistency in the calculation of $H(\phi;\epsilon)$ the level set boundary layer thickness ϵ is the same as that used in the simulations. Integrating $\varepsilon, \varepsilon_w, \varepsilon_a$ in space will give the total dissipation rate for the entire volume, water and air, respectively. Integrating any of the total dissipation rates in time will give the total amount of energy dissipated by viscosity. For the purpose of this work, the volume integration of the dissipation rates is done through biquadratic integration and time integration is done through a cumulative trapezoidal integration scheme. The volumetric rates were calculated with enough frequency in time such that the difference between a trapezoidal scheme of $O(\Delta t)$ and Simpson's rule scheme $O(\Delta t^2)$ is minimal.

Figure 7-1 shows the dissipation rate per unit volume over the entire volume for a non-breaking wave. Figure 7-2 shows the total dissipation rate as a function of time for the entire volume and the water and air volumes. The method of extraction is consistent with the volumetric results on a per-unit volume basis as well as integrated over the entire volume.

7.1.2 Spatial Variation of Dissipation Rate

For non-breaking cases, the dissipation rate per unit volume is fairly uninteresting. Figure 7-3 shows the distribution of the dissipation rate in the volume for another non-breaking wave. The local decrease of the dissipation rate at the crest is believed

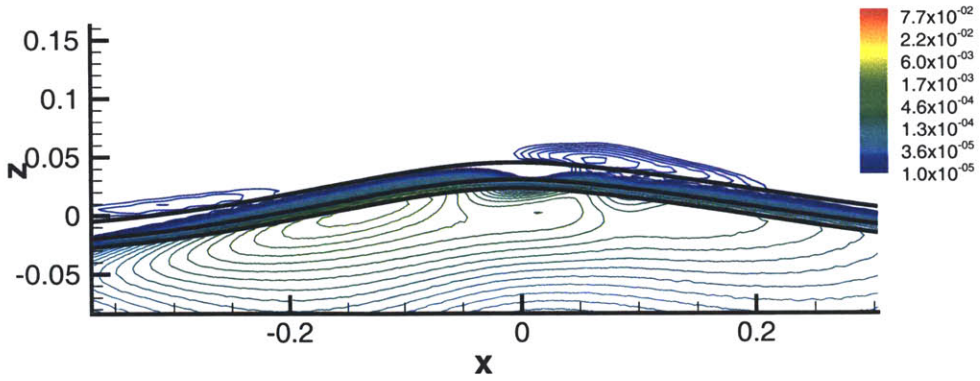

Figure 7-1: Spatial variation of the dissipation rate per unit volume over the entire volume for a non-breaking wave initialized from the two-phase airy wave (case A2P-01).

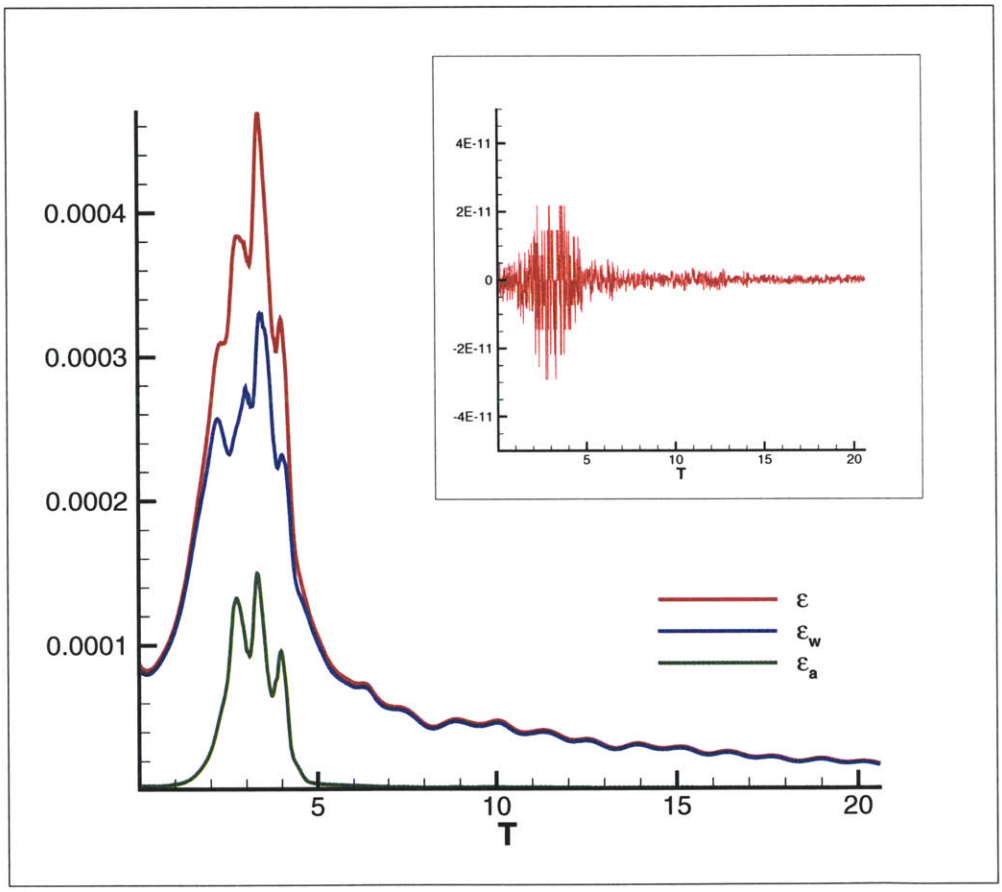

Figure 7-2: Total dissipation rate ε (red) and the extracted components ε_w (blue) and ε_a (green) for forced Airy wave (case A2P-16). Inset is difference between the total and the sum of the extracted components.

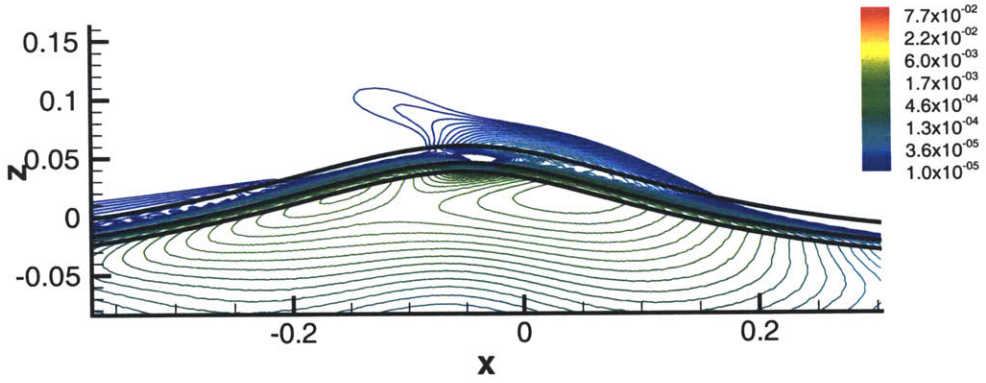

Figure 7-3: Spatial variation of the dissipation rate per unit volume over the entire volume for a non-breaking wave initialized from the flat surface forcing (case SFI-03).

to be from the influence of the standing wave field. Both figures 7-1 and 7-3 are representative for all of the non-breaking cases.

The breaking cases become much more interesting, depending on the type of breaking which occurs. For cases where a gentle-spilling breaker occurs, the dissipation rate has localized regions of very strong dissipation mainly in the water where a small separated region exists. This is seen in figure 7-4. The dissipation rate in the air volume is essentially zero except in two regions near the crest where it must react to the curvature of the water surface. There is a small structure of almost zero dissipation at the front face of the wave in both fluids. The cases which are considered strong-spilling breaking waves have a similarly large dissipation region on the front face of the wave in the water. Figure 7-5 shows a representative case using the same contour levels as the gentle-spilling breaker for comparison. Due to the flow reversal by the air on the crest, the large dissipation region extends into the air flow and is considerably stronger. There is also a very small region of near zero dissipation in the air flow on the back side of the crest in the separated region.

The vorticity field for the strong-spilling breaking wave case is shown in figure 7-6. The vorticity in the air is representative of a flow trying to follow the curvature of the surface. As the air flow, in the reference frame of the crest, comes in to the face, it must make two hard turns, each having a large gradient associate with it (a large u_z for the first corner and a large w_x to follow the second). The small core region of

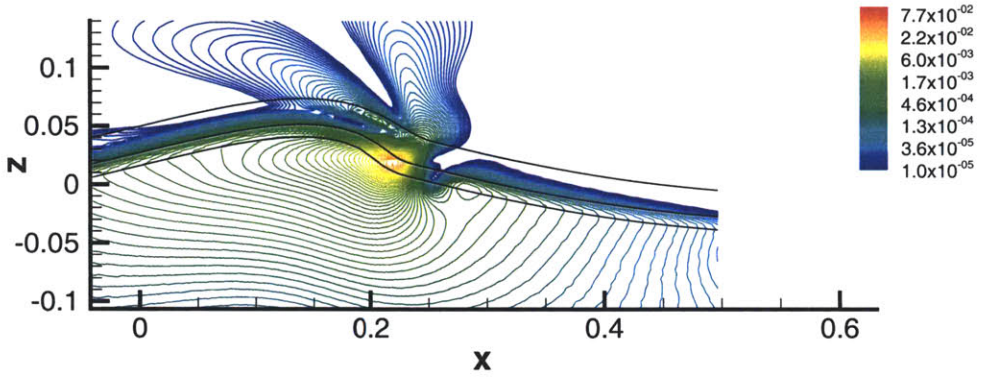

Figure 7-4: Spatial variation of the dissipation rate per unit volume for a gentle-spilling breaker initialized by forcing a two-phase Airy wave (case A2P-02).

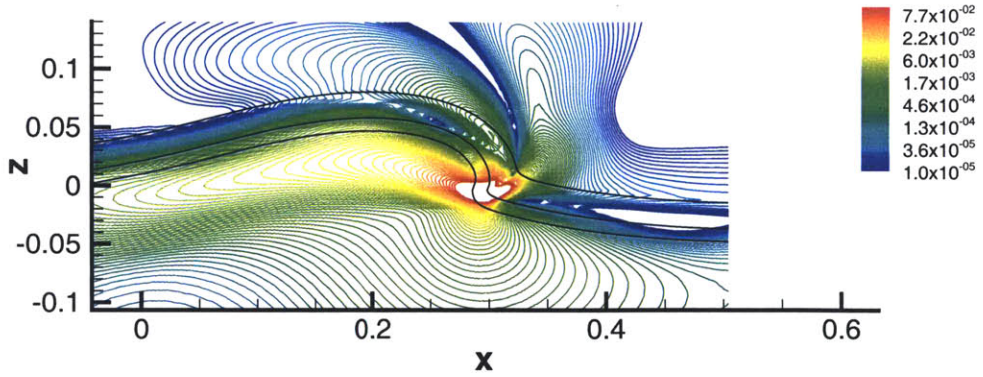

Figure 7-5: Spatial variation of the dissipation rate per unit volume for a strong-spilling breaker initialized by an over-energetic Airy wave (case IAW-04).

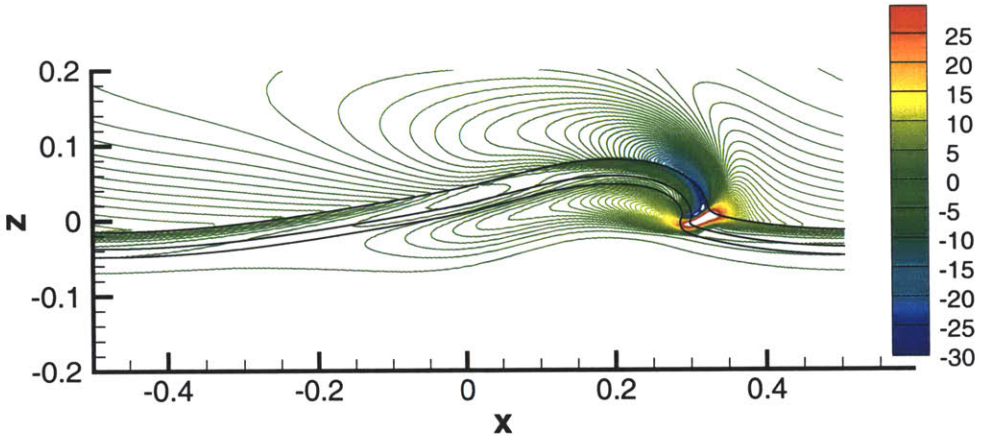

Figure 7-6: Instantaneous vorticity contours for a strong-spilling breaker initialized by an over-energetic Airy wave (case IAW-04). Same instant in time as in figure 7-5.

little dissipation does not correlate to vorticity. This is the separation point of the air.

For cases which are mildly plunging breakers, the flow does not have much opportunity to develop the strong separated region seen in the strong spilling breakers. Thus, the dissipation rate has less localized regions except after the jet impinges the front face of the wave. Figures 7-7 and 7-8 show a time evolution over the main extent of the breaking event for a case started from flat surface forcing. As the crest begins to sharpen and focus, there is a localized region of dissipation due to the curvature of the front face (7-7a). This region becomes stronger and more pronounced in the water as the jet forms (7-7b) and the air develops a similar region as the jet starts enclosing it. After the impact of the jet on the water surface (7-7c), there is a large dissipation region at the point of impact and interestingly, a small core of almost negligible dissipation in the bulk flow beneath the impact point. This core is seen again (7-7d) as the jet impinges on the surface a second and third time (7-8c). After the sheet has broken up (7-8a-c) the original localized dissipation region still exists at the crest, albeit relatively weaker compared to post breaking. This region returns to a progressive Airy wave shortly after breaking (7-8d). As the frame in figure 7-8d has not been altered, the decrease in phase speed of the wave after breaking is evident as the wave crest has moved.

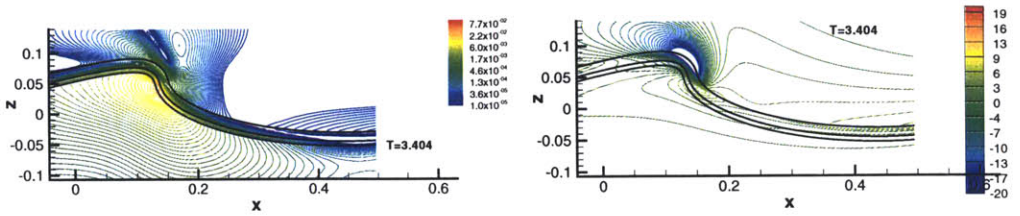

(a) T=3.4

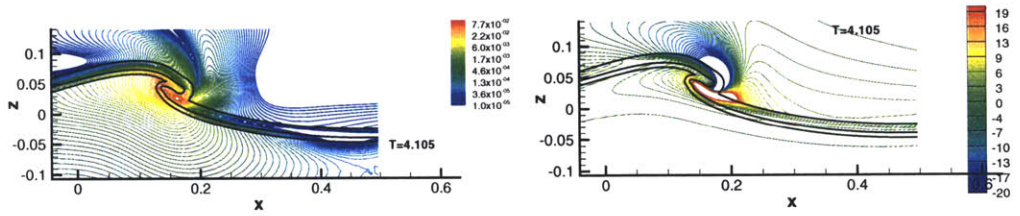

(b) T=4.1

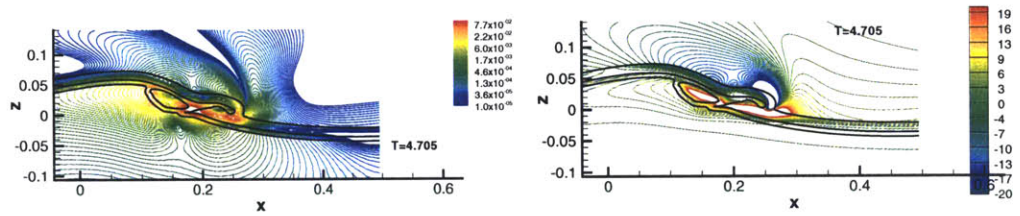

(c) T=4.7

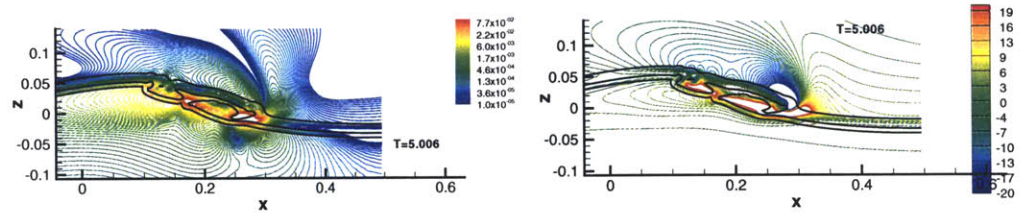

(d) T=5.0

Figure 7-7: Time evolution of dissipation rate (left of pair) and vorticity (right of pair) in a weak plunging breaking wave which forms a jet (case SFI-04).

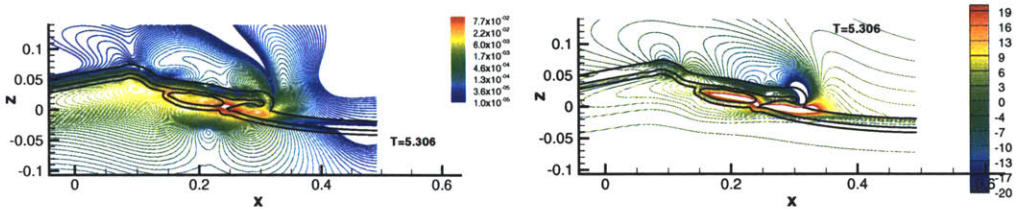

(a) T=5.3

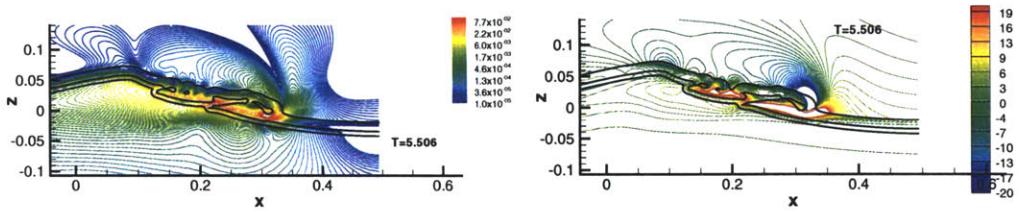

(b) T=5.5

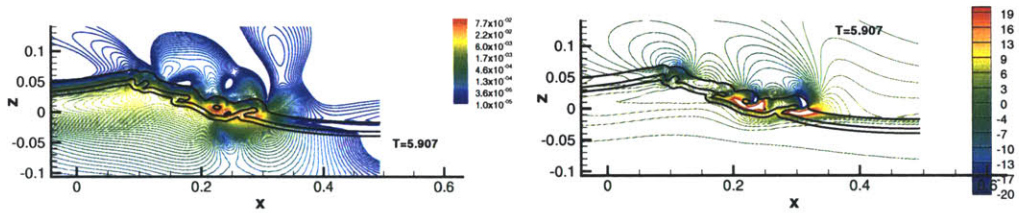

(c) T=5.9

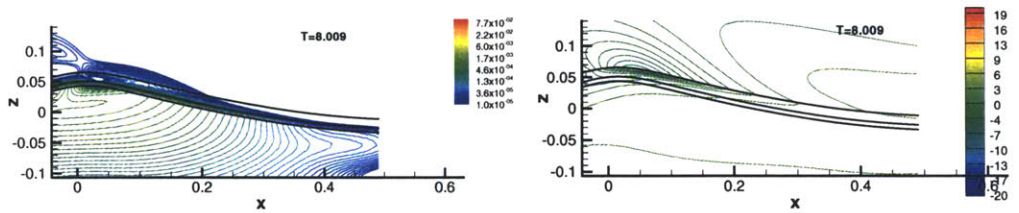

(d) T=8.0

Figure 7-8: Time evolution of dissipation rate (left of pair) and vorticity (right of pair) in a weak plunging breaking wave which forms a jet (case SFI-04).

To understand the evolution and correlation of the vorticity and the dissipation during a spilling breaking event, the dissipation and vorticity at two points along the crest of the wave are shown in figures 7-9 through 7-11, along with the location of the cut on the wave. If we first consider the region where the breaking has not occurred (figure 7-9b), the dissipation follows an expected profile in the water where it reaches a maximum before the air-water interface and then goes to a minimum value at the interface [99, 61]. The air sees a similar behavior with the peak dissipation rate corresponding to the peak region of vorticity. Any kinks seen in these figures is associated with the curvature of the surface as the cuts were taken vertically verses normal to the surface. Where the wave is breaking at the same moment in time (figure 7-9a), the dissipation rate at the air-water interface has increased two orders of magnitude and the peak in dissipation rate below the interface seen in figure 7-9b no longer exists. This again corresponds to the increase in vorticity at the air-water interface and the peak region of vorticity in the air still corresponds to the peak in the air dissipation rate. As this "toe" region moves along the face of the wave, the strong vorticity in the air moves with it (figure 7-10a and 7-10b). The increased value of dissipation in the water persists even though the toe has moved forward and appears in the second cut. Near the end of the breaking event, both locations are beginning to recover a pre-breaking profile. However, the region where the breaking "passed" through (figure 7-11b) is closer to pre-breaking values than the point near where the breaking originated (figure 7-11a). This local persistence of an increased dissipation rate should be expected as the toe region existed in this location for a longer period of time. The motion of the bulge and toe region in these case is not as described in chapter 6. This particular case has a relatively large standing wave energy and the progressive portion of the wave component seems to "surf" along the standing wave. This gives the bulge and toe region the appearance that it is moving. However, the bulge and toe never separates from the wave surface.

To summarize, the spatial variation of the dissipation rate for a range of waves (non-breaking to jet forming) was investigated. In all of the breaking waves, a localized region of strong dissipation exists on the front face of the wave. Depending on

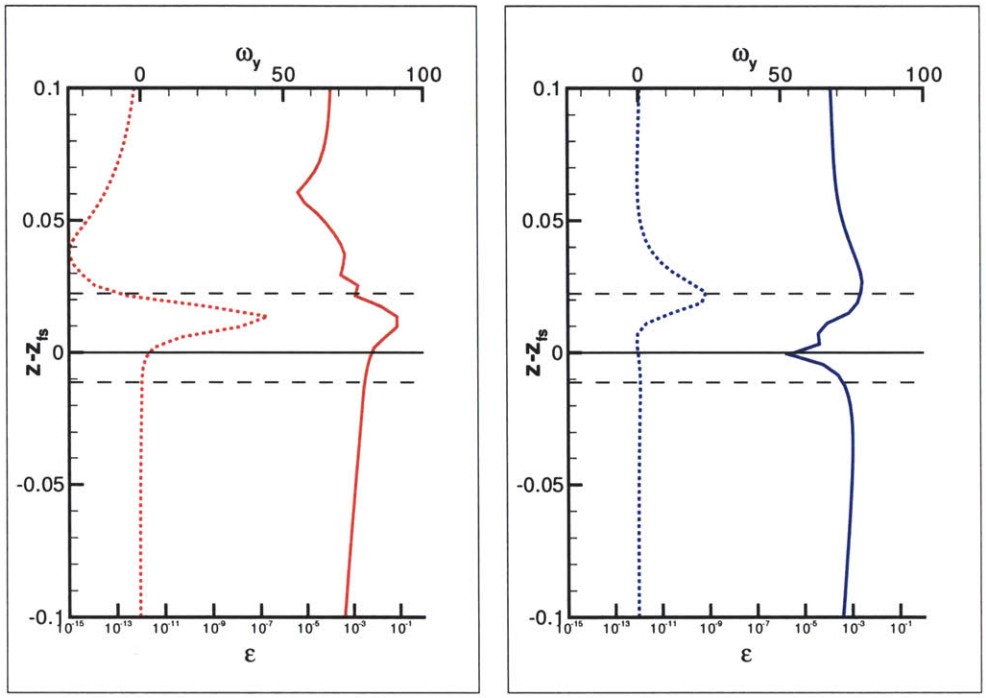

(a) Cut A

(b) Cut B

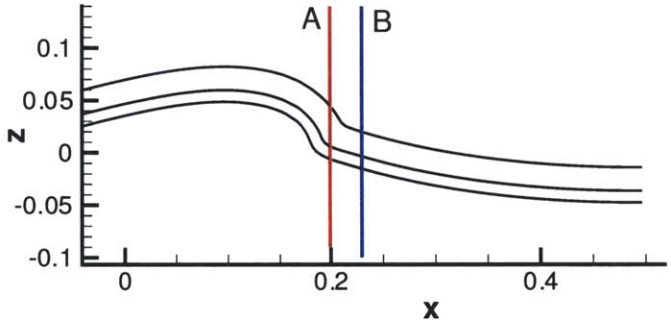

(c) Cut Locations

Figure 7-9: Vertical cuts of the vorticity and dissipation at two locations in a gentle-spilling breaking wave at the onset of breaking (case A2P-02). (...) ω_y; (-) ε

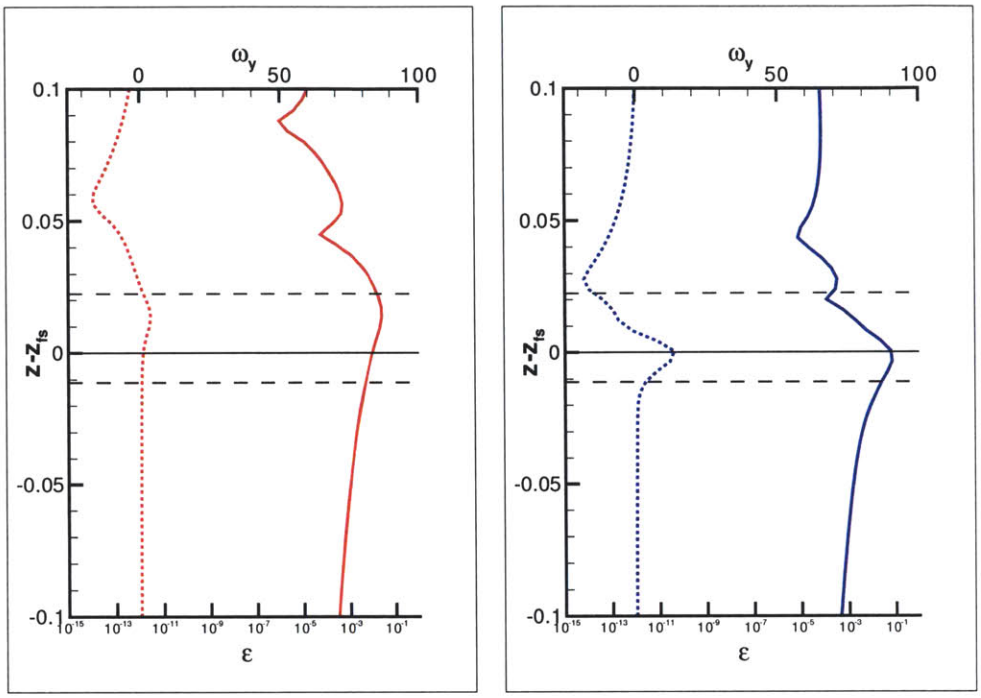

(a) Cut A

(b) Cut B

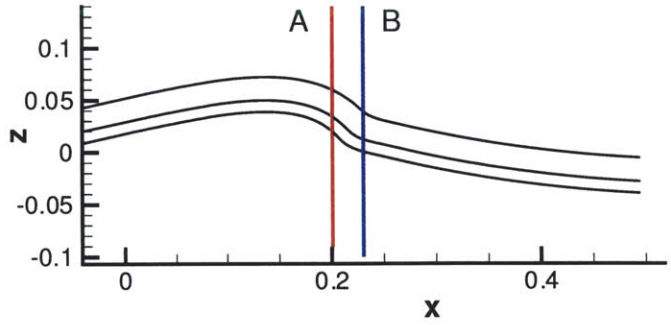

(c) Cut Locations

Figure 7-10: Vertical cuts of the vorticity and dissipation at two locations in a gentle-spilling breaking wave as the toe is moving along the crest (case A2P-02). (...) ω_y; (-) ε

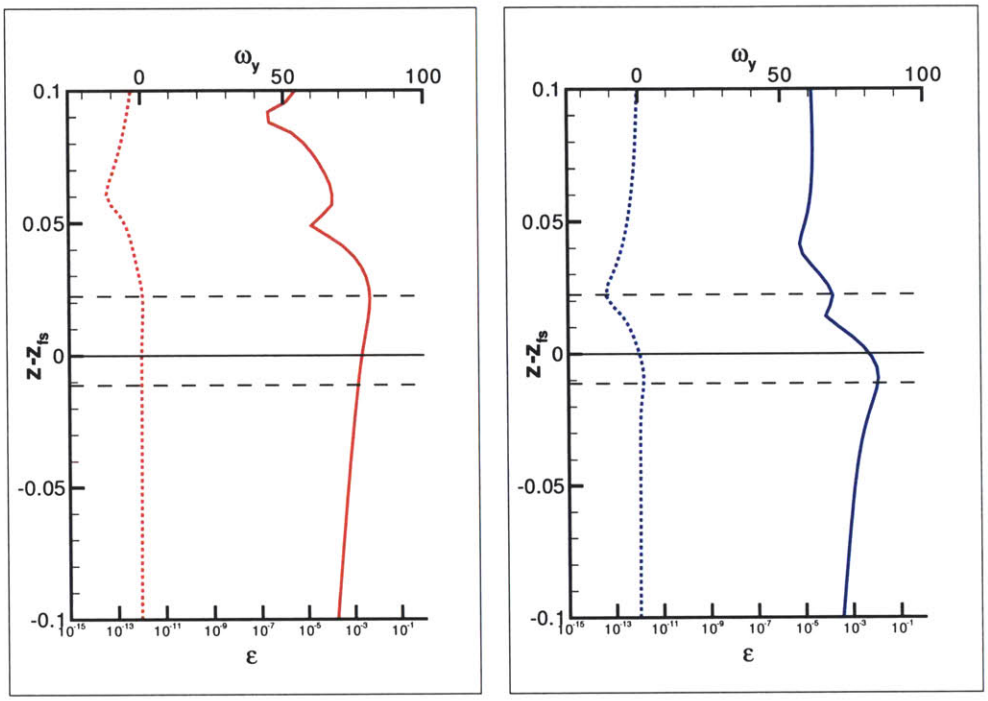

(a) Cut A

(b) Cut B

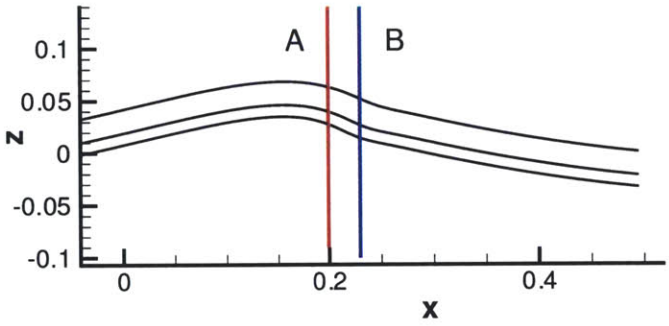

(c) Cut Locations

Figure 7-11: Vertical cuts of the vorticity and dissipation at two locations in a gentle-spilling breaking wave after the toe has moved down the crest (case A2P-02). (...) ω_y; (-) ε

the strength of the breaking wave (i.e. strong-spilling compared to gentle-spilling), the maximum value of this localized region is stronger. The strong regions of dissipation generally correlate to the regions of strong vorticity and separated flow in both the air and water volumes. Cuts along the face of the breaking wave show expected profiles in regions where the breaking region has not passed through. Regions in which the breaking toe has passed through return to pre-breaking profiles shortly after the breaking event while there is a persistence of increased dissipation where the breaking toe originated. Where the jet has impacted the front face of the wave, directly under the impact point there is a large dissipation region but a small core of negligible dissipation exists in the bulk below the impact point.

7.1.3 Total Dissipation Rate

This section looks at the total dissipation rate in both fluids for a variety of waves. By comparing the dissipation rates for breaking and non-breaking waves in this study, we can observe that, for the types of waves generated in this study, the character of the dissipation rate during the breaking process is different for various types of waves, as should be expected. In addition to the water rate, since this study includes the effects of the air above the water surface, the dissipation rates for the air volume over the range of breaking waves are also discussed.

To the best of our knowledge, there is no data in the literature regarding the dissipation rate during the breaking event [74] because of the difficulty of getting velocity measurements during breaking, even in the laboratory. For gentle spilling breaking waves, Haibing and Duncan [90] measured the velocity field and included a discussion of the vorticity but did not continue towards making dissipation calculations. For plunging breaking waves at laboratory scale, there is significant air entrainment making velocity fields difficult at best. Thus, most of the works involve the global amount of energy dissipated in the event which is discussed in section 7.2.

A various number of non-breaking waves were generated as a part of this study. Figure 7-12 shows the dissipation rate for many of the non-breaking waves for both the air and water volumes. The standing wave which has been present in many of

the results and discussed in section 4.4 is clearly visible in these results, but not germane to the discussion. For the wave generation methods, the magnitude of the dissipation rate varies slightly (though it is magnified when using the log scale here). If the dissipation rate is scaled by the total energy in the field $\langle E_{wref} \rangle_0$, the cases collapse onto each other. This is expected because in laminar flows, the dissipation rate should be proportional to the amount of energy in the flow field. For all of the cases, the dissipation rate for the air is an order of magnitude less than the water. A cursory inspection of equation 7.1 reveals that the dissipation rates of the water and the air should differ by the ratio of the two viscosities, which for this study is two orders of magnitude. However, that presumes that everything else is the same. Inspection of the flow field for these cases shows that the vorticity in the air is an order of magnitude greater than the water. Thus, the single order of magnitude difference is as expected.

All of the cases have essentially the same slope of the dissipation rate in time. To have a nonconstant dissipation rate for a plane progressive wave over time may seem to be counter intuitive. However, because the Reynolds number is low for these cases, the effect of viscosity is large enough on the wave amplitude (and thus the velocity field) to show in these cases. This is confirmed if the wave amplitude dissipation rate, equation 4.30, is used to infer a laminar dissipation rate.

$$E_w(t) = E_{wref} e^{-2\Gamma t} \tag{7.5}$$

The 2Γ comes from squaring the amplitude damping rate as the energy is proportional to the amplitude squared.

The dissipation rate for a gentle-spilling breaking wave can be seen if we consider a case in which a non-breaking wave has had energy input into it through a surface force. Figure 7-13 compares the dissipation rate for a representative case. This example is the case of a non-breaking wave generated by the two-phase Airy wave initial condition and the same wave with a modest amount of surface forcing applied to it. The effect of the surface forcing is seen during the initial increase in dissipation

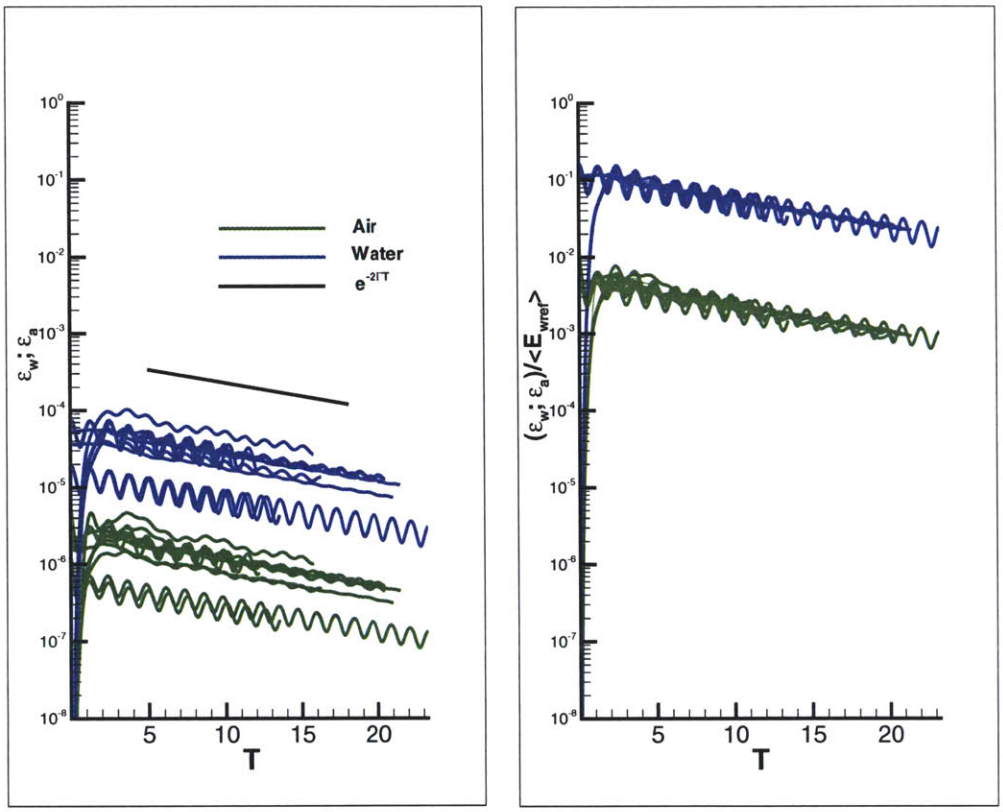

Figure 7-12: Total dissipation rate for water (blue) and air (green) volumes over time for non-breaking wave cases. Left figure is actual dissipation rate. Right figure is scaled by $\langle E_{wref} \rangle_0$. The black line represents an estimation of laminar dissipation rate.

rate. For this case, the surface forcing is completely removed at $T = 2.09$, where the spilling immediately commences. Once the single spilling event has completed near $T_{pb} = 6$, the dissipation returns to a behavior similar to a non-breaking wave. The gap in the dissipation rate post breaking in the left of figure 7-13 is not unexpected. Experience with the non-breaking cases shows that the dissipation rate should scale by the amount of energy in the flow when it is laminar. As energy has been input into the breaking case through surface forcing, there is no reason to expect it to return to the non-forced case value after breaking. If the dissipation rate is scaled by a post-breaking energy value, then the cases collapse onto each other. This implies that the flow returns to a laminar flow post-breaking. This is contrary to results seen in experiments [28, 90, 92] where it takes a number of periods to return to a laminar rate. However this is not unexpected due to the moderate Reynolds number of these simulations.

Figure 7-14 shows all of the gentle-spilling breaking waves in this study. The same behavior can be seen when all of the spilling breaking waves are considered, whether surface forcing is used to generate spilling or the wave spills on its own. If scaled by the energy post breaking (right of figure 7-14), the same laminar behavior can be seen in all cases.

The spilling breaking waves just discussed were mild in nature in that the front face of the wave retains a fairly mild slope and the relative increase in dissipation rate for the air flow is of the same magnitude as the increase for the water flow. Another type of spilling breaking wave, which we call a strong spilling breaking wave, also exists. During this type of breaking event, the front face of the wave becomes fairly steep and may become multi-valued. Figure 7-15 illustrates the difference in surface behavior which is commonly seen. For the strong-spilling breaking wave, the flow field in the water is marked by a strong vortical region on the front face of the wave. The flow field in the air is also marked by a strong vortical region, especially in the cases where the surface becomes multi-valued. In this region, the air flow must actually reverse, causing a great amount of vorticity. All of this strong vorticity creates a fairly increased dissipation rate for both fluids. This is seen in figure 7-16 where

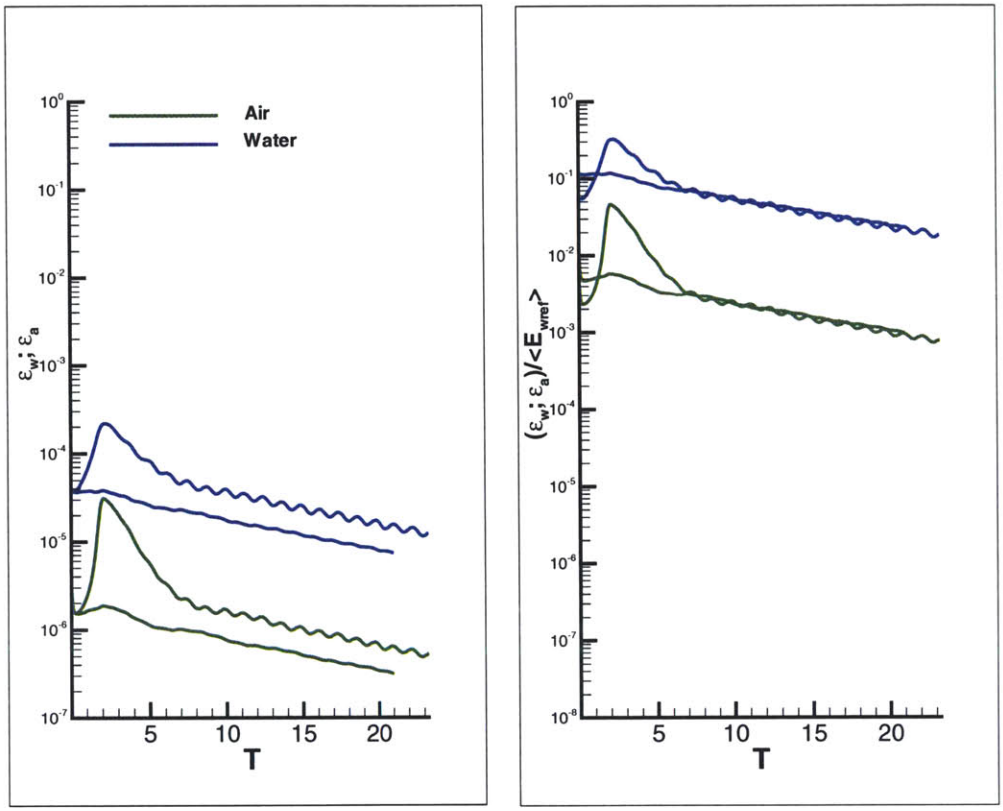

Figure 7-13: Comparison of the dissipation rate between a gentle-spilling and non-breaking wave for water (blue) and air (green) (cases A2P-01 and A2P-02). Left figure is actual dissipation rate. Right figure is scaled by $\langle E_{wref} \rangle$ at $T = 0$ for the non-breaking case and $T = T_{pb}$ for the spilling case.

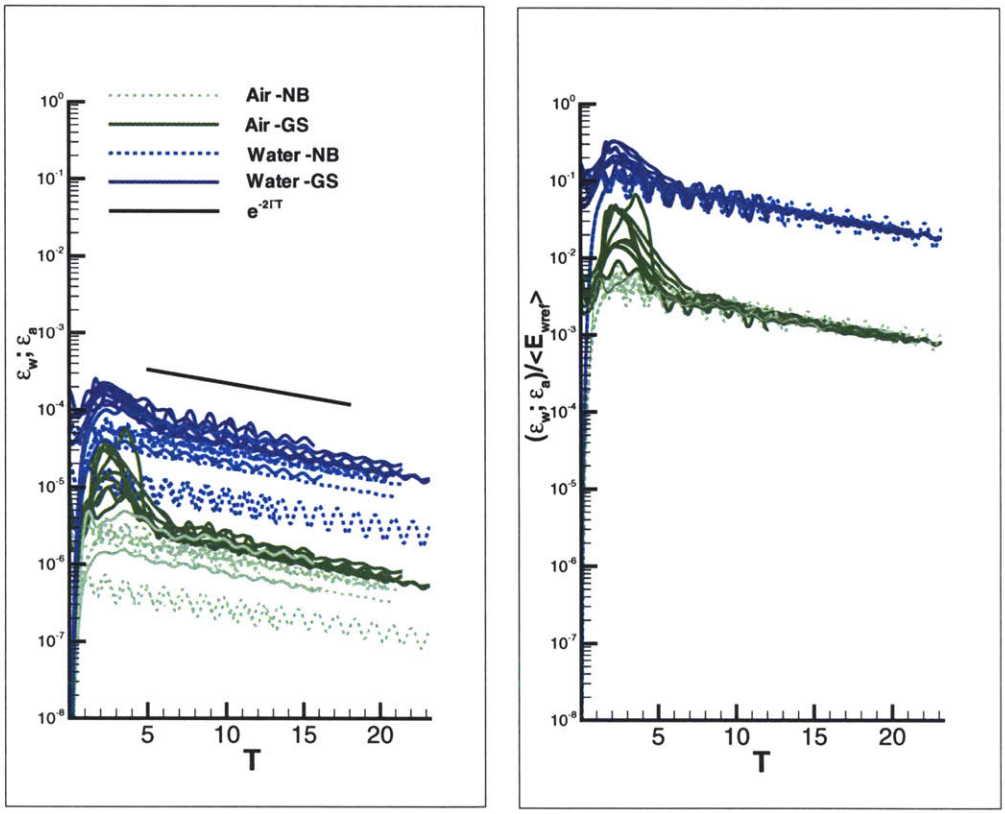

Figure 7-14: Comparison of the dissipation rate for all gentle-spilling and non-breaking waves for water (blue) and air (green). Left figure is actual dissipation rate. Right figure is scaled by E_{wref} at $T = 0$ for the non-breaking case and $T = T_{pb}$ for the spilling cases. The pale blue and green lines represent all of the non-breaking waves in this study. The black line represents an estimation of laminar dissipation rate.

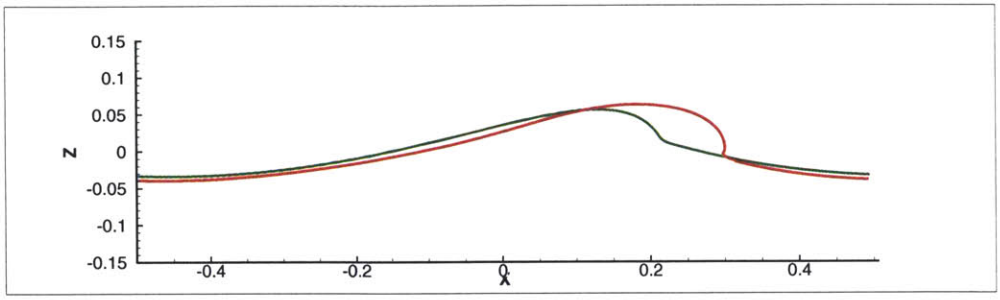

Figure 7-15: Illustration of the difference in surface profiles for a gentle-spilling (case A2P-02) and strong-spilling (case IAW-04) breaking waves.

the dissipation rate of the strong spiling breakers is compared to the gentle-spilling breaking waves.

In addition to the overall increased dissipation rate for these spilling breaking waves, the air flow sees a dissipation rate to within same order of magnitude as the water. This could mean one of two things: (i) there is considerably more (in terms of volume) vorticity in the air flow or (ii) the vorticity or stresses in the air flow are two orders of magnitude greater than the water. Figure 7-17 shows this to be a combination of the two. The region of strong stresses and vorticity in the flow is much larger in the air flow than the water by a factor of about 1.5. The mechanism behind this increased dissipation rate is a "curvature effect" in that the air flow, which sees the crest of the wave more like a wall than a free-surface, must follow the curvature of the wave face. In these cases, the face of the wave is much more pronounced and in some cases causes a flow reversal of the air. Additionally, the air then separates as it comes off the crest of the wave almost like a backward facing step. All of these sharp changes in flow direction cause large amounts of vorticity/stresses and contributes to the increase in dissipation rate.

The dissipation rate of all of the plunging breaking wave cases is compared to the gentle spilling breaking waves in figure 7-18. There are only a few cases of plunging breaking waves in this study, with and without air entrainment. The waves without air entrainment are considered to be weak plunging breaking waves compared to the plunging breaking waves generated by wave focusing in many experiments [92, 80, 54]

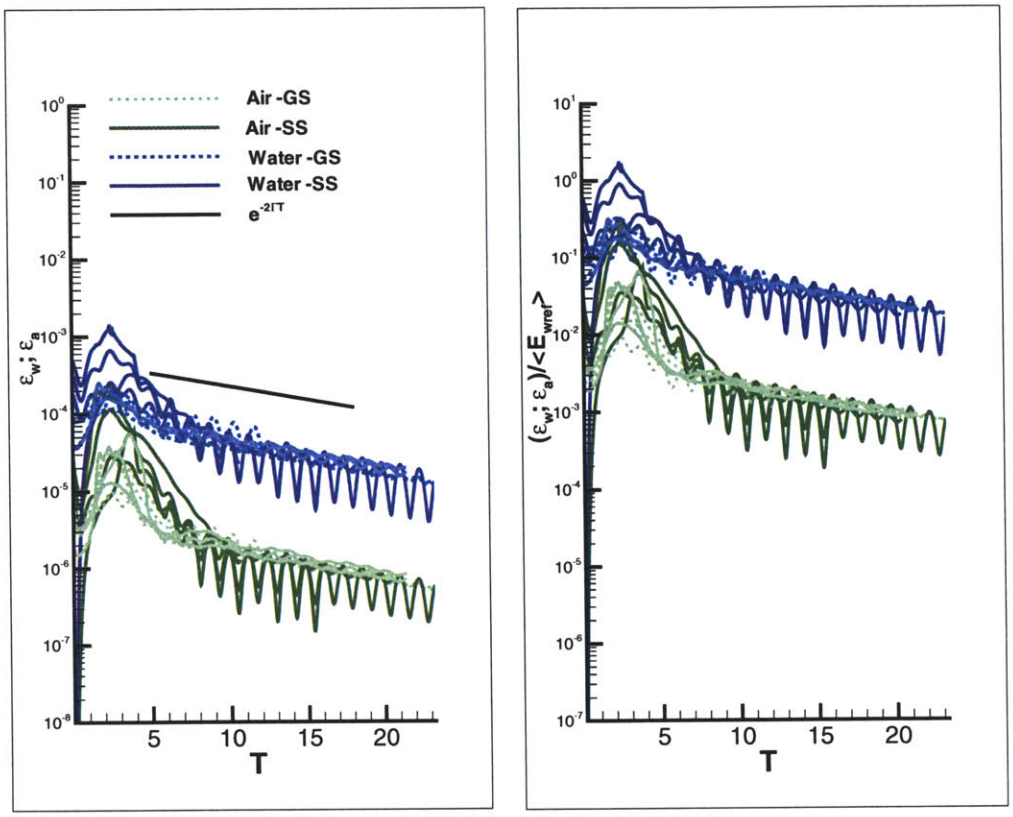

Figure 7-16: Comparison of the dissipation rate between two types of spilling-breaking waves for water (blue) and air (green). Left figure is actual dissipation rate. Right figure is scaled by $\langle E_{wref} \rangle$ at $T = T_{pb}$. The pale blue and green lines represent all of the gentle-spilling breaking waves in this study.

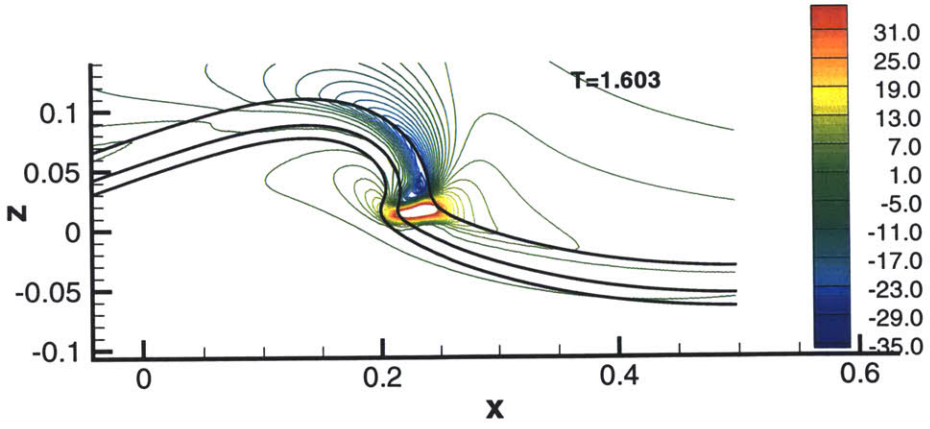

Figure 7-17: Instantaneous contours of transverse vorticity ω_y for case IAW-04.

and are characterized by an ejection of fluid at the crest and will be referenced as jets. The waves with air entrainment are more representative of what is seen in literature and generally have more than one breaking event in a period. For the jets, the dissipation rate in the water increases to the level seen in the gentle-spilling breaking wave cases for about the same amount of time which can be seen in figure 7-19. This dissipation rate is about a factor of two less than the strong spilling breakers (c.f. figure 7-16). The dissipation rate in the air, however, sees a marked increase in dissipation rate in that it becomes practically the same value as the water. An inspection of the dissipation rate in the volume (c.f. figure 7-7) shows the significant increase of the dissipation in the air volume as it is trapped by the jet as it impinges on the surface and breaks up.

For both the air and water flows, the dissipation rate in these jet events, quickly returns to a non-breaking behavior as is seen in the gently spilling breaking wave cases. This is in contrast to what is seen in the work of Rapp & Melville [92]. However, as pointed out previously, the breaking waves generated through wave focusing are much more violent in nature than the jet events generated here. In addition to their large Reynolds number $O(10^6)$ and three-dimensional effects which are outside the scope of this study, there is considerable air entrainment. Instead of collapsing down and entraining air into the wave, the jet which forms at the tip of the wave becomes thin and breaks up. In that sense, the wave, while actually plunging, is more like a spilling breaking wave as the energy lost is attributed to the ejection of the jet verses the amount of energy dissipated by the mechanisms behind the air entrainment and bubble breakup. This is highlighted by the fact that the dissipation rate in the water for these cases looks very similar to the gently spilling cases.

The cases with air entrainment are compared to the jets in figure 7-20. They are marked by a longer period of breaking with a larger relative increase for both fluids in dissipation rate than the jets. This is seen in Lamarre and Melville [55] where they relate the size of the bubble plume to the dissipation rate. Lamarre and Melville propose that the sustained dissipation rate after breaking is a function of the further collapse of the bubbles entrained during breaking. Thus, we should expect that the

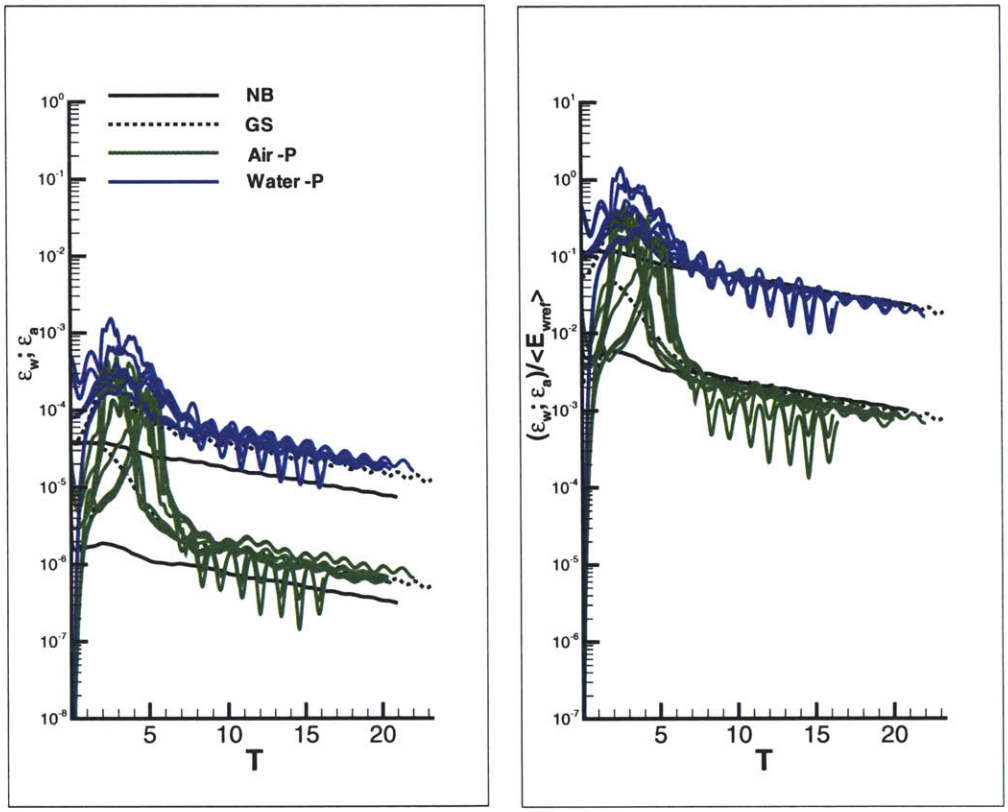

Figure 7-18: Comparison of the dissipation rate between gentle-spilling (black dashed) and plunging-breaking waves for water (blue) and air (green). A non-breaking wave case (black solid) is included for reference. Left figure is actual dissipation rate. Right figure is scaled by $\langle E_{wref} \rangle$ at $T = T_{pb}$.

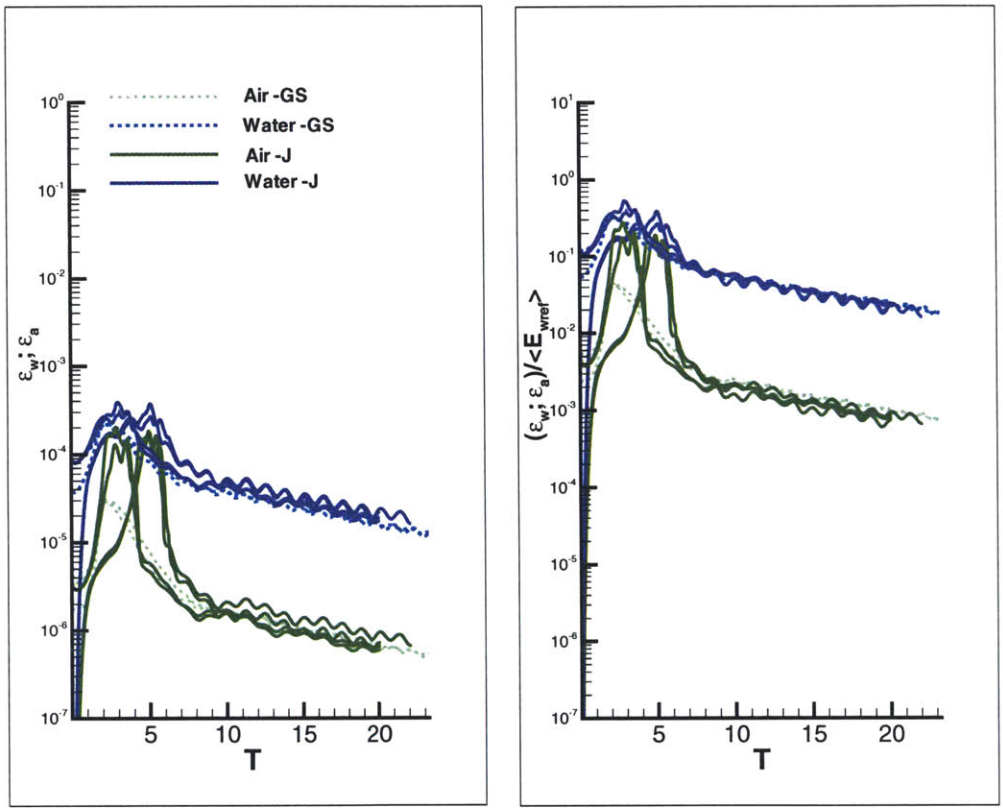

Figure 7-19: Comparison of the dissipation rate between a gently spilling wave and a wave with jet formation for water (blue) and air (green). Left figure is actual dissipation rate. Right figure is scaled by $\langle E_{wref} \rangle$ at $T = T_{pb}$. The pale blue and green lines represent all of the gentle-spilling breaking waves in this study.

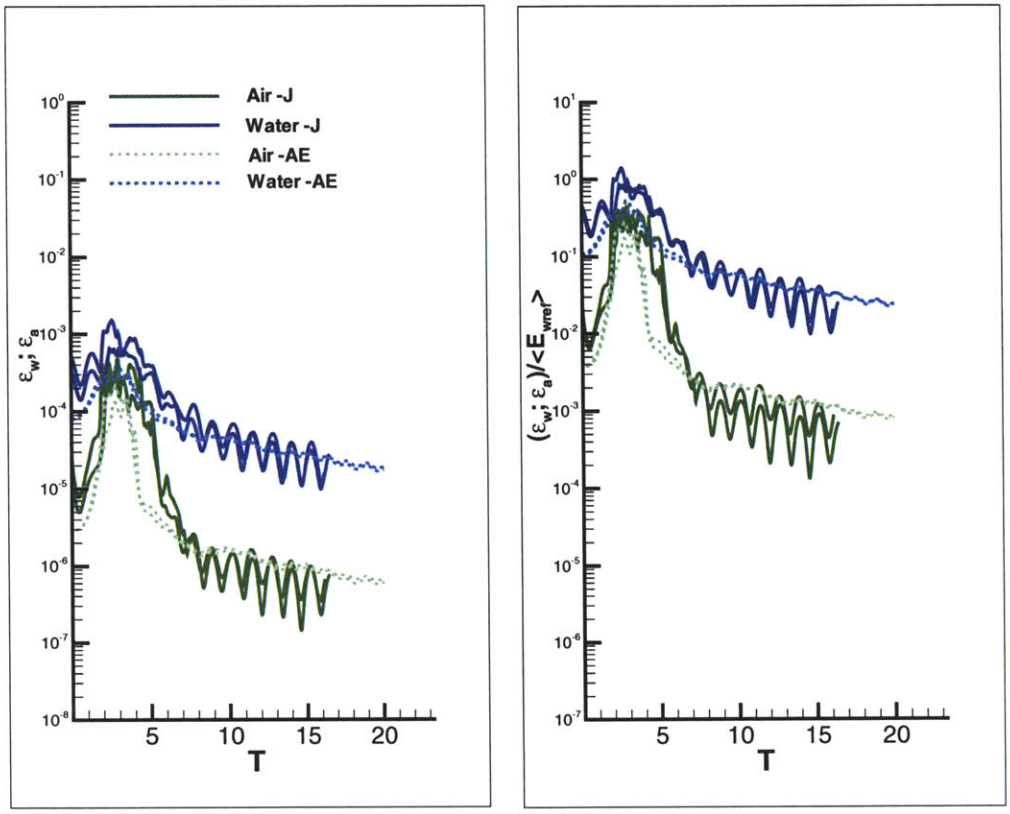

Figure 7-20: Comparison of the dissipation rate between a waves with jet formation and with air entrainment for water (blue) and air (green). Left figure is actual dissipation rate. Right figure is scaled by $\langle E_{wref} \rangle$ at $T = T_{pb}$. The pale blue and green lines represent all of the jet-forming breaking waves in this study.

cases with air entrainment should see larger dissipation rates for longer periods of time. As in the case for the jets, the dissipation rate in the air becomes practically the same value as the water. It is difficult to infer from the figures, but there appears to be an increase in the slope of the dissipation rate post-breaking. Based on the previous analysis, this would infer that the flow is turbulent but it is difficult to say for sure because of the magnitude of the standing wave for these cases.

In summary, our data has shown a range of dissipation rates for various types of breaking waves. Figure 7-21 collects this information for all of the waves in this study. The relative difference between the maximum dissipation rate during the breaking event compared to the dissipation rate prior to the start of breaking for the

air is plotted against that of the water. Additionally, reference lines for one-times, five-times and ten-times the relative increase are also shown for reference. Figure 7-21a has all cases considered. However, because the maximum dissipation rate can be a function of the forcing applied to the wave the cases without forcing are shown in figure 7-21b. In general, the gentle-spilling breakers have around the same relative increase in the dissipation rate for air and water. The strong-spilling breakers have about 5 times relative increase in the air than the water, showing the effect of the stronger separated region in the air flow. The breaking waves with jet formation and air entrainment are closer to 10 times the relative increase in the air than in the water, which brings it to the same order of magnitude as the water as discussed earlier. For all of the cases in this study, it can be said that the dissipation rate in the water never increases by more than a factor of two within the wavelength of the wave unless some type of surface forcing causes it to increase. For most of the cases considered, the dissipation rate quickly returns to the non-breaking behavior and within the arguments of scaling, the same value.

7.2 Global Energy Loss

This section takes a more "experiment" minded approach to calculating energy loss in that control volumes are used pre- and post-breaking. In an laboratory wavetank, the control volumes are chosen well away from the breaking region and the energy loss is calculated as a difference between pre- and post-breaking. In the periodic boundary conditions, the control volume is the domain and it is taken at times well away from the breaking event and the difference between these values is what is considered the global energy loss.

7.2.1 Calculation of Energy Losses

The calculation of the amount of energy lost is done the same way for all the cases, whether there be an initial velocity field or surface forcing or both. Figure 7-22 is a schematic of the total energy in the water volume over time. For this analysis, there

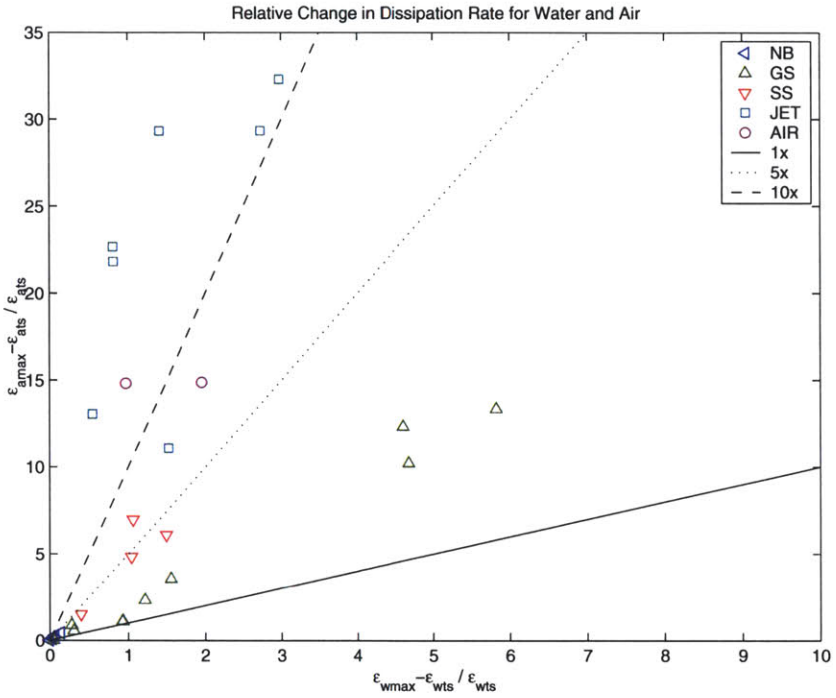

(a) All cases

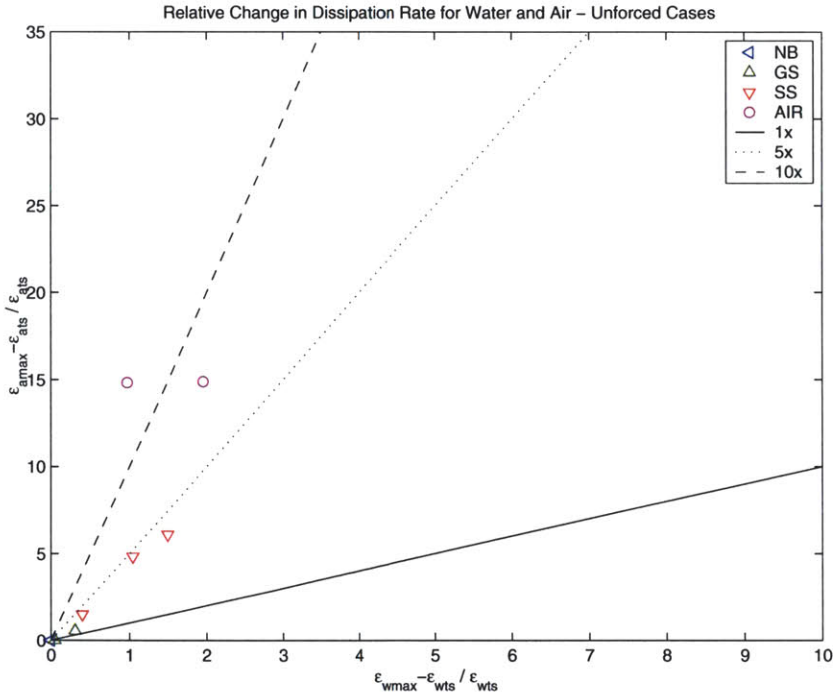

(b) Unforced cases

Figure 7-21: Relative increase in dissipation of the air volume compared to the water volume. Reference lines: (-) 1 times relative increase; (..) 5 times relative increase; and (–) 10 times relative increase.

are four points of interest in time: initial (t_0), start of breaking (t_{st}), post-breaking (t_{pb}), and the stop point (t_{stp}). Referring to a spilling breaking wave as discussed in section 6.1, the period between t_0 and t_{st} represents the development stage. The period between t_{st} and t_{pb} encompasses the entire breaking event such as the sustained breaking and the dissipating stage. The region after t_{pb} includes no breaking event at all and lasts until near the end of the simulation t_{stp}. The kinetic energy in the water volume is calculated by multiplying the kinetic energy at a point by the smoothed Heaviside function, and integrating over the entire volume.

$$\mathrm{ke}_w(t) = \int_\forall \frac{1}{2}\rho(\phi)u_i u_i H(\phi;\epsilon)d\forall \tag{7.6}$$

Determining the potential energy in a multi-fluid flow can be a subtle endeavor. Generally, it is easier to take an initial potential energy and subtract out the work done by gravity at a specific time. From equation 2.53, the work done by gravity is calculated as:

$$\frac{\partial \mathrm{pe}}{\partial t} = \rho(\phi)\frac{w}{\mathcal{F}r^2} \tag{7.7}$$

As in equation 7.6, the total amount of work done by gravity on the water can be calculated by multiplying equation 7.7 by the smoothed Heaviside function to get only what is part of the water volume and integrating it over the entire volume. Then, to determine the change in energy due to this work, it is integrated in time. The amount of "potential energy" at any given time can be taken as this change plus an initial or reference value.

$$\mathrm{pe}_w(t) = \mathrm{pe}_{wref} + \int_{tref}^{t}\int_\forall \rho(\phi)\frac{w}{\mathcal{F}r^2}H(\phi;\epsilon)d\forall dt \tag{7.8}$$

Because the reference value of the potential energy can skew the results in terms of fractions of energy lost, the reference value is taken as an estimate of the initial potential energy in the field which is estimated from an amplitude spectrum of the surface at $t = 0$.

$$\mathrm{pe}_{wref} = \frac{1}{4}\frac{\rho_w}{\mathcal{F}r^2}\sum_i a_i^2 \tag{7.9}$$

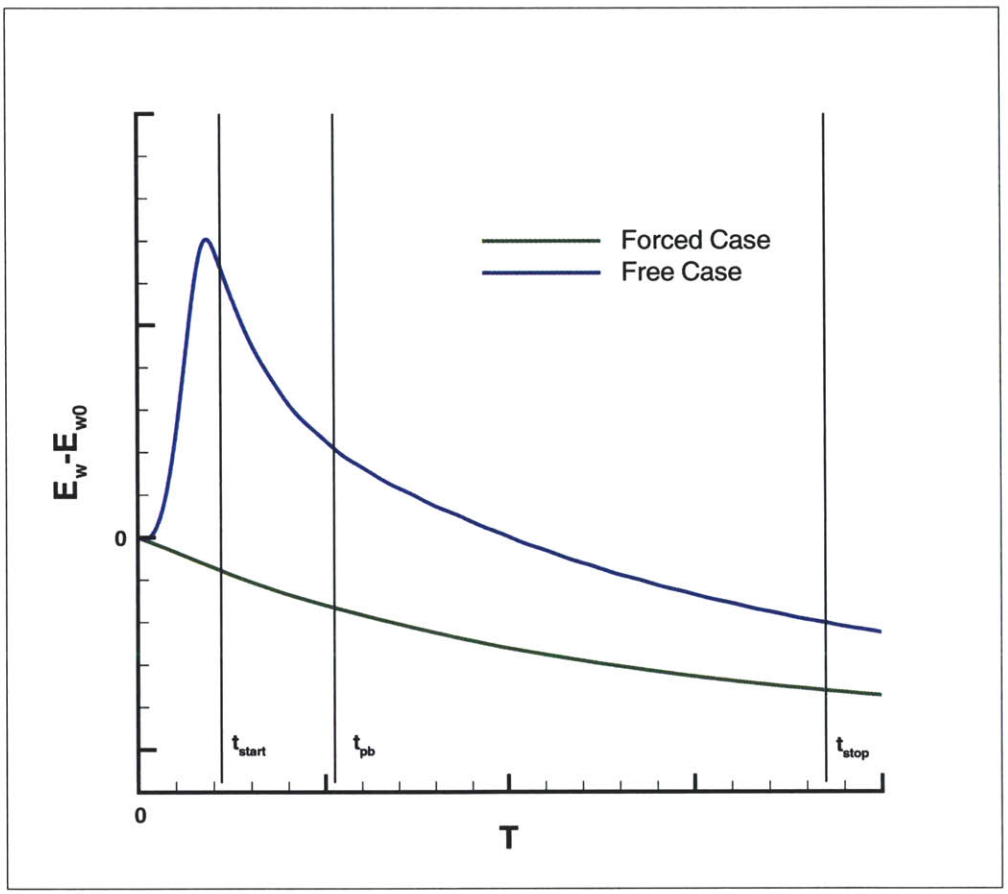

Figure 7-22: Illustration of the points in time used for global energy loss calculations for forced and free cases.

The total energy in the volume at any time is then given as the sum, which is given for completeness.

$$Ew(t) = \mathrm{ke}_w(t) + \mathrm{pe}_w(t) \tag{7.10}$$

Based on these, the loss of energy over the breaking period is estimated as the difference between t_{pb} and t_{st} relative to the initial amount of energy in the field $Ew_0 = Ew(t_0)$:

$$\mathrm{d}Ew = (Ew_{pb} - Ew_0) - (Ew_{st} - Ew_0) \tag{7.11}$$

and the fraction of energy lost is based on t_{st}

$$\%\ \text{Ew lost} = \frac{\mathrm{d}Ew}{Ew_{st}} \tag{7.12}$$

The amount of energy dissipated by viscosity is calculated from integrating the dissipation rate in time. Namely,

$$Ew_\varepsilon = \int_{tref}^{t} \bar{\varepsilon}_w dt \tag{7.13}$$

where

$$\bar{\varepsilon}_w = \int_\forall \varepsilon H(\phi;\epsilon) d\forall \tag{7.14}$$

and ε is given in equation 7.3.

In their work on experiments involving breaking waves, Rapp and Melville defined a slope parameter, S. Their slope parameter is representative of the sum of the slopes in the wave. The experiments used a spectrum which had constant amplitude spread over a finite spectrum (also of constant amplitude). Thus, the estimated slope parameter was given by the input to the wavemaker:

$$S_{RM} = Nak_c \tag{7.15}$$

The central wave number k_c was calculated from the finite depth dispersion relationship at the central frequency of the input packet sent to the wavemaker. Lowan and Melville [70], adopted this slope parameter for their experiments which used a constant slope for a finite number of wave components.

$$S_{LM} = Nak \tag{7.16}$$

In the same spirit, the slope parameter used in this study is calculated as the sum of the slopes calculated from the amplitude spectrum.

$$S = \sum_i a_i k_i \tag{7.17}$$

In practice, the first four wavenumbers were used in equation 7.17. Unlike the experiments which had a fairly wide bandwidth, the bandwidth of the waves in this study is very narrow and using more than four wavenumbers did not change the slope parameter noticeably.

7.2.2 Total Energy Loss

The total energy lost over the breaking event as a fraction of the energy prior to breaking is determined from equation 7.12 and shown in figure 7-23 as a function of the slope parameter at the start of breaking for the various types of breaking events (non-breaking, gentle-spilling, strong-spilling, jets and air entrainment).

After $S \geq 0.4$, there is a bifurcation in the trend of the data where the fraction of energy lost is around either 0.4 or 0.8 with a few outliers near 0.2 (which may be another branch). In general, the strong-spilling breaking waves and plunging-breaking waves with air entrainment are on the higher branch and most of the gentle-spilling breaking waves and plunging breaking waves with jet formation are on the lower branch. The presence of this bifurcation implies that the amount of energy in the waves in this study may be more than a factor of just the slope. In the work of Rapp and Melville and Lowan and Melville, the slope parameter was based on the

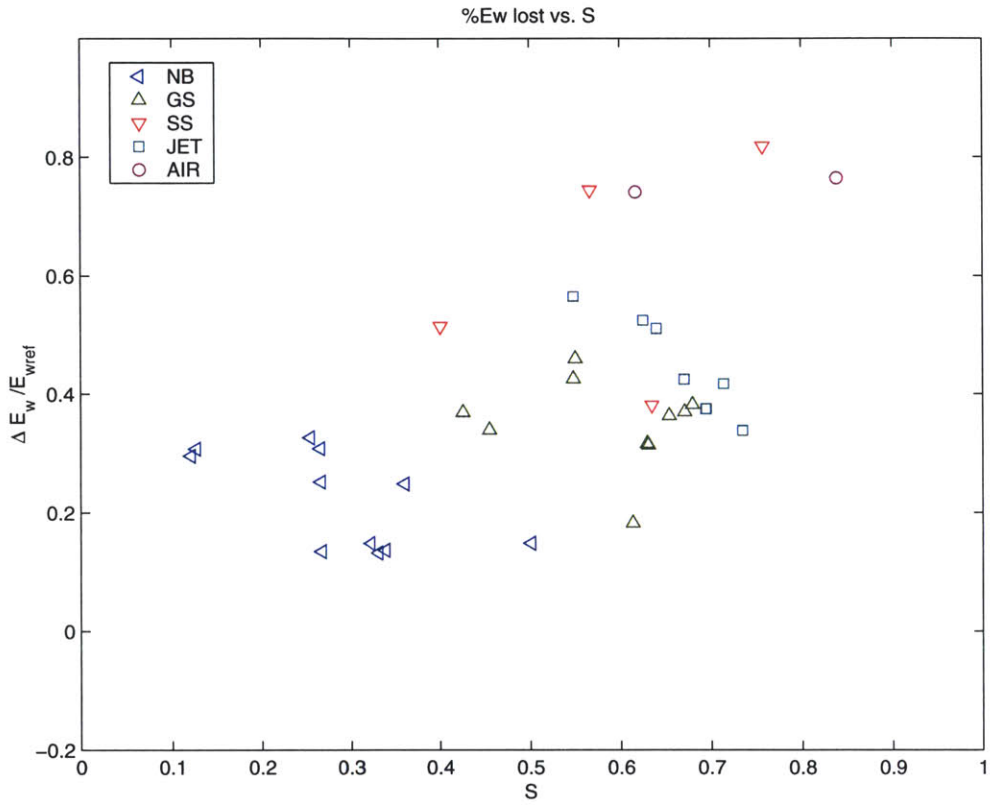

Figure 7-23: Total amount of energy lost in the water volume over the breaking event as a fraction of the amount of energy at the start of the breaking process plotted against slope parameter (at t_{st}) for a variety of waves: ($\triangleleft$) non-breaking, ($\triangle$) gentle-spilling, ($\triangledown$) strong-spilling, ($\square$) jet formation, and ($\circ$) air entrainment.

input to the wavemaker and not the actual wave geometry. All of the breaking waves generated were done through wave-focusing. At the Reynolds number for their waves and in the absence of other inputs, the slope parameter is an adequate gauge of the amount of energy in the wave group. However, in the cases where the waves have more (or less) energy than the slope parameter would imply (such as those that have received input from the wind, shear flow, turbulence or current), calculating energy based on geometric properties and presuming equipartition may not be prudent. As this study has access to the velocity field in the wave, the total amount of energy can be directly calculated. Figure 7-24 shows the same total energy loss as a function of the total amount of energy in the wave prior to breaking, normalized by the total energy in the wave for a Stokes limiting wave of $ka = 0.44$.

Using the total energy in the wave at the start of breaking as a parameter has removed the bifurcation(s) seen in figure 7-23. There is a wide amount of variation (up to 20%) in the total energy lost for cases where $Ew_{st}/Ew_{Stokes} < 1$, even in the non-breaking cases when considering the total energy lost in the wave. Within the context of this study, this variation essentially disappears when there is more energy in the wave that the Stokes limiting wave. The large variability for the cases with less energy than the Stokes limiting wave implies two things: (i) that there is more than one factor at play in wave breaking strength than the amount of energy in the wave and (ii) different breaking mechanisms give different energy losses such that a single curve which covers all cases of wave breaking with little variability may be out of reach.

7.2.3 Energy Loss Due to Breaking

To estimate the amount of energy lost due to breaking, the amount of energy that the wave would have lost if it had not broken should be factored out of the total energy lost. In general, this should just be the viscous effects. The amount lost to viscosity needs to be estimated. In experiments, generally it is enough to factor in potential effects from boundary layers on the sidewalls (and bottom if depth is an issue) of the wavetank. In this study, there are no boundary layers in that the bottom boundary

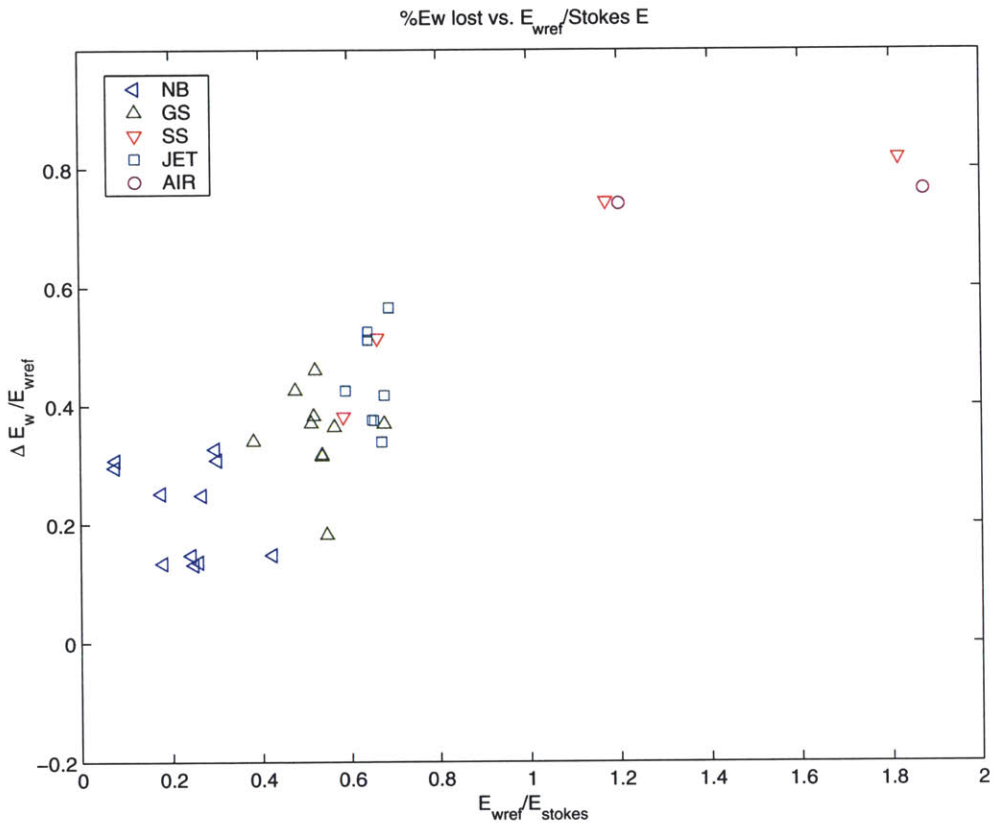

Figure 7-24: Total amount of energy lost in the water volume over the breaking event as a fraction of the amount of energy at the start of the breaking process plotted against the normalized energy (at t_{st}) for a variety of waves: ($\triangleleft$) non-breaking, ($\triangle$) gentle-spilling, ($\triangledown$) strong-spilling, ($\square$) jet formation, and ($\circ$) air entrainment.

is a free-slip boundary. However, because of the moderate Reynolds number, the viscous effects on the wave amplitude are non-negligible. To estimate the amount of energy dissipated due to viscous effects if the wave had not broken, we will assume that the wave flow remains laminar throughout. In that case, the damping rate will be proportional to the energy in the field (or the square of the velocity). Using linear wave flow theory as a guide, we will also assume that the velocity is proportional to the amplitude of the wave. Thus, the rate at which viscous forces are damped out is the same as the rate at which the amplitude is damped (squared). Thus, equation 7.5 can be used to estimate the energy loss for the wave if it had not broken.

$$Ew_\nu = Ew_{st} e^{-2\Gamma(t_{pb} - t_{st})} \tag{7.18}$$

As a check on this estimate, the ratio of estimated viscous losses to calculated viscous losses (using the dissipation rate) is shown in figure 7-25. For most non-breaking cases, the ratio is greater than 0.9. As the breaking becomes more pronounced this quickly drops to 0.5. If we consider this estimated laminar energy loss as our best estimate and remove it from the total energy loss, then the remaining energy loss can be attributed to the breaking event. The loss due to breaking is shown in figures 7-26 and 7-27, plotted against the slope parameter and energy at breaking onset, respectively. Note that this estimate only removes the damping due to viscous effects in the event that the wave does not break. Any viscous dissipation due to the breaking event itself is retained.

When considering the amount of energy lost due to breaking as a function of slope parameter (figure 7-26), the bifurcation which was seen in the total energy loss remains but at a value shifted from 0.4 and 0.8 to about 0.2 and 0.4. There is an additional grouping of points below at about 10% energy loss due to breaking. However, they can also be interpreted within the scatter of points as part of the lower line than a third branch. When considering this energy loss as a function of the amount of energy in the wave at breaking onset, as now expected, the bifurcation disappears. The cases classified as non-breaking have essentially no energy lost within

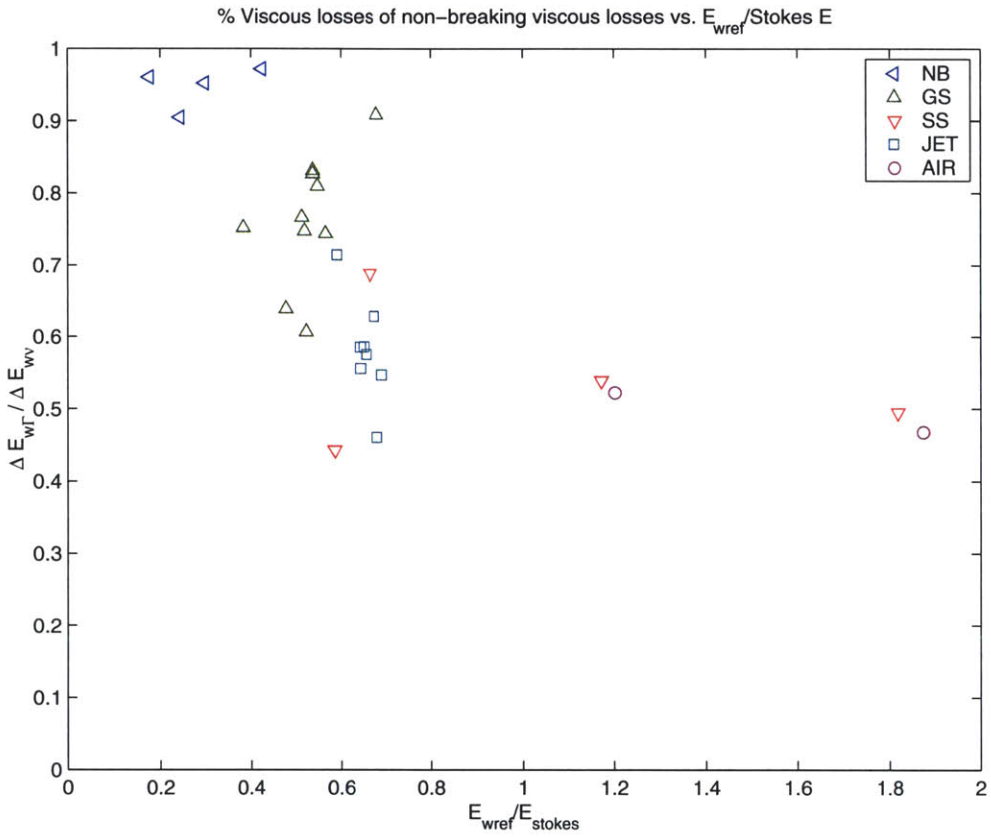

Figure 7-25: Measure of viscous losses due to breaking for a variety of waves: ($\triangleleft$) non-breaking, ($\triangle$) gentle-spilling, ($\triangledown$) strong-spilling, ($\square$) jet formation, and ($\circ$) air entrainment.

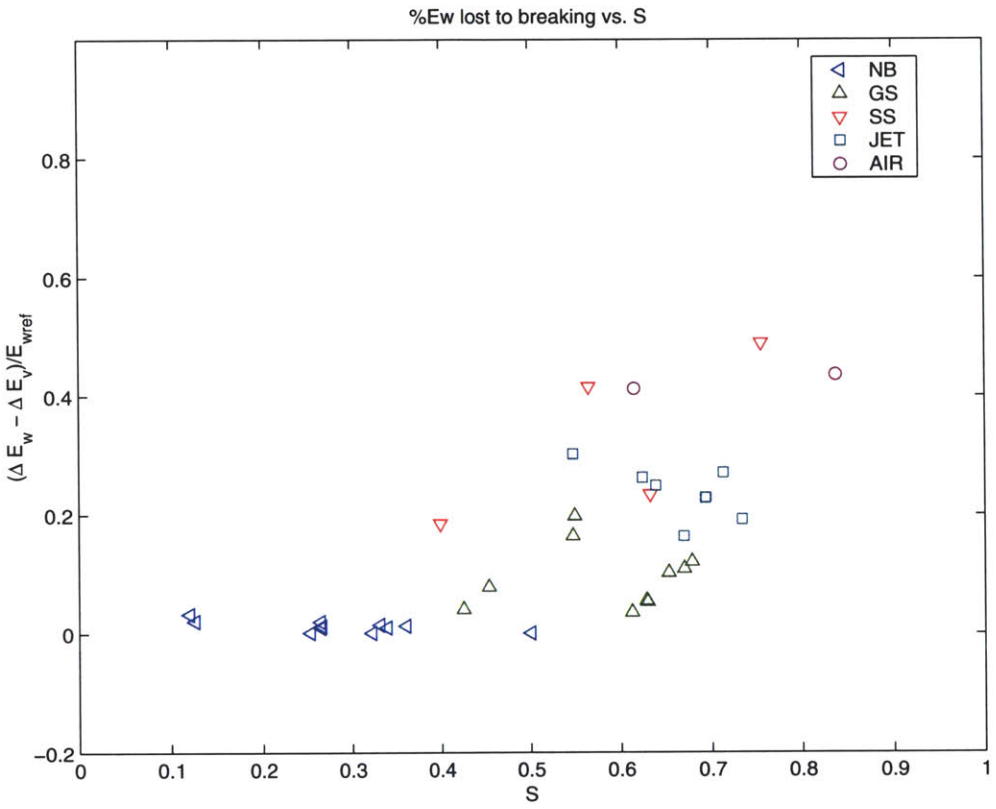

Figure 7-26: Amount of energy lost to breaking in the water volume over the breaking event as a fraction of the amount of energy at the start of the breaking process plotted against slope parameter (at t_{st}) for a variety of waves: ($\triangleleft$) non-breaking, ($\triangle$) gentle-spilling, ($\triangledown$) strong-spilling, ($\square$) jet formation, and ($\circ$) air entrainment.

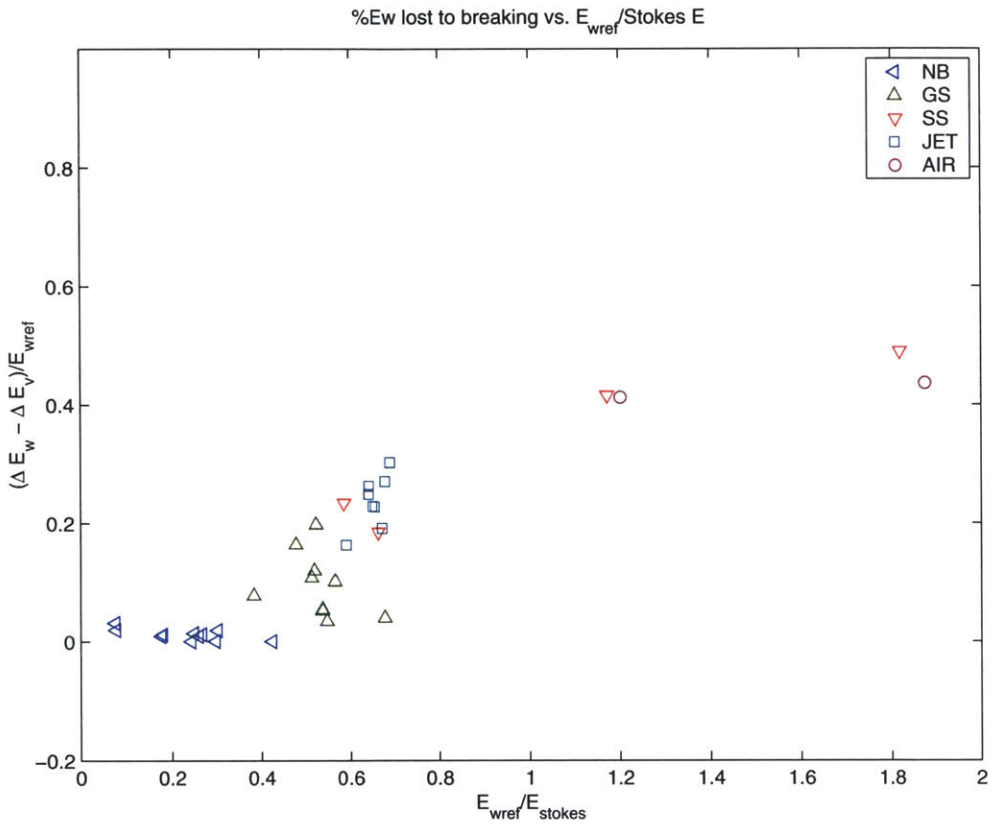

Figure 7-27: Amount of energy lost to breaking in the water volume over the breaking event as a fraction of the amount of energy at the start of the breaking process plotted against the normalized energy (at t_{st}) for a variety of waves: ($\triangleleft$) non-breaking, ($\triangle$) gentle-spilling, ($\triangledown$) strong-spilling, ($\square$) jet formation, and ($\circ$) air entrainment.

the margin of error (see Chapter 5 for a discussion regarding estimating the error in energy calculations). This also affirms our estimation of the non-breaking energy loss due to viscosity from equation 7.18. For waves with less than 40% of the energy of the Stokes limiting wave, there is essentially no breaking. This equates to a slope of about 0.28 using linear theory. Rapp and Melville report a threshold of S=0.25 for a breaking threshold and S=0.3 for a plunging threshold and Lowan and Melville report a similar threshold value at S=0.23 for breaking onset with S=0.28 as a threshold for plunging.

Between 40 and 80% of the energy of the Stokes limiting wave, there is again a rather large variability. Again, there is a cluster of points which has little or no energy loss due to breaking (less than 5%). If these cases are not considered, the variability drops to within the margin of error for these cases. It should be noted that while some of the cases in this cluster of points are the same as the cluster in figure 7-26, they are not all the same. The amount of energy lost in this range is between 10% and 25% depending on the type of breaking waves. The waves which are gentle-spilling breakers lose between 15-20% of their energy during the breaking event.

The energy loss due to breaking for the cases where the jet forms falls right in line with the trend of the curve when plotted against energy at onset. These cases occur when the energy is again 60% of the Stokes limit and lose around 25% of their energy during the breaking process. In this sense, they are much like the spilling-breaking waves in that their dissipation rates do not increase drastically and most of the energy loss is associated with the break-up of the jet.

The cases which are more energetic than the Stokes limiting wave see the greatest amount of total energy loss and loss due to breaking (40-45%). These cases are strong spilling breakers and cases with air entrainment. The strong-spilling cases are where there is a strong vortex on the front face the wave which attributes to a larger dissipation rate than the gentle-spilling breakers which have a weak vortex due to curvature. The cases with air-entrainment see multiple plunging events in a single period as well as large amount of energy loss due to the amount of work necessary to breakup the entrained air bubbles.

In interpreting the data in this study, one should be careful in using the energy at onset as a sole factor in determining energy loss. At 50% of the energy of the Stokes limiting wave, there exists a range of spilling breaking waves which lose between 10-25% of their energy to breaking. Just above 50% of the energy of the Stokes limiting wave are cases which have formed jets and spilling breakers dependant upon the Weber number (as the Weber number was used as a parameter to generate different types of breakers).

In summary, we've shown that the slope parameter used in literature may not be the most effective parameter for judging energy loss due to breaking when considering a variety of mechanisms which generate the breaking wave. In the absence of all other inputs, the slope parameter may be a good judge of the amount of energy in the wave. However, in cases with increased energy input from wind and current as well as already turbulent fields, then it may not be adequate. A more reliable method for this study entailed knowing the amount of energy in the wave. While the energy in the wave field is a better parameter for scaling the energy loss due to breaking in this study, it still fails for some cases showing that other mechanisms are at work.

While it is not an absolute judge of breaking, cases with less that 40% of the energy of a Stokes limiting wave in this study do not break which is not unlike that reported in the literature. There is a range between 40% and 60% which form spilling breakers and jets where the energy loss due to breaking increases dramatically. Finally, while the data is sparse above 70% of the Stokes limiting wave, a maximum amount of energy loss due to breaking of just over 40% is seen once a critical value is reached somewhere above 80% of the Stokes limiting wave.

7.3 Comparison with Experiments

This section takes the highlights of the previous sections regarding dissipation rates and global energy loss and compares them to the experiments and theory found in the current literature. Firstly, the available data in literature which applies to this topic is discussed. Secondly, the global energy loss results of this study in section

7.2 are compared to the most relevant papers in the literature. In terms of global energy lost, experiments generally cite the amount of energy flux lost in breaking as the dissipation. This quantity is calculated as is done by the experiments and compared directly. Thirdly, the dissipation rates of section 7.1 are compared to the small amount of data available for steady and unsteady wave-breaking dissipation rates found in the literature and an attempt is made to asses the scalability of a dimensionless dissipation rate which has appeared in the literature recently. While the cases in this study are two-dimensional and at smaller scales than the experiments, there are many results which compare well.

7.3.1 Discussion of Available Experimental Data

The scope of the literature for breaking waves is very large and encompasses a wide variety of topics. However, when breaking dissipation is used to refine the search, the number of relevant papers is relatively few and have come out only in the past few decades. This gives credence to the difficulty of measuring this type of phenomena as it is only as experimental methodologies have increased in sophistication that this type of result has been published. Additionally, the amount of computational results are also fairly limited in terms of the discussion of dissipation.

The papers relevant to this section are papers devoted to the dissipation in breaking waves. By far the most thorough and cited work is that of Rapp & Melville [92] in which wave focusing was used to generate a range of non-breaking and breaking waves. In this paper and a subsequent paper [76], they discussed the excess momentum flux and energy loss for these waves as a function of their integral slope parameter. Many of their results have been discussed throughout this thesis. The results which are germane to this section are the global energy flux losses which are discussed in section 7.3.2. Another similar study is that of Kway *et al.* [54] where they investigated the effect of different frequency packets on the dissipation of the wave.

An investigation of three-dimensional breaking by wave focusing was performed by Nepf *et al.* [80] and Wu and Nepf [127]. In addition to a detailed survey of

the breaking criteria [127] found in literature and its application to their waves, they reported the energy dissipation for two- and three-dimensional breaking using similar measurement techniques to Rapp and Melville. All three of these experimental investigations reported the effect of breaking on the spectrum of their broadband wave spectrums which was discussed in section 6.3.

There are a set of experiments by Duncan [29, 30] which looks at the quasi-steady breaking in the wave train beneath a towed hydrofoil. In these papers, he was able to discern, within the scope of his study, that the dissipation rate could be scaled by a characteristic phase velocity. There was some fluctuation in this scaling which was a function of the submergence depth, however, the fluctuation was relatively small.

This list is by far not a comprehensive list of the available experiments. They are the significant contributions in the available literature which address energy dissipation.

7.3.2 Global Energy Loss

Generally, global energy loss discussed in the literature is done from the surface elevation. Rapp and Melville provide an extensive derivation for this up through second order and Rapp [91] contains even higher-order terms. The essential argument is that the relative energy loss can be determined from the wave energy density which is proportional to η^2. If a control volume is drawn around the breaking region with vertical bounds at x_1 and x_2, then the amount of energy lost in the control volume is:

$$E(t_2) - E(t_1) + F(x_2) - F(x_1) = -\varepsilon \tag{7.19}$$

Because the energy flux F is equal to the energy density times the group velocity $\rho g \eta^2 C_g$, the change in energy flux is proportional to the change in η^2 assuming that the group velocity does not change (which they admit is a weak assumption). The amount of energy lost by the wave in breaking should remain in the control volume. Thus, the loss of wave energy in the control volume is essentially the loss of energy flux. At the Reynolds number they are investigating $\mathcal{R}e_w \sim O(10^6)$, providing the

measurements are taken well away from the breaking region, this should be sufficient in that assumptions regarding laminar flow and equipartition of energy apply.

In this study, some of the waves produced do not initially fall within the assumption of equipartition. Also, the Reynolds number is three orders of magnitude less than the experiments making Reynolds number effects more apparent. It is not sufficient to call the loss in wave energy only η^2. However, it can represent the loss of potential energy in the field. When considering only the potential energy lost, it should not be a problem to extrapolate these results to the larger Reynolds number experiments. Thus for comparison, the potential energy loss is estimated from the amplitude spectrum defined prior to the start of the breaking process t_{st} to well after the breaking event t_{stp}. After spectrum is calculated for a given time, the potential energy is calculated from the sum of the amplitude squared for each wave number.

$$\mathrm{pe}_w \approx \frac{1}{4}\frac{\rho_w}{\mathcal{F}r^2}\sum_{\text{all k}} a(k)^2 \tag{7.20}$$

As in section 7.2, viscous effects are accounted for using the laminar damping rate as if the wave did not break. The loss in wave amplitude predicted by laminar viscous damping is given by:

$$\eta_\nu^2(t) = \eta_{st}^2 e^{-2\Gamma(t-t_{st})} \tag{7.21}$$

Providing that t_{st} and t_{stp} are taken far away from the breaking region where the surface is not multi-valued such that the spectrum can be calculated and, if possible, the flow can be considered completely laminar, then the loss in potential energy due to breaking can be estimated by:

$$\frac{\Delta\eta^2}{\eta_{st}^2} = \frac{(\eta_{st}^2 - \eta_{stp}^2) - (\eta_{\nu st}^2 - \eta_{\nu stp}^2)}{\eta_{st}^2} \tag{7.22}$$

The fraction of potential energy lost as a function of the slope parameter S for the cases in this study is shown in figure 7-28 along with experimental cases found in literature [92, 80]. To account for the viscous losses in Rapp and Melville, the fraction lost for the non-breaking waves (estimated to be ~ 0.1) is subtracted from all of their

points. While in sections 7.1 and 7.2, we concluded that the slope parameter was not a particularly good parameter to judge scaling for the waves in this study, it is used in this figure as it is what is used in the literature concerning the experiments. Within the limits of this study, the comparison to the experimental data is fairly good. The maximum amount of potential energy lost reported by Rapp and Melville is approximately 10% lower than the maximum cases in this study. However, it should be pointed out that the experiments never attained more than a slope parameter of 0.5 so it is difficult to judge whether or not they reached a peak value. The upper level of diamonds are from Rapp and Melville's study and are for the case with central frequency $f_c = 0.88$ Hz. This case had multiple entry events and thus a larger amount of energy was dissipated. The cases in this study with air entrainment and multiple breaking events also see a rather increased dissipation. Finally, the three-dimensional result of Nepf *et al.* [80] experiences a lower fractional energy loss than the experimental two-dimensional results. They attribute this to the fact that part of the wave is spilling and part is plunging. This three-dimensional result experiences a similar amount of energy loss as some of the spilling events in this study.

Ideally, because of the findings in the previous sections, we would like to consider the amount of potential energy loss as a function of the energy in the wave prior to breaking. However, the experimental data in the literature does not provide this so it must be estimated. For all of the experimental results, the ratio of the energy in the wave group compared to the Stokes limit is estimated as S^2/S^2_{Stokes}. This is shown in figure 7-29. The scatter in the data becomes considerably less as expected. It should be pointed out here that the energy in three-dimensional breaker is likely overestimated by S^2/S^2_{Stokes} making the result seem out of place. The other experimental outliers are from Kway *et al.* [54] where their slope parameter is a function of the gain on the wavemaker as well. Outside of these spurious points, the comparison to experiments improves. However, it now appears that the strong-spilling breakers and cases with air entrainment are 10% larger than the experimental cases at the same energy level. This is not completely unexpected as the breaking event is always two-dimensional in this work. The experiments are not completely two-dimensional after

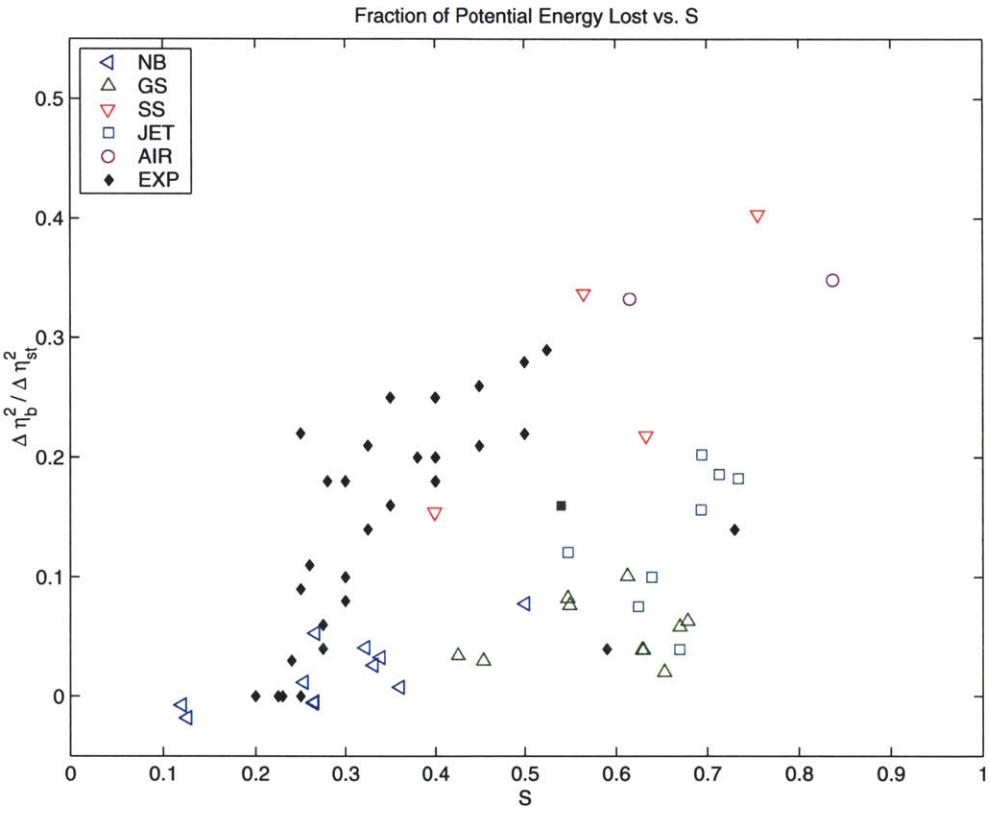

Figure 7-28: Fraction of potential energy lost due to breaking compared to the slope parameter (at t_{st}) for a variety of waves: ($\triangleleft$) non-breaking, ($\triangle$) gentle-spilling, ($\triangledown$) strong spilling, ($\square$) jet, and ($\circ$) air entrainment. Filled symbols represent experiments. Filled square is three-dimensional experimental result.

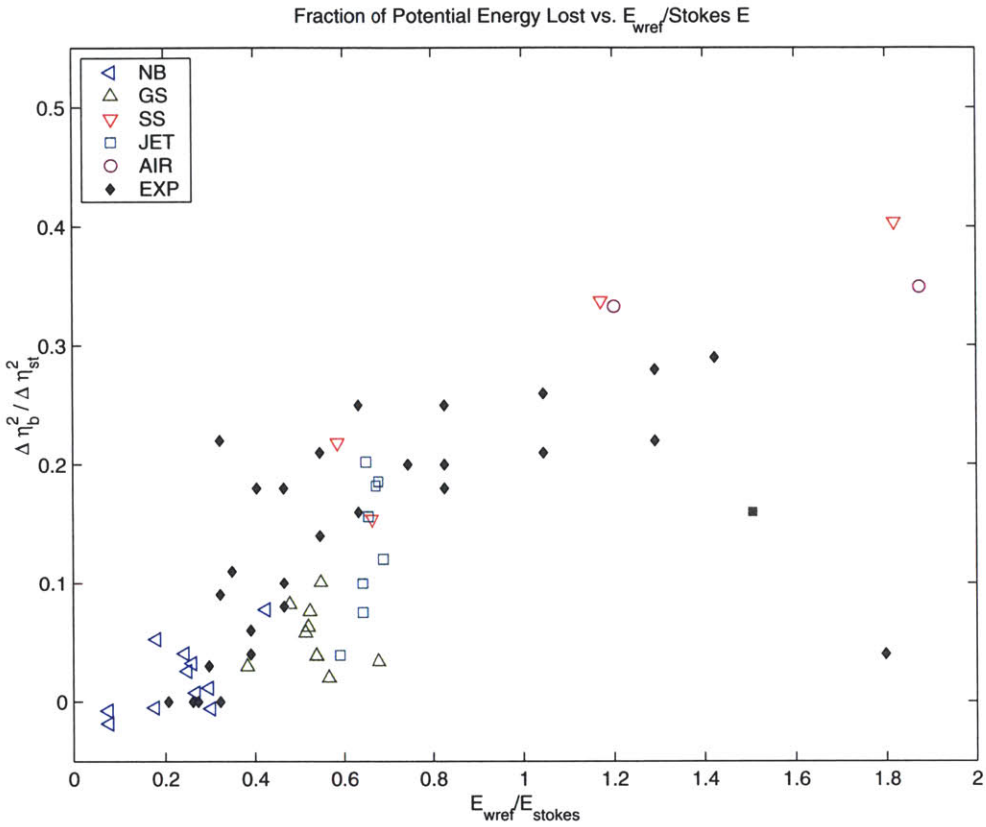

Figure 7-29: Fraction of potential energy lost due to breaking compared to the slope parameter (at t_{st}) for a variety of waves: ($\triangleleft$) non-breaking, ($\triangle$) gentle-spilling, ($\triangledown$) strong spilling, ($\square$) jet, and ($\circ$) air entrainment.

breaking. Thus, one would expect that a two-dimensional version of the turbulence generated by the waves would over-predict the dissipation rate to a certain degree.

7.3.3 Energy Dissipation Rate

As discussed briefly in section 7.1.3, there does not seem to be anything in the literature on dissipation rates during the breaking process for unsteady breaking waves. In his papers on steady breaking waves behind a towed hydrofoil, Duncan [29, 30] determined that the dissipation rate of a breaking wave scaled as a function of a characteristic phase velocity. The first paper [29] gave the dissipation rate per unit

length as:

$$\varepsilon_\ell = (0.044 \pm 0.008)\frac{\rho_w C^5}{g} \tag{7.23}$$

Within the accuracy of the measurements he was able to make and the scope of the study, a constant relation between dissipation rate and a characteristic phase speed was justified. This dissipation rate was used by Phillips [88] to infer statistics of wave breaking. After a further study on the sensitivity of his results as a function of the depth of the hydrofoil [30], Duncan's results show that the dissipation rate is now a function of the inclination angle of the forward face of the wave:

$$\varepsilon_\ell = 0.0075\frac{\rho_w C^5}{g\sin\theta} \tag{7.24}$$

For the range inclination angle seen in his experiments, this modifies the coefficient in equation 7.23 to have a much larger variability (0.066-0.031).

The purpose of this discussion is to not attempt an exact comparison to Duncan's dissipation equation. Melville [74] took this assessment and results from Loewen and Melville [70] to determine relative strength between the dissipation rate of steady and unsteady breaking waves and also back out a coefficient for the dissipation rate of unsteady breaking waves. Depending on his estimate of the integral velocity scale of the turbulent dissipation as a factor of the phase speed of the wave, Melville determined that the dissipation rate per unit length to be from scaling arguments:

$$\varepsilon_\ell \approx (3.2 \times 10^{-3}, 16 \times 10^{-3})\frac{\rho_w C^5}{g} \tag{7.25}$$

However, as Melville points out, since there is an estimation parameter (the fraction of the wave phase speed which represents the turbulent velocity) which is taken to the fifth power, there is quite a large leeway in terms of interpreting this result.

As Melville did not have actual dissipation rates, to estimate the dissipation rate, he took the amount of energy dissipated over the time of the breaking event to give an average unsteady breaking dissipation rate. He plotted this quantity scaled by $g/(\rho_w C^5)$ verses his slope parameter (his figure 3). There was a significant depen-

dence on S which showed that as the wave progressed from spilling to plunging, this dimensionless dissipation rate increased. However, there was considerable scatter in the data if multiple breaking occurred because these multiple breaks, no matter what slope parameter they occurred at would have a larger amount of dissipation associate with them. The order of magnitude of this dimensionless parameter ranged from 4 to 12×10^{-3} which falls in line with equation 7.25. It is pointed out by Melville that, because there is dependence of this dimensionless dissipation rate on the slope parameter for unsteady breaking, the characteristic velocity is not the sole determinant of dissipation rate. Melville also notes that this dimensionless rate is up to an order of magnitude less than that seen in the quasi-steady breaking waves of Duncan. Thus, presuming that the wave breaking in the ocean is a characteristically unsteady event, using estimates from quasi-steady results to infer breaking statistics is questionable.

While this work done by Melville showed no conclusive dependence on phase speed, it is useful to determine whether or not the dissipation rate for the waves in this study follow a similar pattern and magnitude. Figure 7-30 shows the dimensionless dissipation rate from Melville's paper with results from this study, considered in two different ways. The first is to calculate the average dissipation rate by calculating the amount of energy lost due to viscosity divided by the time of the breaking event.

$$\varepsilon_{\mathrm{AVG}} = \frac{1}{t_2 - t_1} \int_{t_1}^{t_2} \overline{\varepsilon}_w dt \tag{7.26}$$

The second method was to just take the maximum value of the dissipation rate during the breaking event and scale it by the phase speed of the wave.

$$\varepsilon_{\mathrm{MAX}} = \max(\overline{\varepsilon}_w)_{t_1 \leq t \leq t_2} \tag{7.27}$$

Figure 7-30 demonstrates that, as Melville stated, for unsteady breaking events, the dissipation rate can not be scaled solely by the phase speed of the wave. There is clearly a dependence on the amount of energy in the wave before breaking as to the strength of the dissipation rate. It also shows that, for the majority of waves considered in this study, the magnitude of the dissipation rate for the unsteady breaking

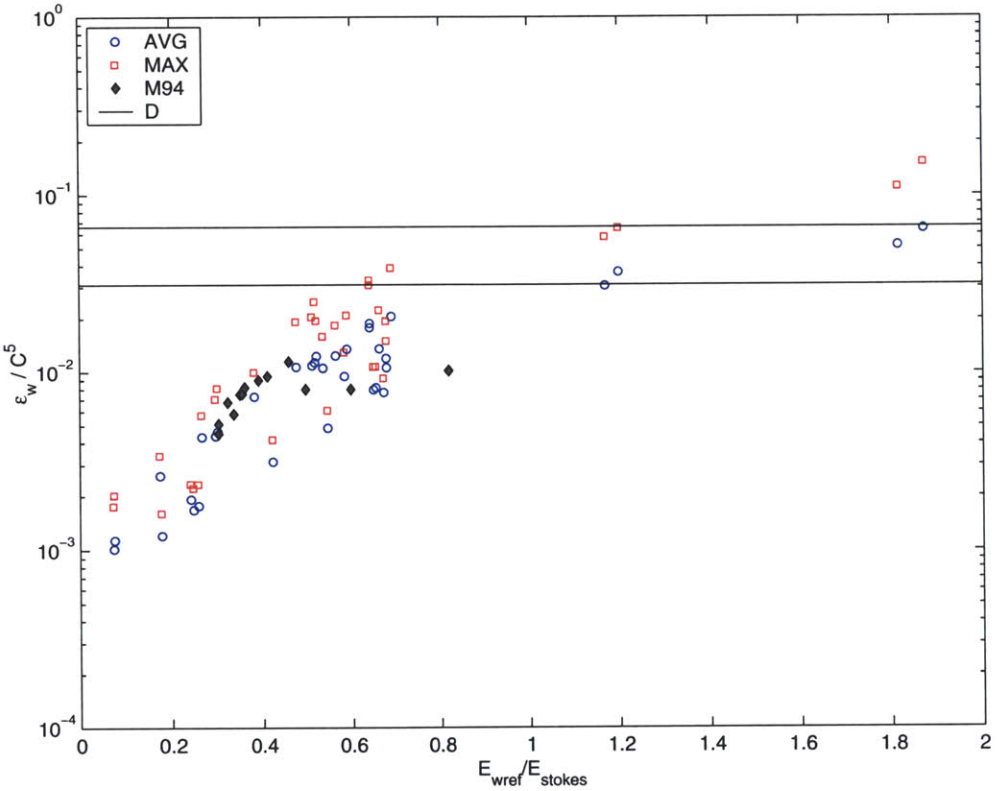

Figure 7-30: Dimensionless dissipation rate $\varepsilon\rho_w/gC^5$ as a function of energy before breaking. ($\circ$) average dissipation rate, ($\square$) maximum dissipation rate, (filled $\diamond$) Melville [74]. The black lines represent the bounds of the rates estimated for quasi-steady breaking.

waves is an order of magnitude less than quasi-steady breaking waves. However, for a few of the cases in this study, the dissipation rate approaches that of the quasi-steady cases. This corresponds to the very strong spilling breaking waves and waves with air-entrainment. For the very strong spilling breaking waves, many of the characteristics are similar to Duncan's over the span of the breaking event. Whereas the presence of Duncan's hydrofoil continues to supply a source of energy for the wave to break, the strong spilling breakers have no source of energy and the event tapers out. All of the cases with air-entrainment see dissipation rates within the order of magnitude of Duncan's hydrofoil. However, as discussed previously, their dissipation may be artificially larger due to the two-dimensional nature of the flow and the relatively large stiffness of two-dimensional "bubbles".

7.4 Energy Growth Rate as a Breaking Criteria

The purpose of this study was not to directly determine a breaking criteria. This is in fact a wide ranging study in and of itself. A review of the range of geometric, kinematic, and dynamic criteria currently available in literature is included in Wu and Nepf [127]. Their general conclusion was that accurate estimation of kinematic quantities such as the ratio of crest speed to phase speed $U/C > 1$ was a simple and robust candidate for a breaking criteria. However, as pointed out by these authors, recent work by Stansell and MacFarlane [105] have shown that waves can break at $U/C > 0.72$. This is an interesting example of the difficulty of trying to characterize a complex process of wave breaking to a single mechanism or number.

In a series of papers, another candidate for wave breaking criteria within the context of wave groups has been proposed [19, 5, 103, 104]. The theory is based on a localized, short-time focusing event within a wave group. The works of Banner [5, 103, 104], which build on the Dold and Peregrine [19] results, show that in all of the cases in their studies, there is a *mean convergence* of the energy density (kinetic and potential) toward a local maximum. Banner and Tian [5] state that this *local* quantity was the only robust measure which determined whether the wave broke or

evolved with a recurrence of the original wave group.

The basis of the theory is the local wave energy density, E:

$$E(x;t) = \int_{-h}^{\eta} \frac{1}{2}\rho_w(u^2 + v^2)dy + \frac{1}{2}\rho_w g\eta^2 \tag{7.28}$$

Banner *et al.* define a diagnostic parameter based on the local maximum energy density, which they call μ. As the wave group is modulated by the carrier wave, this μ can vary significantly. However, they found that if they consider the evolution of its local average value $\langle\mu\rangle$, that there is a critical value of its growth rate which determines whether or not a wave will break. In terms of their notation, the dimensionless growth rate they consider is:

$$\delta = \frac{1}{\omega_c}\frac{D\langle\mu\rangle}{Dt} \tag{7.29}$$

In the paper by Song and Banner [103], they postulate a number of diagnostic parameters. The one that they found to be most fruitful ends up being a measurement of the local wave steepness.

$$\mu = \max\left(\frac{E}{\rho_w g}k^2\right) \tag{7.30}$$

For cases where a group is not well defined (as in the open ocean) or periodic boundary conditions where the realm of growth is bounded, they also mentioned that another parameter which was useful was a normalized wave energy density:

$$\mu = \max\left(\frac{E}{\langle E_T\rangle}\right) \tag{7.31}$$

where $\langle E_T\rangle$ represents the mean energy of the wave group. Based on equations 7.29 and 7.30, Song and Banner determined a common threshold δ_{th} in the range of $(1.3 \times 10^{-3}, 1.5 \times 10^{-3})$ which indicated whether or not a wave would break or recur. In a subsequent paper, Banner and Song determined that this threshold was upheld through wind forcing and the effects of shear currents.

To investigate the connection between this growth rate and breaking criteria for the waves in this study, a few diagnostic parameters were considered. The first effort revolved around the cases where an initially quiescent surface of water is forced on the

surface for a short period of time. For these cases, while there may be some focusing involved, the predominant reason for breaking is the amount of energy imported to the water during the forcing. Thus, a suitable diagnostic parameter can be the mean energy input. As there is no initial energy in the field, this is simply:

$$\mu = \langle E_w \rangle - E_\nu \tag{7.32}$$

where because of the moderate Reynolds number of these cases the laminar damping has been factored out based on equation 7.18. Because all of these cases receive only an input, there is no modulation of the wave energy density and thus, the dimensionless growth rate is defined as the rate of change of μ directly.

$$\delta_0 = \frac{d}{dt}\left(\langle E_w \rangle - E_\nu\right) \tag{7.33}$$

The maximum of this growth rate is shown in figure 7-31 as a function of the amount of energy lost due to breaking. Song and Banner's threshold values are included as a reference. All of the cases which had an energy loss associated with breaking are above $\delta_0 = 1.5 \times 10^{-3}$. While not a definitive conclusion, this shows that, in the cases of energy input, there is a threshold above which, the waves in this study will break. This does not give any conclusion about the role of focusing because the diagnostic parameter used is a total and not a local quantity. After the forcing has been turned off, in the absence of any other inputs, the amount energy in the volume will not change (except due to viscous effects) and any local focusing of energy would be balanced out by a loss of energy some place else. Thus the average energy $\langle E_w \rangle - E_\nu$ will always decrease and δ_0 will always be negative.

To address the effect of a local focusing or convergence of the energy density, two diagnostic parameters were defined which follow the spirit of Banner *et. al.*, if not the letter. Song and Banner define one of their diagnostic parameters as $(E/\rho_w g)k^2$. Within the context of their work which used potential flow, this was a clever way to estimate the local slope without worrying about crest asymmetry. However, within the context of this study, we've shown that the local slope is not a good assessment

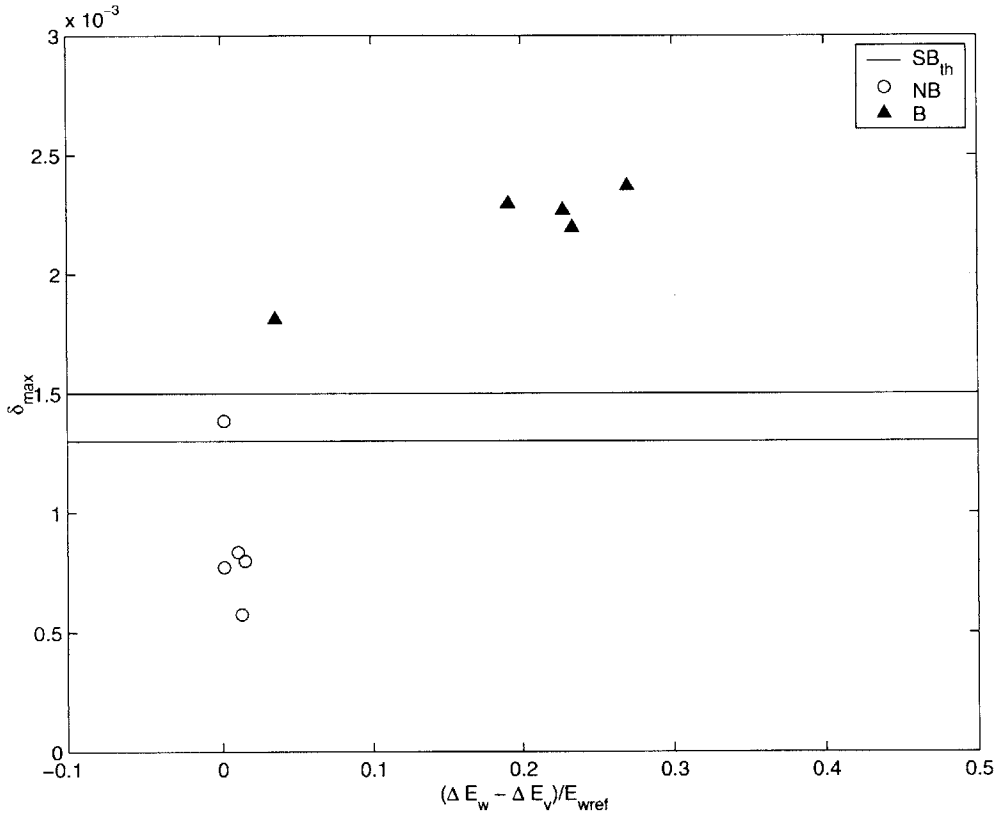

Figure 7-31: Maximum growth rate for cases which were forced from an initially quiet surface using pressure forcing. (-) Song and Banner threshold values; (o) non-breaking cases; (filled $\triangle$) breaking cases.

of the amount of energy in the wave field. Additionally, as there is no wave group perse, the idea of a local wavenumber is difficult to grasp. Thus, the two diagnostic parameters used in this work rely solely on the local energy density: $\mu = \max(E_w)$. The first is μ and the second diagnostic parameter used is the local maximum energy density normalized by the total energy in the wave. The two growth rates based on these definitions are:

$$\delta_1 = \frac{d}{dl}\max(E_w) \tag{7.34}$$

and normalized

$$\delta_2 = \frac{d}{dt}\left(\frac{\max(E_w)}{\langle E_{wT}\rangle}\right) \tag{7.35}$$

The maximum of these two parameters is shown against the amount of energy lost due to wave breaking in figures 7-32 and 7-33, respectively. The waves which were generated by forcing on a flat surface and shown in figure 7-31 are not considered here as their breaking mechanism is not related to energy focusing. However, the results in figures 7-32 and 7-33 include cases where an existing wave has received forcing so the results do include forced as well as non-forced waves.

The first growth rate, δ_{1max} shows a consistent threshold value near the value of the Song and Banner value of $1.3 \times 10^{-3}, 1.5 \times 10^{-3}$, with one outlier. This outlier is the case which we have identified as an incipient breaking case. Without a doubt, it has an increase in dissipation during its breaking event such that it is categorized properly. However, the reason for its appearance below the threshold is unknown. If one considers the normalized maximum local energy density (see figure 7-33), a similar threshold appears, near $\delta_{2max} \approx 2$, with two outliers. The first outlier corresponds to the same incipient breaking case as in figure 7-32. The second outlier corresponds to the same wave which has received surface forcing. This implies that this particular case may have a breaking mechanism which is not solely a function of energy focusing, however, again, the reasons are not clear.

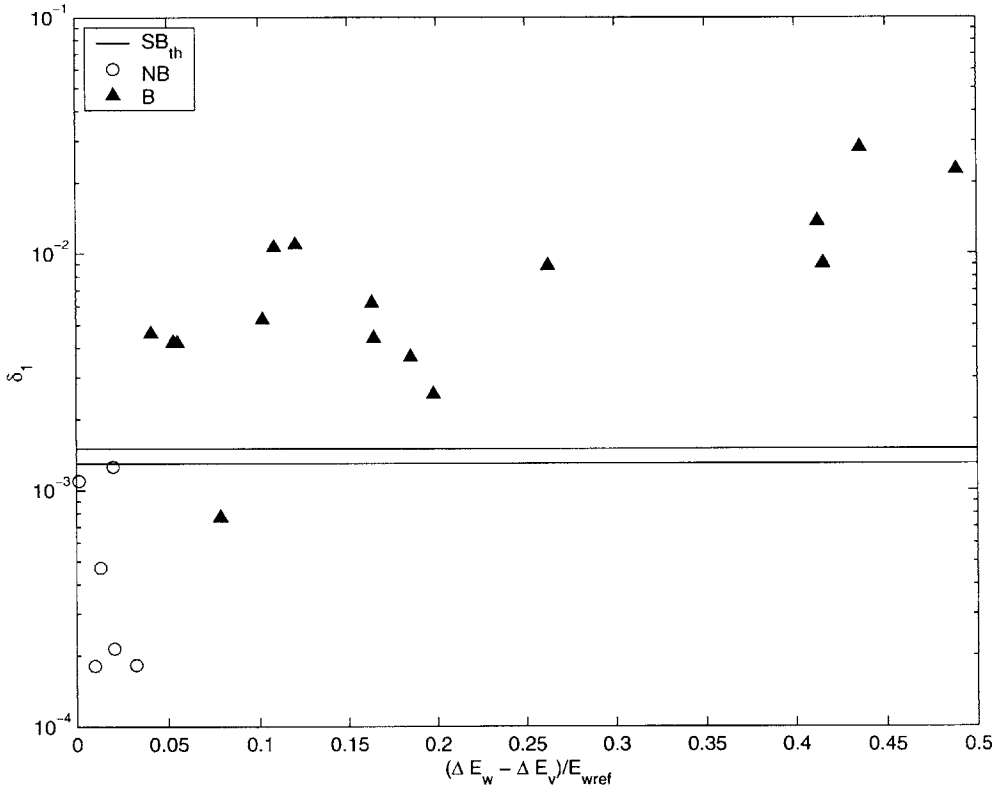

Figure 7-32: Maximum growth rate δ_1 for a variety of forced and un-forced waves. (-) Song and Banner threshold values; (o) non-breaking cases; (filled $\triangle$) breaking cases.

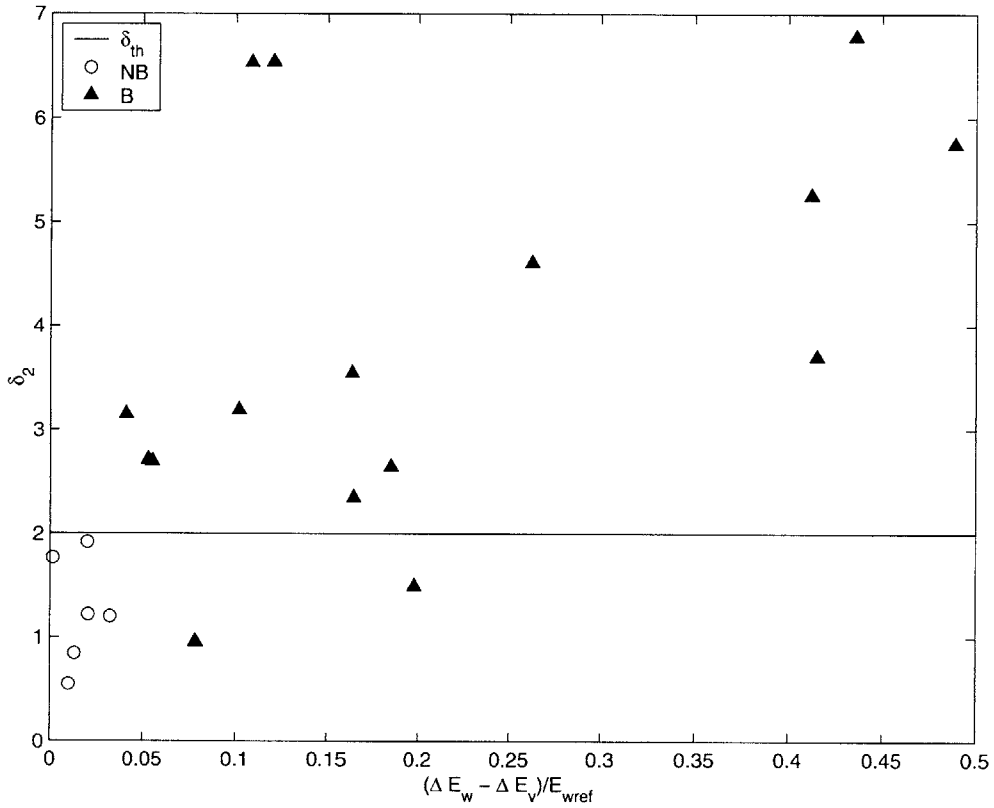

Figure 7-33: Maximum growth rate δ_2 for a variety of forced and un-forced waves. (-) Estimated threshold value; (o) non-breaking cases; (filled $\triangle$) breaking cases.

Song and Banner made a preliminary attempt to tie their δ not only to a breaking criteria but also to the strength of the breaking event. This would imply a trend in the amount of energy lost to breaking as a function of $\delta_{0,1,2}$. In regards to δ_0, figure 7-31 shows an increasing amount of energy being lost to breaking as δ_0 increases. However, the amount of data is sparse to draw any firm conclusions. Inspection of figure 7-32 shows a similar trend for δ_1 with some scatter (which is magnified by the log scale of the plot). Finally, the same could be said for δ_2 with some outliers. It is a bit ambitious to draw any conclusions regarding a relationship between δ and the amount of energy lost to the breaking event based on the data in this study. At most, what can be said is that there is a hint of promise in this direction, but more samples would be needed to be definitive.

In summary, a concept of local convergence of energy density has been examined in the context of this study. While initially proposed for wave groups, application to a general volume without a well defined group showed similar results. Two growth rates were defined as a function of the local maximum energy density. The first being the quantity itself, the second being the quantity normalized by the total amount of energy within the domain. The maximums of both growth rates showed a threshold value to which the wave will either break or progress (with a few outliers). While attempts were made to connect the maximum growth rate to the amount of energy lost due to breaking, there was not enough conclusive evidence and more work in this area is warranted.

7.5 Conclusions

Through direct numerical simulations of non-breaking and breaking waves the energy dissipation of wave breaking has been quantified. To our knowledge, this study has provided a first-ever glimpse at the spatial and temporal variation of the dissipation rate of breaking waves. Because this study includes the effect of the air above the surface, the dissipation rate for the air is also captured for the first time. Depending on the strength of the breaking wave, the relative increase for the dissipation rate in

the water during the breaking process is about twice its initial value, even in cases with air entrainment. If the wave has been forced, this can increase to 5-6 times the initial value depending on the strength of the forcing. Thus, in cases where a wave is receiving an input, the dissipation rate can be tied to the strength and duration of the input. For the air, the relative increase is significantly larger in cases when the wave is plunging. This brings the dissipation rate in the air to the same magnitude as the water for some cases. Spatially, the waves experience regions of strong localized dissipation in the regions with high curvature and vorticity. The localized regions persist longer where the breaking originated verses where the breaking has "passed" through as it has traveled down the face of the wave or experienced a plunging re-entry. Despite this localized persistence, the global dissipation rates for the waves in the air and the water return to non-breaking values post-breaking.

As part of our investigation of the global amount of energy loss due to breaking, we've shown that the amount of energy in the wave prior to breaking onset is an indication of whether or not a wave will break. Yet, the connection between this quantity and the strength of the breaking event is weak. That being said, within the data available for this study, there appears to be a maximum amount of energy lost once a critical value of energy has been reached in the wave.

The computational results have been compared to experimental data in terms of the amount of potential energy lost due to the breaking event. As we only considered potential energy, it is possible to compare these results to experiments which occur at Reynolds numbers which are three orders of magnitude larger. The comparisons are quite favorable considering the two-dimensional nature of the waves in this study.

We've also explored the existence of a breaking criteria which is based on a local mean convergence of the energy density based on recent work in literature. Using three different growth rates, we were able to conclude that a threshold exists above which waves will break. However, like considering the amount of energy in the wave, tieing this breaking criteria to the amount of energy lost to the breaking process is not warranted at this time. While 36 different waves were generated for this study, the amount of data is too sparse to draw a direct conclusion.

Chapter 8

Transfer of Energy at the Air-Water Interface during Breaking

Much attention in the literature has been given to the transfer of energy between the air and the sea over the past few decades. However, the focus of these studies has been on the effect of the wind imparting energy to the waves and subsequently the ocean currents. Additionally, the predominance of the studies in the literature concern how this effects the spectrum of the waves as this knowledge is essential for wave forecasting efforts. In general, the studies in the literature which address the local effects of the wind on the waves treat the problem as air flow over a solid boundary (such as wind over wavy surfaces) which may or may not be moving. Up until the past few years, very little attention has been paid (numerically) to the coupled air-water boundary layer.

Because this study does not include the effects from wind, the type of energy transfer discussed in the literature can not be addressed. However, what can be considered is the transfer of energy through the interface which is a function of the breaking event. Until recent work by Brocchini and Peregrine [10], this type of energy transfer has been seemingly ignored and waved off in the literature and fluid dynamics texts. While the work by Brocchini and Peregrine is significant as it details the

formulation of this transfer in the context of turbulent kinetic energy, this chapter provides a cleaner form of the energy-flux rate at the interface. This is done in section 8.1. Using the waves in this study, this chapter first builds a case for the significance of this term in section 8.2 and then quantifies the amount of energy transferred at the air-water interface between the two volumes in section 8.3. Finally, section 8.4 provides a view of the dominant mechanisms of the energy transfer at the interface for spilling and plunging breaking waves. To our knowledge, this is the first time much of this has been reported.

8.1 Formulation and Discussion

This section revisits the formulation of the term which represents the transfer of energy across the air-water interface. It begins with the energy equation derived in chapter 2 and more fully explores the term. An interpretation of the term and a discussion of what is expected from the term is also included. The rate of change of kinetic energy per unit volume can be written by slightly modifying equation 2.67:

$$\underbrace{\frac{\partial}{\partial t}\kappa_w}_{I} + \underbrace{\nabla\cdot\left(\vec{F}_w - \frac{\vec{\Sigma}_w}{\mathcal{R}e_w}\right)}_{II} = \underbrace{-\frac{\varepsilon_w}{\mathcal{R}e_w}}_{III} + \underbrace{\Theta_w}_{IV} + \underbrace{\delta(\phi;\epsilon)\nabla\phi\cdot\left(\vec{F} - \frac{\vec{\Sigma}}{\mathcal{R}e_w} - \kappa\vec{\mathbf{u}}\right)}_{V} \tag{8.1}$$

where

$$\begin{aligned}
\{\cdot\}_w &= \{\cdot\}H(\phi;\epsilon)\\
\vec{F} &= (\kappa+\Pi)\,\vec{\mathbf{u}}\\
\vec{\Sigma} &= \tau\cdot\vec{\mathbf{u}}\\
\Theta &= \text{Work done by other forces}
\end{aligned}$$

and $\delta(\phi;\epsilon)$ is the smoothed delta function used throughout this work. The change in kinetic energy per unit volume (term I) is a function of four mechanisms. The first is represented by term II which is the energy density flux and is composed of two parts.

The first is due to actual transfer of fluid mass at the interface. This is the flux of pressure work at the interface and is present even in the absence of viscosity. The second part is due to internal friction and only exists in the presence of viscous effects. The dissipation by viscosity is represented by term III. It is defined in chapter 7 as $\varepsilon_w = 2\frac{\mu(\phi)}{\mathcal{R}e_w} S_{ij}^2 H(\phi;\epsilon)$. Term IV represents all of the work done by other forces such as gravity, surface tension and surface forcing. Finally, term V represents the flux of energy at the interface and is the term of interest for this chapter. As equation 8.1 is the rate of change of kinetic energy per-unit volume, it can be integrated over a volume to get the total rate of change of kinetic energy in the water. For the purposes of this study, the control volume is defined to be the entire domain. This helps simplify the equation as term II yields zero contribution because of the conditions used at the boundaries (no flux top and bottom boundaries and periodicity horizontally). This yields the following energy equation for the entire water volume:

$$\frac{\partial}{\partial t}\overline{\kappa}_w = -\frac{\overline{\varepsilon}_w}{\mathcal{R}e_w} + \overline{\Theta}_w + \underbrace{\overline{\delta \nabla\phi \cdot \left(\vec{F} - \frac{\vec{\Sigma}}{\mathcal{R}e_w} - \kappa\vec{\mathbf{u}}\right)}}_{\overline{\chi}} \tag{8.2}$$

where

$$\overline{\{\cdot\}}_w = \int_\forall \{\cdot\} H(\phi;\epsilon)\mathrm{d}\forall \qquad \text{and}$$
$$\overline{(\cdot)} = \int_\forall (\cdot)\,\mathrm{d}\forall$$

In this equation, the energy flux at the interface is represented by a volume integral. However, the presence of the smoothed delta function in the integral reduces the volume integral to a surface integral of the energy flux along a finite thickness of the air-water interface. This is defined as $\overline{\chi}$ and represents the transfer of energy across the air-water interface. The presence of this term has been noted in some fluid dynamics texts [58] as the energy flux through a surface bounding the volume but it receives little discussion. It also appeared recently in an archival journal paper by Brocchini and Peregrine [10]. Their work, however, is based on a phase weighted

averaged form of the turbulent kinetic energy equation. This in turn makes the number of interfacial terms grow and appear complex. In this simplified form, the origin and mechanisms behind it are cleaner. The form of $\overline{\chi}$ in equation 8.2 can be simplified further if the definitions of $\vec{F}$ and $\vec{\Sigma}$ are substituted back into it.

$$\overline{\chi} = \int_{\forall} \delta \nabla \phi \cdot \left(\Pi \vec{\mathbf{u}} - \frac{\tau \cdot \vec{\mathbf{u}}}{\mathcal{R}e_w} \right) \mathrm{d}\forall \tag{8.3}$$

This form of $\overline{\chi}$ allows us to note that as with the energy-density flux, it is made up of two parts, the work done by the pressure field (not including surface tension as that is included in Θ_w) and the work done by viscous forces. As $\nabla\phi$ represents a vector which points in the normal direction of the interface, $\overline{\chi}$ is then the flux of energy normal to the air-water interface. In general, as the Reynolds number becomes large, the second term of equation 8.3 becomes fairly small leaving the inviscid work of the pressure field as the dominant contributor to the energy transfer at the interface. While the effects of the viscous term are relatively small for large Reynolds number flows, they are included in this study. The moderate Reynolds number of the waves in this study dictate that it be included.

The relationship between the sign of $\overline{\chi}$ and the direction of the energy transfer is dependent upon the definition of the level set function ϕ. In this work, ϕ is defined positive in the water and negative in the air. Thus, $\nabla\phi$ will produce a normal vector which points into the water surface. Based on equation 8.3 and the direction of $\nabla\phi$, a positive $\overline{\chi}$ represents a global transfer of energy from the air to the water and a negative $\overline{\chi}$ represents a global transfer of energy from the water to the air.

The first step in understanding the relative importance of the energy transfer at the air-water interface is to determine how this term behaves for special cases. First, consider a truly plane progressive wave which is not evolving or being modulated in any way. The flux of energy normal to the interface is zero for this case. This can be seen if the flow is in a reference frame fixed with the crest. The velocity field is surface following and made up only of a surface parallel component. Thus, the flux of any quantity normal to the interface in this frame is zero. Second, consider a standing

wave which does not progress at all. In this case, there will be a component of the velocity field normal to the interface. However, as the standing wave field is cyclic in time, the energy transfer will also be oscillatory in nature.

Figure 8-1 shows the energy transfer rate for four representative non-breaking wave cases. $\overline{\chi}$ is calculated directly in the form represented in equation 8.2 and is shown with the rate of change of the total energy for the water volume. For all four cases, the rate of transfer of energy is one to two order of magnitudes smaller than the rate of change of total energy in the water. There is a period of adjustment as the wave develops from its initial condition where the energy transfer at the interface is larger and then reduces to an essentially constant and small value as it becomes a decaying plane progressive wave. The oscillatory nature of the energy transfer rate in the presence of standing waves can also be seen in figure 8-1. These cases also experience an adjustment period where the wave is developing into a plane progressive wave. Once the wave has completely developed, the mean value of the oscillation is essentially constant and small.

As a final verification that the nearly zero value of energy transfer rate results in essentially zero energy transferred between the air and water volumes for non-breaking (and non-evolving) waves, the total amount of energy transferred over the entire simulation is shown in figure 8-2. This is calculated as a cumulative integral in time:

$$\underline{\overline{\chi}}(t) = \int_{t_{ref}}^{t} \overline{\chi} dt \tag{8.4}$$

For comparison, the total energy transferred is shown along with the total amount of energy in the water volume. For these non-breaking cases, the mechanism which is dominant is the dissipation by viscosity as the surface tension is either a very weak or non-existent effect. Figure 8-2 shows that the amount of energy transferred for these non-breaking cases is negligible throughout the length of the simulation, even for cases where the standing wave component is relatively significant.

Based on these arguments, any wave in which there is a surface normal velocity component at the air-water interface will have a local non-zero interfacial energy

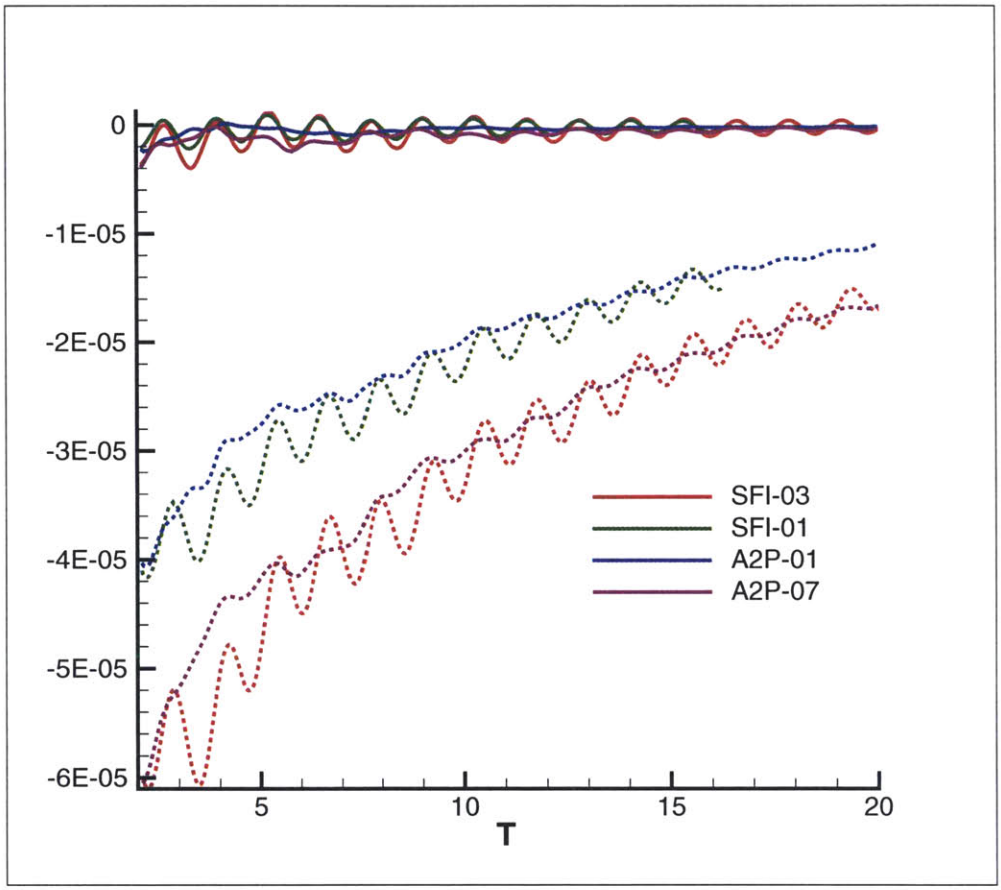

Figure 8-1: Rate of energy transfer at the interface (solid lines) and rate of change of total energy of the water volume (dashed lines) for four non-breaking wave cases.

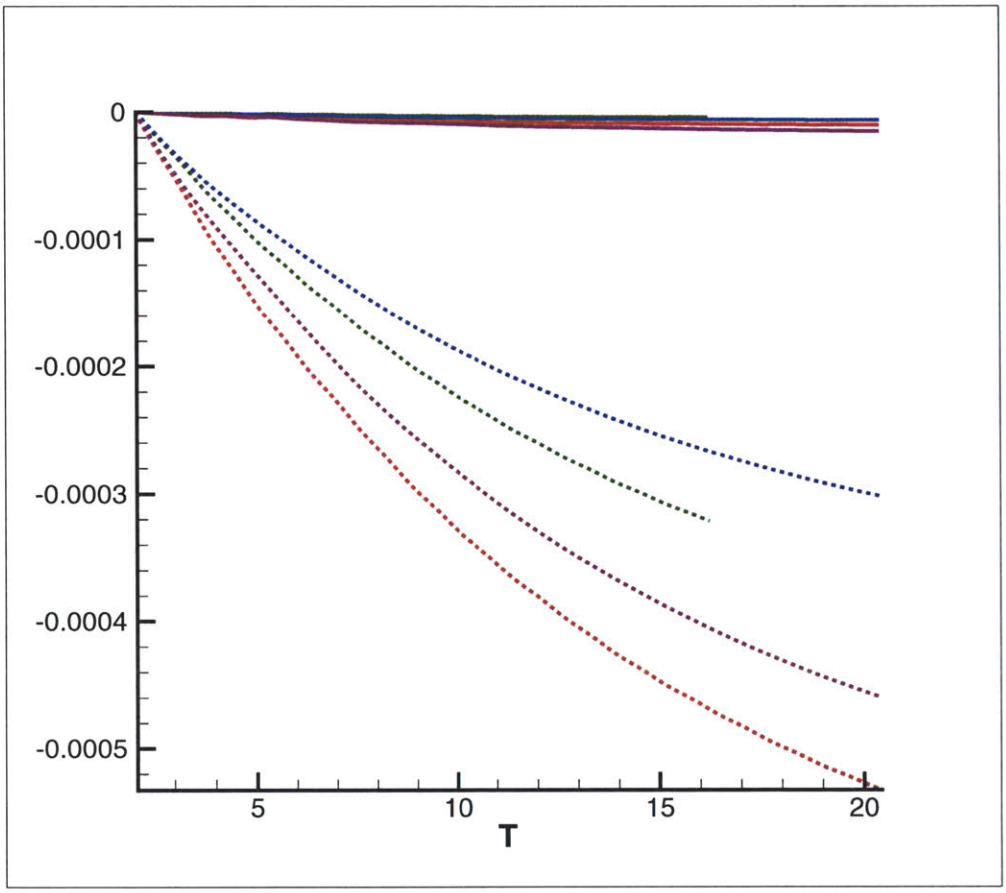

Figure 8-2: Cumulative amount of energy transferred at the air-water interface (solid lines) and total energy of the water volume (dashed lines) for four non-breaking cases (same as figure 8-1).

flux. If the wave develops a crest asymmetry such that over the wavelength the flux contributions do not cancel, $\overline{\chi}$ will also be non-zero. It follows from our knowledge of breaking waves that any wave which breaks will have a non-zero $\overline{\chi}$. Thus, breaking waves have the ability to transfer energy from the water to the air. It remains to be seen how significant this flux is.

It should be pointed out that there is an equal and opposite term when one considers the air equation. This can be derived in the same manner as equation 8.2 from the total energy equation by multiplying equation 2.59 by $1 - H(\phi;\epsilon)$ instead of $H(\phi;\epsilon)$.

$$\frac{\partial}{\partial t}\overline{\kappa}_a = -\frac{\overline{\varepsilon}_a}{\mathcal{R}e_w} - \underbrace{\overline{\delta\nabla\phi\cdot\left(\vec{F} - \frac{\vec{\Sigma}}{\mathcal{R}e_w} - \kappa\vec{\mathbf{u}}\right)}}_{-\overline{\chi}} + \overline{\Theta}_a \tag{8.5}$$

While this energy flux rate term has been seen in texts and recent archival journal papers, it has not received any attention from experiments regarding breaking waves. The most thorough set of breaking wave experiments in the literature to date is Rapp and Melville [92]. In this paper, the change in energy is defined as in an early paper by Whitham [124].

$$\frac{\partial E}{\partial t} + \frac{\partial F}{\partial x} = -\varepsilon \tag{8.6}$$

In equation 8.6, the energy density E, horizontal energy flux F, and viscous dissipation ε are averaged over the water column and in the case of Rapp and Melville's application, integrated over the carrier wave. The term of importance for this equation is the horizontal energy flux in the water column.

$$F = \int_{-d}^{\eta}\left(P + \frac{1}{2}\rho\vec{\mathbf{u}}\cdot\vec{\mathbf{u}} + \rho g\eta\right)u\mathrm{d}z \tag{8.7}$$

Compared to the flux rate in equation 8.1, the first item of note is that the viscous contribution to the energy flux $\tau\cdot\vec{\mathbf{u}}$ is not included. For inviscid flows with a stress free surface, this is an acceptable form. Second item of note is that equation 8.6 only includes the horizontal energy flux as the vertical flux has been neglected as a small

quantity. This is also a acceptable assumption providing that the wave slope is small.

Based on Rapp and Melville's equation 2.27, the change in energy in their control volume is purely driven by the amount of energy no longer crossing the horizontal boundaries of the control volume. The control volume in Rapp and Melville's study used a relatively large control volume in which the horizontal boundaries were sufficiently far enough away from the breaking region. Thus, the concept that the change in energy in the control volume itself is reflected on what is no longer fluxing through it is valid. Even if their analysis included the surface flux term, it would be true. As the energy has not left the control volume, something has happened to it during the breaking event. Thus, it is a loss due to breaking. Rapp and Melville were able to measure the kinetic energy in the control volume for a few of their cases and determined that most of the kinetic energy in the control volume dissipated after approximately four periods. Thus, they attributed all of the energy lost in the control volume to be dissipated away by turbulence. However, based on equation 8.2, we know that some of this energy lost is not necessarily attributed to viscous dissipation. It remains to be seen how much, if any, of the energy lost during breaking is transferred to the air.

One might argue that in a modeling sense, especially in the context of wave forecasting, that "energy lost is lost" whether it be dissipated out or lost to the air. However, in coupled air-water boundary layer problems where the air is considered, the type of knowledge quantified by this term is essential. For cases where the air is not modeled but the turbulence is, such as single-phase Large Eddy Simulations (LES) or Reynolds Averaged simulations (RANS), this type of knowledge is also critical for proper modeling. Assuming that the turbulence models provide accurate dissipation of the wave breaking as detailed in chapter 7, they will result in an under-prediction of the energy lost due to breaking if the energy flux to the air is a significant portion of the energy lost during the breaking event.

8.2 Evidence of Energy Transfer During Wave Breaking

The waves generated in this study allow a unique opportunity to investigate the energy transfer at the interface. The numerical method provides information regarding both the water and air volumes such that all of the kinematics and dynamics at the coupled boundary layer have been directly simulated verses modeled in some manner. Also, there exists a variety of non-breaking and breaking waves such that baseline comparisons can be made. To build a case for the presence of this energy transfer, we first will return to the topic of energy losses. Chapter 7 includes a detailed discussion of the energy losses during a breaking event. As a part of that chapter, the total amount of (total) energy lost was shown in section 7.2.2 which included all of the mechanisms involved such as viscosity and surface tension. Based on equation 8.2, it inherently included the transfer of energy at the interface.

For $\overline{\chi}$ to be non-zero, the amount of energy lost during breaking due to viscous effects and other sources of work does not equal the total amount of energy lost. Figure 8-3 shows the fraction of total energy lost due to viscosity in the water volume for the waves in this study using the notation defined in chapter 7. All of the non-breaking waves lose their energy to viscous effects to within the margin of error of the calculations for the energy conservation. As the waves begin to experience breaking, this drops to only 70% for some cases and in general 80-90% for the predominance of waves. Thus, for many of the waves, up to 30% of the total energy lost during the breaking event was due to a different mechanism besides viscosity.

The sources of other work also has the potential to be significant as there are cases in this study where the Weber number is relatively small. As the amount of energy lost represents the total amount of energy lost, the sources of work represented by Θ_w in equation 8.2 which are a part of this discussion are the surface tension and surface forces. As the breaking event occurs after the surface forcing has been removed, this estimation only considers surface tension effects. Figure 8-4 shows the fraction of total energy lost due to the work done by these surface forces for the same waves.

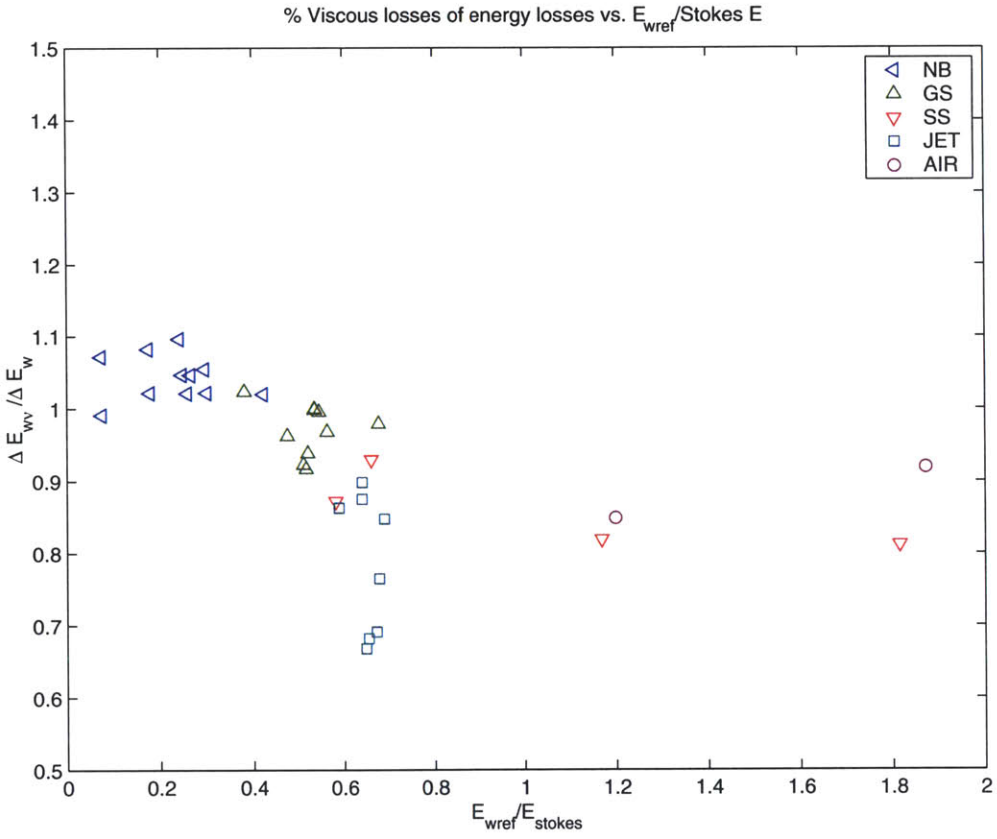

Figure 8-3: Losses due to viscosity as a percentage of energy lost in the water for all of the waves in this study plotted against the normalized energy (at t_{st}) for a variety of waves: ($\triangleleft$) non-breaking, ($\triangle$) gentle-spilling, ($\triangledown$) strong-spilling, ($\square$) jet formation, and ($\circ$) air entrainment.

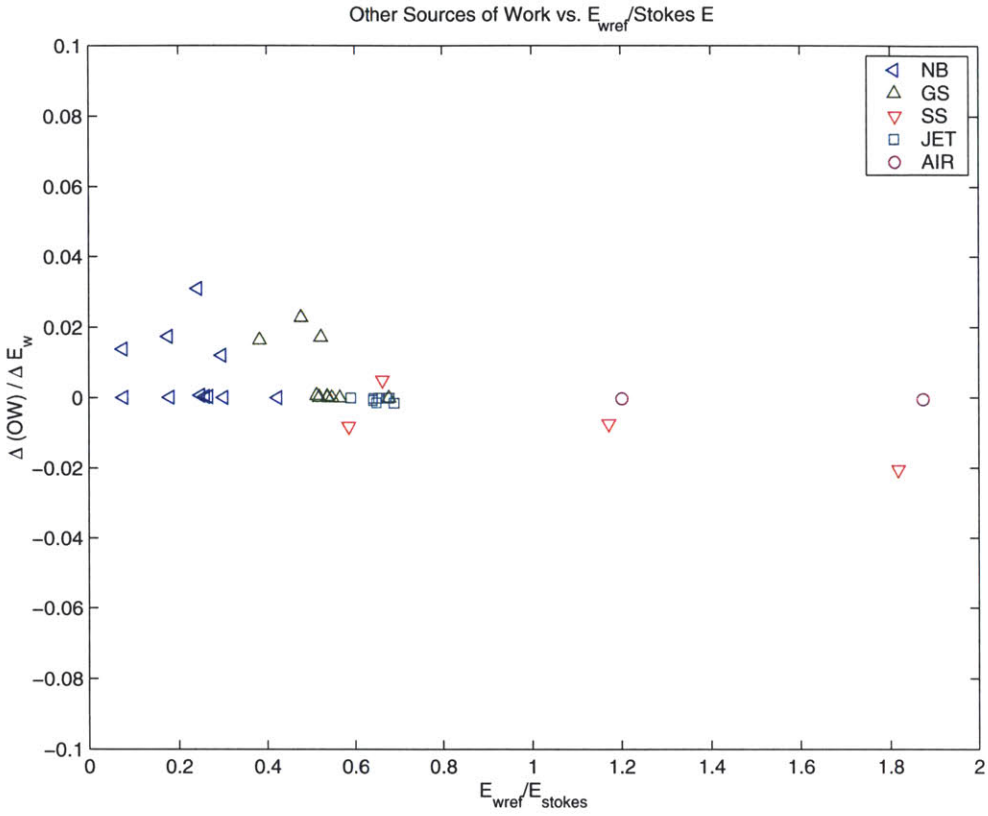

Figure 8-4: Amount of work done by surface tension as a percentage of energy lost in the water plotted against the normalized energy (at t_{st}) for a variety of waves: ($\triangleleft$) non-breaking, ($\triangle$) gentle-spilling, ($\triangledown$) strong-spilling, ($\square$) jet formation, and ($\circ$) air entrainment.

For all of the cases, this is within 2-4%.

This leaves a considerable amount of total energy lost which is unaccounted by viscosity and surface tension. Based on equation 8.2, the only remaining mechanism is the transfer of energy between the two volumes. Additionally, based on the above, the energy flux goes from the water to the air and it can be up to 25% of the total energy lost during the breaking event.

If we now consider the total amount of energy in both the air and water volumes during a breaking event, the effect of the energy transfer becomes even more evident. Figure 8-5 shows the total amount of energy in each volume and the amount of energy lost due to viscosity (breaking and laminar effects included). As figure 8-4 showed,

the amount of energy lost to surface tension effects is minimal so it is not shown here. All of the quantities in figure 8-5 have had a reference value subtracted from them which is before the breaking onset and after the end of the surface forcing. This allows the relative increases and decreases to be seen clearly. During the breaking event ($4 \leq T \leq 6$), the energy in the air sees a significant increase to maximum near T=5. Plots of the kinetic and potential energy of the air (not shown) reveal that the predominance of the energy increase occurs in the kinetic energy. The only mechanism available for this increase is for it to receive energy from the water volume. In fact, at the point of maximum energy increase (marked by the vertical dashed line in the figure), the difference in the amount of energy lost and the amount of energy dissipated in the water volumes is equivalent to the increase in energy of the air accounting for its viscous losses. Based on this evidence, there is a clear case for a transfer of energy at the air-water interface during the breaking event. Quantifying this amount of energy in terms of the energy lost due to breaking is discussed in section 8.3.

8.3 Quantifying Energy Transfer

In section 8.2, a case was built for the existence of energy transfer at the air-water interface during the breaking event. In this section, we will quantify how much energy is transferred between the air and water volumes during breaking and what fraction of the total energy lost this represents.

While we have an equation for $\overline{\chi}$ such that it can be calculated directly and we have done so for some cases in section 8.2, there is some difficulty calculating it directly for all of the breaking cases in this study. Equation 8.3 shows that $\overline{\chi}$ is essentially a function of the pressure and viscous terms at the interface. As the work due to gravity, surface tension and surface forcing are wrapped into Θ_w, the pressure Π at the interface should only be due to the dynamics of the flow and not a function of any surface forces. Unfortunately, due to the method of implementation, the pressure which results from the solution of the projection operator includes the

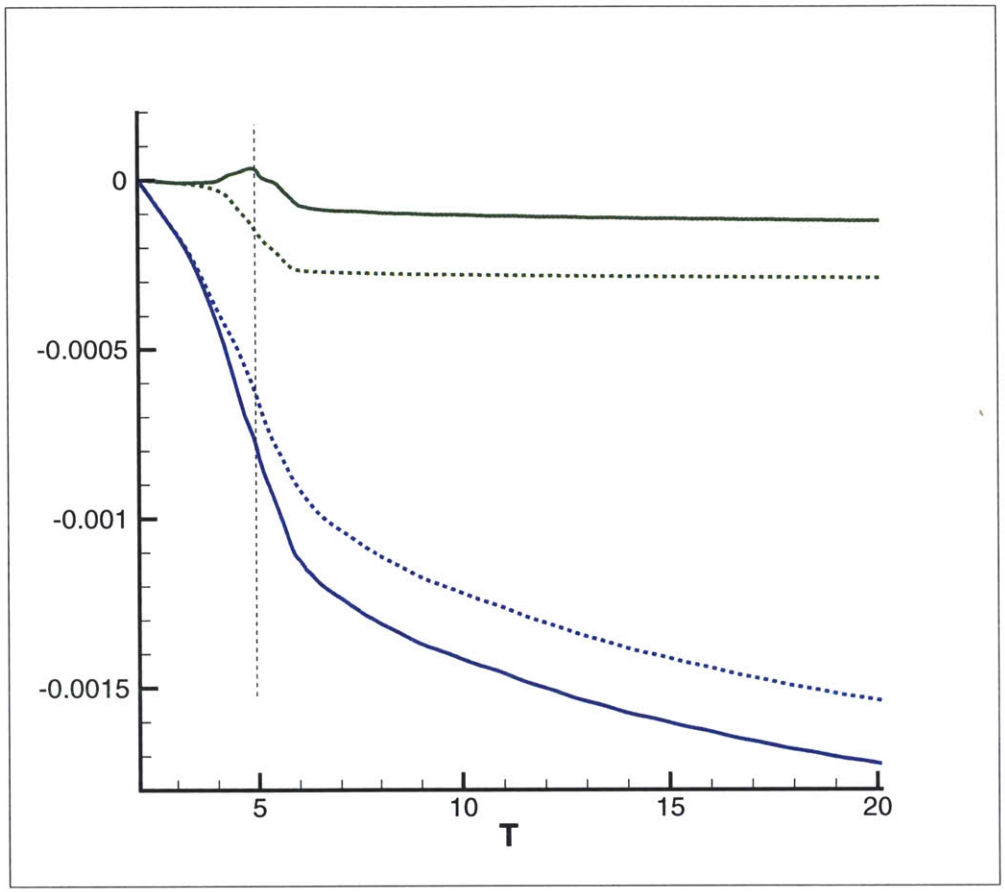

Figure 8-5: Total amount of energy in volume (solid lines) and amount of energy lost due to viscosity (dashed) lines for the air (green) and water (blue) volumes for a breaking case. (case SFI-04) Reference value at $T = 2.09$ subtracted. Vertical line represents point of maximum energy in the air.

effect of the surface tension and some surface forcing. Thus, there is a modest amount of "double booking" in the calculation of the right-hand side of equation 8.2 for the direct $\overline{\chi}$ calculations. While the direct $\overline{\chi}$ was shown in figure 8-1, these cases had very little surface tension effect from either the use of infinite Weber number or very little curvature effects. The direct calculations were also begun after any surface forcing had been removed. This helped minimize any double booking effect in the direct calculations shown. However, as we do not have a clean direct calculation of $\overline{\chi}$ for all of the waves in this study, to ensure that there is enough data for comparison, we will calculate the energy at the interface in an indirect manner.

Providing that the total energy in the volume is conserved to within a reasonable amount, the energy transferred between the volumes can be calculated from the amount of total energy in the water volume and the energy lost to dissipation and all other sources of work except the energy transfer at the interface.

$$\underline{\overline{\chi_i}}(t) = E_w(t) - \underline{\overline{\varepsilon}_w}(t) - \underline{\overline{\Theta}}_w(t) \tag{8.8}$$

where the underline notation represents the cumulative integration in time as used/defined in equation 8.4. Figure 8-6 shows the indirect calculation over time for a breaking wave compared to the direct calculation. For this case, the indirect and direct calculations are relatively close during the breaking event. As expected after the breaking event, the direct calculation shows no appreciable change in energy transferred as the wave has returned to a plane progressive wave. The indirect calculation, slopes upward slightly. As this is a cumulative based calculation, this hints at a cumulated error associated with the energy calculation (see chapter 5). Finally, figure 8-7 shows a comparison of the direct and indirect calculations for all of the waves in this study. In general, the difference between the two is between 5-10% with the indirect calculation being considered more reliable. Based on this and the knowledge of the double booking in the direct calculation, the indirect method will be used to calculate the energy transferred at the air-water interface only over the breaking event.

This being said, figure 8-8 shows the amount of energy transferred across the

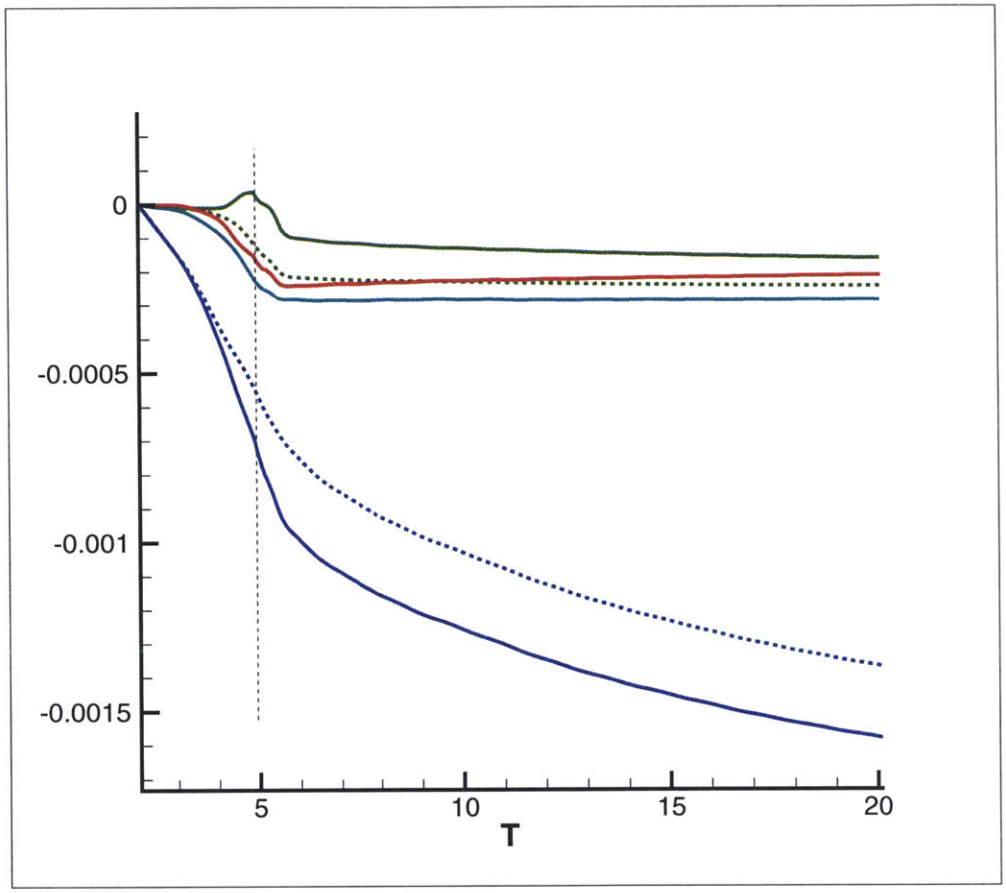

Figure 8-6: As in figure 8-5 for case SFI-11. (cyan) direct calculation and (red) indirect calculation.

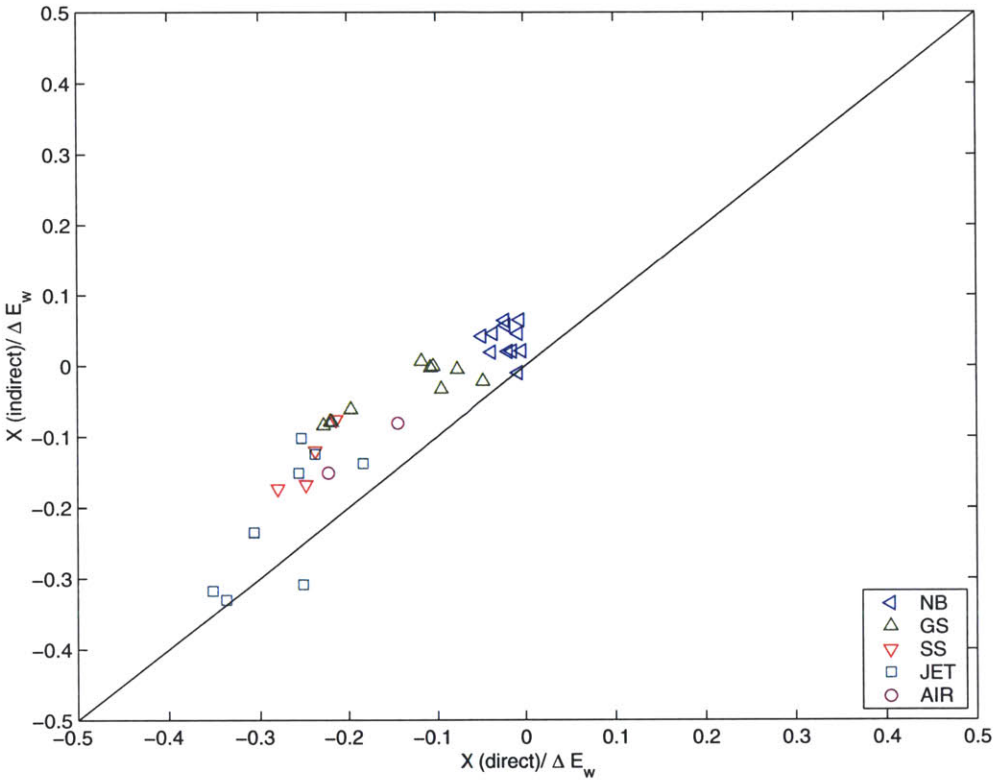

Figure 8-7: Comparison of the direct and indirect calculations. Black line represents exact comparison. (◁) non-breaking, (△) gentle-spilling, (▽) strong-spilling, (□) jet formation, and (○) air entrainment.

interface using the indirect calculation. It is shown first as a fraction of the total amount of energy lost during the breaking event (figure 8-8a) and second as a fraction of the energy lost due to breaking only (figure 8-8b). The energy lost due to breaking is calculated as in section 7.2 where laminar losses if the wave had not broken are subtracted out. Because of this, there are no non-breaking waves in figure 8-8b. For the non-breaking cases, this fraction of energy transferred across the interface is essentially zero. In the cases where breaking occurs, this varies radically between 5-35% of the total energy lost during breaking and is always from the water to the air (negative). If we consider the amount of energy transferred at the interface as a fraction of just the energy lost due to the breaking event, there is also a wide variability of 10-35%.

As this is an indirect calculation, the error in the energy calculation should be considered. As shown in chapter 5, the energy conservation for the entire volume is in general good for all of the waves considered. However, it degrades slightly when the air and water volumes are extracted and the direct calculation of $\overline{\chi}$ is used for reasons discussed already. The associated error is calculated as the residual in the calculation of the total energy in the entire volume as a fraction of the energy lost during breaking. Figure 8-9 is figure 8-8a with the error estimates included. For most waves where the error is relatively small, the energy transfer across the air water interface is appreciable.

Even after the associated error is considered, there are some conclusions which can be drawn regarding the significance of the energy transferred during a breaking event. For breaking waves, the energy transferred at the interface is O(10-20)% of the energy lost. For most cases, this a fairly consistent value except for a few of the plunging breaking wave cases. The jet cases which lie at greater than 20% are all cases which use the surface forcing method (SFI) to initiate the wave and have jet ejections (see chapter 6). In these cases, the jet pinches off from the wave face early in the breaking event and disintegrates. At this point in the discussion, it is unclear if the jet disintegration contributes to this increased energy transfer rate. Within the scope and capabilities of this study, we postulate that the amount of transfer of

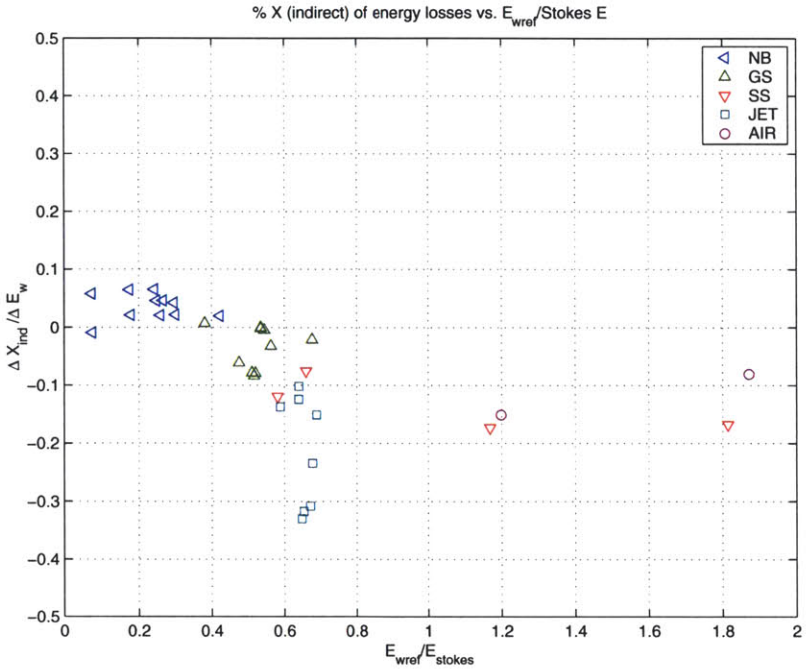

(a) Fraction of total energy lost during breaking.

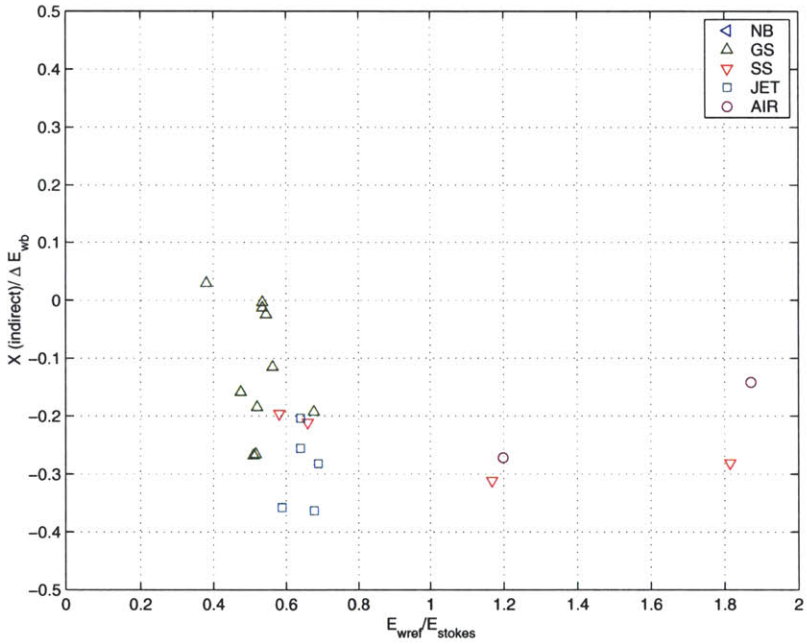

(b) Fraction of energy lost due to breaking only.

Figure 8-8: Amount of energy transferred at the air-water interface plotted against the normalized energy (at t_{st}) for a variety of waves: ($\triangleleft$) non-breaking, ($\triangle$) gentle-spilling, ($\triangledown$) strong-spilling, ($\square$) jet formation, and ($\circ$) air entrainment.

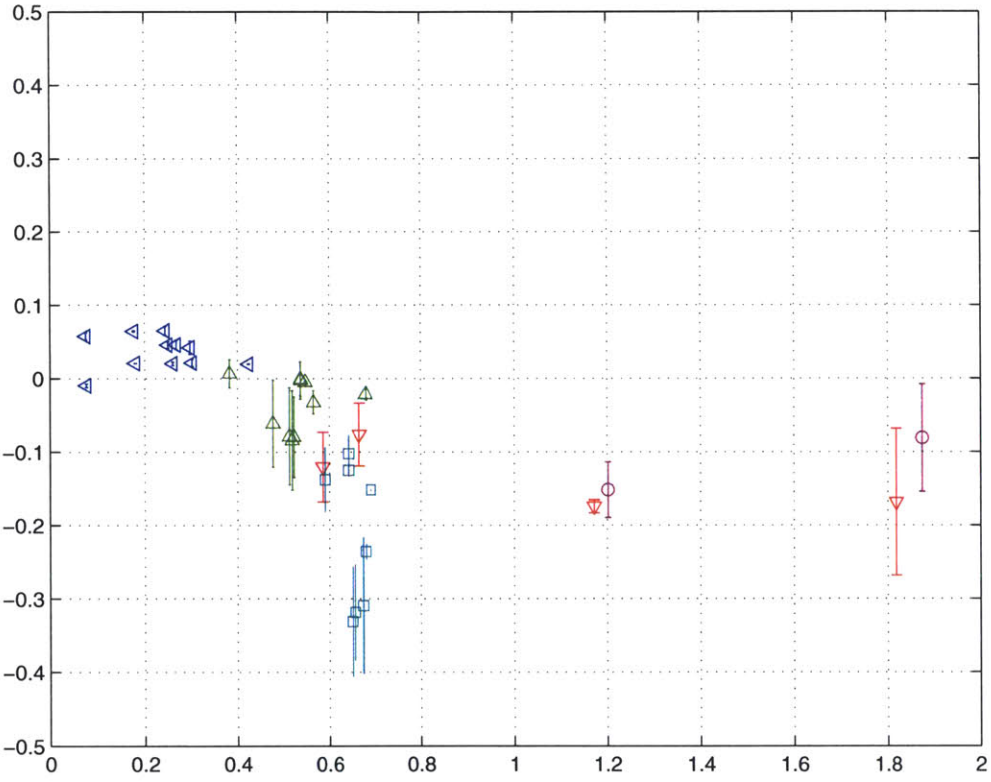

Figure 8-9: As in figure 8-8 with error bars included.

energy at the interface is not overly sensitive to the strength of the breaking event, only on the existence of a breaking event.

8.4 Localization of Energy Transfer

Up until this point, the energy transferred between the air and water volumes has been considered a global quantity or certainly a quantity over the wavelength of a wave. This section discusses the localization of the energy flux rate at the air-water interface for a breaking wave.

In this section, the energy flux rate per unit volume is calculated by equation 8.3 within the reference frame of the crest motion as the energy flux rate is directly tied to the existence of a surface normal velocity component. The first wave considered is a strong-spilling breaking wave. Figure 8-10 shows the local contribution for a strong-spilling breaking wave for the inviscid and viscous components separately. In this figure, the colored contoured regions represent the extent of the smoothed delta function. It is over this region that the energy flux occurs. This moment in time of the breaking event represents the point of maximum energy transfer rate for this wave (and it is globally a negative value). The rest of the wave has essentially zero energy transfer at the air-water transfer. As discussed in section 8.3, for some waves in this study the direct calculation of the energy flux rate had issues when surface tension effects were included. Because this is a strong spilling breaking wave, surface tension effects are present (see chapter 6) and the Weber number for this simulation is 738. However, this wave has a very low error estimate in the error estimate for the indirect calculation. The overall transfer of energy across the air-water interface for this wave is $17\% \pm 1\%$ of the energy lost during the breaking event (from the water to the air).

Based on figure 8-10, the work done by the pressure field at the interface ($\Pi \vec{u} \cdot \nabla\phi\delta(\phi;\epsilon)$ is responsible for the transfer of energy from the water to the air during the breaking event. This is dominated by the large region on the face of the bulge during the breaking event. Figure 8-11 shows the pressure field Π with the velocity

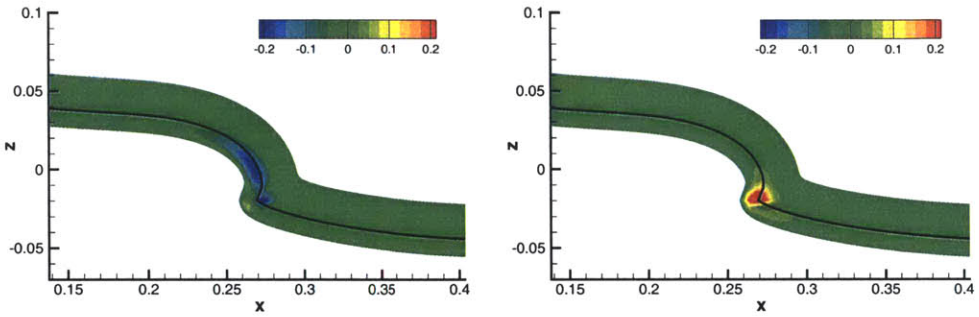

(a) Inviscid Component (b) Viscous Component

Figure 8-10: Components of energy flux rate for a strong-spilling breaking wave (case IAW-04) using direct calculations of equation 8.3 within the reference frame moving with the crest. Black line represents air-water interface.

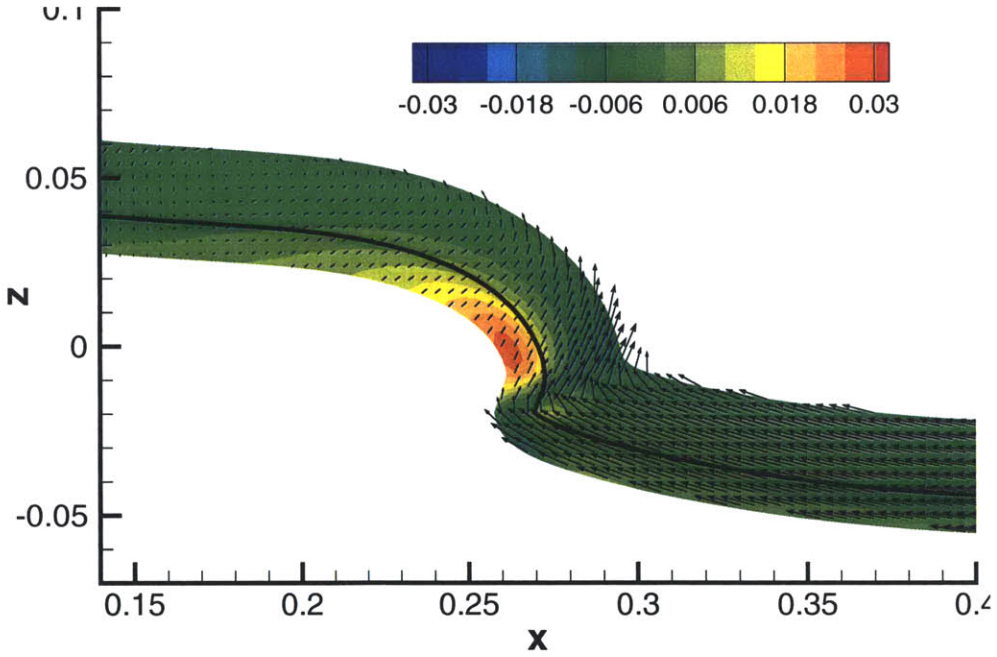

Figure 8-11: Contours of pressure field with velocity vectors in the reference frame moving with the crest for figure 8-10a

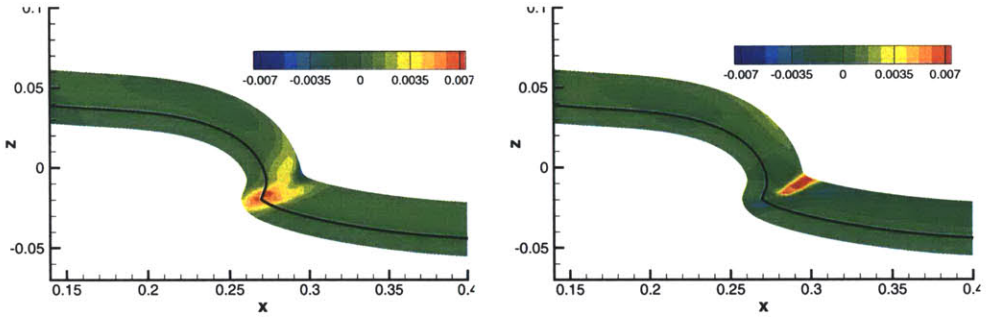

(a) $(\tau_{11}u + \tau_{13}w)\frac{\partial\phi}{\partial x}$ (b) $(\tau_{31}u + \tau_{33}w)\frac{\partial\phi}{\partial z}$

Figure 8-12: Stress components of the viscous energy flux rate for a strong-spilling breaking wave (case IAW-04) within the reference frame moving with the crest. Black line represents air-water interface.

field (relative to the crest). There is a region of large positive pressure in the bulge of the wave. The velocity field in the bulge has a significant surface normal component, opposite in direction to the $\nabla\phi$ which points into the water. Thus, this region of large pressure in the bulge is transferring energy from the water to the air.

Interestingly, the viscous contributions $(-\tau\vec{\mathbf{u}}\cdot\nabla\phi\delta(\phi;\epsilon)/\mathcal{R}e_w)$ are from the air to the water in this wave. Shown in figure 8-12 are the two contributions to the viscous component, $-\tau\cdot\vec{\mathbf{u}}\cdot\vec{\mathbf{i}}\frac{\partial\phi}{\partial x}/\mathcal{R}e_w$ and $-\tau\cdot\vec{\mathbf{u}}\cdot\vec{\mathbf{k}}\frac{\partial\phi}{\partial z}/\mathcal{R}e_w$. The first of the two contributions is responsible for the positive energy flux rate. Inspection of each portion (not shown) reveals that this is due to the flux of the shear stress component $\tau_{13}w$. At this location, this term is two orders of magnitude larger than the flux from the normal stress. Referring back to chapter 6 figure 6-10 where the shear and normal stresses for a strong spilling breaker are shown, the normal stresses actually change sign from negative just below the toe to positive in the bulge. This leaves a near zero region right at the cusp of the toe. The toe itself is the beginning of the strong shear layer in the strong-spilling breaking waves. Thus, the dominant mechanism of the energy flux at the toe itself is due to the presence of the shear layer. This location is also the source of vorticity in the wave as well. The viscous shear stresses due to the separation of the air flow at the toe is causing an influx of energy to the water at this point. However, as seen in figure 8-10, this influx of energy is overshadowed by the inviscid energy flux from the water to the air along the front of the bulge.

For the spilling breaking waves in this study, the energy flux at the interface from the water to the air is dominated by the inviscid component. The region of increased pressure effects combined with the surface normal velocity field at the air-water interface is significantly larger in size (not magnitude) than any effect which occurs at the toe. For gently-spilling waves, the net effect is smaller as reflected by the lower overall energy transfer for these waves seen in figure 8-8. This is because in these waves, the surface normal velocity component is much smaller in both the air and water flow fields as both are able to follow the surface curvature relatively well and no significant regions of separation are seen. The dominant effect of the viscous terms is the shear component. Waves which see significant shear at the surface have a larger contribution to the viscous energy flux. Additionally, this term is also positive implying that the energy flux is *into* the water volume at that point. As this point is also the source of vorticity in the flow, this is not entirely surprising. However, this region is confined only to the toe of the bulge making its influence rather small.

One comment which should be made refers to the discussion in chapter 6 regarding the motion of the bulge in spilling breaking waves. In experiments (and theory), the presence of capillary waves at the toe of the bulge triggers a shear instability which then causes the bulge to move down the face of the wave [66]. In this study, the capillary wave train is not present for reasons discussed in chapter 6. Thus, the bulge does not travel down the face of the wave. As the bulge moves down the front face of the wave, there is an associated flow reversal and region of strong shear [90]. As was shown here, the flow reversal and strong shear will effect the energy flux at the air-water interface. There are two possibilities as to how it will effect this. First, as the flow reversal will generate larger surface normal velocity in the bulge where there are strong pressure effects, the energy flux at the air-water interface could become larger than what is shown here (but remain negative or from the water to the air). Second, as the bulge moves down the face of the wave, the shear region at the toe becomes larger in size and magnitude. Depending on the increased magnitude of the shear and the relative Reynolds number for the wave, the viscous energy flux could become as significant as the inviscid energy flux. As this contribution is positive (from

the air to the water) in the spilling breaking waves, the global energy flux which is now negative could decrease to the point of being near-zero or actually positive. Unfortunately, there is not enough data in this study to allow for any conclusion to be made. There is also insufficient data in the literature to draw any conclusions as information regarding the pressure field is non-existent.

As seen in figure 8-8, many of the plunging breaking events see approximately the same amount of energy transfer at the interface. However, as discussed in chapter 6, the flow fields between the spilling and plunging breaking waves are different, especially as there is very little surface normal velocity up until the point of jet formation. Especially for the plunging waves which see more energy transfer from the water to the air, it is wise to consider the localized energy transfer rate throughout the breaking event to determine if the mechanisms are the same and if the sheet breakup contributes to an additional transfer of energy from the water to the air. To remove any issue with the surface tension in the direct calculations, the wave chosen for this comparison is SFI-04 which has an infinite Weber number and small error in the energy calculation. This wave transfers $23\% \pm 1\%$ of the total energy lost during the breaking event from the water to the air.

Figures 8-13 and 8-14 show the time evolution of the energy transfer rate for this plunging breaking wave which has a jet ejection. As in the spilling breaking wave, the two components are plotted separately so their sign and magnitude can be compared. The left of each pair is the inviscid effects $\Pi\vec{\mathbf{u}}\cdot\nabla\phi\delta(\phi;\epsilon)$. The right of each pair is the viscous effects including the negative sign $-\tau\vec{\mathbf{u}}\cdot\nabla\phi\delta(\phi;\epsilon)/\mathcal{R}e_w$. The velocity field used for the calculation is the velocity field in the reference frame moving with the crest speed. The total energy transfer rate at each point is the sum of the two. The contoured area represents the area of integration for the calculation of the integral to get the total energy transfer rate $\overline{\chi}$. The times shown correspond to the times shown in the dissipation and vorticity in figures 7-7 and 7-8 in chapter 7 for comparison. Figure 8-15 shows the total energy in each volume, the amount of energy dissipated by viscosity and the direct calculation of the total energy transferred for this same case. The dashed vertical lines represent the times shown in the temporal evolution

figures.

Prior to the jet formation, the energy transfer rate is extremely small over the entire wavelength of the wave even though there is a crest asymmetry. Even at the time where the surface is near vertical (figure 8-13a), there is very little contribution from either the inviscid and viscous components. As determined in chapters 6 and 7, the point of the jet formation is a region of relatively strong stresses and thus dissipation as well as vorticity. While there is also a region of large pressure gradients at the point of ejection, the pressure itself is relatively small. There is also very little surface normal velocity at this point and while the two components are large, the energy flux is insignificant at the moment of jet formation.

After the jet has formed (figure 8-13b), pockets of localized energy flux rate appear at the jet tip and on the front face of the wave beneath the jet itself. The jet tip will always be a source of energy flux as the velocity of the jet is in the direction of the surface normal at that point. As the normal velocity is positive, the sign of the energy flux will be dependant upon the sign of the pressure or stress components at that point. However, due to its relative size compared to the rest of the wave, the tip of the jet is considered a negligible contribution to this effect. Underneath the jet, the inviscid component is localized to "kinks" in the surface and at this point in time is positive, meaning that air is transferring energy to the water at the surface through pressure. After the impact event (figure 8-13c), the inviscid energy transfer rate becomes more complex. Under the air pocket, there is a region of positive and negative contribution from the inviscid effects. Investigation of the pressure field shows that the pressure changes sign along this region. Thus the changing sign of the inviscid energy transfer under the air pocket is based on the pressure field itself verses the surface normal velocity field. A large region of positive pressure also exists under the impact region from the impulse of the impact which contributes to region of strong energy flux into the water. As the plunging event continues and the jet pinches off of the front face of the wave and the second impact event occurs (figures 8-13c-d and 8-14), the inviscid contributions only are significant at regions where curvature effects are significant or impact has occurred.

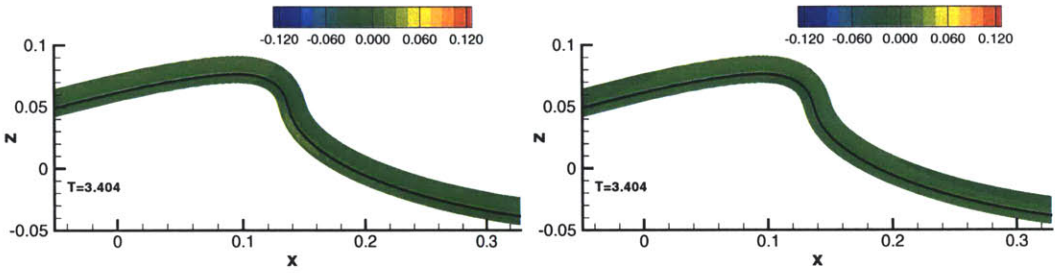

(a) T=3.4

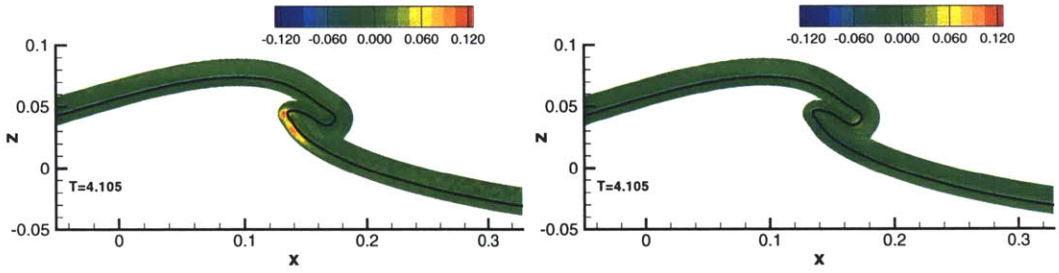

(b) T=4.1

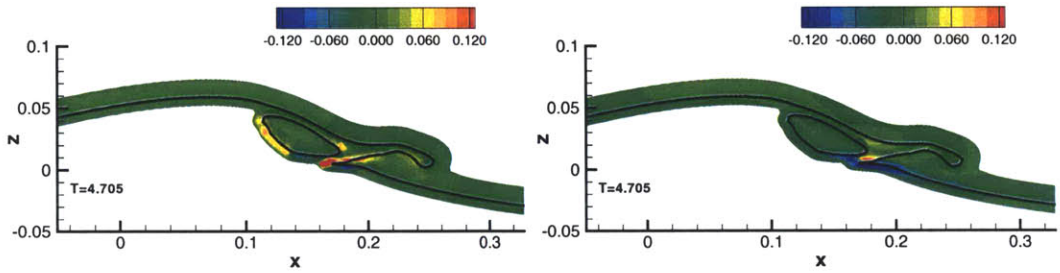

(c) T=4.7

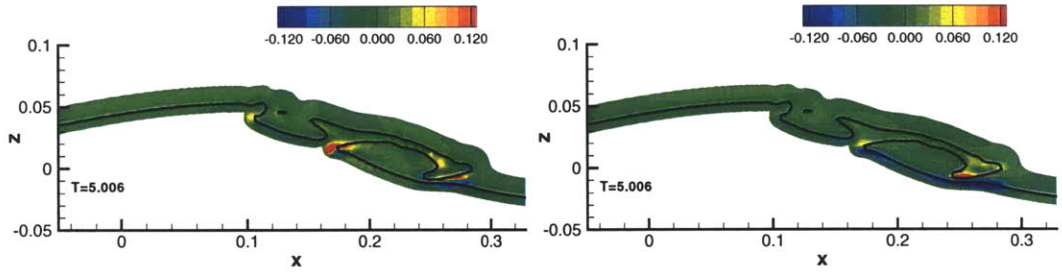

(d) T=5.0

Figure 8-13: Time evolution of energy transfer rate. Left of pair is inviscid effects. Right of pair is viscous effects. Black line represents air-water interface. (case SFI-04).

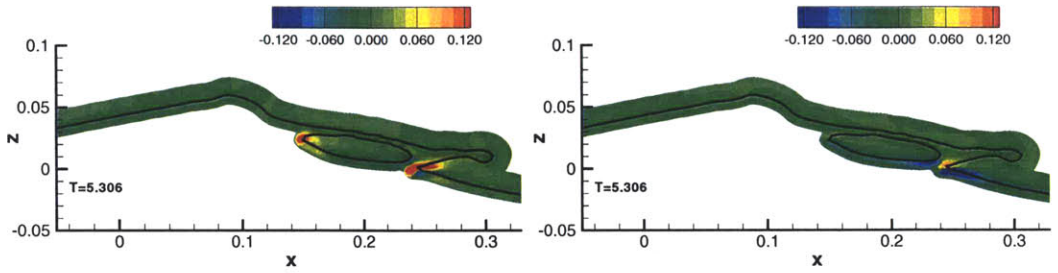

(a) T=5.3

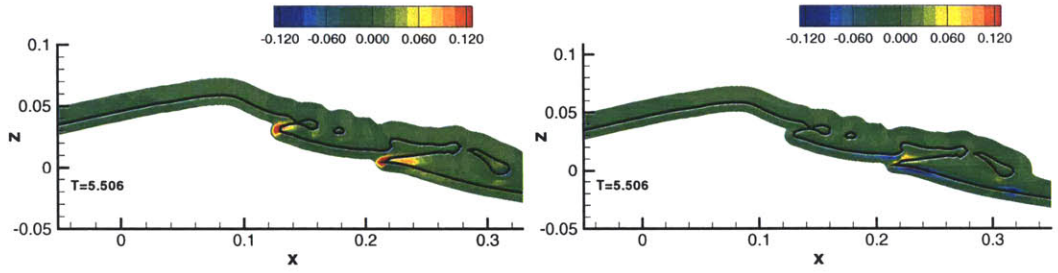

(b) T=5.5

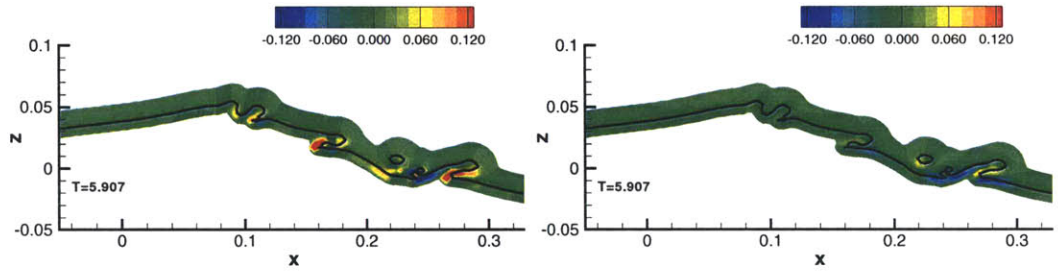

(c) T=5.9

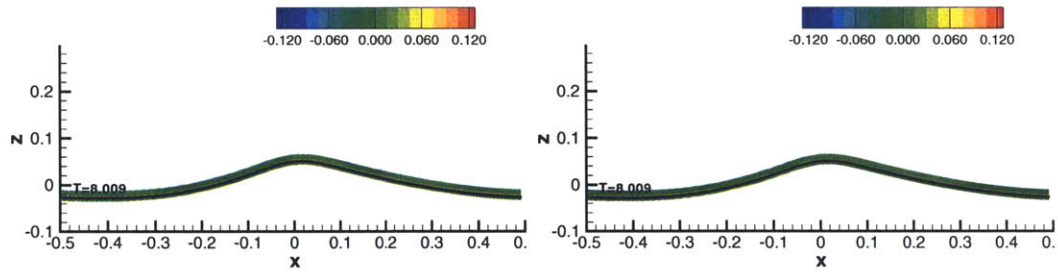

(d) T=8.0

Figure 8-14: Time evolution of energy transfer rate. Left of pair is inviscid effects. Right of pair is viscous effects. Black line represents air-water interface. (case SFI-04).

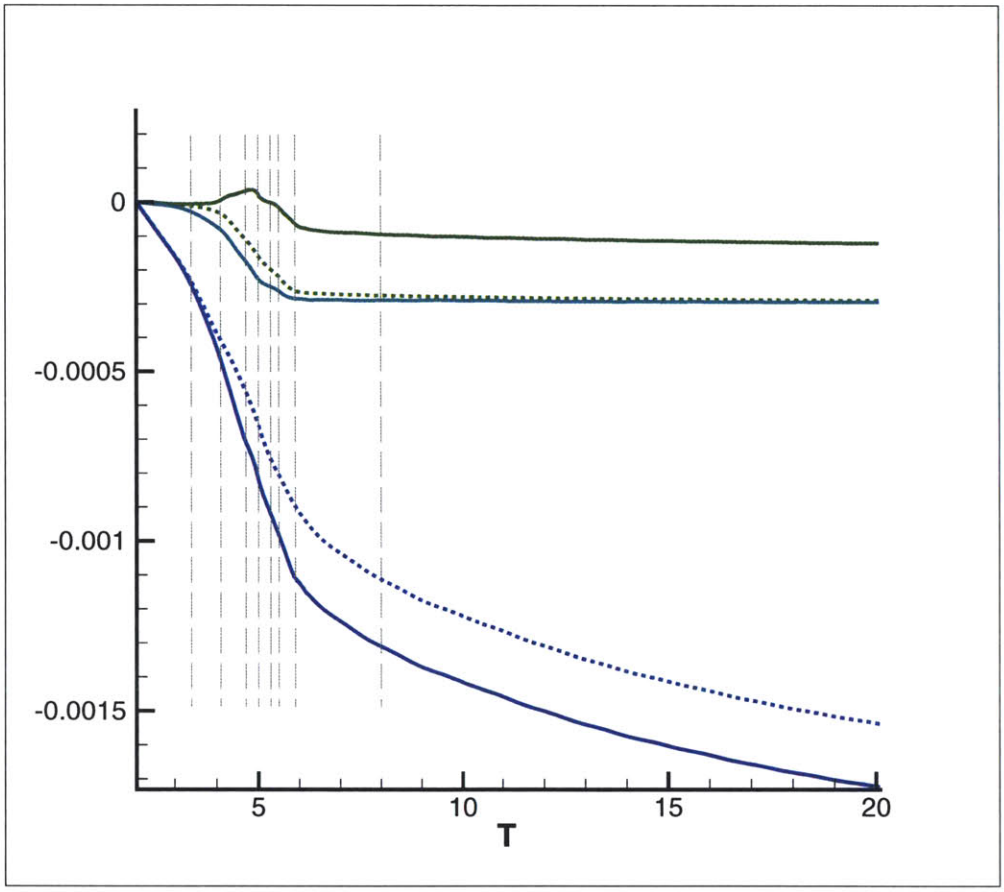

Figure 8-15: Total amount of energy in volume (solid lines) and amount of energy lost due to viscosity (dashed) lines for the air (green) and water (blue) volumes for a breaking case. (case SFI-04) Reference value at $T = 2.09$ subtracted. Vertical lines represents times shown in figures 8-13 and 8-14.

Returning to figure 8-13b, after the jet has formed, the viscous components cover the entire region underneath the jet even though they are smaller in magnitude to the inviscid components. Thus, because $\overline{\chi}$ is negative, the energy transfer is dominated by the viscous component due to the size of the region it effects. This negative component is due to the large region of stresses on the front face of the wave underneath the jet after it has formed. After the jet impacts the surface (figure 8-13c), the energy flux due to viscous effects again sees a peak region under the jet associated with a large dissipation region at that point. Where the inviscid components have localized to regions where the surface is highly distorted, the viscous components span the front face of the wave with peaks where the jet has impacted. At the point of maximum energy transfer to the air ($T' \sim 5$), the bulk of the energy transfer has been dominated by the stresses in the flow field caused by the jet verses the pressure work.

This trend of localized inviscid effects at points of extreme curvature and high regions of viscous effects near the jet ejection/impact points continues through the second and third jet impact (figures 8-14a-c) until well after the breaking event (figure 8-14d) where there is essentially no contribution from either component.

As the jet pinches off and forms droplets ($4.7 \leq T \leq 5.5$ in figures 8-13 and 8-14), there is no appreciable source of energy flux except for the very tip of the jet. As discussed earlier, because of the shape of the tip and the direction of motion of the tip, it will always have a surface normal component to the velocity field but will have small contribution due to its size. Before the droplets form, the jet itself has very little pressure or stresses. Thus, in the context of this study, sheet disintegration and droplet formation are not a significant source of energy transfer between the two volumes.

To summarize, for this plunging breaking wave with jet ejection, as expected, the interfacial energy flux rate is essentially zero before and well after the breaking event. Even as the jet is beginning to form and the crest steepens to near vertical, because the velocity field in the reference frame of the crest is predominantly surface parallel, the contribution to the energy transfer rate is relatively small. Once the jet forms, however, the energy transfer rate develops localized regions for both the inviscid and

viscous components. The inviscid component generally follows changes in curvature as the pressure changes signs in those regions and has significant contribution at points of severe curvature. Because of the large stresses at the interface underneath the jets and increased shear along the surface, the viscous components are significant despite the Reynolds number scaling. The pinch off and breakup of the jet contribute very little to the energy transfer rate.

While both spilling and plunging breaking waves transfer energy from the water to the air, the plunging breaking wave poses a different picture of the mechanisms involved when compared with the spilling breaking wave. In the spilling wave, the dominant contribution is the inviscid energy flux. For the waves in these cases, as the Reynolds number increases, the inviscid energy flux should remain the dominant influence providing the toe region remains small and localized. However, as the bulge does not move down the face of the wave as in many spilling breaking waves, it is difficult to make definitive conclusions if the viscous energy flux becomes stronger as the stresses in the toe region become stronger and take up a larger portion of the wave face. Somewhat surprisingly, the plunging breaking waves are dominated by viscous effects as the pressure at the surface is relatively small except at points of extreme curvature or impact. The stresses, in general, are relatively larger and include not only the impact regions but regions under the jet itself. Without knowing the relative increase of the stresses at higher Reynolds numbers, it is difficult to determine whether the Reynolds number scaling in the viscous flux term would make it retain its dominance in the energy flux rate. If the Reynolds number did make the viscous flux term less significant, one could argue that the energy transfer for plunging breaking waves would be small. It would only be affected by the actual impact event as the predominance of the plunging events have little surface normal velocity field.

The only caveat to this conclusion is the effect of the air pocket collapse in the plunging event. Unfortunately, the case with air entrainment which has somewhat physical air pocket collapse has an associated error of the size of the energy transferred between the volumes which makes it an unreliable candidate for this type of analysis. Also, as the collapse of the air pocket is a three-dimensional effect and highly

dependent upon the compressibility of the air, even if a case was available with small associated errors, the applicability of the conclusions drawn would be questionable.

8.5 Conclusions

This chapter began with the investigation of the term associated with the energy flux across the air-water interface. This transfer of energy contains an inviscid and viscous component. For developed, plane progressive waves which do not evolve further, this energy-flux rate is zero as there is no surface normal velocity component in the reference frame moving with the wave crest. For cases where the surface normal velocity component is appreciable, such as standing waves or waves evolving into breaking waves, this term is non-zero and potentially significant.

The evidence support the existence of this term for breaking waves was also discussed. Within the context of the amount of energy lost during the breaking event, the amount of energy lost in the water volume to viscosity and surface tension effects does not account for all of the energy lost during breaking. As the energy is conserved to within a reasonable margin of error in this study, the only other possible explanation is that energy is being transferred from the water volume to the air volume during breaking. This can also be seen by the *increase* in energy in the air volume during the breaking event while all other energy is being removed by dissipation. This increase in energy in the air is seen predominantly in the kinetic energy.

The energy transferred between the two volumes was quantified for all of the waves in this study. In general, 10-35% of the energy lost in the water to the breaking event is lost not to viscous effects but as energy transferred to the air volume. There was no direct correlation between the strength of the breaking event and the amount of energy transferred within the available data.

Two distinctly different descriptions of the local energy-flux rate were discovered between spilling and plunging breaking waves. For the spilling waves, the dominant mechanism is the inviscid energy-flux rate. This is due to the presence of a surface normal velocity field in the bulge where a larger pressure region exists. While the

stresses in the wave face were large at the toe and yielded a transfer of energy into the water from the air volume, the localized region of the toe area made the viscous energy flux contribution small. It is uncertain in spilling breaking waves where the toe moves on the front face of the wave, whether or not this would remain true as there is no available data to make any firm conclusions. For plunging breaking waves, the dominant mechanism is actually the viscous component. As the pressure in the wave during the breaking event is small except at regions of large curvature or jet impact, its contribution is confined to these areas. The stresses at the interface are more widespread making their influence dominant. It is uncertain how this would scale to larger Reynolds number as the viscous stresses at the air-water interface are unknown for these types of waves. Nor is it clear how the air pocket collapse would effect this analysis as it is dominated by effects not included in this study.

Finally, it should be noted that as the energy transfer rate for spilling-breaking waves is dominated by inviscid effects, the transfer from the water to the air will scale to the open ocean. The predominance of the breaking waves at sea are spilling breaking waves with air entrainment or microbreakers. These inviscid components will scale to these length scales. Much attention has been addressed to the energy transfer from the wind to the waves to the current with little understanding of the affect that breaking has on this transfer in the opposite direction. The greater than 10% energy loss of the breaking wave to the air should be considered in all modeling for coupled air-boundary layer effects.

Chapter 9

Conclusions

9.1 Contributions of the Thesis

This dissertation has made new contributions to both the technical and scientific issues associated with the numerical study of steep breaking water waves. Through the inclusion of the coupled air-water interface and direct numerical simulation, unique insight into the kinematics, dynamics, dissipation and energy fluxes of breaking waves was obtained. This study provides an initial step towards the development of physics-based turbulence models for the study of wave breaking at larger scales.

9.1.1 Technical Contributions

Simulating the coupled air-water interface through direct numerical simulation provides numerous technical issues. The effective modeling of the physics involved in this topic requires a methodology which robustly handles the complex topology changes associated with breaking water waves. As interface tracking methods which use points on the interface to track its location require special treatment of the interface at breakup or re-entry, an interface capturing method based on the level set method was chosen. The level set method provides a natural treatment of the complex surface topology in wave breaking and also provides efficient coupling of the air-water interface dynamics by mapping discontinuous quantities such as the density and viscosity

to a smooth function which represents the distance of a point on an Eulerian grid to the interface.

While the level set method is robust in terms of handling the surface topology changes, through a detailed analysis of the level set method, we discovered that there were technical issues associate with its implementation which needed to be addressed. First and foremost, the physics of the air-water interface problem posed the greatest issue. While many applications of the level set method exist in the literature, there have been few which have been successful when the two fluids involved have the properties of air and water. Because of the relative magnitude between the densities and viscosities of the two fluids, the relative magnitude between the gradients of the velocities at the interface is significant. For a Poiseuille-Couette flow, the relative velocity gradient is 100:1 between the air and the water. Thus, the numerical resolution to adequately resolve the gradients in the air flow can be 100 times larger. This can quickly become very restrictive even in two-dimensional flows.

The traditional implementation of the level set method uses a smoothing function which is symmetric about the interface. The smoothing is used for the constitutive properties to remove the difficulties associated with numerically taking derivatives of functions which vary a few orders of magnitude over only a few points. Yet, even with this traditional smoothing, simulations involving air and water are prone to spurious vorticity in the air which are a function of poorly resolving the gradients in the viscous air boundary layer. To this end, we developed a modified smoothing function which satisfies the same characteristics as the traditional function but was asymmetric about the interface, reaching further into the viscous air boundary layer. This allowed the large gradients in the air to be smoothed out over a larger distance and removed the spurious vorticity. To our knowledge, the analysis of the level set method for air-water interface flows and the subsequent development of a modified smoothing function which takes into account the physics of the problem being modeled is the first of its kind associated with this numerical method.

The other technical issues encountered and resolved in this dissertation were associated with the numerical implementation of the level set method verses its core

formulation. The numerical implementation used a staggered-MAC type grid which is highly desirable for ensuring continuity of the flow and ensuring that the pressure and velocity field is coupled. This type of implementation is standard in the literature involving not just the level set method but other interface capturing techniques such as the volume of fluid method. However, the staggered nature of the implementation requires the movement of variables between locations on the grid. Providing that the grid is Cartesian and that quantities do not vary significantly from grid point to grid point, this is usually performed with an average and has served the field of computational fluid dynamics adequately for decades. As Eulerian interface capturing techniques became popular, the same averaging technique was applied to the constitutive properties as well. Yet, these quantities do vary significantly over a few points, especially for air-water flows. In this work, the traditional averaging technique takes the information provided in the level set function, namely the distance to the interface which is a smooth function that varies slowly, and interpolates that value between the various grids. The constitutive properties were then evaluated based on this interpolated value in lieu of averaging them directly. For very little additional computational effort, this method proved to be superior to the averaging method prevalent in the literature in terms of numerical dissipation and adequate solution for the pressure field. Additional improvements to the treatment of the stress forces compared to the literature were also made which reduced the numerical dissipation in the treatment of the shear forces.

The final contribution of a technical nature was the implementation of the reinitialization of the level set function. A critical aspect of the level set formulation, in particular to the accurate calculation of derivatives and curvature, is that the level set retain its distance function property as it is advected. The level set governing equation relies on Lagrangian invariance. However, the typical implementation of the level set method uses the velocity field of the fluid at the point where the level set function is defined. For the zeroth level set, or the interface between the two fluids, it has been proven that this is correct and is actually the kinematic boundary condition at the air-water interface. However, away from the interface, the velocity of

the field no longer satisfies this Lagrangian invariance and stretching and bunching of the level set function can occur. This then allows the level set function to drift from representing a distance function. To correct for this, reinitialization of the level set function has been adopted in many of the implementations in the literature and in this thesis. However, reinitialization can lead to small errors or drift in the location of the interface which results in a loss of volume. The reinitialization technique adopted for this work is based on relatively standard technique in the literature. This yields a volume conservation of 2% over the course of a simulation as is generally reported in the literature which uses this technique. However, by including a sub-cell fix which ensures that the method of characteristics is not violated, we were able to ensure a volume conservation of 0.2% for most waves. The idea of the sub-cell fix is not necessarily new as it was published in an archival journal [95]. However, to our knowledge no one has given it much notice.

9.1.2 Scientific Contributions

The key findings of this thesis represent new contributions to the study of breaking waves in three distinct areas. The first area is in the kinematics and dynamics of breaking waves. This numerical study simulated a variety of spilling and plunging breaking waves throughout the various stages of the breaking process. For spilling breaking waves, the developmental stage consists of the formation of a bulge and toe on the wave face. The bulge represents a region of localized vorticity and stresses in the flow which are a function of its curvature. Within the reference frame of the wave, all of these quantities were associated with curvature as the surface parallel velocity field (of the water) attempted to follow the curvature of the bulge. As the air sees the wave face more like a solid wall than a shear-free surface, the bulge is also a significant source of separation and vorticity for the air flow. We identified two types of spilling breaking waves – gentle and strong – which are similar in characteristic but different in terms of the length of the breaking event, the strength of the vorticity and dissipation, and overall effect of the curvature. While the stresses in the water for the gentle spilling breaker were confined to the bulge area, a significant shear layer

existed in strong-spilling waves that reached almost the extent of the wave crest. Good quantitative comparisons to experiments and theory were made in terms of the velocity and vorticity fields. Qualitative agreement was seen in the surface evolution except for the presence of a capillary wave train which is seen in experiments and not in this study. Suggested reasons for this difference were posed ranging from numerical resolution to physical scales. The capillary wave train is attributed to the movement of the bulge down the front face of the wave and an associated flow reversal as this occurs. As these phenomena do not occur in the spilling breaking waves in this study, we are not entirely surprised that the wave train is not seen.

For plunging breaking waves, two types were also identified – jet forming and air entraining. The developmental stage of the plunging breaking wave was analyzed for both types. It was found that a large pressure gradient appeared at the point of the jet formation as well as region where the speed of the crest was greater than the phase speed of the wave. Both of these findings are consistent with the literature. As in gentle spilling breaking waves, a localized region of stresses and vorticity occur at the point of the jet formation which is a function of the surface parallel velocity field following the almost near vertical profile of the air-water interface. However, this region is very thin and weak when compared to spilling breaking waves. This agrees with experimental results which show, within the extent that they have resolved the viscous boundary layer, that the flow is essentially irrotational up until the jet forms. However, based on arguments regarding curvature effects, the flow must be rotational in the regions where we have found vorticity.

The impact stage of the jet for both types of plunging events was also shown. The waves which feature a jet ejection have a much thinner jet which forms. Because of its thinness, the jet is subject to pinch of and disintegration as it is impacting the wave face. The pinch-off and breakup process compared well to the theory available in the literature even though in the literature it is described as a three-dimensional process. For the waves which entrained air, the jet which forms is significantly thicker and does not pinch off or disintegrate before the first or second re-entry and splash up event. This allows the air pocket which forms underneath the jet to pinch off

into larger bubbles or air pockets. The bubbles either become unresolvable, breakup into smaller bubbles or burst at the surface which is qualitatively what should be expected. After one to two periods beyond the breaking event, there are essentially no bubbles left in the wave. As the bubbles in this study are considered overly stiff because they are two-dimensional and incompressible, no comparison to the literature was attempted.

Within the context of the narrowbanded spectrum of the waves in this study, the evolution of the spectrum throughout the breaking event was studied. We showed that there was a loss of energy at low wavenumbers prior to breaking which corresponded to an increase in energy at higher wavenumbers. These higher wavenumbers are essential to developing the wave steepness necessary for the wave. The energy remains in the higher wavenumbers for approximately one wave period after the breaking event before it is fully dissipated. This behavior and the potential energy loss is consistent with findings in the literature.

The second area is in the dissipation of breaking waves. Because direct numerical simulation was used in this study, there was no appreciable artificial dissipation in the simulation due to turbulence closure models (providing the numerical dissipation of the implementation was small, which it is). Thus, this study captured the instantaneous dissipation effects of wave breaking in a manner which no experiment has provided to date. Because of the coupled air-water interface dynamics, this study provided a unique set of the same information for the air. The spatial and temporal evolution of the dissipation rate for both spilling and plunging breaking waves showed a high degree of localization and unsteadiness which was also a function of the type of breaking wave which formed. For the water, it was found that the dissipation rates increase by at least a factor of two for even a spilling breaking wave. For the air, this increase varied up to an order of magnitude as in plunging breaking waves it attained the same order as the dissipation rate in the water.

The global amount of energy lost during the breaking event was considered in a control volume approach similar to experimental techniques. With the laminar viscous losses removed, the amount of energy lost to the breaking event alone was calculated

and shown as an increasing function of the energy in the wave prior to breaking. We showed that the use of the slope parameter, as is done in all experiments which use dispersive focusing techniques to generate breaking waves, is only a useful measure of wave breaking in the absence of all other inputs.

In this study, waves with less than 40% of the energy of the Stokes limiting wave do not break. This is consistent with many of the findings in experiments if the energy in the wave is estimated through an integral slope parameter. There is a range between 40% and 60% which form spilling breakers and jets where the energy loss due to breaking increases dramatically with appreciable variability. Finally, while the data is sparse above 70% of the Stokes limiting wave, a maximum amount of energy loss due to breaking of just over 40% is seen once a critical value is reached somewhere above 80% of the Stokes limiting wave. The variability in the data showed that while the energy in the wave prior to breaking showed some correlation to the strength of the breaking event, that other factors may be involved.

Comparisons of the potential energy lost due to wave breaking were compared to experiments. As potential energy is not a functions of Reynolds number effect, it is possible to directly compare the waves in this numerical study with experiments. Despite some of the limitations of this study (two-dimensional, moderate Reynolds number), the comparisons were quite good. Additional comparisons were made in regards to a dimensionless dissipation rate which has received some attention in the literature. We showed that, like experiments in unsteady breaking waves, the dimensionless dissipation rate scaled by more than just the phase speed of the wave as was proposed. We also found that the dissipation rate was an order of magnitude less than steady breaking waves except in the cases of some of the strong-spilling breakers. As the strong spilling breakers had many similar characteristics to the steady breakers except in terms of duration, this is not entirely surprising.

There is an area of study in the literature devoted to determining a universal breaking criteria for waves. This criteria would not only determine whether or not a wave would break but what its effects would entail. The existence of a universal criteria aside, we found that a criteria tied to the growth rate of the wave proved to

be a potential candidate for predicting whether or not a wave would break. Despite the fact that the theory involved wave groups, a similar concept which concentrated on a mean convergence of the energy density in the wave was shown to be a fairly reliable criteria for wave breaking within the context of this study. While the amount of data was sparse to make definitive conclusions, there was evidence that this criteria had potential in not only predicting wave breaking but to the strength of the energy dissipation as well.

The third and final area is the transfer of energy at the air-water interface. This area has not received much attention in the literature. The formulation of a term in the energy equation which accounts for the energy flux rate at the air-water interface was derived. While not necessarily a new term, the term has been neglected until just recently in the study of free-surface turbulent flows. The energy flux rate at the interface contains an inviscid and viscous component. Unless there is a surface normal component to the velocity field, this term is relatively negligible.

For the breaking waves in this numerical study, there is evidence that this quantity is appreciable. Within the context of the amount of energy lost during the breaking event, the amount of energy lost due to viscosity and surface tension effects does not account for all of the energy lost during breaking. Since the energy is conserved within a reasonable margin of error in this study, the only other explanation based on the energy equation is a flux of energy between the air and water at the interface. Evidence shows that there is an increase in the kinetic energy in the air during the breaking event which results from the increased separation on the flow. This increase in energy is balanced by the additional decrease in the energy in the water which is not accounted for by viscosity or surface forces. Although the calculation of this term is sensitive to errors associated with the conservation of energy, values as high as 25% of the energy lost to breaking are found. Investigation of this energy transfer showed that there was no direct correlation between the strength of the breaking event and the amount of energy transferred within the available data.

At the Reynolds numbers in this study, the dominant mechanism for each type of wave was identified as two distinctly different mechanisms between spilling and

plunging breaking waves. For the spilling waves, the dominant mechanism is the inviscid energy flux rate. This is due to the presence of a surface normal velocity field in the bulge where a larger pressure region exists. While the stresses in the wave face were large at the toe and yielded a transfer of energy into the water from the air volume, the localized region of the toe area made the viscous energy flux contribution small. It is uncertain in spilling breaking waves where there is considerable shear as the toe moves on the front face of the wave whether this would remain true as there is no available data to make any firm conclusions. For plunging breaking waves, the dominant mechanism is actually the viscous component. As the pressure in the wave during the breaking event is small except at regions of large curvature or jet impact, its contribution is confined to these areas. The stresses at the interface are more widespread making their influence dominant. It is uncertain how this would scale to larger Reynolds number as the viscous stresses at the air-water interface are unknown for these types of waves. Nor is it clear how the air pocket collapse would effect this analysis as it is dominated by effects not included in this study.

Finally, it should be noted that as the energy transfer rate for spilling breaking waves is dominated by inviscid effects, the transfer from the water to the air should apply to scales in the open ocean. The predominance of the breaking waves at sea are spilling breaking waves with air entrainment or microbreakers and while much attention has been (deservedly) addressed to the energy transfer from the wind to the waves to the current, little effort has been addressed to the transfer in the opposite direction. The $\sim 10\%$ energy loss of the breaking wave to the air should be considered in all modeling for coupled air-boundary layer effects.

9.2 Future Work

Throughout the course of this dissertation, it became obvious that for there to be a (timely) defined end to this investigation that it would ultimately define a beginning to the next. While this investigation contributed to the numerical method and the understanding of steep breaking water waves, it serves only as a first step towards

viscous numerical simulations advancing the knowledge of the role of wave breaking in air-sea interactions. Any future effort along the lines of this dissertation should include many of the improvements mentioned here. This section identifies three areas where future efforts should be directed. They are improvements to the numerical method, expansion of the numerical study and how to apply the knowledge gained in this study.

One of the contributions of this thesis was an improvement to the numerical method itself in the development of the asymmetric smoothing function which is better suited for the simulation of air-water interface flows. Initial investigation of the level set method with a sharp interface showed significant difficulty in accurately capturing the kinematics and dynamics near the interface. Thus, a smoothed interface was adopted for this study. Questions arose throughout this dissertation regarding this choice and whether or not the smoothed interface was significantly affecting the physics. This was the origin of section 2.7 and the asymmetric smoothing function. The physics of the problem at hand, namely the relative size of the viscous boundary layers in the air and the water, dictate that there will be large gradients at the interface in the air. To resolve these gradients and all of the scales necessary for DNS of the air portion of the flow requires a considerably large number of points in the air at the interface. Thus, the asymmetric smoothing function was used to smooth these large gradients and reduce the resolution required for DNS of the air flow.

However, many find a sharp interface conceptually desirable and some authors have improved the implementation of the level set method using a sharp interface. The two primary techniques of interest are the use ghost fluid techniques to take derivatives across the interface and a robust method for solving the Poisson equation with a sharp interface using a multi-grid method. If these methods stand up to rigorous testing within the context of simulating steep breaking water waves, a similar investigation of breaking waves with a sharp (coupled) interface is warranted. This does not remove the issue regarding the resolution required for DNS of the airflow as discussed. In fact, it most likely makes it a central issue. Adaptive gridding techniques may relieve this problem. As in this study, a balance between the necessary resolution

and computational costs will likely have to be struck.

As this numerical method was implemented with an eye on robust and accurate simulations verses computationally quick algorithms, there is room for improvement which will increase the efficiency of the numerical method. For most time-accurate Navier-Stokes solvers, the bulk of the computational effort is in the solution of the Poisson equation for the pressure field at every time step. The method used in this implementation (line SOR) is quite basic and the test for convergence is quite restrictive. Conjugate gradient and multi-grid methods have been adapted for the solution of variable coefficient Poisson solvers. However, in the conjugate gradient method, due care must be taken in the treatment of the surface tension term if it is included. Also, as the location of the air-water interface is imbedded in the matrix of the Poisson equation, special care must be taken to ensure that the location of the interface is not lost across the various grids. These details aside, improvement of the computational efficiency of the Poisson solver would certainly expedite future studies.

The other improvement to numerical efficiency would be the implementation of an implicit time-stepping algorithm which included surface tension effects. The implicit time integration algorithm is not a trivial step. With the level set function also treated implicitly, the variable coefficient Poisson solver is dependant upon information which has not necessarily converged. Also, including surface tension effects is a non-trivial step as it involves nonlinear components due to the calculation of the curvature. Some semi-implicit schemes have been presented in the literature; however, their treatment of the surface tension terms are done explicitly. Thus, depending upon the Weber number of the problem, the time step restriction due to surface tension effects can become the dominant term and the numerical model will resort to being explicit in time.

With some improvements to the numerical efficiency of this implementation, it is possible to extend the bounds of this investigation into other types of waves. This study focused on deep water unsteady breaking waves which were predominantly made of a single frequency. Yet, much of the application of the study of unsteady breaking waves concerns waves which have broadband spectrums or exist as part

of wave groups. Thus, expanding this study to include wave groups, the effects of a wavemaker, or the capability of using an input spectrum are all regions which could greatly increase the applicability of these results. Chapter 4 outlined the process which could be used to include the effects of a wavemaker. The inclusion of a wavemaker facilitates the study groups and dispersively focused wavebreaking as is performed in experiments. It also allows the study of an impulsive "push". Waves generated through this impulse will certainly have a broadband spectrum and break relatively close to the wavemaker compared to dispersively focused waves. This second application would reduce the domain size necessary for the simulation and still capture many of the effects of broadband spectrum waves which were not included in this study.

This numerical investigation focused on unsteady breaking waves. The study of steady breaking waves opens the door to the entire area of application for Naval engineering. Naval design tools are in dire need of robust wave breaking dissipation models which can simulate the drag effect of the breaking bow wave and potentially model the entrainment of air into the bubbly wake of the surface ship. Recent work couples the viscous level set method with a coupled air-water interface to an inviscid boundary element method which solves for the flow around a hydrofoil. This method is primarily used to study the waves breaking beneath a submerged hydrofoil as in Duncan's experiments. In chapter 4, a technique which can be used to simulate the effect of a submerged object through the use of a body force method was described. This technique focused on the fact that merely the influence of the body was necessary to develop breaking waves. As these are the primary focus of the study, resolving the flow about the hydrofoil and its turbulent wake are secondary matters. Providing that only the effect of the body is all that is necessary to generate the breaking wave, this type of modification would facilitate the study of steady breaking waves with a coupled air-water interface.

The body force method which is described as helpful for studying steady breaking waves could also be modified such that bottom effects could be studied. This type of breaking could consider wave shoaling or the flow of a wave over a bump. Both

mechanisms generate plunging breaking waves and are of importance to the study of coastal erosion, etc.

On a more pragmatic side, the study of the waves using a three-dimensional version of this numerical implementation is also warranted. While three-dimensional breakers are another class of waves which deserve study, a wave which is initially two-dimensional and breaks contains three-dimensional flow components. A numerical capability which allows for this type of flow is necessary to discuss the effects of air entrainment and strong turbulence in wave breaking. However, efforts to improve the numerical efficiency of the code as discussed earlier should be implemented as well to keep the computational costs at a reasonable level.

The effect of a larger Reynolds number should also be included through a basic Large Eddy Simulation (LES). While this type of turbulence closure would be based on basic models verses models specifically designed for the physics of wave breaking, it would allow the simulation of Reynolds numbers of one to two orders of magnitude larger than the present study could attain. While this is only the lower limit of the Reynolds number at laboratory scales, it is another necessary step towards the simulation of breaking waves at larger scales.

Finally, the question of how to apply the knowledge gained in this study to future efforts still remains. Some might argue that the Reynolds numbers available to DNS are too restrictive to be useful for study of the effects of breaking waves at the scales which matter to engineering applications. There is some validity to this argument as it is unlikely that directly scaling the results from DNS to field scales would be entirely fruitful. This is even the case when discussing laboratory scales as the largest waves are still an order of magnitude less than scales seen in the open ocean. Yet, DNS provides important information about physical mechanisms during breaking as simulations using potential flow techniques provide for the pre-breaking phase. An extensive database of high-resolution DNS results for a variety of breaking waves is considered quite valuable. This type of database could be used to develop statistical descriptions of wave breaking. It can also be used to test the applicability of current turbulence closure models in the context of breaking waves and the development of

new ones if necessary. Without the validity of the turbulence closure models in place, there is no degree of certainty that the turbulence models are not masking some of the physics involved. Thus, numerical studies such as LES and LWS that involve wave breaking at larger scales such as the laboratory may provide qualitative information only if they can not attest to the validity of their closure models.

Yet, if physics-based turbulence closure models are developed and validated, a similar process can be applied to go from the laboratory to the field scale using advanced LES and LWS. At these scales, many of the questions about the effects of the coupled air-water interface during breaking on the transfer rates can be answered more authoritatively. A similar database at laboratory scale can be used to determine statistical descriptions and test closure models appropriate for RANS (steady or unsteady). With validated RANS closure models in place, quantitative simulation of the near field flow of a surface ship for design purposes is an attainable goal.

Bibliography

[1] D. Adalsteinsson and J. A. Sethian. A fast level set method for propagating interfaces. *J. Comp. Phys.*, 120(1):269–277, 1995.

[2] E. Baba. Study on separation of ship resistance components. Technical Report 59, Mitsubishi Heavy Ind. Tech. Bull., Tokyo, Jpn, 1969. pp. 16.

[3] M. L. Banner. The importance of wave breaking on the sea surface. In A. Brandt, S. E. Ramberg, and M. F. Shlesinger, editors, *Nonlinear Dynamics of Ocean Waves*, pages 178–189, Singapore, May 1992. The Johns Hopkins University Applied Physics Laboratory, World Scientific.

[4] M. L. Banner and D. H. Peregrine. Wave breaking in deep water. *Annu. Rev. Fluid Mech.*, 25:373–397, 1993.

[5] M. L. Banner and X. Tian. On the determination of the onset of wave breaking for modulating surface gravity water waves. *J. Fluid Mech.*, 367:107–137, 1998.

[6] C. M. Bender and S. A. Orszag. *Advanced Mathematical Methods for Scientists and Engineers I: Asymptotic Methods and Perturbation Theory.* Springer, NY, 1999.

[7] E. J. Boettcher, J. Fineberg, and D. P. Lathrop. Turbulence and wave breaking effects on air-water gas exchange. *Physical Review Letters*, 85(9):2030–2033, August 2000.

[8] P. Bonmarin. Geometric properties of deep-water breaking waves. *J. Fluid Mech.*, 209:405–433, 1989.

[9] J. U. Brackbill, D. B. Kothe, and C. Zemach. A continuum method for modeling surface tension. *J. Comp. Phys.*, 100:335–354, 1992.

[10] M. Brocchini and D. H. Peregrine. The dynamics of strong turbulence at free surfaces. part 2. free-surface boundary conditions. *J. Fluid Mech.*, 449:255–290, 2001.

[11] G. F. Carrier and C. E. Pearson. *Partial Differential Equations: Theory and Technique.* Academic Press, Boston, 2nd edition, 1988.

[12] Y. Chang, T. Y. Hou, B. Merriman, and S. Osher. A level set formulation of eulerian interface capturing methods for incompressible fluid flows. *J. Comp. Phys.*, 124:449–464, 1996.

[13] G. Chen and C. Kharif. Two-dimensional navier-stokes simulation of breaking waves. *Phys. of Fluids*, 11(1):121–133, 1999.

[14] E. D. Christensen and R. Deigaard. Large eddy simulation of breaking waves. *Coastal Engineering*, 42(1):53–86, January 2001.

[15] R. Cointe and M. Tulin. A theory of steady breakers. *Journal of Fluid Mechanics*, 276:1–20, 1994.

[16] D. Dabiri and M. Gharib. Experimental investigation of the vorticity generation within a spilling water wave. *J. Fluid Mech.*, 330:113–139, 1997.

[17] R. A. Dalrymple and P. L. Liu. Waves over soft muds: A two-layer fluid model. *J. Phys. Oceango.*, 8(6):1121–1131, 1978.

[18] A. A. Dimas and L. T. Fialkowski. Large-wave simulation (lws) of free-surface flows developing weak spilling breaking waves. *J. Comp. Phys.*, 159:172–196, 2000.

[19] J. W. Dold and D. H. Peregrine. Water-wave modulation. In *Proc. 20th Conf. Coastal Eng.*, volume 1, pages 163–175, Taipei, 1986. ASCE.

[20] D. Dommermuth, G. Innis, T. Luth, E. Novikov, E. Schlageter, and J. Talcott. Numerical simulation of bow waves. In *Proceedings of 22nd Symposium on Naval Ship Hydrodynamics*, pages 159–172, 1998.

[21] D. G. Dommermuth. private communication.

[22] D. G. Dommermuth. The laminar interactions of a pair of vortex tubes with a free surface. *J. Fluid Mech.*, 246:91–115, 1993.

[23] D. G. Dommermuth. The initialization of nonlinear waves using an adjustment scheme. *Wave Motion*, 32:307–317, 2000.

[24] D. G. Dommermuth, D. K. Yue, W. M. Lin, R. J. Rapp, E. S. Chan, and W. K. Melville. Deep-water plunging breakers: a comparison between potential theory and experiments. *Journal of Fluid Mechanics*, 189:423–442, 1988.

[25] M. Donelan, M. S. Longuet-Higgins, and J. S. Turner. Periodicity in whitecaps. *Nature*, 239:449–451, 1972.

[26] M. A. Donelan. *Wind-over-Wave Couplings*, chapter Wind-induced growth and attenuation of laboratory waves., page 356 pp. Clarendon Press, 1999.

[27] B. D. Dore. Some effects of the air-water interface on gravity waves. *Geophys. Astrophys. Fluid Dynamics*, 10:215–30, 1978.

[28] J. Duncan, H. Qiao, V. Philomin, and A. Wenz. Gentle spilling breakers: crest profile evolution. *J. Fluid Mech.*, 379:191–222, 1999.

[29] J. H. Duncan. An experimental investigation of breaking waves produced by a towed hydrofoil. *Proc. Royal Soc. London, A*, 377(1770):331–348, July 1981.

[30] J. H. Duncan. The breaking and non-breaking wave resistance of a two-dimensional hydrofoil. *J. Fluid Mech.*, 126:507–520, 1983.

[31] J. H. Duncan. Spilling breakers. *Annu. Rev. Fluid Mech.*, 33:519–547, 2001.

[32] J. H. Duncan. Air entrainment in 2d+t experiments on breaking bow waves. ONR Ship Wave Breaking and Bubbly Flow Review, 2004.

[33] G. E. Forsythe and W. R. Wasow. *Finite Difference Methods for Partial Differential Equations.* John Wiley and Sons, NY, 1960.

[34] C. J. Galvin. Breaker type classification on three laboratory beaches. *J. Geophys. Res.*, 73(12):3651–3659, 1968.

[35] L. Gentaz, C. Maury, B. Alessandrini, and G. Delhommeau. Numerical simulations of a two-dimensional wave tank in a viscous fluid. *Int. J. Offshore and Polar Engineering*, 10(1):1–9, Mar 2000.

[36] A. G. Godfrey, C. R. Mitchell, and R. W. Walters. Practical aspects of spatially high-order accurate methods. *AIAA J.*, 31(9):1634–1642, 1993.

[37] R. A. Granger. *Fluid Mechanics*, chapter 5. Dover Publications, 1995.

[38] M. Greenhow. Free-surface flows related to breaking waves. *J. Fluid Mech.*, 134:259–275, 1983.

[39] F. H. Harlow and J. E. Welch. Numerical calculation of time-dependent viscous incompressible flow of fluid with free surface. *Phys. Fluids*, 8(12):2182–2189, December 1965.

[40] A. Harten. High-resolution schemes for hyperbolic conservation laws. *J. Comp. Phys.*, 49:357–393, 1983.

[41] A. Harten. On a class of high-resolution total-variation-stable finite-difference schemes. *SIAM J. Numer. Anal*, 21:1, 1984.

[42] A. Harten. Preliminary results on the extension of eno schemes to two-dimensional problems. In *Proceedings of the International Conference on Hyperbolic Problems*, Saint-Eitenne, January 1986.

[43] K. Hasselmann. On the nonlinear energy transfer in a gravity-wave spectrum. part 1: General theory. *J. Fluid Mech.*, 12:481–500, 1962.

[44] P. F. Hoffman, A. J. Kaufman, G. P. Halverson, and D. P. Schrag. A neoproterozoic snowball earth. *Science*, 281(5381):1342 1346, August 1998.

[45] A. Iafrati and E. F. Campana. A domain decomposition approach to compute wave breaking (wave-breaking flows). *Int. J. Numer. Meth. Fluids*, 41:419–445, 2003.

[46] A. Iafrati, A. D. Mascio, and E. F. Campana. A level set technique applied to unsteady free surface flows. *Int. J. Numer. Meth. Fluids*, 35(3):281–297, 2001.

[47] H. W. Iversen. Laboratory study of breakers. In *Gravity Waves*, volume 521 of *Natl. Bur. Stand. Circ.*, pages 9–32. 1952.

[48] G. Jin and M. Braza. A nonreflecting outlet boundary condition for incompressible unsteady navier-stokes calculations. *J. Comp. Phys.*, 107:239–253, 1993.

[49] B. C. V. Johansson. Boundary conditions for open boundaries for the incompressible navier-stokes equation. *J. Comp. Phys.*, 105:233–251, 1993.

[50] S. P. Kjeldsen and D. Myrhaug. Kinematics and dynamics of breaking waves. In *Ships in Rough Seas*, number STF60 A78100, chapter Part 4. Norwegian Hydrodynamic Laboratories, Trondheim, Norway, 1978.

[51] G. J. Komen, L. Cavaleri, K. Hasselmann, S. Hasselmann, and P. Janssen. *Dynamics and Modeling of Ocean Waves*. Cambridge University Press, Cambridge, 1994.

[52] G. J. Komen, L. Cavaleri, K. Hasselmann, S. Hasselmann, and P. Janssen. *Dynamics and Modeling of Ocean Waves*. Cambridge University Press, Cambridge, 1994.

[53] D. B. Kothe. *Free Surface Flows*, chapter Perspective on Eulerian Finite Volume Methods for Incompressible Interfacial Flows. Springer, 1998.

[54] J. H. Kway, Y.-S. Loh, and E.-S. Chan. Laboratory study of deep-water breaking waves. *Ocean Engng*, 25(8):657–676, 1998.

[55] E. Lamarre and W. K. Melville. Air entrainment and dissipation in breaking waves. *Nature*, 351:469–472, 1991.

[56] S. H. Lamb. *Hydrodynamics*, chapter Art. 267. Cambridge University Press, 6th edition, 1932.

[57] S. H. Lamb. *Hydrodynamics*, chapter Art. 348. Cambridge University Press, 6th edition, 1932.

[58] L. Landau and E. M. Lifshitz. *Fluid Mechanics*. Butterworth-Heinemann, 2nd edition, 1987.

[59] J. C. Lin and D. Rockwell. Evolution of a quasi-steady breaking wave. *J. Fluid Mech.*, 302:29–44, 1995.

[60] P. L. F. Liu and K. Al-Banaa. Solitary wave runup and force on a vertical barrier. *J. Fluid Mech.*, 505:225–233, April 2004.

[61] S. Liu, K. Hendrickson, X. Dong, L. Shen, and D. K. Yue. Numerical investigation of coupled boundary layers air-sea transfer (cblast) at small scales. accepted to the 16th Symposium on Boundary Layers and Turbulence, August 2004.

[62] Y. M. Liu, M. Xue, and D. K. Yue. Computations of fully nonlinear three-dimensional wave-wave and wave-body interactions. part 2. nonlinear waves and forces on a body. *J. Fluid Mech.*, 438:41–66, 2001.

[63] M. Longuet-Higgins. Progress towards understanding how waves break. In *Proc. 21st Symp. Nav. Hydrodyn.*, pages 7–28, Trondheim, Nor., 1997.

[64] M. S. Longuet-Higgins. Parametric solutions for breaking waves. *J. Fluid Mech.*, 121:403–424, 1982.

[65] M. S. Longuet-Higgins. Capillary rollers and bores. *J. Fluid Mech.*, 240:659–679, 1992.

[66] M. S. Longuet-Higgins. Shear instability in spilling breakers. *Proc. Royal Soc. London, A*, 446:399–409, 1994.

[67] M. S. Longuet-Higgins. On the disintegration of the jet in a plunging breaker. *J. Phys. Oceango.*, 25:2458–2462, October 1995.

[68] M. S. Longuet-Higgins and E. D. Cokelet. The deformation of steep surface waves on water. i. a numerical method of computation. *Proc. Royal Soc. London, A*, 350:1–26, 1976.

[69] M. S. Longuet-Higgins and E. D. Cokelet. The deformation of steep surface waves on water. ii. growth of normal mode instabilities. *Proc. Royal Soc. London, A*, 364:1–28, 1978.

[70] M. R. Lowan and W. K. Melville. Microwave backscatter and acoustic radiation from breaking waves. *J. Fluid Mech.*, 224:601–623, 1991.

[71] M. A. Mason. Some observations of breaking waves. In *Gravity Waves.*, volume 521 of *Natl. Bur. Stand. Circ.*, pages 215–220. 1952.

[72] C. C. Mei and L. F. Liu. The damping of surface gravity waves in a bounded liquid. *J. Fluid Mech.*, 59:239–256, 1973.

[73] W. K. Melville. The instability and breaking of deep-water waves. *J. Fluid Mech.*, 115:168–185, 1982.

[74] W. K. Melville. Energy dissipation by breaking waves. *Journal of Physical Oceanography*, 24:2041–2049, October 1994.

[75] W. K. Melville. The role of surface-wave breaking in air-sea interaction. *Annu. Rev. Fluid Mech.*, 28:279–321, 1996.

[76] W. K. Melville and R. J. Rapp. Momentum flux in breaking waves. *Nature*, 317(6037):514–516, October 1985.

[77] W. K. Melville, F. Veron, and C. White. The velocity field under breaking waves: coherent structures and turbulence. *J. Fluid Mech.*, 454:203–233, 2002.

[78] A. R. Mitchell and D. F. Griffiths. *The Finite Difference Method in Partial Differential Equations.* John Wiley and Sons, NY, 1980.

[79] G. Muller and T. J. T. Whittaker. An evaluation of design wave impact pressures. *ASCE Journal of Waterw. Port, Coastal and Ocean Engng*, 122(1):55–58, 1996.

[80] H. M. Nepf, C. H. Wu, and E. S. Chan. A comparison of two- and three-dimensional wave breaking. *J. Phys. Oceango.*, 28:1496–1510, July 1998.

[81] A. L. New. A class of elliptical free-surface flows. *J. Fluid Mech.*, 130:219 239, 1983.

[82] H. Oka and K. Ishii. Numerical analysis on the motion of gas bubbles using level set method. *J. Phys. Soc. Jpn.*, 68(3):823 832, 1999.

[83] S. Osher and R. Fedkiew. *Level Set Methods and Dynamic Implicit Surfaces*, volume 153 of *Applied Mathematical Sciences.* Springer, 2003.

[84] S. Osher and J. A. Sethian. Fronts propagating with curvature-dependent speed: algorithms based on hamilton-jacobi formulations. *J. Comp. Phys.*, 79(1):12–49, 1988.

[85] M. Perlin, J. He, and L. P. Bernal. An experimental study of deep water plunging breakers. *Phys. Fluids*, 8(9):2365–2374, September 1996.

[86] C. S. Peskin. Numerical analysis of blood flow in the heart. *J. Comp. Phys.*, 25:220–252, 1977.

[87] O. M. Phillips. *The Dynamics of the Upper Ocean.* Cambridge, 2 edition, 1977.

[88] O. M. Phillips. Spectral and statistical properties of equilibrium range in wind-generated gravity waves. *Journal of Fluid Mechanics*, 156:505–531, 1985.

[89] W. H. Press, S. A. Teukolsky, W. T. Vetterling, and B. P. Flannery. *Numerical Recipes in Fortran 77*, volume 1. Press Syndicate of University of Cambridge, 1992.

[90] H. Qiao and J. Duncan. Gentle spilling breakers: crest flow-field evolution. *J. Fluid Mech.*, 439:57–85, 2001.

[91] R. J. Rapp. *Laboratory measurements of deep water breaking waves.* PhD thesis, Massachusetts Institute of Technology, 1986.

[92] R. J. Rapp and W. K. Melville. Laboratory measurements of deep-water breaking waves. *Philos. Trans. Royal. Soc. London A*, 331:735–800, 1990.

[93] E. P. Rood. *Mechanics USA*, volume 47, chapter Myths, math and physics of free-surface vorticity, pages S152 S156. American Society of Mechanical Engineers, June 1994. part 2.

[94] E. P. Rood. *Fluid Vortices*, chapter Vorticity interactions with a free surface, pages 687 730. Kluwer Academic Publishers, Netherlands, 1995. Chapter XVI.

[95] G. Russo and P. Smereka. A remark on computing distance functions. *J. Comp. Phys.*, 163:51–67, 2000.

[96] J. L. Sarmiento and C. LeQuéré. Oceanic carbon dioxide uptake in a model of century-scale global warming. *Science*, 274(5291):1346–1350, November 1996.

[97] J. A. Sethian. Fast marching methods. *SIAM Review*, 41(2):199 235, 1999.

[98] J. A. Sethian and P. Smereka. Level set methods for fluid interfaces. *Annu. Rev. Fluid Mech.*, 35:341–372, 2003.

[99] L. Shen, X. Zhang, D. K. Yue, and G. S. Triantafyllou. The surface layer for free-surface turbulent flows. *J. Fluid Mech.*, 386:167–212, 1999.

[100] C.-W. Shu and S. Osher. Efficient implementation of essentially non-oscillatory shock-capturing schemes. *J. Comp. Phys.*, 77:439–471, 1988.

[101] C.-W. Shu and S. Osher. Efficient implementation of essentially non-oscillatory shock-capturing schemes, ii. *J. Comp. Phys.*, 83:32–78, 1989.

[102] I. N. Sneddon. *Elements of Partial Differential Equations.* McGraw-Hill Book Company, New York, 1957.

[103] J. B. Song and M. L. Banner. On determining the onset and strength of breaking for deep water waves. part i: Unforced irrotational wave groups. *J. Phys. Oceango.*, 32:2541–2558, September 2002.

[104] J. B. Song and M. L. Banner. On determining the onset and strength of breaking for deep water waves. part ii: Influence of wind forcing and surface shear. *J. Phys. Oceango.*, 32:2541–2558, September 2002.

[105] P. Stansell and C. MacFarlane. Experimental investigation of wave breaking criteria based on wave phase speeds. *J. Phys. Oceango.*, 32(5):1269–1283, 2002.

[106] G. G. Stokes. On the theory of oscillatory waves. *Trans. Cambridge. Phil. Soc.*, 8:441–455, 1847.

[107] M.-Y. Su, M. Bergin, P. Marlev, and R. J. Myrick. Experiments on nonlinear instabilities and evolution of steep gravity wave trains. *J. Fluid Mech.*, 124:45–72, 1982.

[108] T. Sur and K. Chevalier. Field measurements of bow spray droplets. Final Report N00014-03-C-0105, Science Applications International Corporation, San Diego, CA, 2003.

[109] M. Sussman and D. G. Dommermuth. The numerical simulation of ship waves using cartesian-grid methods. In *Proc. of the 23rd Symp. on Naval Hydro.*, pages 762–779, Nantes, France, 2001.

[110] M. Sussman and E. Fatemi. An efficient, interface-preserving level set redistancing algorithm and its application to interfacial incompressible fluid flow. *SIAM J. Sci. Comput.*, 20(4):1165–1191, 1999.

[111] M. Sussman, E. Fatemi, P. Smereka, and S. Osher. An improved level set method for incompressible two-phase flows. *Computers & Fluids*, 27(5-6):663–680, 1998.

[112] M. Sussman and P. Smereka. Axisymmetric free boundary problems. *J. Fluid Mech.*, 341:269–294, 1997.

[113] M. Sussman, P. Smereka, and S. Osher. A level set approach for computing solutions to incompressible two-phase flow. *J. Comp. Phys.*, 114:146–159, 1994.

[114] P. N. Swarztrauber. Fftpack. URL: http://www.netlib.org/fftpack. Reference: P.N. Swarztrauber, Vectorizing the FFTs, in Parallel Computations (G. Rodrigue, ed.), Academic Press, 1982, pp. 51–83.

[115] Y. t. Yao, P. Wang, and M. P. Tulin. Wave-groups, wave-wave interactions and wave breaking. In *Proc. 20th ONR Symp. on Naval Hydrodynamics*, pages 551–567, Santa Barbara, 1994. Natl. Academy Press.

[116] G. I. Taylor. The dynamics of thin sheets of fluid ii. waves on fluid sheets. *Proc. Royal Soc. London, A*, 253:296–312, 1959.

[117] J. J. Thomson and H. F. Newall. On the formation of vortex rings by drops falling into liquids and other allied phenomena. *Proc. Royal Soc. London, A*, 39:417, 1885.

[118] W.-T. Tsai and D. K. Yue. Effects of soluble and insoluble surfactant on laminar interactions of vortical flows with a free surface. *J. Fluid Mech.*, 289:315–349, 1995.

[119] M. P. Tulin. *Breaking of ocean waves and downshifting*, pages 177–190. Kluwer Acad., Dordrecht, Neth., 1996.

[120] M. P. Tulin and M. Landrini. Breaking waves in the ocean and around ships. Proc. 23rd ONR Symposium on Naval Hydrodynamics, Val de Reuil, France, 2000.

[121] S. O. Unverdi and G. Tryggvason. A front-tracking method for viscous, incompressible, multi-fluid flows. *J. Comp. Phys.*, 100:25–37, 1992.

[122] P. Wang, Y. Yao, and M. P. Tulin. Wavegroup evolution, wave deformation and breaking: simulation using longtank, a numerical wave tank. *Int. J. Offshore and Polar Eng.*, 4:200–205, 1994.

[123] J. Wen and P. L. Liu. Mass transport of interfacial waves in a two-fluid system. *J. Fluid Mech.*, 297:231–254, 1995.

[124] G. B. Whitham. Mass, momentum and energy flux in water waves. *J. Fluid Mech.*, 12:135–147, 1962.

[125] M. W. Williams, D. B. Kothe, and E. G. Puckett. Accuracy and convergence of continuum surface tension models. Technical Report LA-UR-98-2268, Los Alamos National Laboratory, 1998.

[126] J. H. Williamson. Low-storage runge-kutta schemes. *J. Comp. Phys.*, 35:48–56, 1980.

[127] C. H. Wu and H. M. Nepf. Breaking criteria and energy losses for three-dimensional wave breaking. *Journal of Geophysical Research*, 107(C10):1–17, 2002.

[128] M. Xue, H. B. Xu, Y. M. Liu, and D. K. Yue. Computations of fully nonlinear three-dimensional wave-wave and wave-body interactions. part 1. dynamics of steep three-dimensional waves. *J. Fluid Mech.*, 438:11–39, 2001.

[129] J. Zhu. *Solving Partial Differential Equations on Parallel Computers*, chapter 2. World Scientific, Singapore, 1994.